

Stimuli-Responsive Supramolecular Systems: From Dynamic Combinatorial Libraries to Photoswitchable Rotaxanes on Surfaces

Dissertation to obtain the academic degree

Doctor rerum naturalium (Dr. rer. Nat.)

submitted to the Department of Biology, Chemistry and Pharmacy
of Freie Universität Berlin

by

Felix Benjamin Schwarz, M. Sc.

from Berlin

2016

Die vorliegende Arbeit wurde im Zeitraum von Oktober 2012 bis Dezember 2016 am Institut für Chemie und Biochemie des Fachbereichs Biologie, Chemie, Pharmazie der Freien Universität Berlin unter der Anleitung von Prof. Dr. Christoph A. Schalley durchgeführt.

1. Gutachter: Prof. Dr. Christoph A. Schalley

2. Gutachter: Prof. Dr. Rainer Haag

Disputation am: 23.01.2017

Ich versichere, dass ich die vorliegende Arbeit selbstständig verfasst und keine anderen als die angegebenen Quellen und Hilfsmittel benutzt habe.

Felix Benjamin Schwarz

08.12.2016

V

Abstract

Within the umbrella theme of stimuli-responsive supramolecular systems, the present thesis deals with different photoswitchable rotaxanes in solution and on surfaces and, in a side project, with the study of a dynamic combinatorial library using mass spectrometry.

Two novel photoswitchable binding sites for Hunter-Vögtle-type tetralactam macrocycles based on spiropyran and azobenzene chromophors have been developed, that both can be reversibly switched between a binding and a non-binding state. The binding sites were used for constructing different photoswitchable rotaxanes that could be reversibly switched between two distinct states, which induced a shift of the macrocycle along the axle. The switching processes of both the spiropyran- and azobenzene-based rotaxanes have been characterised in detail in solution using UV-Vis and NMR spectroscopy.

With an axle containing the azobenzene binding site, a photocontrolled deposition into well-ordered surface-bound macrocycle multilayers to form pseudorotaxanes was demonstrated. Glass, silicon and gold surfaces have been functionalised with pyridine-terminated SAMs and subsequently with multilayers of macrocycles through layer-by-layer self-assembly. The photocontrolled deposition of the axle into the surface-bound macrocycle-multilayers was monitored by UV-Vis, XPS and NEXAFS spectroscopy. Angle-resolved NEXAFS spectra revealed a preferential orientation of the macrocycles with even more pronounced linear dichroism effects upon photoinduced binding of the axle.

The azobenzene-based rotaxane was functionalised with either a terpyridine or an alkyne group and deposited in a monolayer on glass and silicon surfaces using either layer-by-layer self-assembly or azide-alkyne click chemistry. The photoinduced switching processes on the surface have been studied in detail with contact angle measurements, UV-Vis, XPS and NEXAFS spectroscopy. Both, the covalently and the coordinatively bound monolayers of rotaxanes could be reversibly switched between two distinct states on the surfaces. NEXAFS spectroscopy revealed a preferential orientation in the monolayers, which reversibly changes upon photoswitching of the rotaxane.

In the side project, a dynamic combinatorial library of tetrahedral M_4L_6 cages was analysed with ESI-FTICR MS and IRMPD experiments. A qualitative and quantitative analysis of the DCL constitution was performed, whereby all constitutional isomers of cages and their relative abundances were measured. The DCL was shown to be responsive to the addition of either a crown ether or a C_{70} fullerene, resulting in a specific reconstitution.

Kurzzusammenfassung

Die vorliegende Dissertation beschäftigt sich unter dem Oberthema der stimuli-responsiven supramolekularen Systeme mit photoschaltbaren Rotaxanen in Lösung und auf Oberflächen, sowie in einem Nebenprojekt mit der Untersuchung einer dynamischen kombinatorischen Bibliothek mittels Massenspektrometrie.

Zwei neue photoschaltbare Bindungsstationen für Hunter-Vögtle-Tetralactam-Makrozyklen wurden unter Einsatz von Azobenzol und Spiropyran als photoschaltbare Elemente entwickelt und untersucht. Beide Bindungsstationen können reversibel zwischen einem bindenden und einem nicht-bindenden Zustand geschaltet werden. Auf Grundlage dieser Bindungsstationen wurden verschiedene photoschaltbare Rotaxane synthetisiert, in denen ein Licht Stimulus zu einer Verschiebung des Makrozyklus entlang der Achse führt. Die reversible Photoschaltung der Rotaxane wurde detailliert in Lösung mit UV-Vis- und NMR-Spektroskopie untersucht.

Es konnte eine lichtgesteuerte Pseudorotaxanbildung der Azobenzol-Bindungsstation mit geordneten Makrozyklus-Multilagen auf Oberflächen gezeigt werden. Glas-, Silizium- und Goldoberflächen wurden hierzu mit pyridinterminierten SAMs gefolgt von Multilagen von Tetralactam-Makrozyklen mittels *layer-by-layer self-assembly* beschichtet. Die lichtgesteuerte Einlagerung der Bindungsstation in die oberflächengebundenen Multilagen konnte mit UV-Vis-, XPS- und NEXAFS-Spektroskopie verfolgt werden. Mit Hilfe von winkelabhängigen NEXAFS-Messungen wurde eine Vorzugsorientierung der Makrozyklus-Multilagen nachgewiesen, welche durch die Einlagerung der Azobenzol-Bindungsstation verstärkt wurde.

Ein azobenzolbasiertes photoschaltbares Rotaxan konnte mit einer Terpyridin- oder Alkingruppe funktionalisiert und mittels *layer-by-layer self-assembly* oder Azid-Alkin-Clickchemie in einer Monolage auf Glas- und Siliziumoberflächen abgeschieden werden. Die Photoschaltung auf der Oberfläche wurde detailliert mit Kontaktwinkelmessungen, UV-Vis-, XPS- und NEXAFS-Spektroskopie untersucht. Sowohl die kovalent als auch die koordinativ gebundenen Rotaxane konnten mit Licht verschiedener Wellenlängen reversibel zwischen zwei Zuständen geschaltet werden. Mit NEXAFS-Spektroskopie wurde eine Vorzugsorientierung der Rotaxane nachgewiesen, welche sich durch die Photoschaltung reversibel ändert.

Eine dynamische kombinatorische Bibliothek von M_4L_6 -Käfigen wurde mit ESI-FTICR-MS- und IRMPD-Experimenten untersucht, wobei eine qualitative und quantitative Bestimmung aller konstitutionellen Isomere und ihrer relativen Konzentrationen durchgeführt wurde. Die Zugabe eines Kronenethers oder eines C_{70} -Fullerens beeinflusste die konstitutionelle Zusammensetzung der DCL.

Table of contents

1. Introduction	1
2. Research objectives	5
3. Theoretical background.....	9
3.1. Supramolecular chemistry.....	9
3.1.1. Host-guest complexes.....	10
3.1.2. Mechanically interlocked molecules	13
3.2. Stimuli-responsive rotaxanes	16
3.2.1. Chemically switchable rotaxanes.....	18
3.2.2. Electrochemically switchable rotaxanes	19
3.2.3. Photoswitchable rotaxanes.....	21
3.3. Interface chemistry – organic thin films on surfaces	37
3.3.1. Self-assembled monolayer (SAM) on gold, glass and silicon surfaces	38
3.3.2. Mono- and multilayer architectures on surfaces	41
3.3.3. Switchable supramolecular assemblies on surfaces.....	47
3.3.4. Analytical methods for surfaces.....	52
3.4. Dynamic combinatorial libraries (DCLs)	64
3.4.1. ESI-FTICR MS as analytical tool for the analysis of complex systems	67
4. Photoswitchable (pseudo-)rotaxanes in solution and on surfaces.....	71
4.1. Spiropyran-based rotaxanes	71
4.2. Azobenzene-based (pseudo-)rotaxanes.....	87
4.2.1. Photocontrolled on-surface pseudorotaxane formation with well-ordered macrocycle multilayers	87
4.2.2. A photoswitchable rotaxane operating in monolayers on solid support.....	103
5. Stimuli responsive dynamic combinatorial libraries.....	117
5.1. Catenation and encapsulation induce distinct reconstitutions within a dynamic library of mixed-ligand Zn_4L_6 cages	117
6. Conclusions and perspectives	135

7. Experimental section	139
7.1. General methods	139
7.2. Instrumentation	139
7.3. Experimental procedures for chapter 4.1	141
7.4. Experimental Procedures for chapter 4.2.1	156
7.5. Experimental procedures for chapter 4.2.2.....	169
7.6. Experimental procedures for chapter 5.1.....	187
8. Acknowledgements	209
9. Appendix	210
9.1. Publications	210
9.2. Oral and poster presentations	211
9.3. Curriculum Vitae	212
10. References	214

1. Introduction

Nature uses molecular-scale responses towards external stimuli as a key-concept for information processing through signal transduction networks in living organisms. Many biological processes rely on the specific responses of (macro-)molecules like nucleic acids, proteins and polypeptides to changes in their surroundings. Nature found ways to produce changes in conformation or configuration of biomolecules in response to a stimulus with a remarkable complexity, specificity, reproducibility and self-repair ability.

A typical example for a stimuli-responsive biological process is the human vision. When a photon hits the human eye, a complex signal cascade leads to changes in membrane potential of the photoreceptor cell that is transduced into a nerve impulse. At the molecular level, the impact of a photon induces the isomerisation from 11-*cis*-retinal to all-*trans*-retinal, a cofactor in transmembrane proteins in the opsin photopigments (Figure 1). The initial *cis*-configuration is restored by an enzyme under the consumption of ATP. Until then, the photopigment cannot respond to light, which is called bleaching. When a large group of photopigments is bleached, the eye sends information to the central nervous system as if opposite visual information is perceived – the reason why we see negative afterimages after a bright flash of light.^[1]

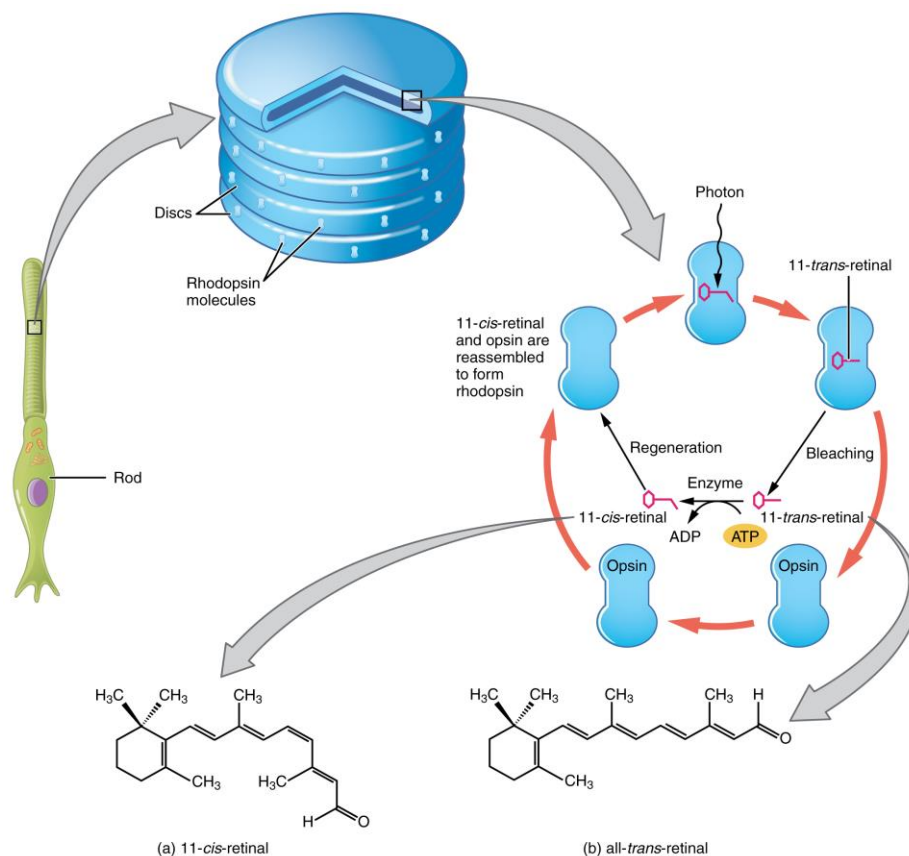


Figure 1: Signal transduction pathway in the opsin pigments of a human eye. Reprinted from reference [1], CC-BY 3.0)

For many years, chemists from various subdisciplines have been fascinated by the idea of creating artificial systems to understand and mimic the natural stimuli-responsive activities. Inspired by the natural archetypes, chemists have created numerous examples of simple stimuli-responsive systems that are capable of performing specific tasks.^[2] Starting from the smallest available building blocks, atoms and molecules, larger defined structures have been created. This procedure is referred to as the bottom-up approach and represents the fundamental opposite to the state-of-the-art top-down approach in industry where existing macroscopic structures are refined to get ever smaller.^[3]

Such bottom-up fabricated stimuli-responsive molecular assemblies are commonly referred to as molecular machines, which were defined by Fraser Stoddart as “an assembly of a distinct number of molecular components that are designed to perform machine-like movements (output) as a result of an appropriate external stimulation (input).”^[4] Molecular machines do not only differ from their macroscopic analogues in size, but also in how their mode of action is influenced by external factors. Molecular machines exhibit a negligible moment of inertia, and their components undergo continuous random movements as a result of Brownian motion. The precise control over the motion of subcomponents in molecular machines relative to each other is a challenging task that has been approached in various examples using chemical, electrochemical or photochemical stimuli.^[4-5] The great interest in and the importance of this research area was reflected by the Nobel prize in chemistry in 2016, which was awarded to Jean-Pierre Sauvage, Fraser Stoddart and Ben Feringa, three pioneers of this field, for “the design and synthesis of molecular machines”.^[6] Jean-Pierre Sauvage introduced the template synthesis as a straightforward route to catenanes and rotaxanes, that enables the accessibility of substantial amounts of these systems - a prerequisite for further developments.^[7] Based on that, he later was able to create a [2]catenane, in which a controlled stimuli-induced movement of one ring along the other one was achieved (Figure 2a).^[8] Fraser Stoddart was the first to show controlled translational isomerism in a rotaxane shuttle.^[9] A more elaborate example of his works is the “molecular elevator”, a stimuli-responsive rotaxane where the motion of a moving plane between two stations over a distance of 0.7 nm could be controlled (Figure 2b).^[10] Ben Feringa was the first to demonstrate a molecule capable of a controlled unidirectional rotation along its axis. Using overcrowded alkenes, the unidirectional rotation was achieved through cycles of light irradiation and thermal relaxation (Figure 2c).^[11]

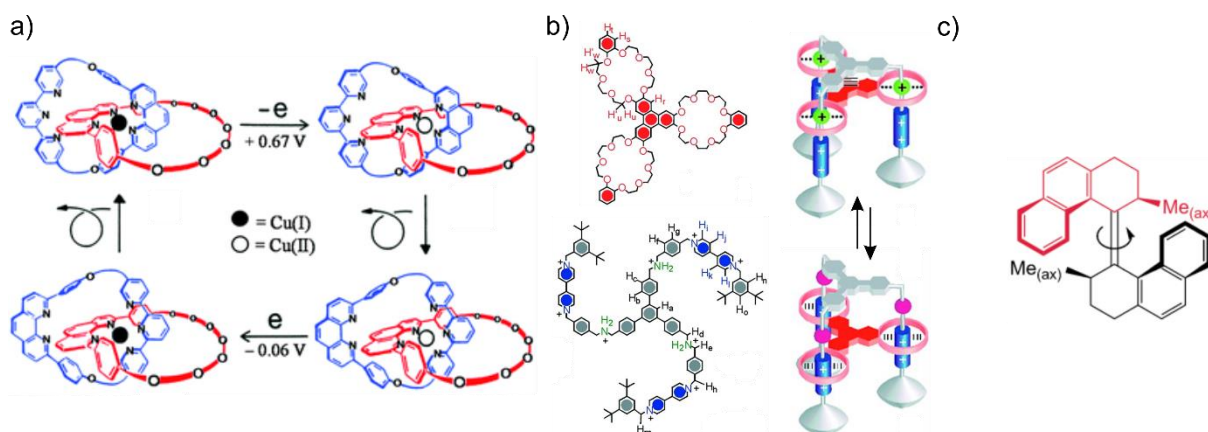


Figure 2: Examples of prototypical molecular machines. a) Switchable catenane from Jean-Pierre Sauvage, b) molecular elevator from Fraser Stoddart and c) molecular motor from Ben Feringa. Reprinted with permission from a) S. Durot, F. Reviriego, J.-P. Sauvage, *Dalton Trans.* **2010**, 39, 10557-10570. Copyright (2010) The Royal Society of Chemistry and b) J. D. Badjić, V. Balzani, A. Credi, S. Silvi, J. F. Stoddart, *Science* **2004**, 303, 1845-1849. Copyright (2004) The American Association for the Advancement of Science.

Major challenges in the creation of more complex and useful molecular machines that can actually deliver macroscopic work include the implementation of directional processes and the addressing of individual molecules in larger systems. In solution, molecules are randomly oriented, resulting in incoherent behaviour. Where nature uses membranes to arrange molecules in an ordered way, chemists found means to deposit ordered layers of molecular machines on surfaces and at interfaces. Several promising examples have been reported for assemblies of molecular machines at interfaces, not only from the Nobel laureates but also from many other groups.^[12]

Although these systems represent the great advances that have been made, they are still subject of basic academic research and far away from being used in real applications. By now, the first examples have been reported where assemblies of molecules can deliver macroscopic effects.^[13] However, no example of a molecular machine that actually delivers useful macroscopic work has been reported so far. Compared to the industrial revolution in the 19th century that changed our world with inventions like the steam engines and electric motors, the development of molecular machines is still in an early phase. Although it is too early to foresee whether this field of research has the potential to significantly change our world, it is definitely worth following and contributing to this fascinating topic.

2. Research objectives

Within the umbrella theme of stimuli-responsive supramolecular systems, the objectives of this thesis were the design, synthesis and examination of different photoswitchable rotaxanes in solution and on surfaces and, as a side project, the study of a dynamic combinatorial library with mass spectrometry.

The main research objective is embedded in the layer-by-layer self-assembly project of the Schalley group, in which complex architectures of supramolecules are deposited in ordered multilayers on surfaces. The long-term goal is the creation of multi-stimuli responsive multilayers of switchable rotaxanes on surfaces. Using orthogonally responsive rotaxanes would allow a specific addressing of individual layers (Figure 3). By depositing the rotaxanes in highly ordered layers, unidirectional concerted motion and potential macroscopic effects might be achieved.

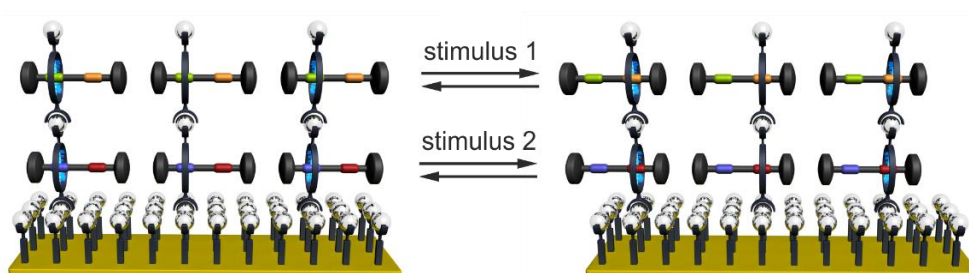


Figure 3: Schematic representation of a surface functionalised with two orthogonally responsive layers of rotaxanes.

The layer-by-layer self-assembly research project was established within previous dissertations in the Schalley group.^[14] Different pyridine or terpyridine substituted monomolecular or mixed self-assembled monolayers were deposited and analysed on gold surfaces (Figure 4a). These SAMs were used to deposit Hunter-Vögtle-type tetralactam macrocycles (TLM) in ordered mono- and multilayers on gold surfaces using metal-ion pyridine/terpyridine coordination chemistry, whereby the deposition sequence of different metal ions and macrocycles could be programmed (Figure 4b). The concept was transferred to glass and silicon substrates and also functionalised nanoparticles were deposited (Figure 4c). Successful on-surface switching could be demonstrated with multilayers of a chemically switchable rotaxane on gold surfaces, that changes the macrocycle position by adding or removing chloride ions (Figure 4d).

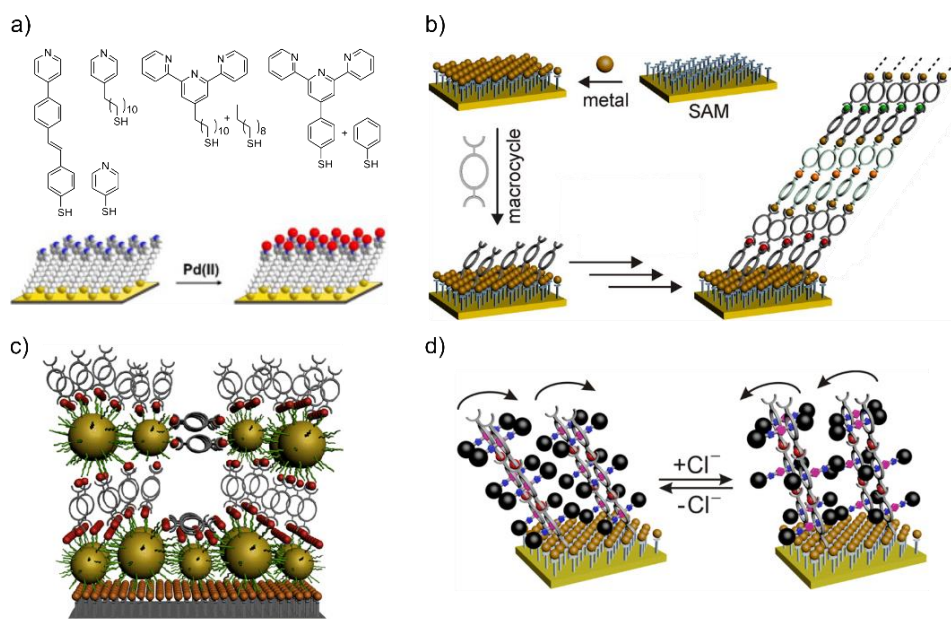


Figure 4: Previous studies within the layer-by-layer self-assembly project of the Schalley group: a) analysis of different pyridine or terpyridine terminated SAMs on gold surfaces, b) programmable multilayers of different macrocycles and metal ions on gold surfaces, c) layer-by-layer deposition of macrocycles and gold nanoparticles on silicon substrates and d) on-surface switching in mono- and multilayers of a chloride-responsive rotaxane. Adapted from references [15].

The aim of the present thesis was the development, analysis and surface deposition of photoswitchable rotaxanes with Hunter-Vögtle-type TLM, that can be integrated into the established multilayer systems later on. Addressing responsive surfaces with light is of great interest within the overall layer-by-layer self-assembly project, as it can be accomplished with high temporal and spacial accuracy. Furthermore, it does not bring in any impurities and therefore allows for an unambiguous analysis of structural changes on the surface. The availability of suitable photoswitchable rotaxanes in combination with chemically switchable rotaxanes would enable the deposition of orthogonally responsive rotaxanes in distinct layers on surfaces.

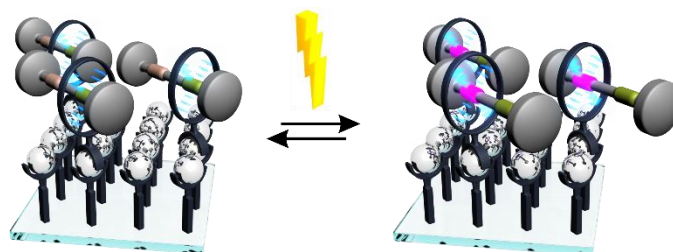


Figure 5: Schematic representation of a photoswitchable rotaxane on a surface.

The following milestones were defined:

- a) Development of different photoswitchable binding sites for tetralactam macrocycles based on spiropyran and azobenzene chromophors.
- b) Photocontrolled on-surface pseudorotaxane formation of these binding sites to multilayers of macrocycles.
- c) Synthesis of photoswitchable rotaxanes that bear pyridine or terpyridine groups for the deposition on surfaces using layer-by-layer self-assembly.
- d) Deposition and reversible on-surface photoswitching of rotaxanes.

In a side project in cooperation with the group of Prof. Jonathan Nitschke, a stimuli-responsive dynamic combinatorial library of tetrahedral M_4L_6 -cages should be studied. Two cages composed of diamine subcomponents containing either naphthalene diimide or porphyrin moieties have been prepared in the Nitschke group. When mixed, the two cages were observed to form a DCL of seven constitutionally isomers. The complexity of the system made NMR analysis impractical and the labile nature of these cages prevented analysis by standard chromatographic separation techniques. The aim within this thesis was to perform a detailed characterisation of the single cages and the DCL using ESI-FTICR MS and tandem MS experiments. A key question was to investigate the responsiveness of the DCL towards different templates and the resulting constitutional changes.

3. Theoretical background

3.1. Supramolecular chemistry

Supramolecular chemistry refers to the chemistry of non-covalently associated molecules and molecular assemblies and focuses on the development of larger molecular systems or molecular arrays through self-assembly processes. Jean-Marie Lehn – one of the founders and Nobel price winners in 1987 – defined supramolecular chemistry as the “chemistry beyond molecules”^[16] in which the main focus is not set on the single molecule and its specific structure anymore but on the development of larger structures with defined properties and functions.

One of the earliest studies that from today's point of view belongs to the field of supramolecular chemistry was conducted in the 18th century by Cronstedt and Priestly on clathrates, the first known inclusion complexes.^[17] The investigation of enzyme substrate complexes by Fischer in the 19th century represents a foundation for later systematic studies on host-guest complexes. In the early 20th century, the first fundamental investigations of non-covalent interactions were conducted by Latimer and Rodebush on hydrogen bonds,^[18] but it took more than further 50 years with fundamental studies from Pedersen, Lehn and Cram before supramolecular chemistry received noteworthy recognition.^[19] In 1987, they were awarded the Nobel price "for their development and use of molecules with structure-specific interactions of high selectivity."^[20] Since then, supramolecular chemistry and self-assembly processes have evolved to be one of the most important fields in modern chemical research of the past thirty years.^[21]

Most non-covalent interactions between molecules or ions exhibit a smaller binding energy than a covalent bond and form reversibly (Table 1). As a result, self-assembly processes with a dynamic error correction in bond formation are enabled. Molecules with complementary steric and electronic information can self-assemble under suitable conditions to the structure with the energetically lowest local state. Due to the reversibility of the interactions, errors in potential self-assembly by-products can be corrected on the way to the final structure. Therefore, carefully designed small molecules combined in the right stoichiometry can form complex, large, and specific aggregates with defined geometry and properties. The combination of multiple non-covalent interactions within such an assembly of small molecules can lead to an overall very strong intermolecular binding and thus to the formation of stable supramolecules.

Table 1: Binding energies of non-covalent interactions.^[17, 22]

Interaction	Binding energy / kJ*mol ⁻¹
ion-ion	100-350
coordinative bond	100-300
ion-dipole	50-200
hydrogen bond	4-160
cation- π	5-80
dipole-dipole	5-50
π - π	2-50
van-der-Waals	< 5

3.1.1. Host-guest complexes

Especially host-guest chemistry has received great interest within supramolecular chemistry in the past decades.^[23] Most host-guest systems use large macrocyclic host molecules that have a cavity capable of incorporating smaller organic or inorganic guest molecules (Figure 6).

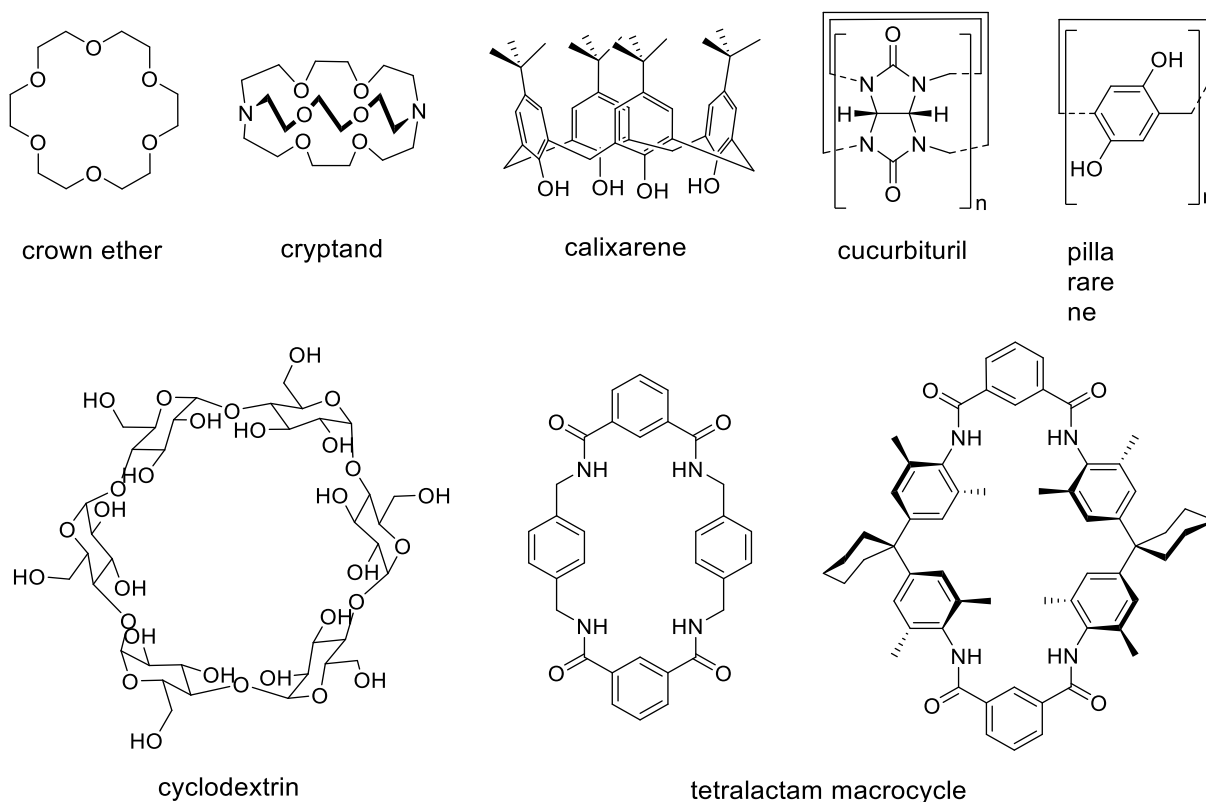


Figure 6: Common macrocycles used as hosts in supramolecular chemistry.

Cyclic polyethers like crown ethers or cryptands have a strong binding affinity towards positively charged metal ions or organic molecules like protonated amines. The size of the inner cavity thereby leads to a preferred binding of apposite guests. 15-Crown-5 for instance selectively binds sodium ions, while 18-crown-6 has a strong binding affinity for potassium ions. Calixarenes and pillararenes are electron-rich and thus bind electron-poor species and cations. Cucurbiturils and cyclodextrins have hydrophilic outer parts which make them water soluble and exhibit hydrophobic cavities. Thus, they can be used to bind non-polar species in an aqueous environment. Tetralactam macrocycles are efficient host molecules for molecules bearing hydrogen-bond acceptor groups and anions.

In general, the binding of a guest to a macrocycle is influenced by enthalpic and entropic contributions. Attractive non-covalent forces like hydrogen bonds, ion-dipole or cation- π interactions between guest and host molecule direct the formation of the inclusion complex. The complex formation is entropically disfavoured as a state of higher order is achieved. Depending on the surrounding solvent, this negative contribution is often compensated by the displacement of solvent molecules from the cavity of the host through the guest molecule.

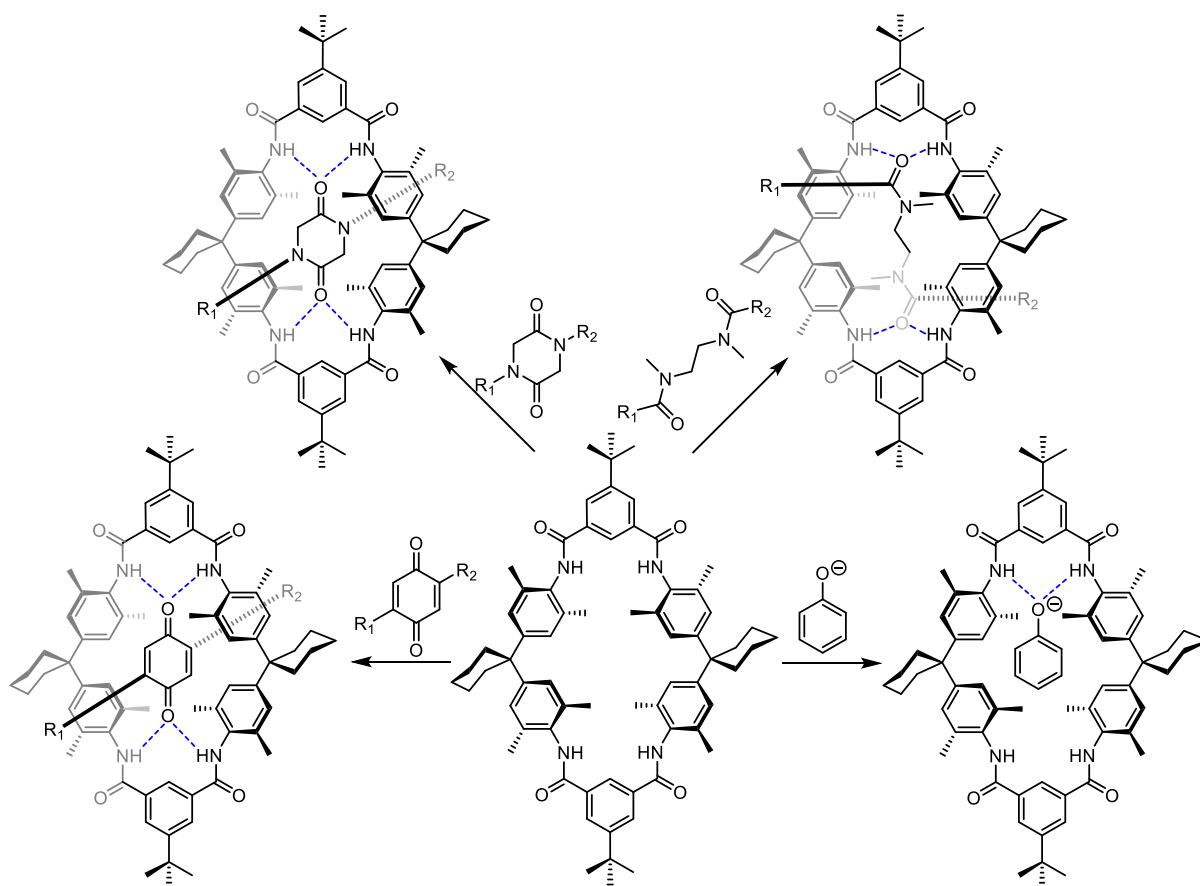


Figure 7: Host-guest complexes of a Hunter-Vögtle-type TLM with various guests.

Of particular importance for this thesis are Hunter-Vögtle-type tetralactam macrocycles (TLM).^[24] They bear four amide groups that can form hydrogen bonds to suitable guest molecules. Additionally, π - π and CH- π interactions can contribute to their overall binding characteristics. Common guest for TLM are diketones or diamides with electron-rich keto groups in an appropriate distance, that act as hydrogen-bond acceptors. Anions acting as hydrogen-bond acceptors can form strong complexes with TLM as well. Reported examples describe complexes of linear diamides, cyclic diamides like diketopiperazine, p-benzoquinone or phenolates (Figure 7).^[25]

The typical synthesis of a TLM starts with the condensation of dimethylaniline and cyclohexanone under acidic conditions to form the Hunter diamine that is subsequently treated with isophthalic acid chloride to give the extended diamine. Cyclisation of extended diamine with a second isophthalic acid chloride under high dilution conditions affords the TLM (Figure 8). By using differently substituted isophthalic acid chlorides, TLM can be easily functionalised.^[26] The selective functionalisation of TLM is of particular importance for this thesis and sets the basis for the deposition of TLM in mono- and multilayers on surfaces.

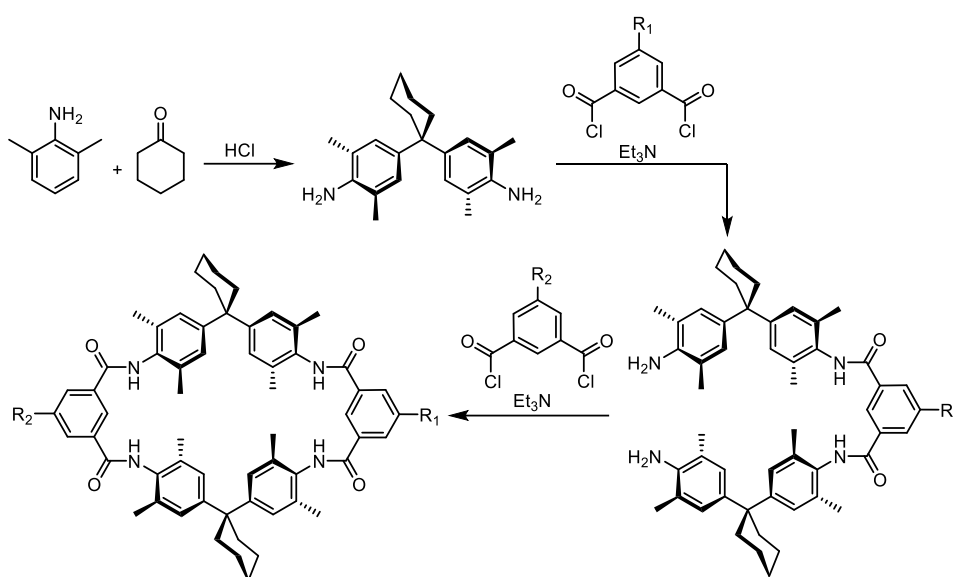


Figure 8: Synthesis of a Hunter-Vögtle-type TLM.

3.1.2. Mechanically interlocked molecules

Mechanically interlocked molecules (MIMs) are a class of compounds in which two or more molecules are connected mechanically to each other but without any covalent bonds between them. MIMs are stable complexes that cannot be separated into their single compounds without breaking a covalent bond or supplying a significant amount of energy.^[27] The most important types of MIMs are rotaxanes and catenanes. In rotaxanes (Figure 9, left), a macrocyclic compound is threaded on a linear molecule, the axle. Sterically demanding groups at both ends of the axle prevent a deslipping of the macrocycle. Pseudorotaxanes (Figure 9, middle) are precursors of rotaxanes in which the macrocycle is threaded on an axle without or with only one stopper group and can therefore easily deslip. Catenanes (Figure 9, right) are comprised of interlocked macrocycles.^[28] Further reported examples of MIMs include Borromean rings^[29] and different types of knots.^[30]

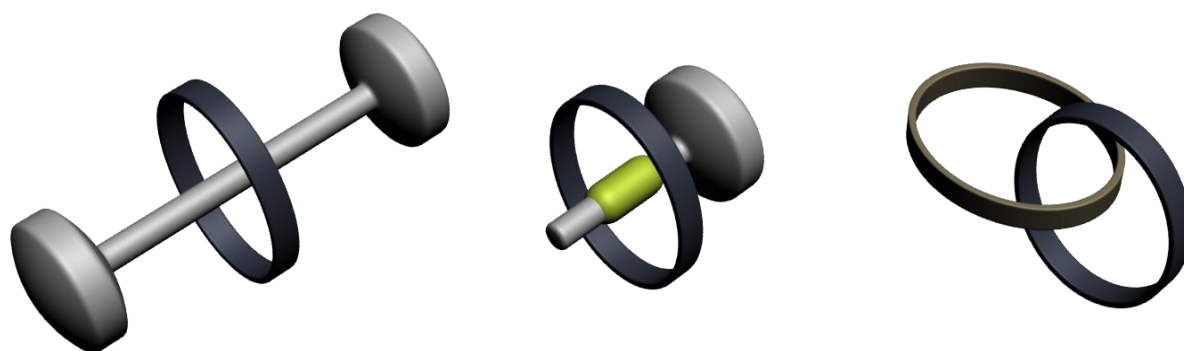


Figure 9: Schematic representation of a rotaxane, a pseudorotaxane and a catenane.

The first synthesis of a mechanically interlocked molecule was accomplished in the early 1960s by Wasserman and coworkers with the successful preparation of a [2]catenane.^[31] The applied synthetic method was based on a pure statistical approach without any preorganisation of the building blocks which resulted in very low yields of the interlocked species. A major step forward in the synthesis of mechanically interlocked molecules was achieved by Sauvage and coworkers^[7, 32] in 1983 with the successful preparation of a [2]catenane from two substituted phenanthroline ligands (Figure 10). Tetrahedrally coordinating Cu(I) ions were used to preorganise the ligands in a way that the subsequent ether synthesis yielded an interlocked structure. The catenane was prepared with a yield of 27%, which represented a huge improvement compared to the previously achieved 1-2% in statistical synthesis approaches.

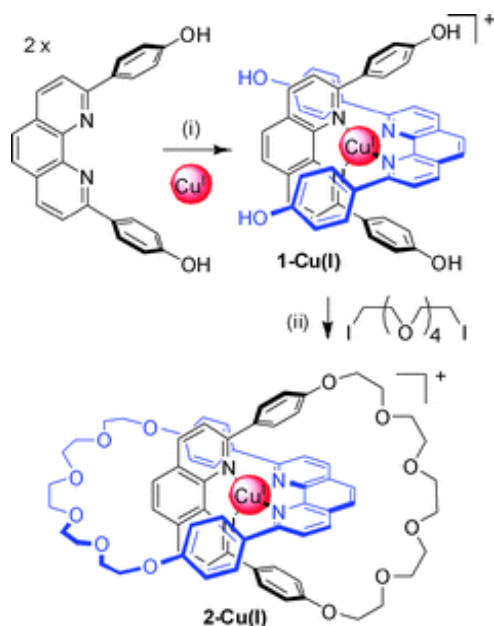


Figure 10: Templated catenane synthesis by Sauvage.^[7, 32] Reprinted from J. D. Crowley, S. M. Goldup, A.-L. Lee, D. A. Leigh, R. T. McBurney, *Chem. Soc. Rev.* **2009**, 38, 1530-1541 with permission from The Royal Society of Chemistry.

The development of the templated synthesis represented a milestone in the field of interlocked molecules and led to the development of various new structures with different properties.^[33] Besides metal ion templates as used by Sauvage, other non-covalent interactions, for example π - π interactions,^[34] cation- π interactions^[35] or hydrogen bonds^[36] have been used as template strategies for the synthesis of MIMs.

Three different synthetic strategies have been established for the synthesis of rotaxanes: the slipping, the clipping and the capping method.^[37] All methods are usually employed under the use of a template to generate a reasonable amount of the interlocked product. In the slipping method, a solution of preformed axle and macrocycle is supplied with energy, usually by heating it up, until the macrocycle can slip over the stopper on the axle. Upon subsequent cooling to ambient conditions, the activation barrier for a dethreading is too high and a stable rotaxane is formed. The slipping method requires carefully designed stopper units that are small enough to enable slipping at elevated temperatures, but large enough to prevent slipping at ambient conditions. In the clipping method, the macrocycle is synthesised around a preformed axle. This method only works well for specific macrocycles. The attractive interactions between macrocycle and axle that direct the formation of the interlocked compound often demand a complete macrocyclic structure. The most versatile approach is the capping method, in which first a pseudorotaxane of an axle without any or with only one stopper unit is formed followed by subsequent attachment of the missing stoppers to complete the interlocked structure.

An example for a hydrogen bond templated rotaxane synthesis by the capping method was reported by Vögtle and coworkers (Figure 11).^[25b] Tritylphenol was deprotonated to act as anion template for a tetralactam macrocycle, forming a pseudorotaxane. Subsequent ether synthesis with the second axle building block bearing a benzyl bromide as reactive center leads to rotaxane formation. The oxo-anion bound to the macrocycle is only accessible for the nucleophilic substitution reaction through the macrocycle due to the bulky nature of the trityl group that blockes the other side of the molecule. This leads to a formation of the ether rotaxane in a very high yield of 95%.

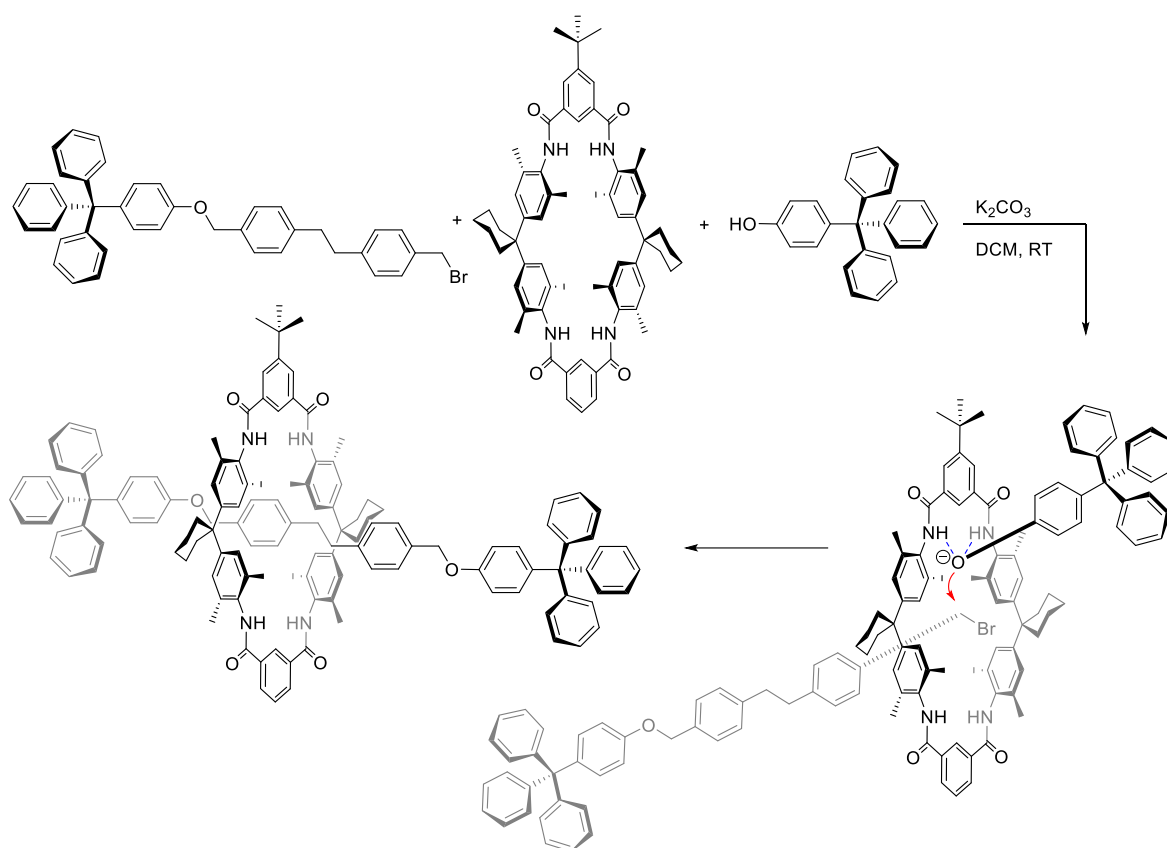


Figure 11: Anion-templated rotaxane synthesis by Vögtle and coworkers^[25b]

The implementation of molecular switches in rotaxanes enables the control of the position of axle and macrocycle relative to each other, which makes them an interesting class of molecules that is described in the following chapter.

3.2. Stimuli-responsive rotaxanes

Stimuli-responsive MIMs capable of performing molecular motion are of great interest for the development of functional materials and molecular machines.^[38] They allow the positional control of their subcomponents relative to each other by altering binding strengths of specific parts of the molecules. Of particular interest for this thesis are stimuli-responsive two-station rotaxanes where the movement of the macrocycle along the axle can be controlled. A stimuli-responsive two-station rotaxane is comprised of a macrocycle and an axle with two different binding sites, whereby one exhibits stronger attractive interactions towards the macrocycle than the other. An external stimulus is used to modify the system in a way that either the binding to the previously weaker binding site becomes energetically more favoured or that the previously stronger binding site becomes disfavoured, which induces the dislocation of the macrocycle to the second binding site. A second external stimulus recreates the initial binding affinities and the macrocycle returns to its original position.^[5] A schematic representation of a stimuli-responsive two-station rotaxane is depicted in Figure 12. Initially, the macrocycle resides at the preferred binding site (green). Upon applying a stimulus (yellow arrow), the second binding site (orange) gets transformed to a more attractive binding site (yellow), which causes the macrocycle to move towards the now preferred site. With a second stimulus (blue arrow), the yellow binding site is switched back to the orange form, resulting in the return of the macrocycle to its former position.

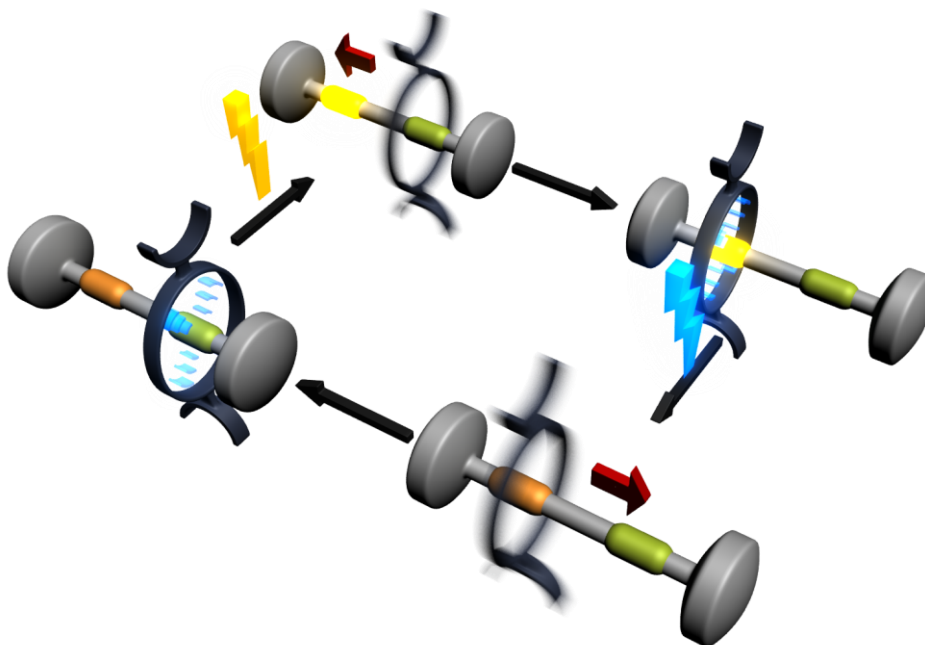


Figure 12: Schematic representation for the switching cycle of a stimuli-responsive two-station rotaxane.

The distribution of the macrocycle between the two binding sites is a dynamic equilibrium influenced by the respective binding energies and the temperature. It is important to note that the external stimulus does not directly induce motion of the macrocycle by applying an actual force, but rather leads to a change of the potential energy landscape of the system and creates a new energy minimum that causes the macrocycle to relaxate to this position (Figure 13). The movement of the macrocycle thereby occurs through Brownian motion.

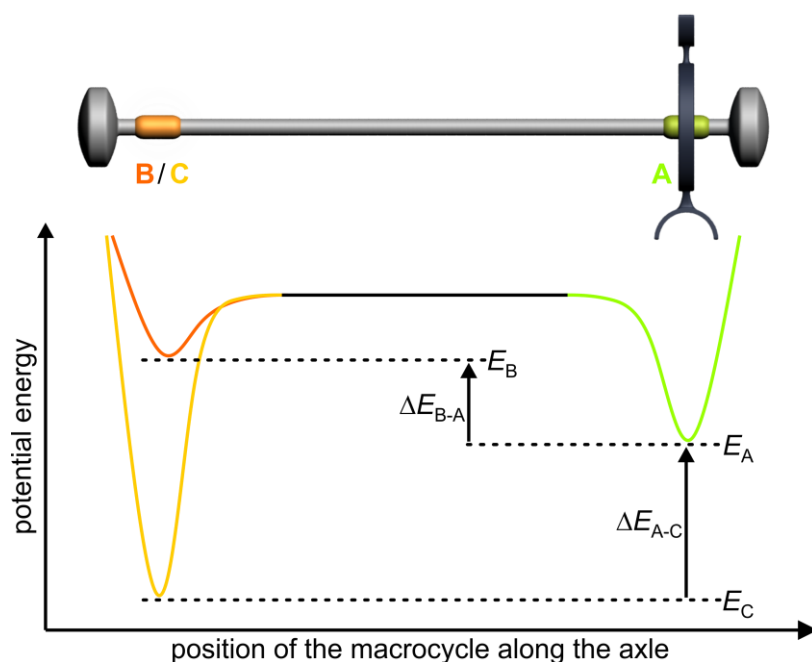


Figure 13: Idealised potential energy diagram of a stimuli responsive two-station rotaxane.^[5]

Depending on the energetic differences between the two binding sites on the potential energy surface, the macrocycle shuttles between the two sites or preferably resides at one of them. To achieve an occupancy of more than 95% at one binding site at room temperature, the difference in potential energy between the respective translational co-conformers has to exceed a value of $8.4 \text{ kJ} \cdot \text{mol}^{-1}$.^[5]

Various examples for switchable rotaxanes that are responsive towards chemical, electrochemical or photochemical stimuli are reported in literature.^[4-5] These types of rotaxanes including representative examples are described in more detail below with particular emphasis on photoswitchable systems.

3.2.1. Chemically switchable rotaxanes

The most obvious way to trigger switching in a rotaxane is the addition of a chemical. Common chemical stimuli include acids and bases, specific ions, oxidants or reductants.

The first example for a switchable rotaxane was reported by Kaifer, Stoddart and coworkers^[9] in 1994. They synthesised a two-station molecular shuttle with a cyclobis(paraquat-p-phenylene) cyclophane macrocycle and an axle bearing a biphenol and a benzidine unit (Figure 14). Both biphenol and benzidine can bind to the macrocycle over π - π -interactions. At room temperature, the macrocycle shuttles quickly between the two stations. Low-temperature NMR measurements allowed the distinction of both states that were present with a ratio of 84:16 favouring the encapsulation of the benzidine site. Protonation of the benzidine site with trifluoroacetic acid resulted in a preferred binding of the macrocycle to the biphenol unit with a ratio of more than 98%. Deprotonation with pyridine restored the initial state, proving the system to be fully reversible.

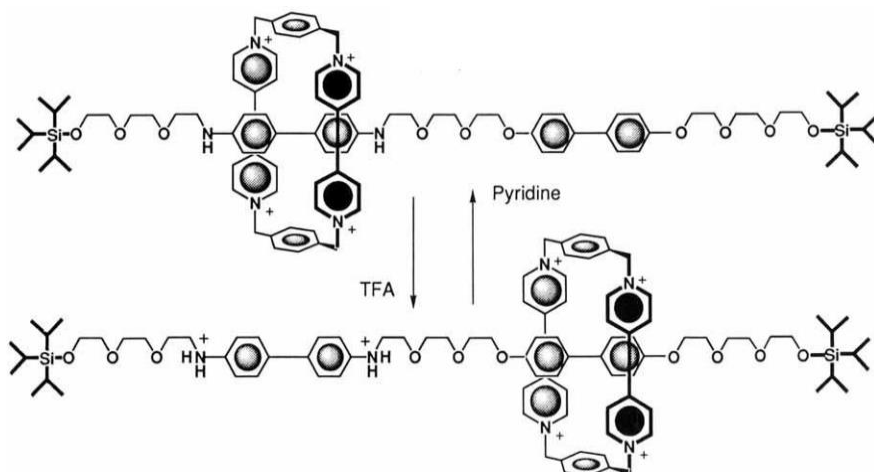


Figure 14: Switchable molecular shuttle rotaxane reported by Kaifer, Stoddart and coworkers. The macrocycle shuttles quickly between the benzidine and the biphenol site. Upon protonation of the benzidine with TFA, the equilibrium is shifted towards a preferential encapsulation of the biphenol site. Deprotonation with pyridine restores the initial state. Reprinted with permission from R. A. Bissell, E. Cordova, A. E. Kaifer, J. F. Stoddart, *Nature* **1994**, 369, 133-137. Copyright (1994) Nature Publishing Group.

A rotaxane responsive to anions was reported by Smith and coworkers^[39]. The rotaxane axle bears a central squaraine unit that binds to a tetralactam macrocycle over hydrogen bonds (Figure 15). Addition of chloride ions induced a lateral displacement of the macrocycle away from the squaraine site to one of the adjacent phenol units. This could be reverted upon addition of a silver salt to remove the chloride ions from solution. The rotaxane showed only a very weak response to bromide ions and no response to iodide ions. The switching of the rotaxane could be easily followed with the naked eye as it produced a shift of the squaraine absorption band of approximately 30 nm, resulting in a colour change of the rotaxane solution.

from green to light blue. The motion of the macrocycle can also be tracked by fluorescence spectroscopy since the charge-transfer between anthracene and squaraine exhibits a fluorescence signal. Addition of chloride shifts this charge transfer band to a smaller wavelength. The hydroxyl groups on the benzene rings adjacent to the central squaraine are crucial for the switching process. Studies with a similar rotaxane substituted with two hydrogen atoms instead of the hydroxyl groups did not respond to the addition of chloride ions. In addition, the hydroxyl groups greatly enhance the stability of the usually very sensitive squaraine unit.

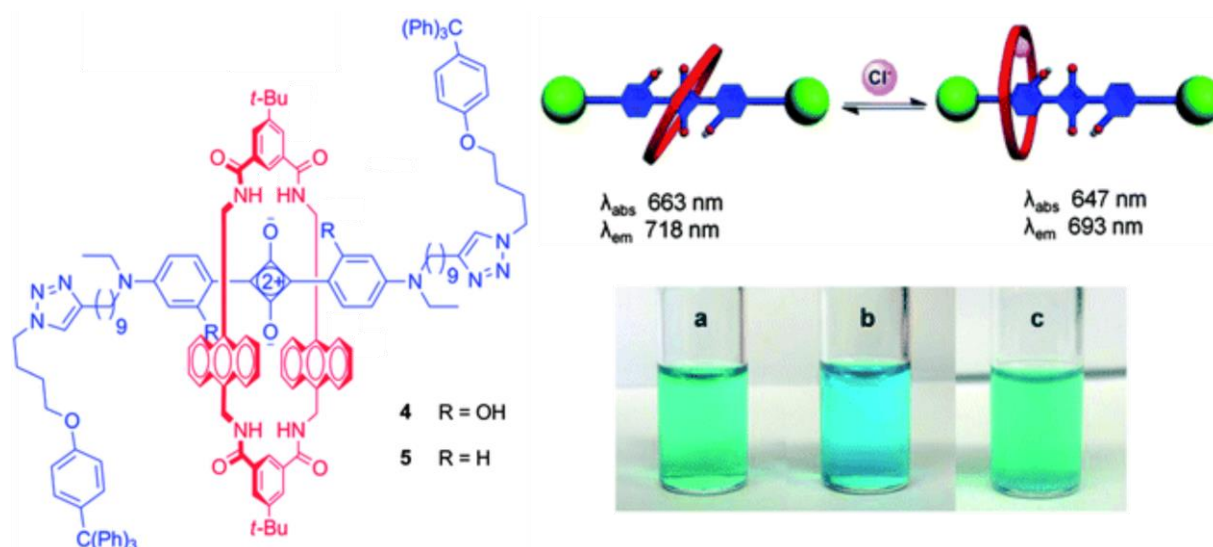


Figure 15: Structure of the squaraine-based rotaxane (left). Schematic representation of the rotaxane switching upon addition and removal of chloride ions (right). The switching changed absorption and fluorescence properties of a solution of the rotaxane in acetone, as seen in the images of a solution of the pristine rotaxane (a), after addition of TBACl (b) and subsequent addition of AgPF₆ (c). Adapted from C. G. Collins, E. M. Peck, P. J. Kramer and B. D. Smith, *Chem. Sci.*, 2013, 4, 2557 with permission from The Royal Society of Chemistry.

3.2.2. Electrochemically switchable rotaxanes

An electric potential can be used to induce redox reactions that alter the binding characteristics in a switchable rotaxane. This is in particular employed in rotaxanes that incorporate redox-active metal centers or are based on π -electron donor-acceptor interactions.

An example for an electrochemically switchable rotaxane in which the oxidation state of a metal ion affects the position of the macrocycle relative to the rotaxane axle was presented by Sauvage and coworkers.^[40] The rotaxane is comprised of an axle bearing a terpyridine and a phenantroline binding site and a macrocycle bearing a phenantroline binding site as well. A Cu(I) ion tetrahedrally coordinates the two phenantroline units of macrocycle and axle (Figure 16). Oxidation of Cu(I) to Cu(II) was accomplished by bulk electrolysis of a rotaxane solution in acetonitrile. As Cu(II) preferentially adopts a pentacoordination geometry, the macrocycle

shuttles from the phenantroline site to the terpyridine site. The resulting pentacoordination geometry of the macrocycle's phenantroline site and the axle's terpyridine site has a higher stability compared to the tetracoordination geometry of two phenantroline units. Electrochemical reduction of the Cu(II) to a Cu(I) ion induces back-shuttling of the macrocycle to the phenantroline site of the axle.

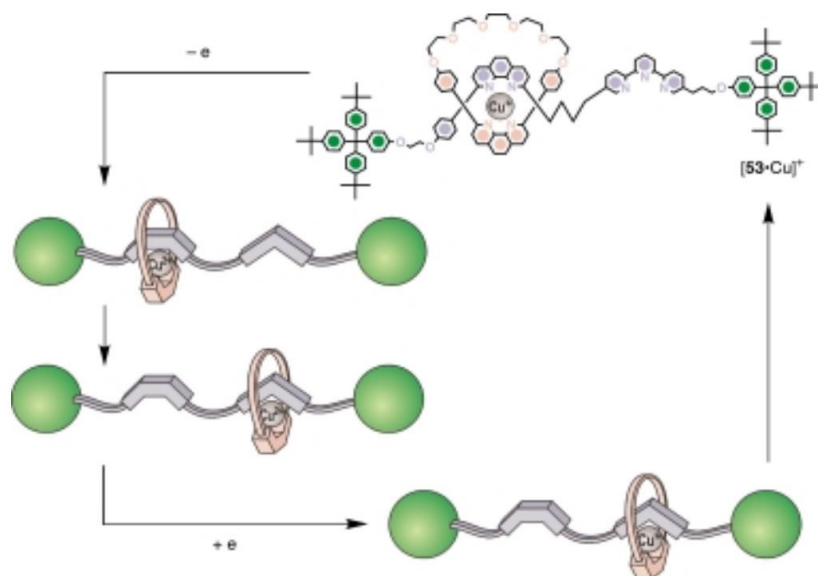


Figure 16: Electrochemically switchable rotaxane reported by Sauvage. The macrocycle encapsulates the phenantroline site when the copper ion is in its +I oxidation state and moves to the terpyridine site when the copper ion gets oxidised to the +II state. Reprinted with permission from V. Balzani, A. Credi, F. M. Raymo, J. F. Stoddart, *Angew. Chem. Int. Ed.* **2000**, 39, 3348-3391. Copyright (2000) John Wiley and Sons.

An electrochemically switchable rotaxane in which the redox-active unit is directly incorporated in the rotaxane axle was reported by Stoddart and coworkers.^[41] The rotaxane axle bears a 1,5-dioxynaphthalene (DNP) and a tetrathiafulvalene (TTF) binding site, that can both bind to the electron deficient cyclobis(paraquat-p-phenylene) macrocycle through π - π interactions (Figure 17). The TTF station thereby represents the stronger π -electron donor and thus the favorite position for the macrocycle. Upon chemical or electrochemical oxidation of the TTF unit from its neutral to a doubly positively charged state, the binding strength is greatly reduced, which leads to the macrocycle shuttling to the DNP binding site. The position of the macrocycle was followed with UV-Vis and NMR spectroscopy. UV-Vis spectra of the rotaxane show intense charge-transfer absorption bands at 846 nm when the macrocycle resides at the TTF site and at 530 nm when it encircles the DNP site. Reduction of the TTF²⁺ to its neutral form induced shuttling of the ring away from the DNP back to the TTF binding site. Within each switching step, the macrocycle covered a distance of 3.7 nm, which is around 40 % of the overall length of the axle.

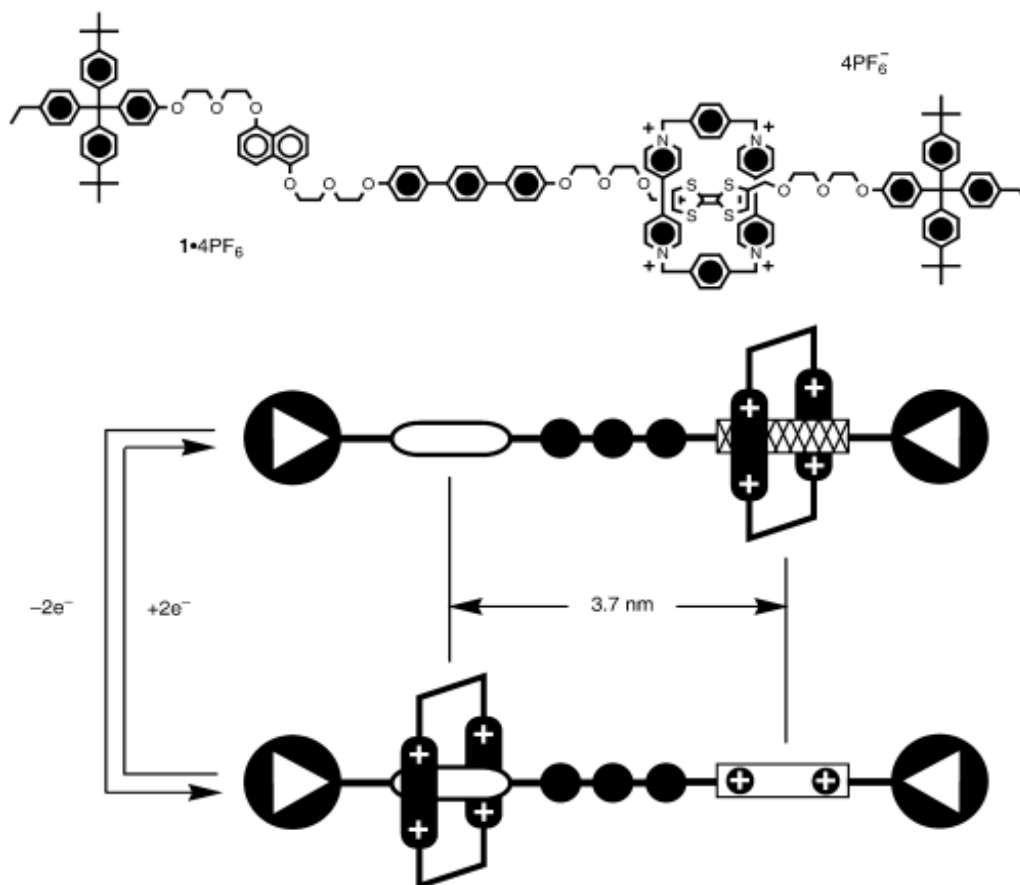


Figure 17: Electrochemically switchable rotaxane reported by Stoddart and coworkers. Upon oxidation and reduction of the TTF unit, the position of the ring can be switched between the TTF and the DNP binding site, which represents a mechanical displacement of the ring by around 40% along the axle. Reprinted with permission from H.-R. Tseng, S. A. Vignon, J. F. Stoddart, *Angew. Chem. Int. Ed.* **2003**, *42*, 1491-1495. Copyright (2003) John Wiley and Sons.

3.2.3. Photoswitchable rotaxanes

Especially photoswitchable supramolecular systems are of great interest in current research.^[42] In photoswitchable compounds, the necessary activation energy for a reaction is supplied in the form of irradiation with light. To initiate a photochemical process, the supplied light must be absorbed by the respective atom or molecule, a fundamental principle of photochemistry known as Grotthus-Draper law.^[43] The principle that each absorbed photon causes a chemical or physical reaction is known as Stark-Einstein law, the second basic law of photochemistry.^[44] Photochemical reactions do not proceed exclusively in the electronic ground state, but involve electronically excited states along the reaction coordinate.^[45] In this context, light refers to the part of electromagnetic radiation that is able to cause electronic transitions in atoms or molecules, which applies to the wavelength range of approximately 100 nm to 1000 nm, or in other words from UV light over visible light to the near IR region.

An interesting aspect is that specific reactions are only possible under irradiation with light. The principle of the conservation of orbital symmetry states that the symmetry of molecular orbitals of starting materials and products of a reaction has to remain unchanged. Reactions that comply with this principle exhibit a low activation barrier while reactions not following this principle have a significantly higher one. As electronically excited states have a different orbital symmetry than the corresponding ground states, photochemical reaction control enables specific reactions that would not or only very slowly proceed under thermal activation.^[46]

Most photoswitchable units offer a fast, clean and reversible photoisomerisation which makes them ideal candidates for the control of switching states in supramolecular systems. Additionally, a light stimulus can be delivered with high temporal and spacial precision and does not bring in any chemical contaminations. Photochromic systems that give a mechanical response upon applying a light stimulus are of particular interest for the use in photoswitchable rotaxanes to control the movement of a macrocycle relative to the axle (Figure 18).

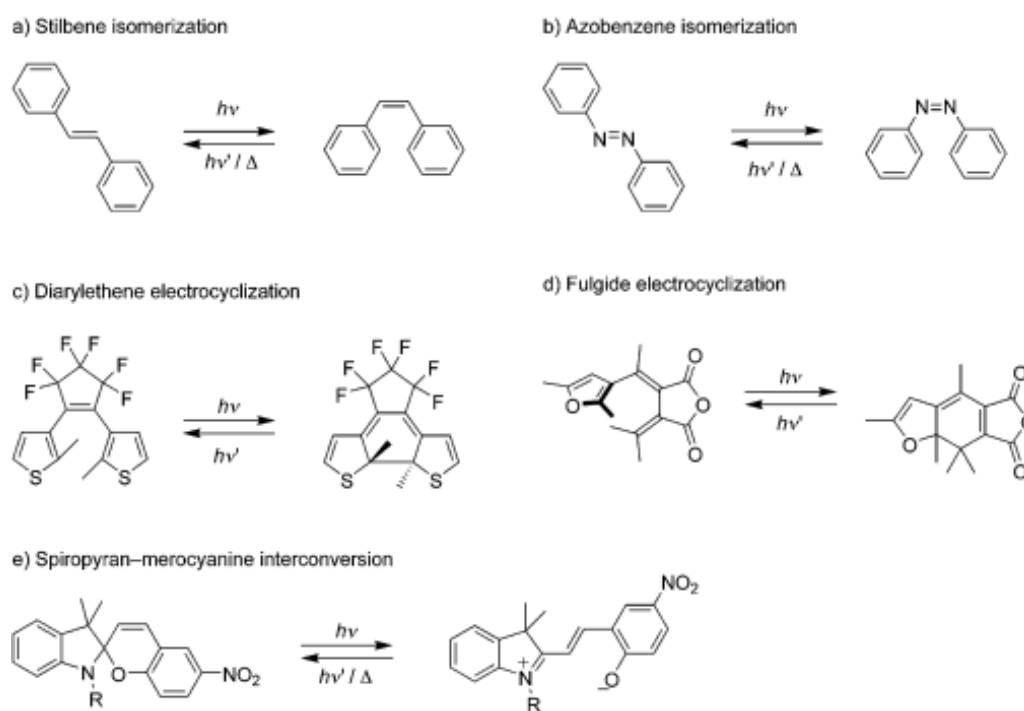


Figure 18: Examples of photochromic systems that give a mechanical response. Reprinted with permission from E. R. Kay, D. A. Leigh, F. Zerbetto, *Angew. Chem. Int. Ed.* **2007**, *46*, 72-191. Copyright (2007) John Wiley and Sons.

Every photoswitch has its specific properties qualifying or disqualifying it for a particular application. Stilbenes and azobenzenes for instance undergo a photoinduced *cis-trans* isomerisation. They are easily synthetically accessible and offer a large change in their geometry accompanied with the photoisomerisation. A disadvantage of this class is the usually non-quantitative photoconversion between the two states.^[47] The photoinduced

electrocyclisation of diarylethenes only exhibits a small geometrical change between the two switching states, but shows a great reversibility without significant photodegradation.^[48] Fulgides have, unless most other photoswitches, two thermally stable switching states that are only converted photochemically inbetween each other.^[49] The spiropyran-merocyanine interconversion is accompanied by a significant change in their chemical and geometric properties, but is often associated with photodegradation. Besides light, spiroyrans are also responsive towards different other stimuli, which can be an advantage or disadvantage depending on the desired application.^[50]

In this thesis, azobenzene and spiropyran were used as photoswitchable units to control the movement of a macrocycle relative to the axle in rotaxanes and to control the assembly and disassembly of pseudorotaxanes. The photochemistry of these chromophors and reported examples of switchable systems using spiropyran or azobenzene are set out in more detail below.

3.2.3.1. Azobenzenes

Azobenzenes represent a class of chromophors that are comprised of two benzene rings linked by an azo group (N=N). Azobenzenes have two distinct structural isomers, *cis*- and *trans*-azobenzene, that can be converted photochemically into each other (Figure 19a). While the first azobenzene dye was described by Mitscherlich in 1834,^[51] it took until 1937 with the discovery of the *cis-trans* isomerisation of azobenzene by Hartley^[52] in 1937 that the photochemistry of azobenzenes was systematically investigated. Besides their use as one of the most important class of dyes,^[53] azobenzenes have been incorporated variously in dynamic materials^[54] and biomolecules^[55] and have been used in a variety of applications including lithography, non-linear optical devices, optic switches and data storage.^[54]

The *trans*-isomer of azobenzene exhibits an almost planar structure and has almost no electronic dipole moment.^[56] The *cis*-isomer in contrast exhibits a bent conformation with the phenyl rings twisted approximately 55° out of plane from the azo group (Figure 19b). The non-symmetric structure gives rise to a dipole moment in the order of 3 Debye. The carbon-carbon distance of the carbon atoms in para position of the two phenyl rings is 9.0 Å in the *trans*-isomer and 5.5 Å in the *cis*-isomer.^[57]

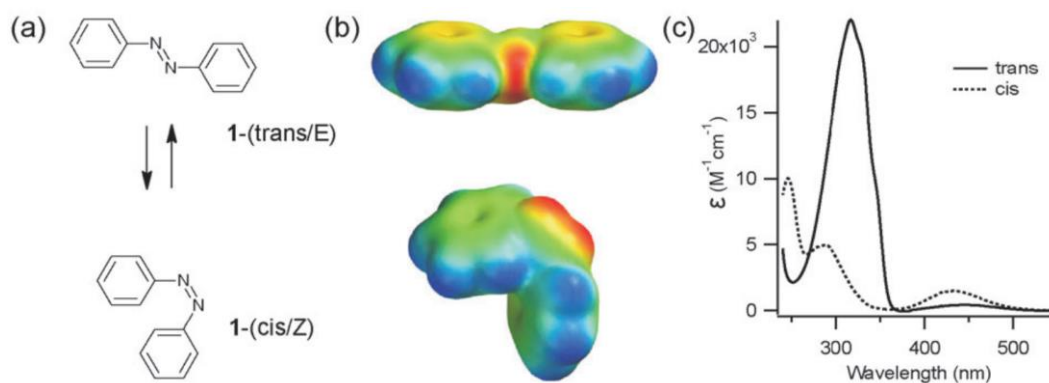


Figure 19: Structures of *trans*- and *cis*-isomers of azobenzene (a), spacefilling models coloured by the electrostatic potential from red – negative to blue – positive (b) and UV-Vis spectra of *trans*- and *cis*-azobenzene in ethanol. Reprinted from A. A. Beharry, G. A. Woolley, *Chem. Soc. Rev.* **2011**, *40*, 4422-4437 with permission from The Royal Society of Chemistry.

The UV-Vis absorption spectra of *cis*- and *trans*-azobenzene display three absorption bands (Figure 19c) that can be attributed to three electronic transitions and are best discussed with reference to a MO diagram.^[58] The MO energy diagram of the azobenzene system shows the three highest occupied and lowest unoccupied π -orbitals and the two non-bonding orbitals of the azo-nitrogens n_a and n_s (Figure 20). If the azobenzene bears an additional electron-donating group with lone-pair electrons, an additional π -orbital has to be added in the MO diagram (shown in parentheses). The absorption band at 440 nm for the *trans*-isomer and 430 nm for the *cis*-isomer is attributed to the energetically lowest $n_s \rightarrow \pi^*$ transition. The strong absorption band at 310 nm for the *trans*-isomer which is the less pronounced at 280 nm for the *cis*-isomer are attributed to the $\pi \rightarrow \pi^*$ transition. The difference of this absorption band between the isomers can be explained with the non-planar configuration of the *cis*-isomer that hampers the conjugation over the molecule. The third absorption band at 230-240 nm for both isomers is attributed to the $\varphi \rightarrow \varphi^*$ transition. In general, electron donating or withdrawing substituents have a huge influence of the electronic transitions and the resulting absorption spectra of azobenzenes, thus the previous discussion primarily relates to unsubstituted azobenzene.

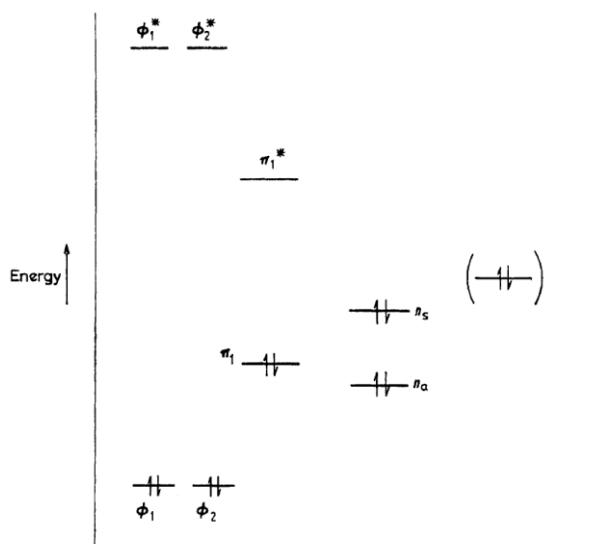


Figure 20: Crude MO energy diagram for the azobenzene system. The orbital in parentheses is present in azobenzenes containing a substituent with lone-pair electrons in conjugation with the π -electron system. Reproduced from J. Griffiths, *Chem. Soc. Rev.* **1972**, 1, 481-493 with permission from The Royal Society of Chemistry.

Absorption of a photon in the absorption band of *trans*-azobenzene induces the photochemical conversion from *trans*- to *cis*-azobenzene, that is typically carried out by irradiation with UV light between $\lambda = 300 - 380$ nm. The activation barrier for the photoexcited state is in the range of $200 \text{ kJ} \cdot \text{mol}^{-1}$.^[59] The photoisomerisation proceeds fast and clean without generating side products. Absorption of a photon in the absorption band of *cis*-azobenzene consequently induces the back-isomerisation, typically carried out by irradiation between $\lambda = 400 - 450$ nm. The *trans*-isomer almost always represents the thermodynamically more stable isomer with an energy difference of about $50 \text{ kJ} \cdot \text{mol}^{-1}$ compared to *cis*-azobenzene.^[60] In the dark, the *trans* to *cis* ratio usually exceeds a ratio of 99:1 in an equilibrated solution.^[61] The *cis*-isomer is metastable and thermally reverts back to *trans*-azobenzene. The activation barrier for the thermal reversion is in the order of $90 \text{ kJ} \cdot \text{mol}^{-1}$.^[62] The lifetime of the *cis*-isomer greatly depends on its substitution pattern and can reach from seconds to years. The irradiation of azobenzene leads to the formation of a photostationary state with a specific ratio of the *cis*- and *trans*-isomer, that depends on the rates of photoisomerisation in one or both directions and the thermal isomerisation. These isomerisation rates depend on the quantum yields of the photoisomerisation ($\phi_{\text{trans}}/\phi_{\text{cis}}$), the irradiation intensity and wavelength, temperature and the chemical environment.^[54]

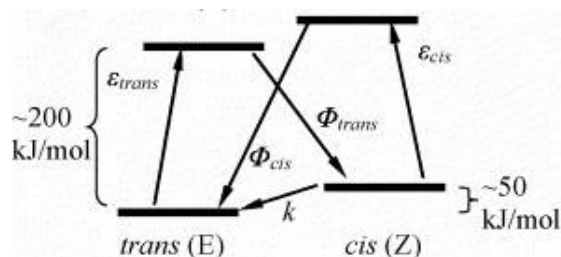


Figure 21: Simplified state model for azobenzenes with (ϵ) extinction coefficients, (ϕ) quantum yields of photoisomerisation and (k) rate of thermal relaxation. Reprinted with permission from K. G. Yager, C. J. Barrett, *Journal of Photochemistry and Photobiology A: Chemistry* **2006**, 182, 250-261. Copyright (2006) Elsevier.

Several mechanistic studies have been conducted to reveal the isomerisation mechanism of azobenzenes, resulting in two possibilities: the rotation and the inversion mechanism.^[63] The inversion at a nitrogen atom is induced by an $n \rightarrow \pi^*$ transition ($S_0 \rightarrow S_1$), while the rotation results from a $\pi \rightarrow \pi^*$ transition ($S_0 \rightarrow S_2$) (Figure 22). Recent studies indicate that the isomerisation occurs preferably through the inversion mechanism.^[64]

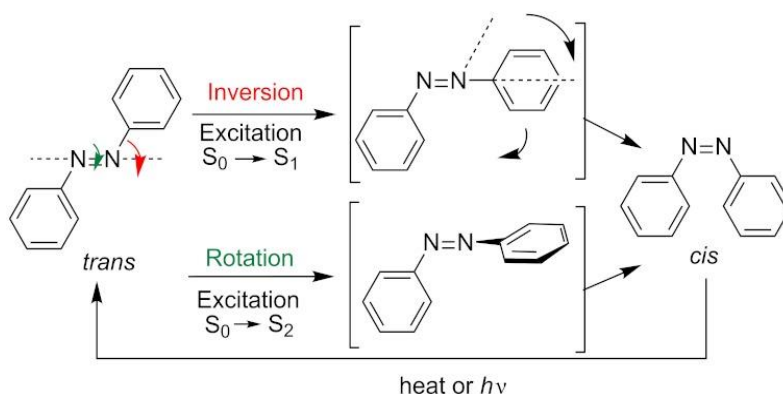


Figure 22: Inversion and rotation mechanism for the cis-trans isomerisation of azobenzene. Reprinted from E. Merino, M. Ribagorda, "Control over molecular motion using the *cis-trans* photoisomerization of the azo group", *Beilstein J. Org. Chem.* **2012**, 8, 1071-1090 (CC-BY 2.0).

A couple of examples are reported in literature where azobenzenes have been incorporated as key element in switchable rotaxanes to direct the movement of the macrocycle along the axle.^[65] An often used binding motif is the azobenzene/cyclodextrin system. Cyclodextrins form a stable inclusion complex with *trans*-azobenzene, but do not bind the *cis*-isomer. Nakashima and coworkers^[66] for example constructed a molecular shuttle comprised of an α -cyclodextrin and a symmetrical axle with a central azobenzene unit that is functionalised on both sides with methylene spacers followed by bis-pyridinium groups (Figure 23). NMR spectra revealed that the cyclodextrin encircles the azobenzene group in its *trans*-configuration. Upon irradiation with UV light at $\lambda = 360$ nm, the azobenzene isomerises to the *cis*-configuration, pushing the cyclodextrin away to one of the methylene spacers. Back-isomerisation to the *trans*-configuration with light at $\lambda = 450$ nm lead to the cyclodextrin encircling the azobenzene.

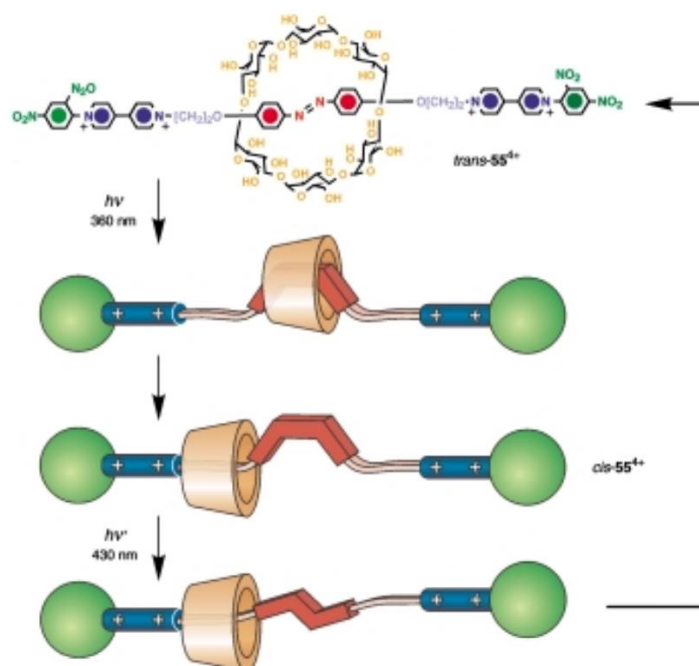


Figure 23: Photoswitchable molecular shuttle reported by Nakashima and coworkers.^[66] The shuttling of the macrocyclic component along its axle can be controlled reversibly by photoisomerizing the azobenzene unit. Reprinted with permission from V. Balzani, A. Credi, F. M. Raymo, J. F. Stoddart, *Angew. Chem. Int. Ed.* **2000**, 39, 3348-3391. Copyright (2000) John Wiley and Sons.

An example where azobenzene was not directly used as switchable binding site but to control whether or not a macrocycle can move along a rotaxane axle was reported by Stoddart and coworkers (Figure 24).^[65b] The rotaxane design was based on the well-known redox-switchable system comprised of an electron poor cyclobis(paraquat-p-phenylene) macrocycle, a TTF unit as the primary π -electron-donating binding site and DNP unit as second binding site. The two binding sites are separated by a central azobenzene group. The macrocycle is able to pass the azobenzene in its *trans*-configuration, but can not overcome the *cis*-configured azobenzene due to steric hinderance. This enables the locking of an electrochemically written switching state in the rotaxane by a photochemical stimulus. In the reduced state, the macrocycle encircles the TTF binding site. Electrochemical oxidation of the TTF induced the dislocation of the macrocycle to the DNP site. The photochemical switching of the azobenzene group to its *cis*-configuration locked the position of the macrocycle at the DNP site, and the following reduction of the TTF unit to its neutral state did not lead to the movement of the macrocycle to the TTF. Only upon photochemical or thermal back-isomerisation to the *trans*-configuration of the central azobenzene group, the macrocycle regained its initial position.

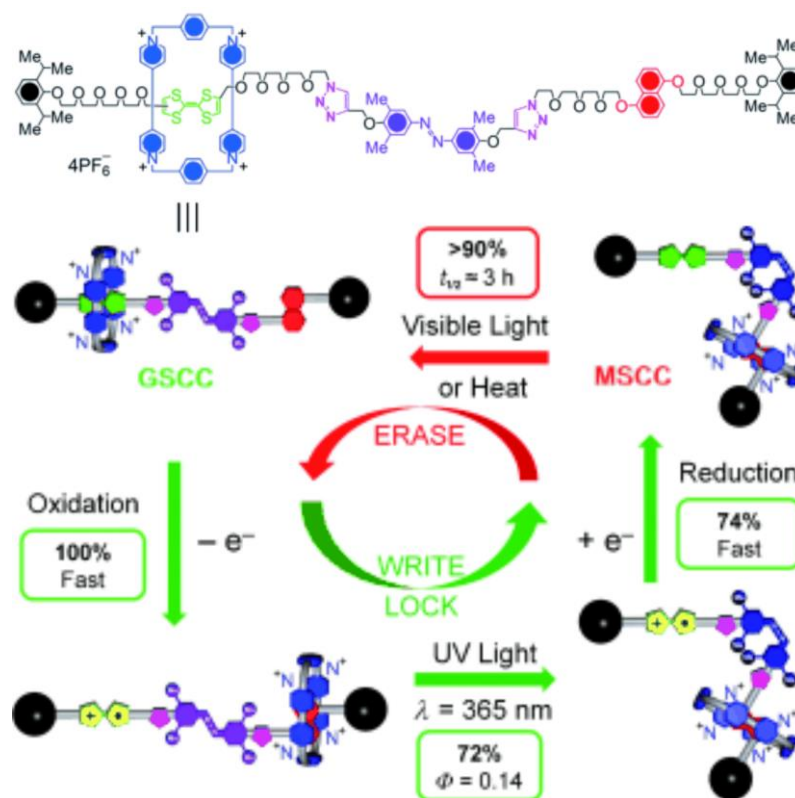


Figure 24: Chemically and photochemically triggered memory switching cycle of a [2] rotaxane. Adapted with permission from T. Avellini, H. Li, A. Coskun, G. Barin, A. Trabolsi, A. N. Basuray, S. K. Dey, A. Credi, S. Silvi, J. F. Stoddart, M. Venturi, *Angew. Chem. Int. Ed.* **2012**, 51, 1611-1615. Copyright (2012) John Wiley and Sons.

Further examples reported in literature also include photoswitchable pseudorotaxanes using azobenzene as key element. Credi and coworkers^[65a] for instance utilised an azobenzene group to photochemically control the unidirectional transit of a non-symmetric molecular axle through a dibenzo-24-crown-8 macrocycle (Figure 25). The axle is comprised of a protonated amine as recognition site for the crown ether, that is bound to an azobenzene at one side and a cyclopentyl unit as pseudo-stopper at the other side. The macrocycle preferentially threads on the axle at the *trans*-azobenzene side. Photochemical isomerisation to *cis*-azobenzene leads to a destabilisation of the inclusion complex and blocks the dethreading along the azobenzene side, as the *cis*-isomer is too sterically demanding. Addition of potassium ions displaced the macrocycle from the axle over the cyclopentyl side. Back-switching to *trans*-azobenzene resets the system to its initial state.

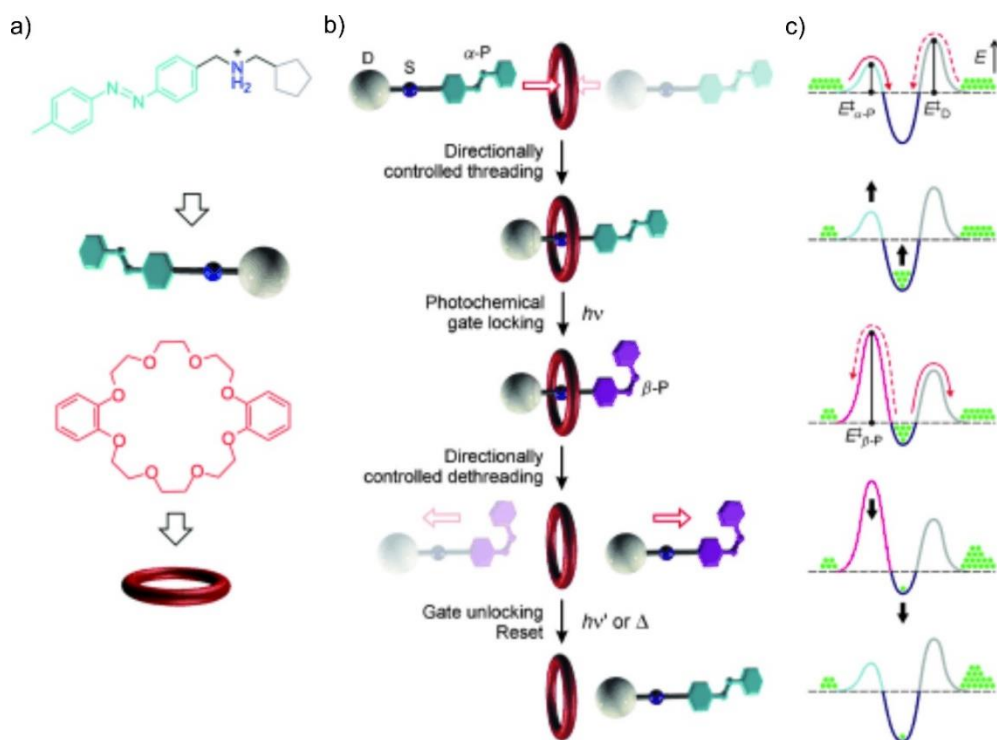


Figure 25: a) Structural representation of the pseudorotaxane axle and the dibenzo-24-crown-8 macrocycle, b) schematic representation of the strategy for the photoinduced unidirectional transit of the non-symmetric axle through the crown ether and c) simplified potential energy curves for the states shown in (b). Adapted with permission from M. Baroncini, S. Silvi, M. Venturi, A. Credi, *Angew. Chem. Int. Ed.* **2012**, *51*, 4223-4226. Copyright (2012) John Wiley and Sons.

A further example in which azobenzene was utilised to photochemically control the assembly and disassembly of a pseudorotaxane was reported by Jeong *et al.*^[67] They incorporated an azobenzene group into a rigid xanthene backbone to bring it in a fixed position adjacent to a diamide binding site. The *cis-trans* photoisomerization of the azobenzene was utilised to influence the binding strength towards a tetralactam macrocycle by steric hindrance. While the azobenzene blocks the binding site in its *trans*-configuration, it becomes available upon switching to the *cis*-isomer (Figure 26). The macrocycle substituted with nitro groups at the two isophthaloyl sites was used to increase the binding strength towards diamide guests. In a solution in CDCl_3 , the axle with the azobenzene in *trans*-configuration and the macrocycle are separated, but form an inclusion complex upon irradiation at $\lambda = 365 \text{ nm}$, as followed with ^1H NMR studies. Thermal equilibration for 12 h at $50 \text{ }^\circ\text{C}$ lead to the reisomerisation to *trans*-azobenzene and subsequent dissociation of the pseudorotaxane.

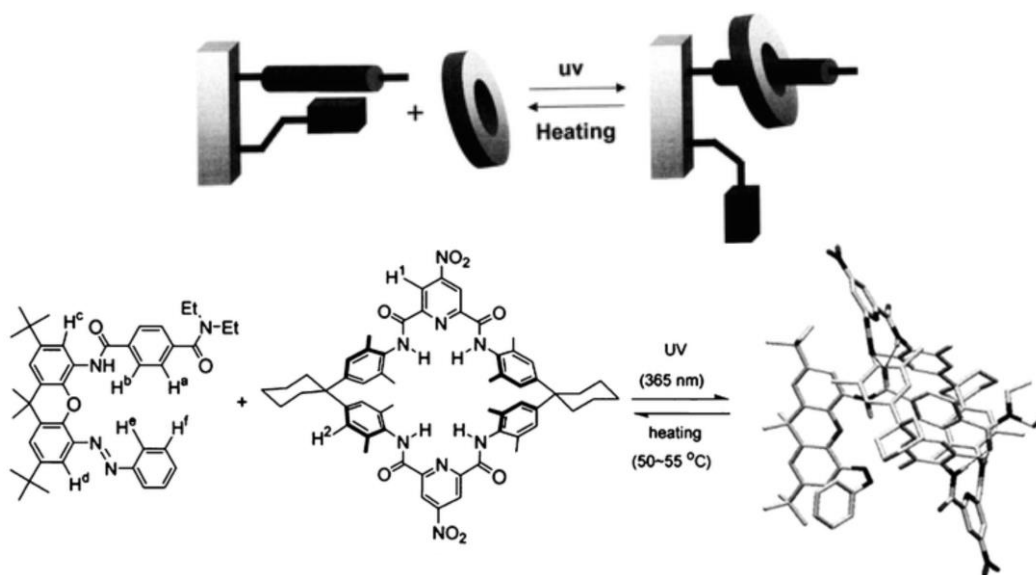


Figure 26: Schematic and structural representation of a photoswitchable pseudorotaxane comprised of a xanthene axle substituted with a diamide binding site and an adjacent azobenzene photoswitch and a tetralactam macrocycle. Reproduced from K.-S. Jeong, K.-J. Chang, Y.-J. An, *Chem. Commun.* **2003**, 1450-1451 with permission from The Royal Society of Chemistry.

3.2.3.2. Spiropyrans

Starting with the discovery of the photochromic behaviour of spiropyrans in 1952 by Fisher and Hirshberg,^[68] spiropyrans and the closely related molecules like spirooxazines have been widely used as photoswitches.^[50, 69]

A spiropyran is comprised of an indoline and chromene part that are arranged orthogonal to each other and connected through a spiro junction (Figure 27). The spiropyran can be photochemically converted to the open merocyanine form by irradiation with UV light, typically at $\lambda = 365$ nm. The photoisomerisation follows a first-order kinetic process.^[70] The merocyanine form has a planar structure with an extended π -conjugation. It is metastable at ambient conditions and thermally reverts back to the closed spiropyran in a ring closure reaction following first order kinetics as well.^[71] Irradiation with visible light, typically at $\lambda > 450$ nm accelerates the ring closure. Besides the common photoinduced switching, spiropyrans can also show responsiveness to pH,^[72] temperature,^[73] solvent polarity,^[74] redox potential,^[75] metal ions^[76] and mechanical force.^[77] Addition of acid to a spiropyran for instance leads to ring opening in the absence of UV light (Figure 27, bottom). Protonation occurs first at the indole nitrogen, which quickly isomerises to the merocyanine with a shift of the proton to the phenolate due to the higher basicity of the merocyanine.

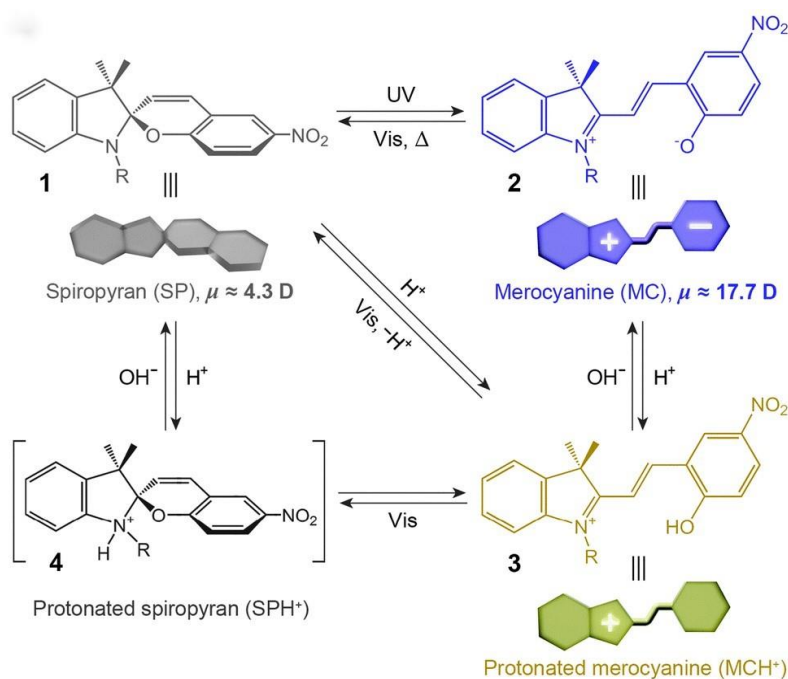


Figure 27: Photochromism and acidochromism of spiropyran. Reversible transformations between the four states: spiropyran (SP) **1**, merocyanine (MC) **2**, protonated merocyanine (MCH⁺) **3** and protonated spiropyran (SPH⁺) **4**. Reprinted from R. Klajn, *Chem. Soc. Rev.*, 2014, **43**, 148. Published by The Royal Society of Chemistry (CC BY 3.0).

The ring-opening mechanism of spiroopyran to merocyanine has been studied in great detail. For the photochemical isomerisation, the reaction proceeds over a heterolytic C-O bond cleavage (Figure 28, left). If the reaction is controlled thermally, the ring opening takes place in a 6π -electron electrocyclic reaction.^[69] Both reaction pathways yield the *cis*-merocyanine, that is transformed by a rotation about the central C-C bonds to the more stable *trans*-merocyanine.^[76, 78] The merocyanine exhibits two resonance forms.^[79] The zwitterionic structure is stabilised in polar media, while the quinoidal structure preferably exists in non-polar environments.

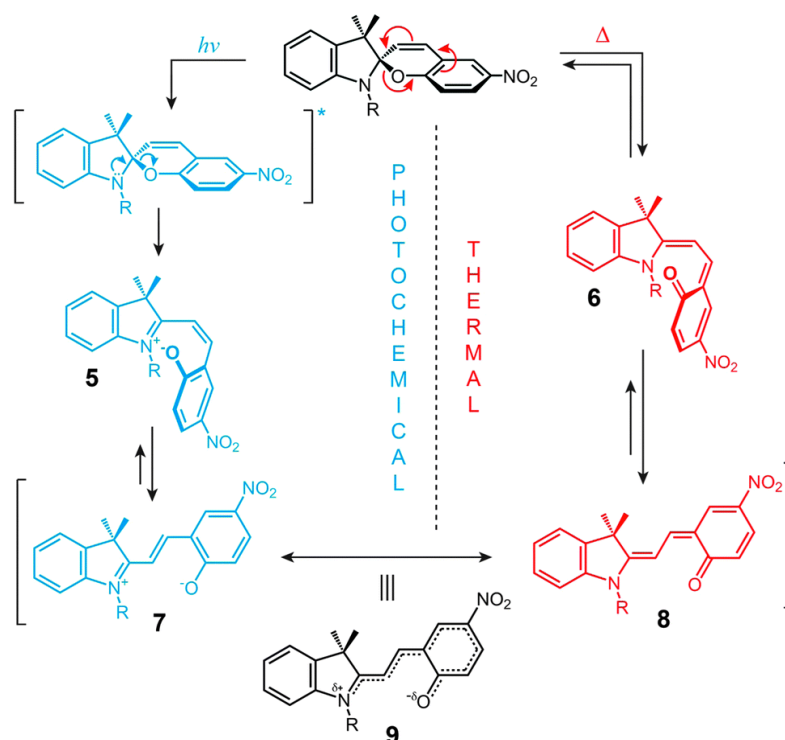


Figure 28: Mechanism of photochemical and thermal isomerisation of spiroopyran. Reprinted from R. Klajn, *Chem. Soc. Rev.*, 2014, **43**, 148. Published by The Royal Society of Chemistry (CC BY 3.0).

The different switching states of spiroopyrans can be easily followed by UV-Vis spectroscopy. Figure 29 displays UV-Vis spectra of a solution of 1',3',3'-trimethyl-6-nitrospiro[chromene-2,2'-indoline] (6-nitro BIPS) in acetonitrile. The UV-Vis spectrum of the spiroopyran solution exhibits two absorption bands at approximately 290 nm and 340 nm that are attributed to the $\pi \rightarrow \pi^*$ transition in the indoline part and the $\pi \rightarrow \pi^*$ transition in the chromene part of the molecule.^[80] As the solutions of spiroopyran does not absorb light in the visible region, it appears colourless. The UV-Vis spectrum of the merocyanine solution exhibits a strong absorption band at 570 nm for the $\pi \rightarrow \pi^*$ transition of the extended π -system, which causes the solution to appear deep blue to purple. Solutions with protonated merocyanine in contrast exhibit a characteristic absorption band at approximately 420nm, resulting in a yellow colour. Due to the different

colours of spiropyran, merocyanine and protonated merocyanine, the switching states can also be easily differentiated with the naked eye.

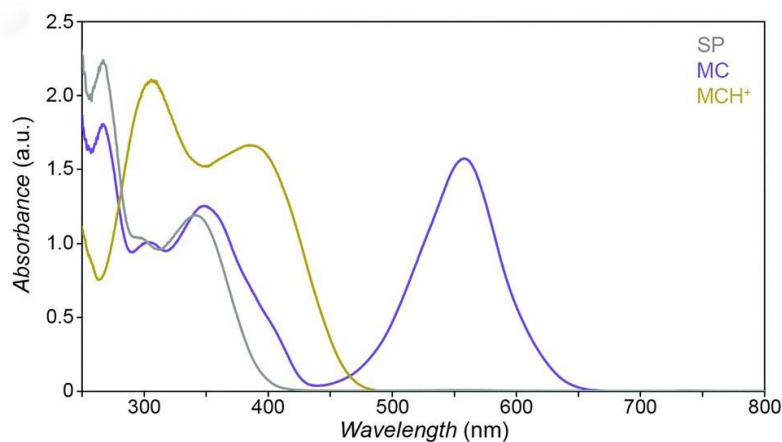


Figure 29: UV-Vis spectra of the parent spiropyran 6-nitro BIPS before (grey) and after (purple) UV irradiation and after the addition of HCl (yellow). Reprinted from R. Klajn, *Chem. Soc. Rev.*, 2014, **43**, 148. Published by The Royal Society of Chemistry (CC BY 3.0).

Besides the different optical characteristics, spiropyran and merocyanine exhibit major differences in their electrical dipole moment, structure and occupied volume, emission characteristics and basicity.^[69] Spiroyrans have been used for instance to control metal ion complexation,^[81] the mechanical properties of polymers^[82], enzymatic activity,^[83] the electrical properties of electrodes,^[84] or the aggregation of nanoparticles.^[85] However, there only exist very few examples for spiropyran incorporated in supramolecular systems or MIMs.

The only example for a photoresponsive rotaxane using spiropyran as photoswitchable element was reported by Li and coworkers.^[86] They synthesised a rotaxane comprised of a tetralactam macrocycle and an axle bearing a diamide binding site and a spiropyran unit. The spiropyran serves both as photoswitchable binding site and stopper unit. If the spiropyran is in the closed form, the macrocycle resides at the diamide binding site. Upon photoinduced spiropyran to merocyanine interconversion, the oxo-anion of the merocyanine represents the favourite binding site, which induces the movement of the macrocycle from the diamide to the spiropyran (Figure 30 left). The ester group adjacent to the spiropyran is used as second half of the binding site to strengthen the binding of the merocyanine, although it only represents a weak binding site by itself. Back switching was conducted either by thermal equilibration or by irradiation with visible light, which resulted in ring closure of the merocyanine to the spiropyran form and subsequent shifting of the macrocycle to its initial position at the diamide site. The switching of the rotaxane was followed by NMR and UV-Vis spectroscopy. In the UV-Vis spectrum, the characteristic absorption band for the merocyanine at 570 nm appeared after irradiation of a solution of the rotaxane in acetonitrile with UV light, while no absorption in this region was present for the spiropyran form of the rotaxane. The absorption band of the

merocyanine had a higher intensity for the rotaxane compared to the free axle, which indicates a stabilisation of the merocyanine through the macrocycle. The system showed a good reversibility over six switching cycles.

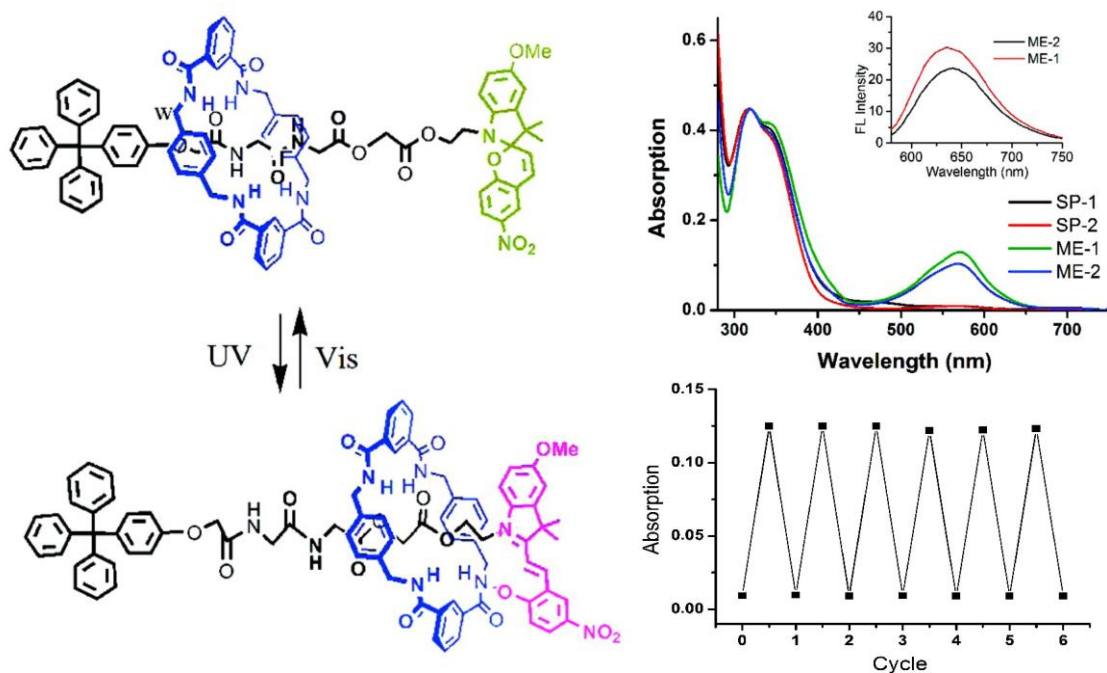


Figure 30: Structure and photoswitching of a spiropyran-based rotaxane (left). UV-Vis spectra of the rotaxane (SP-1 / ME-1) and the corresponding free axle (SP-2 / ME 2) in their spiropyran (SP) and merocyanine (ME) states (top right). Reversibility of the rotaxane switching tested over 6 switching cycles (bottom right). Reprinted with permission from W. Zhou, D. Chen, J. Li, J. Xu, J. Lv, H. Liu, Y. Li, *Org. Lett.* **2007**, 9, 3929-3932. Copyright (2007) American Chemical Society.

Further examples are reported for spiropyran-based switchable pseudorotaxanes. Tiburcio and coworkers^[87] for instance used the spiropyran-merocyanine interconversion to control the assembly and disassembly of a pseudorotaxane. Their design of the pseudorotaxane is based on the bis(pyridinium)ethane recognition motif for 24-membered crown ethers (Figure 31). One of the pyridinium-units was replaced by a spiropyran, which is connected to the binding site at its indole nitrogen. In the closed spiropyran state the recognition motif is incomplete due to the neutral indole nitrogen. The molecule did not show any association with dibenzo-24-crown-8. Upon photoinduced spiropyran to merocyanine interconversion, the indole nitrogen bears a positive charge, which completes the recognition motif, leading to the pseudorotaxane formation. Additionally, the spiropyran to merocyanine interconversion could be triggered chemically by addition of an acid, which likewise induced the pseudorotaxane formation. The disassembly of the pseudorotaxane was conducted by irradiation with visible light or by addition of a base in case of the chemically induced switching.

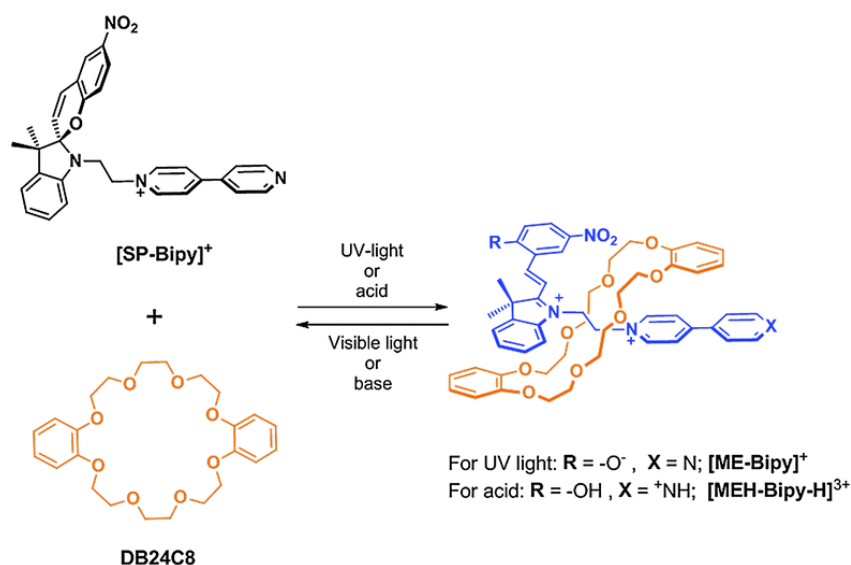


Figure 31: Isomerisation of a spiropyran-based axle (black) to the merocyanine form (blue) by irradiation with UV light or addition of acid and its association behaviour with dibenzo-24-crown-8. Reprinted from D. Hernandez-Melo, J. Tiburcio, *Chem. Commun.* **2015**, 51, 17564-17567 with permission from The Royal Society of Chemistry.

Credi and coworkers^[88] photochemically controlled the assembly and disassembly of a photoinactive but pH-switchable pseudorotaxane by using a spiropyran as photoacid (Figure 32). The pseudorotaxane was comprised of a calix[6]arene and a 4,4'-bipyridinium guest. One pyridinium unit was substituted with an alkyl chain and therefore bears a permanent positive charge, while the other can be protonated and deprotonated. The protonated axle forms the very stable inclusion complex $[\text{C}\cdot\text{AH}]^{2+}$ with the calixarene [$K = (6 \pm 2) \times 10^6 \text{ M}^{-1}$], while the deprotonated axle does not show any binding behaviour. The spiropyran **SP** is converted into the protonated merocyanine **MEH**⁺ in the presence of an acid. Irradiation with visible light causes **MEH**⁺ to isomerise back to the closed spiropyran under release of a proton. The pseudorotaxane $[\text{C}\cdot\text{AH}]^{2+}$ exhibits a charge-transfer absorption band in the UV-Vis spectrum at 478 nm, while none of the individual components shows absorptions in this region. Upon addition of the spiropyran **SP** to a solution of the pseudorotaxane and equilibration of the mixture in the dark, the charge transfer band slowly disappears, indicating the disassembly of the pseudorotaxane. Simultaneously, a new absorption band at 417 nm appeared that is typical for a protonated merocyanine **MEH**⁺. Irradiation of the solution with visible light leads to the disappearance of the **MEH**⁺ absorption band and full restoration of the charge transfer band for the pseudorotaxane. The acid strength of **SP** and **MEH**⁺ is therefore smaller and larger, respectively than the one of the protonated axle **AH**⁺. This allows the photocontrolled protonation and deprotonation of the axle and therefore the control of threading and dethreading of the pseudorotaxane.

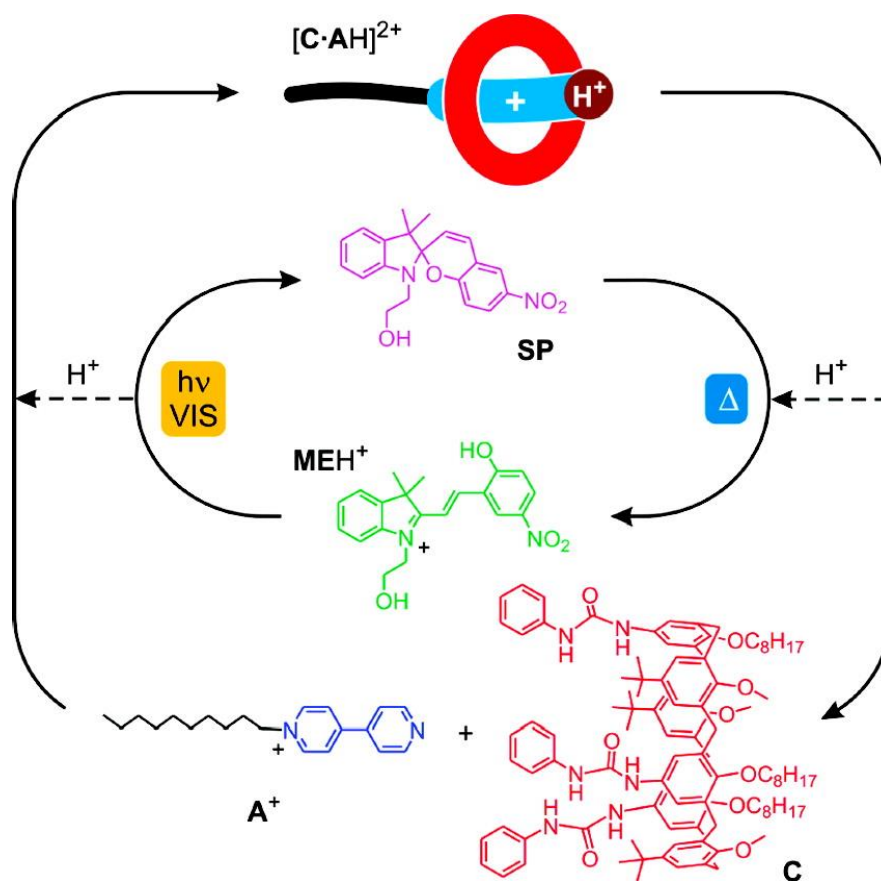


Figure 32: Pseudorotaxane. Reprinted with permission from S. Silvi, A. Arduini, A. Pochini, A. Secchi, M. Tomasulo, F. M. Raymo, M. Baroncini, A. Credi, *J. Am. Chem. Soc.* **2007**, 129, 13378-13379. Copyright (2007) American Chemical Society.

3.3. Interface chemistry – organic thin films on surfaces

The field of interface chemistry deals with physical and chemical processes at solid-gas, solid-liquid or liquid-gas interfaces. First research activities in surface chemistry started more than a century ago in the area of heterogeneous catalysis. Nowadays, interface chemistry plays an important role in academic and industrial research ranging from catalysis, corrosion, coatings, opto- and molecular electronics and semiconductors through to the development of molecular machines in recent academic research.^[89] As there is a limitation to what inorganic materials can provide, most of these research areas share the requirement for thermally stable, ordered organic or organometallic molecular systems.^[90]

Pioneering work on the deposition of organic layers on interfaces has been done by Langmuir and Blodgett in the beginning of the 20th century.^[91] Amphiphilic molecules form ordered monolayers at a water-air interface, where the hydrophilic part of the molecules points towards water and the hydrophobic part towards air. If a solid substrate is immersed and subsequently slowly pulled out, the monolayer is transferred from the water surface to the solid substrate. Repetition of this process allows the creation of multilayered Langmuir-Blodgett films on surfaces. The polar part of the molecule is thereby physisorbed to the surface. Physisorbed molecules stick to the surface due to van-der-Waals forces, comparably weak non-covalent interactions with binding strengths between 4 and 60 kJ·mol⁻¹.^[89] Stronger and more stable interactions can be achieved with chemisorption, the covalent or ionic attachment of organic molecules on surfaces. Chemisorbed monolayers were first investigated by Zisman and coworkers^[92] in 1946, but it took until the 1980s when advanced surface characterisation techniques were available, that surface bound monolayers were investigated in greater detail. Studies from Sagiv,^[93] Nuzzo^[94] and Allara^[95] first presented monolayers of thiols and organosilanes on metal and metal-oxide surfaces, respectively. These so called self-assembled monolayers (SAMs) represent nowadays the most important method of surface functionalisation, as they enable the deposition of highly-ordered, densely packed stable organic thin films, that can be easily modified with functional groups for specific applications or further functionalisation and set the basis for more complex molecular architectures on surfaces.

Within this thesis, SAMs on gold, silicon and glass surfaces are used as templates to deposit mono- and multilayers of supramolecules, which is set out in more detail below.

3.3.1. Self-assembled monolayer (SAM) on gold, glass and silicon surfaces

A self-assembled monolayer is an ordered monomolecular organic thin film that forms spontaneously on a surface. A self-assembled monolayer can be divided into three functional sections: head group, spacer units and terminal group (Figure 33).^[90] The reactive head group chemisorbs to the surface. Specific reactive groups are thereby required for each type of surface material. The formation of attractive interactions between surface and head group represents the major energetic contribution to the overall process.^[96] The middle part of a SAM consists of spacer units. Attractive interactions between spacer units are crucial for the formation of a SAM. For aliphatic spacer units such as alkyl chains, the interactions between the molecules are van-der-Waals forces, while for aromatic systems also π - π interactions are implicated. The interplay of interactions between head group and surface and the spacer units among each other causes the SAM to be tightly packed. SAM formation is a dynamic process including error correction.^[97]

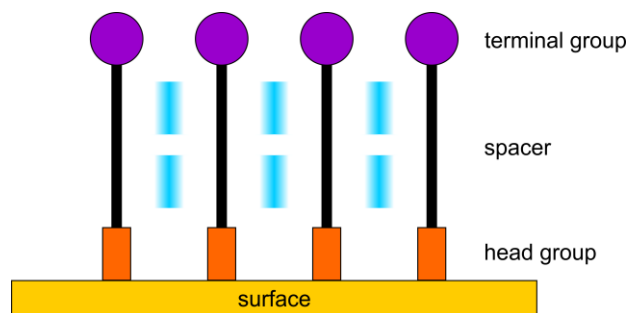


Figure 33: Schematic representation of a SAM on a surface.

The terminal group of a SAM determines the chemical properties of the functionalised surface. Unfunctionalised or fluorinated alkyl chains for example yield an unreactive and hydrophobic or superhydrophobic surface, while hydroxyl or carboxy terminated SAMs have hydrophilic properties. The use of reactive groups or binding sites as terminal groups of a SAM enables on-surface reactions for further functionalisation or deposition of different molecular or supramolecular structures.

A variety of SAMs with variable properties has been developed suitable for the deposition on different substrates. Sulphur compounds such as organothiols, thioacetates and disulfides are used for the formation of SAMs on metal surfaces like gold, silver, copper or palladium.^[96, 98] Organosilanes and organophosphonates form SAMs on hydroxylated metal surfaces,^[99] carboxylic acids on metal oxides,^[94, 100] and alkenes and alkynes are used to functionalise silicon or germanium surfaces.^[101] In this thesis, two types of SAMs have been used: organothiols on gold surfaces and alkoxy silanes on hydroxylated silicon and glass surfaces.

SAMs of organothiols and disulfides on gold represent the most frequently used and best characterised system. Gold surfaces are easy to handle as they are unreactive towards most chemicals and do not get oxidised in ambient condition. Their strong affinity for sulphur compounds allows a defined functionalisation. Due to the strong gold-sulphur bond with a binding strength around $180\text{-}200\text{ kJ}\cdot\text{mol}^{-1}$, monolayers of thiols on gold are highly stable.^[98a] The formation process of an alkyl thiol SAM on gold starts with the disordered physisorption of the alkyl thiols, which lay flat on the surface. In the next step, the chemisorption occurs by oxidative addition of thiol to gold followed by reductive elimination of hydrogen, resulting in the formation of a sulphur-gold bond.^[102] The molecules begin to straighten and form small highly ordered domains, which finally results in a densely packed monolayer covering the whole surface. The distance between the alkyl chains in an ordered SAM is in the order of 5 \AA .^[103] Unfunctionalised alkyl thiols on gold surfaces usually have tilt angles of approximately 30° relative to the surface normal.^[97]

In practice, the deposition is typically achieved by immersing a freshly cleaned gold surface into a low concentrated solution of the organothiol in a polar solvent at room temperature for 24 h. Surface cleaning can be accomplished with plasma or ozone cleaners or by immersing the surface in a solution of concentrated HCl or a mixture of sulphuric acid and hydrogen peroxide.^[15a]

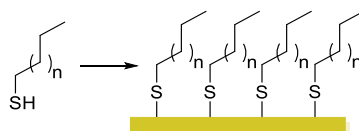


Figure 34: Formation of a SAM of an alkyl thiol on a gold surface.

Marder and coworkers^[104] investigated SAMs of different stilbene thiols on gold surfaces. They found out that the SAMs are densely packed with the long molecular axes of the thiolates almost perpendicular to the surface (Figure 35, left). This illustrates the difference in geometry of alkylthiol and arylthiol SAMs. Such an upright arrangement is advantageous for further functionalisation of SAMs with large molecules. In this thesis, the analogous pyridine substituted stilbene thiol **PST** (Figure 35, right) was used for further functionalisation of gold surfaces.

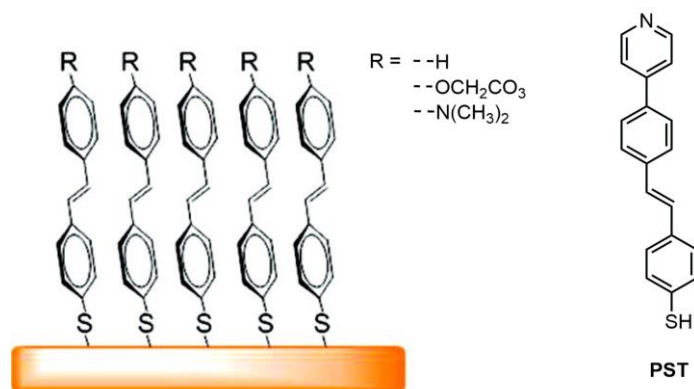


Figure 35: Upright arrangement of a SAM of differently substituted thiol silbenes on a gold surface (left). Pyridine-substituted stilbene thiol **PST** used within this thesis. Adapted with permission from M. Malicki, Z. Guan, S. D. Ha, G. Heimel, S. Barlow, M. Rumi, A. Kahn, S. R. Marder, *Langmuir* **2009**, *25*, 7967-7975. Copyright (2009) American Chemical Society.

The deposition of SAMs of organosilanes on hydroxylated surfaces is well documented for a variety of organic molecules.^[102b, 105] Common substrates for this type of SAMs are silicon oxide, glass, mica, aluminium oxide, titan oxide or zirconium oxide. The SAM formation is initiated by physisorption of hydrolysed silanes to the surface and therefore always requires a small amount of water.^[106] Condensation of adjacent molecules under formation of Si-O-Si bonds yields first small highly ordered domains of polysiloxanes on the surface, which merge in a surface polymerisation reaction to a crosslinked polysiloxane network. The SAM molecules are therefore not only connected to the surface, but also among each other. The Si-Si distance is in the order of 4.5 Å. The Si-O network adapts a chair-like conformation with the organic substituents in axial positions (Figure 36).^[105]

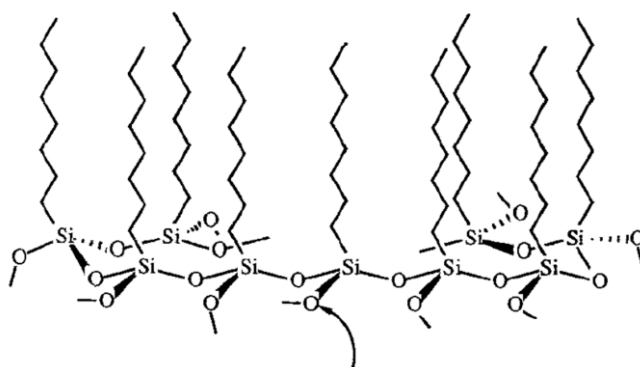


Figure 36: A schematic description of a polysiloxane at the monolayer-substrate interface. The arrow indicates an equatorial Si-O bond that can be connected either to another polysiloxane chain or to the surface. Reprinted with permission from A. Ulman, *Adv. Mater.* **1990**, *2*, 573-582. Copyright (1990) John Wiley & Sons.

In practice, the deposition is typically set out by immersing a freshly cleaned surface into a low-concentrated solution of the SAM for 24h.^[15c] While most SAMs form completely at ambient

conditions, some require elevated temperatures for a complete formation of the covalent polysiloxane network.

3.3.2. Mono- and multilayer architectures on surfaces

The functionalisation of a surface with a SAM bearing reactive terminal groups enables the deposition of additional layers or on-surface reactions. In principle, all reactions that work in solution can be used for post-functionalisation of SAMs, as long as the reaction conditions are compatible with the SAM. A selection of successfully performed reactions on SAMs is depicted in Table 2.

Table 2: Selected examples of reactions on SAMs.^[107]

terminal group of SAM	type of reaction	reagent	Product
azide	1,3-dipolar cycloaddition	alkyne	triazole
alkene	oxidation	potassium permanganate	ketone / diol
	metathesis	terminal alkene	alkene
amine	nucleophilic substitution	acid chlorides, active esters	amide
	nucleophilic addition	isothiocyanates, diisocyanates, isocyanates	thiourea, carbamate, urethane
alcohol	acylation	acid chlorides, anhydrides	esters
carboxylic acid	acylation	amine	amide
aldehyde	nucleophilic substitution	amine	amide
epoxide	nucleophilic substitution	primary amines	secondary amine
hydroquinone	Diels-Alder reaction	cyclopentadiene	cyclohexene

Besides reactions that form covalent bonds from the SAM to the added reagent, also the attachment of molecules on a SAM via non-covalent interactions is possible. Reported examples include the deposition of compounds on a surface using electrostatic interactions with positively and negatively charged molecules,^[13a] the hydrogen bond-mediated deposition

of molecules,^[108] and the deposition of metal-ions and organic molecules using coordination chemistry.^[15a]

To achieve the functionalisation of surfaces with more complex structures, layer-by-layer (LbL) assembly represents a powerful technique.^[109] Layer-by-layer assembly describes the alternating deposition of components with complementary reactive centers or binding motifs to build up layered structures. The first example of a LbL assembly was described in 1966 by Iler^[110] with the alternating deposition of positively and negatively charged colloidal particles, but it took until the 1990s with the reports from Decher and coworkers to establish the method and develop a general procedure.^[111] The use of non-covalent interactions as binding principle in a LbL process leads to a thermodynamically controlled deposition which is referred to as LbL self-assembly. The reversible nature of non-covalent binding processes allows error correction and therefore the formation of highly ordered structures.

LbL self-assembly is a simple and low-cost method that can be conducted in the laboratory using beakers and tweezers but can also easily be scaled up for industrial processes. Starting with a templated surface, usually a SAM with a specific binding site as terminal group, layers of complementary binding substances are deposited by simply immersing the surface into a solution of the respective compound (Figure 37). After each deposition step, the surface is washed with pure solvent to remove any unspecific bound molecules. The versatile approach of LbL self-assembly offers a great freedom regarding the choice of materials, layering sequence and overall number of layers.

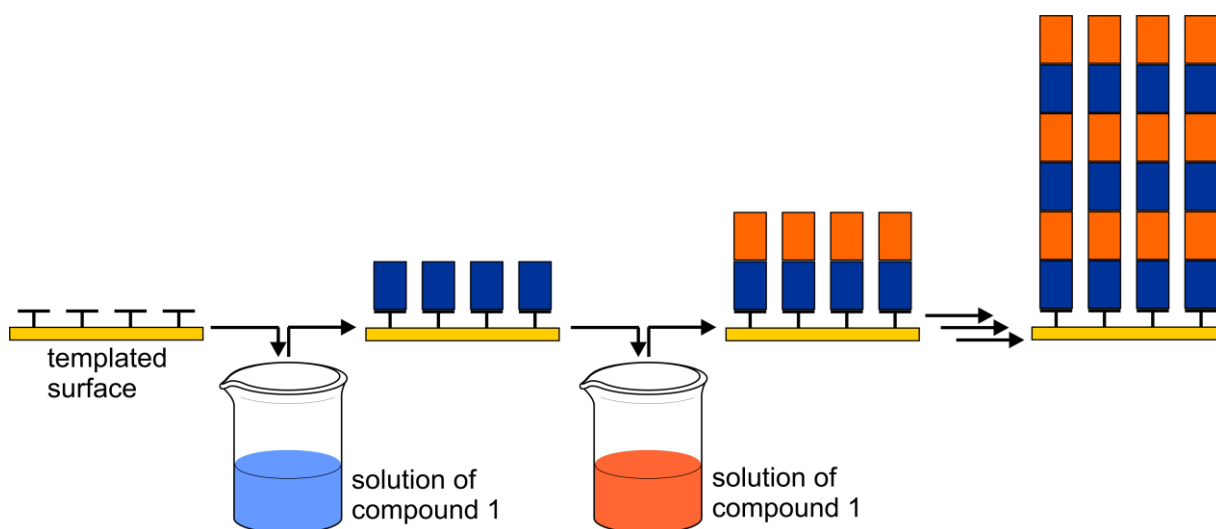


Figure 37: Schematic representation of the LbL self-assembly process.

Whithin this thesis, azide terminated SAMs were functionalised covalently with a 1,3-dipolar cycloaddition and pyridine terminated SAMs were functionalised over pyridine/terpyridine metal-ion coordination chemistry.

3.3.2.1. Pyridine/terpyridine metal-ion coordination chemistry on surfaces

Coordination chemistry can be used for the non-covalent functionalisation of SAMs and the construction of metal-organic multilayers through LbL self-assembly. Metal ions are used to connect layers of organic molecules that act as ligands. Most coordinative bonds are reversible under appropriate conditions but still offer a high stability compared to other non-covalent binding motifs. The well-documented coordination chemistry in solution facilitates the transfer to surface-bound systems in addition.

Of particular interest are pyridine or terpyridine based systems which form highly stable complexes with transition metals.^[112] Octahedral coordinating metals like Fe(II), Zn(II), Co(II) or Ni(II) are used to connect two terpyridine ligands, while square planar coordinating metals like Cu(II), Pd(II) or Pt(II) connect two pyridine ligands or a pyridine and a terpyridine ligand. Numerous examples for LbL self-assembly on surfaces using metal-ion pyridine/terpyridine coordination chemistry have been reported.^[113]

Van der Boom and coworkers^[113] for instance created palladium coordinated multilayers of a rigid-rod chromophore containing two pyridine ligands on silicon and glass substrates. The substrates were functionalised with a siloxane-based template layer containing a terminal pyridine group, followed by alternating deposition of palladium ions and the organic ligand (Figure 38).

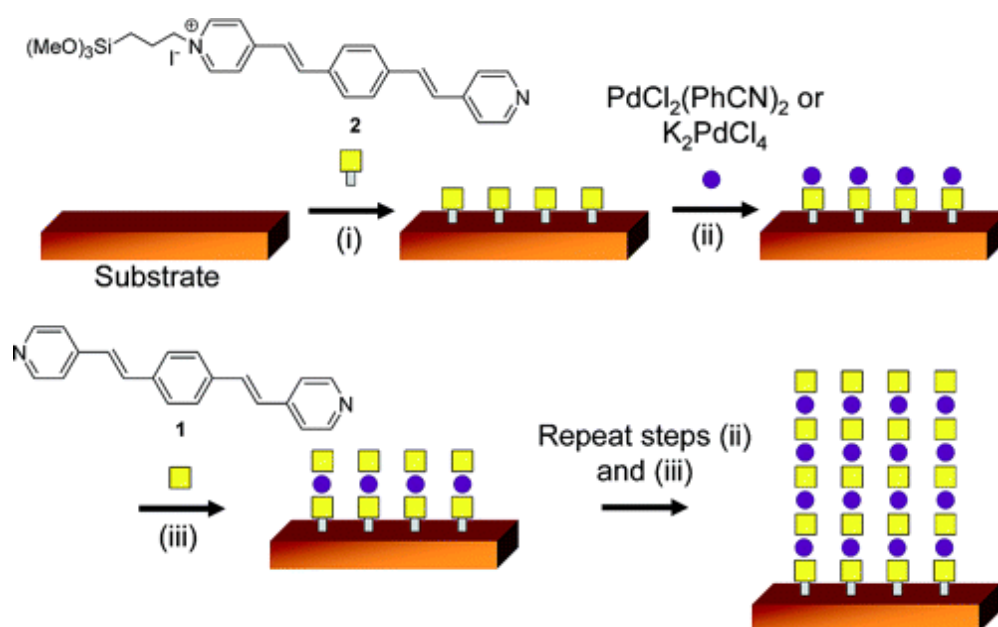


Figure 38: Schematic representation of the two-step LbL solution-based multilayer assembly. Reprinted with permission from M. Altman, A. D. Shukla, T. Zubkov, G. Evmenenko, P. Dutta, M. E. van der Boom, J. Am. Chem. Soc. 2006, 128, 7374-7382. Copyright (2006) American Chemical Society.

The use of both colloidal palladium or Pd(Cl₂(PhCN)₂) resulted in successful multilayer formation. Twelve consecutive deposition steps were conducted, resulting in structurally

regular assemblies with an equal amount of organic ligand and palladium added in each molecular bilayer. The orientation of the entire multilayer assembly is determined by the template layer with a tilt angle of approximately 20° relative to the surface normal. Subsequent layers retain this orientation, showing that structural features of a SAM can be kept and enhanced along greater distances.

A coordination-based LbL self-assembly using terpyridine ligands was reported by Licciardello and coworkers.^[113k] They used a terpyridine-functionalised SAM as template on gold surfaces and subsequently deposited multilayers of bis-terpyridine ligands connected by Fe(II) or Co(II) metal centers. The obtained multilayers are highly ordered, robust and could be grown up to 40 nm in height. The electrical properties of the assembly were investigated using a junction based on Hg electrodes. The multilayers proved to be highly conductive, and the conductance did not decrease significantly with the length of the assembly, but was influenced by the type of metal-ion used as coordinating centre.

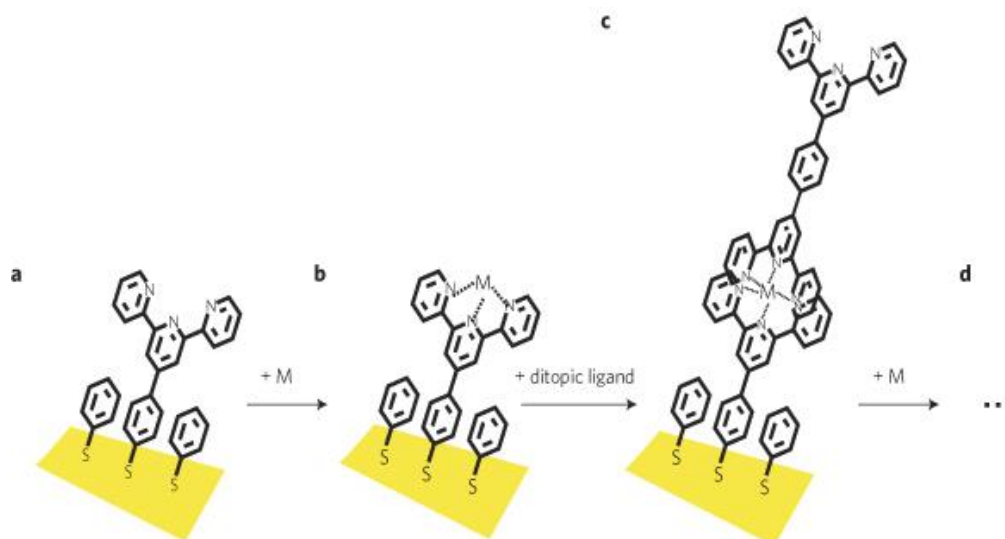


Figure 39: Coordination-based assembly of bis-terpyridine ligands on a gold surface. Reprinted with permission from N. Tuccitto, V. Ferri, M. Cavazzini, S. Quici, G. Zhavnerko, A. Licciardello, M. A. Rampi, *Nat. Mater.* **2009**, *8*, 41-46. Copyright (2009) Nature Publishing Group.

3.3.2.2. Click chemistry on surfaces

The Cu-catalysed 1,3-dipolar cycloaddition of azides and alkynes, commonly referred to as “click reaction”, is a widely used method for the post-functionalisation of SAMs. It regioselectively forms 1,4-disubstituted triazols in high yields.^[114] Mild reaction conditions, the tolerance of a broad range of functional groups and solvents as well as an easy synthetic availability of both azides and alkynes in addition make it the method of choice for a lot of different applications.^[115]

The proposed catalytic cycle for the Cu(I)-catalysed 1,3-dipolar cycloaddition starts with the formation of Cu(I) acetylide. Upon the addition of an azide, no [3+2] cycloaddition but a stepwise annealing sequence proceeding via the six-membered copper containing intermediate **III** occurs, which explains the near perfect regioselectivity towards 1,4-disubstituted 1,2,3-triazole products (Figure 40).

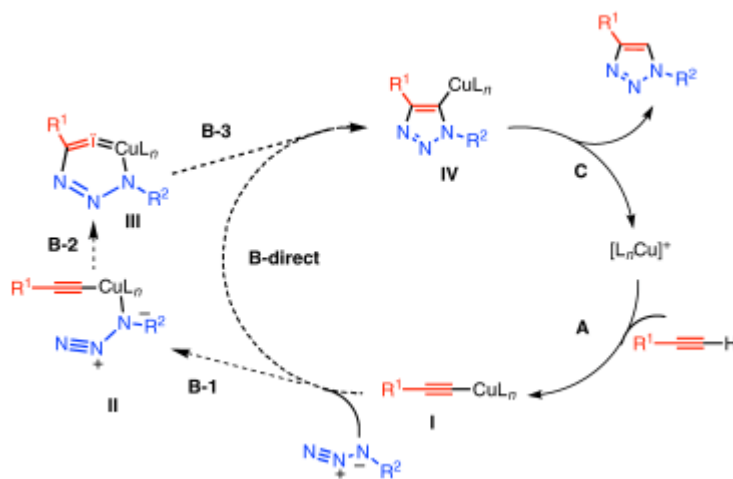


Figure 40: Proposed catalytic cycle for the Cu(I) catalysed 1,3 dipolar cycloaddition. Reprinted with permission from V. V. Rostovtsev, L. G. Green, V. V. Fokin, K. B. Sharpless, *Angew. Chem. Int. Ed.* **2002**, *41*, 2596-2599. Copyright (2002) John Wiley and Sons.

Chidsey and coworkers^[116] for example used a copper-catalysed 1,3-dipolar cycloaddition to deposit oligonucleotides on a gold surface (Figure 41). The surface was therefore functionalised with a mixed SAM of 1-azidoundecane-11-thiol and an unfunctionalised alkyl thiol. Different mixed SAMs were used to reduce the number of reactive sites on the surface in order to control the density of the deposited oligonucleotides.

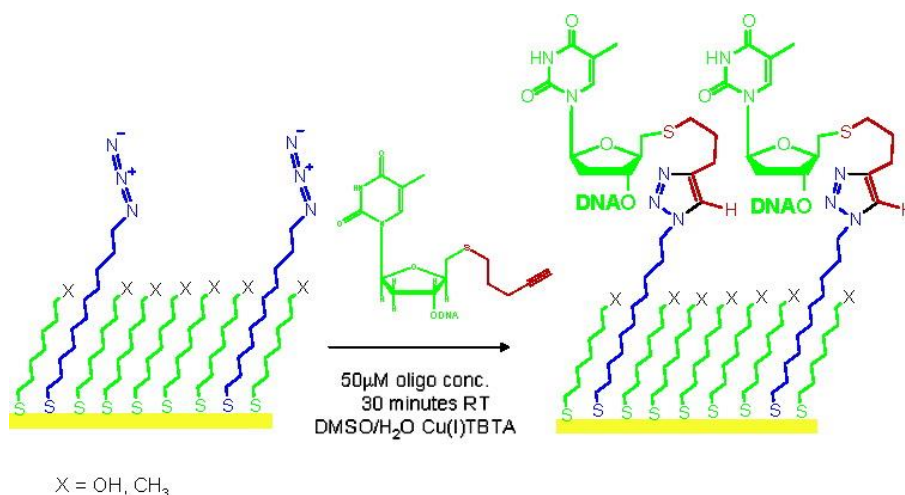


Figure 41: Surface modification of a mixed SAM on gold by chemoselective coupling of acetylene-bearing oligonucleotides. Reprinted with permission from N. K. Devaraj, G. P. Miller, W. Ebina, B. Kakaradov, J. P. Collman, E. T. Kool, C. E. D. Chidsey, *J. Am. Chem. Soc.* **2005**, *127*, 8600-8601. Copyright (2005) American Chemical Society.

The deposition of multilayers on surfaces using click chemistry was shown for example by Caruso and coworkers.^[117] They used an LbL approach for the alternating deposition of azide and alkyne-functionalised poly(acrylic acid) on gold, silicon and quartz substrates (Figure 42). A linear growth of the poly(acrylic acid) film on the surface with each deposition step was achieved, as measured with UV-Vis and IR spectroscopy. The obtained multilayer films were highly stable.

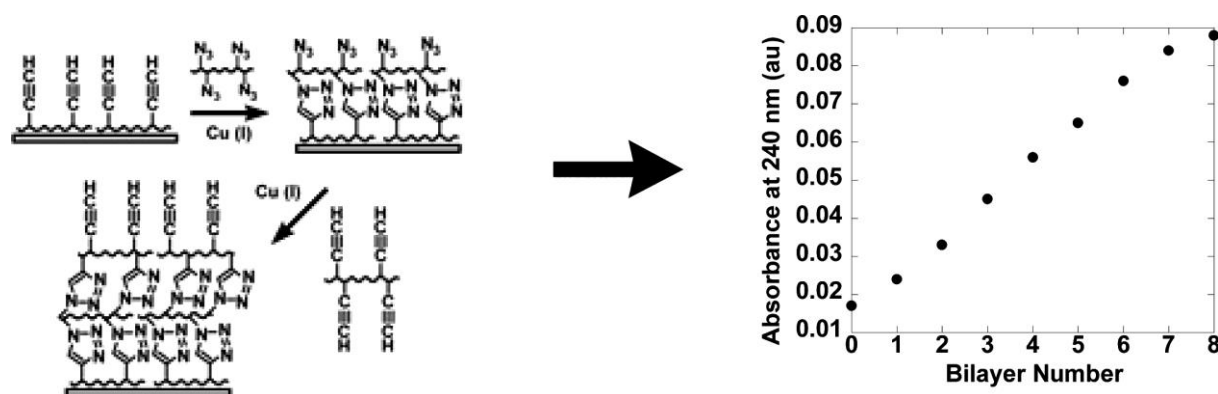


Figure 42: Layer-by-Layer assembly of azide and alkyne functionalised poly(acrylic acid) films on surfaces using click chemistry (left) and tracking of the layer growth with each deposition step by UV-Vis spectroscopy (right). Reprinted with permission from G. K. Such, J. F. Quinn, A. Quinn, E. Tjijto, F. Caruso, *J. Am. Chem. Soc.* **2006**, *128*, 9318-9319. Copyright (2006) American Chemical Society.

3.3.3. Switchable supramolecular assemblies on surfaces

With the methods described for surface functionalisation, even complex molecules and supramolecules can be deposited on surfaces. Of particular interest in the context of functional bottom-up assemblies towards molecular machines is the deposition of molecular switches and switchable mechanically interlocked supramolecules on surfaces. As explained previously, the deposition of molecular switches and machines is a prerequisite for coupled molecular processes to gain macroscopic effects. As this thesis focuses on the deposition of switchable rotaxanes on surfaces, only switchable supramolecular assemblies and no molecular switches deposited on solid supports^[118] are discussed in this chapter. Assemblies on nanoparticles^[119] are not discussed in here as well.

A popular example for the immobilisation of a presynthesised switchable rotaxane on a surface was reported by Stoddart and coworkers.^[13b] They constructed a switchable palindromically constituted [3]rotaxane consisting of two cyclobis(paraquat-*p*-phenylene) rings and a symmetric axle with two tetrathiafulvalene (TTF) and two naphthalene binding sites (Figure 43a). Upon oxidation of the TTF units, the two rings move from the TTF to the naphthalene binding sites, changing the inter-ring distance from 4.2 nm to 1.4 nm. Reduction of the TTF units restores the initial state. The switching was conducted either chemically by adding oxidation and reduction agents or electrochemically by applying the respective potentials. By substituting the rings with disulphide tethers, the [3]rotaxane could be deposited in a self-assembly process on gold surfaces. One side of a gold microcantilever was functionalised with a layer of [3]rotaxanes and treated with aqueous chemical oxidants and reductants, which induced a bending of the microcantilever that could be repeated over several cycles (Figure 43b). This example illustrates that cumulative microscopic movements of surface-bound muscle-type molecules can be utilised to achieve macroscopic effects.

Especially, surfaces functionalised with photoresponsive units have been of great interest in recent research.^[42a, 118a, 120] Addressing responsive surfaces by inducing a chemical stimulus unavoidably brings impurities into the system and therefore hampers an unambiguous analysis of structural changes on the surface. When switchable supramolecular assemblies on surfaces are fully controlled by light stimuli, the observed changes can be clearly attributed to the respective photoinduced processes. However, the photoisomerisation of chromophors immobilised on surfaces can bring up other difficulties. While azobenzene for instance readily photoisomerises in both gas and solution phases, the isomerisation is quenched, if it is immobilised directly on conductive surfaces.^[121] The problem can be avoided by electronic decoupling of the chromophore from the surface. Establishing spatial distance between surface and chromophore, for instance by an insulating SAM, or using semiconductive or non-conductive substrates instead of metal surfaces leads to the desired result.^[122]

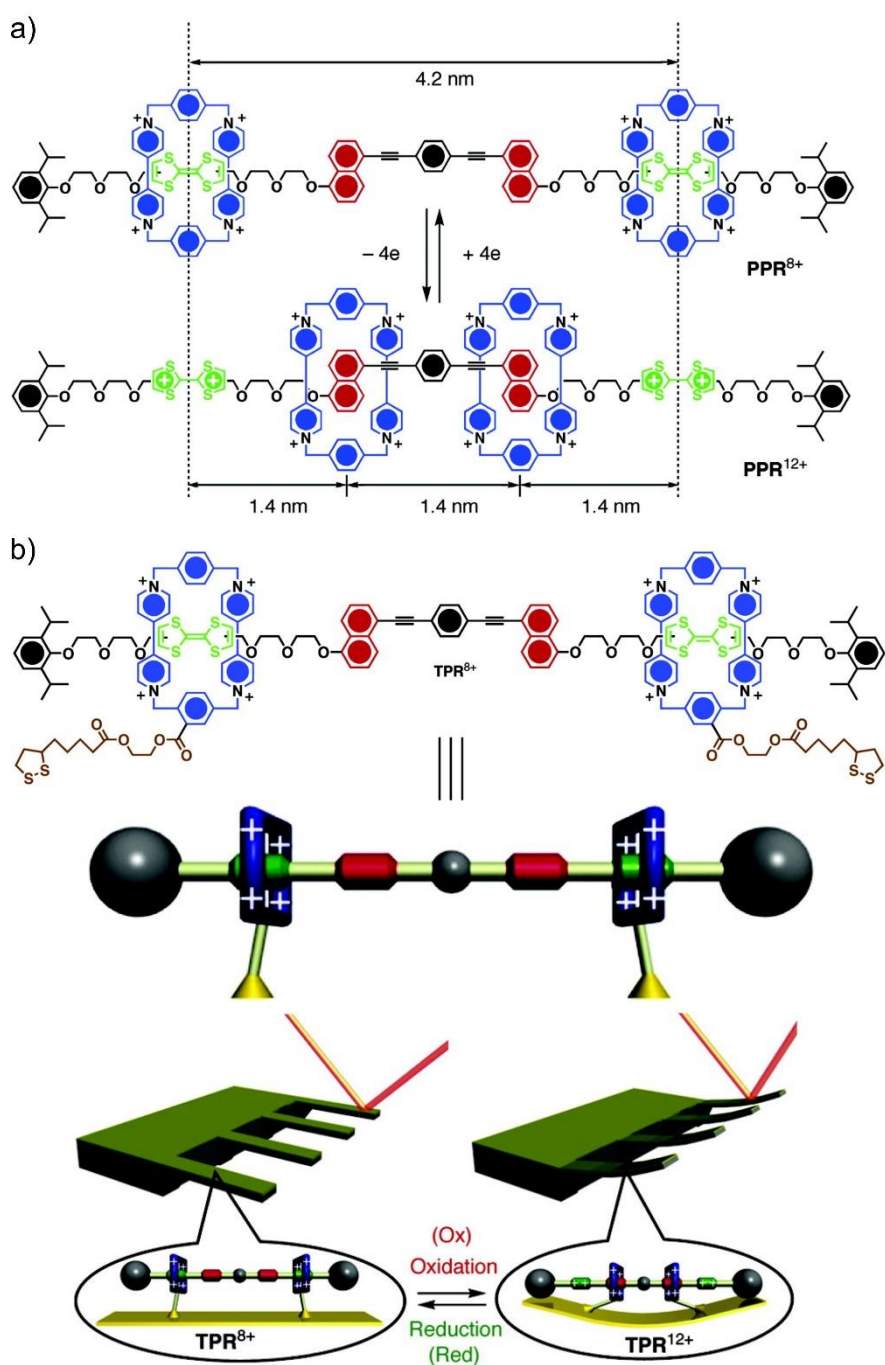


Figure 43: a) Structure of the contracted and extended states of a switchable [3]rotaxane and b) the [3]rotaxane functionalised with a disulphide tether for surface deposition. Schematic representation of the rotaxane deposited on a microcantilever with the proposed mechanism of the device's operation. Reprinted with permission from Y. Liu, A. H. Flood, P. A. Bonvallet, S. A. Vignon, B. H. Northrop, H.-R. Tseng, J. O. Jeppesen, T. J. Huang, B. Brough, M. Baller, S. Magonov, S. D. Solares, W. A. Goddard, C.-M. Ho, J. F. Stoddart, *J. Am. Chem. Soc.* **2005**, *127*, 9745-9759. Copyright (2005) American Chemical Society.

An example for the deposition of a photoresponsive supramolecular switch on surfaces was reported by Leigh and coworkers.^[13a] They synthesised a rotaxane comprised of a tetralactam macrocycle and an axle with two diamide binding sites. One binding site bears an alkene

functionality that can be photochemically switched from its *trans*- to its *cis*-configuration, while the other binding site is comprised of fluorinated alkanes. The alkene moiety represents the favoured binding site in its *trans* configuration (Figure 44a). The rotaxane was physisorbed onto a gold surface functionalised with a SAM with terminal carboxylic acid groups (Figure 44b). A droplet of diiodomethane was positioned on the surface and the surface irradiated with UV-light on one side of the droplet. Upon irradiation with UV light, the alkene binding site switches from *trans* to *cis* and thus induces the movement of the macrocycle to the fluorinated station. The concealing of the fluoroalkane residues by the macrocycle alters the surface tension. This effect proved to be sufficient enough to transport a microliter drop of diiodomethane about 1.5 mm up a twelve-degree incline (Figure 44c). Back switching to the initial state within this system cannot be achieved photochemically but only by thermal equilibration.

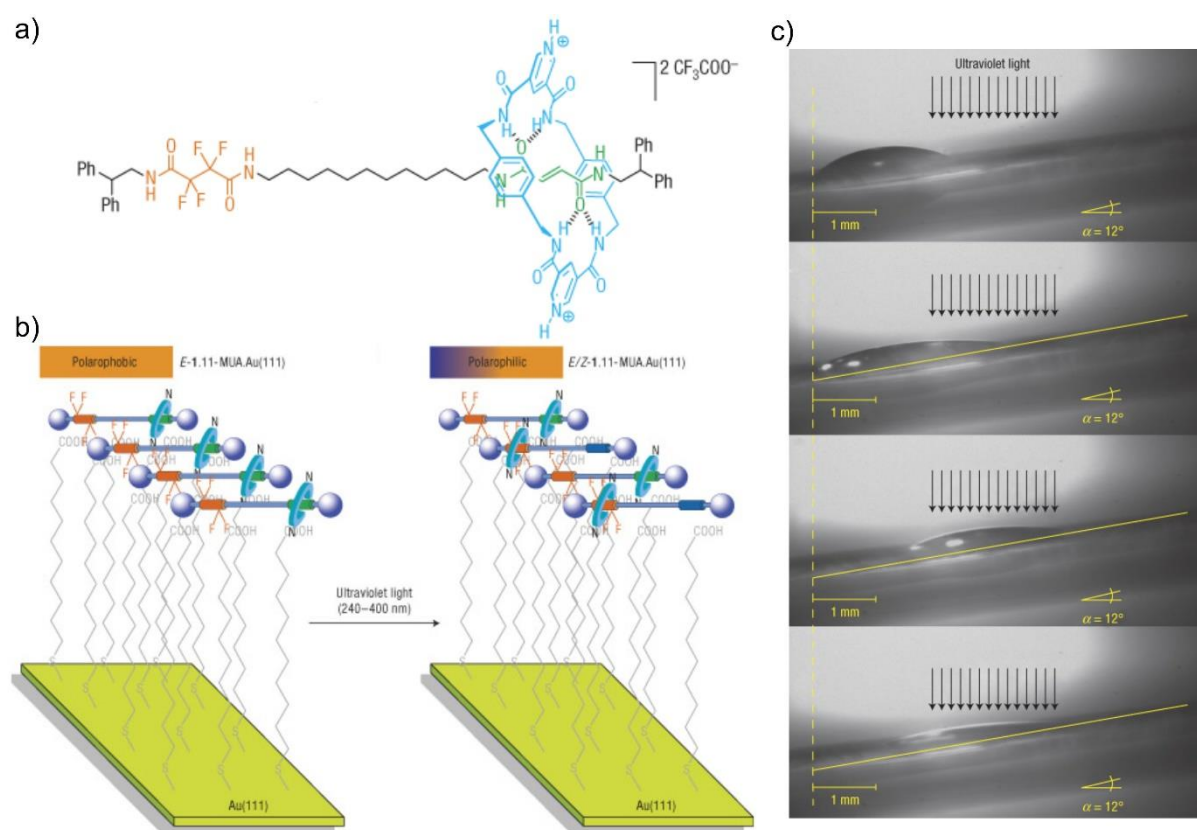


Figure 44: a) Molecular structure of the photoswitchable rotaxane, b) light-switching of a monolayer of rotaxanes physisorbed to a gold surface functionalised with a carboxylic acid terminated SAM and c) photoinduced transport of a droplet of diiodomethane on a surface up a twelve-degree incline. Reprinted with permission from J. Berna, D. A. Leigh, M. Lubomska, S. M. Mendoza, E. M. Perez, P. Rudolf, G. Teobaldi, F. Zerbetto, *Nat. Mater.* **2005**, *4*, 704–710. Copyright (2005) Nature Publishing Group.

In the previously described examples, presynthesised switchable MIMs were deposited as a whole on surfaces. Alternatively, switchable supramolecular assemblies can be constructed directly on the surface using host-guest chemistry.^[123]

An example where a photoswitchable rotaxane was directly assembled on a gold surface was reported by Willner and coworkers.^[124] They functionalised a gold wire electrode with a SAM of cystamine and subsequently attached an azobenzene unit and a long alkyl chain, threaded a ferrocene substituted β -cyclodextrin (CD) and stoppered the assembly with a bulky anthracene (Figure 45). Deslipping of the CD from the thread is prevented by the gold surface on one side and the anthracene on the other. The CD complexes the azobenzene in its *trans* configuration and therefore brings the ferrocene in close proximity to the gold electrode. Upon photoinduced *trans* to *cis* isomerisation of the azobenzene by irradiation with UV light, the CD is displaced to the alkyl chain, increasing the distance of gold electrode and ferrocene. Irradiation with visible light induced backswitching and restored the initial state. The position of the ferrocene relative to the gold electrode was measured with chronoamperometry. A fast current decay ($k = 65 \text{ s}^{-1}$) was observed when the azobenzene was in its *trans*-configuration, while a substantially lower electron transfer rate ($k = 15 \text{ s}^{-1}$) was observed for the *cis*-configuration, which is clear evidence for the expected photoinduced dislocation of the CD. The device is thus able to transduce an optical signal into an electronic signal.

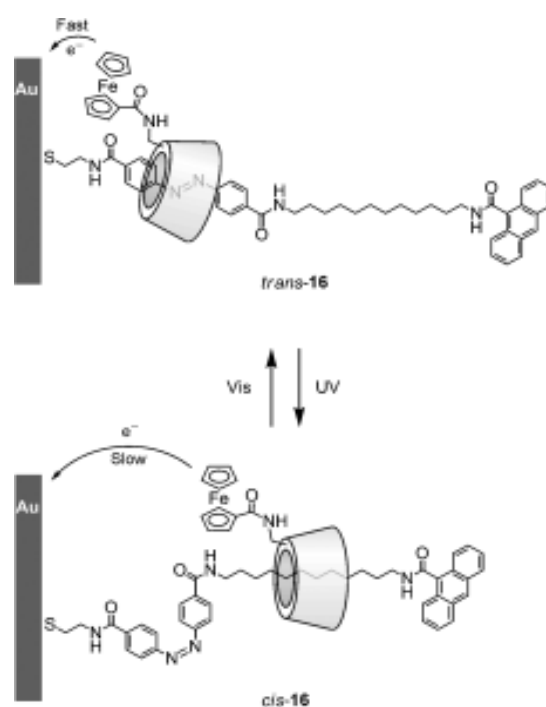


Figure 45: Schematic representation of the surface-bound photoswitchable rotaxane by Willner and coworkers.^[124] Reprinted with permission from V. Balzani, A. Credi, M. Venturi, *ChemPhysChem* **2008**, 9, 202-220. Copyright (2008) John Wiley and Sons.

Furthermore, several examples for surface bound stimuli responsive pseudorotaxes are reported, where an external stimulus is used to control the binding or detaching of molecules on solid support.^[125]

An example for a surface-bound photoresponsive pseudorotaxane is the system comprised of azobenzene-functionalised peptide nanotubes and an α -cyclodextrin monolayer on gold substrates reported by Matsui and coworkers (Figure 46).^[126] They used peptide nanotubes that incorporate amide sites to anchor hydroxyazobenzenecarboxylic acid via hydrogen bonding between the carboxylic acids and the amide groups. Azobenzene forms a stable inclusion complex with α -CD in its *trans*-configuration, but does not bind to the CD in its *cis*-configuration. Photolithographically patterned gold substrates were functionalised with a SAM of thiolated α -CD and immersed in a solution of the azobenzene functionalised peptide nanotubes in the dark, which induced the formation of an inclusion complex on the surface. Upon irradiation of the surface with UV light in a stirred solution, the peptide nanotubes detached from the surface. Equilibration in the dark for 24 h induced rebuilding of the complex.

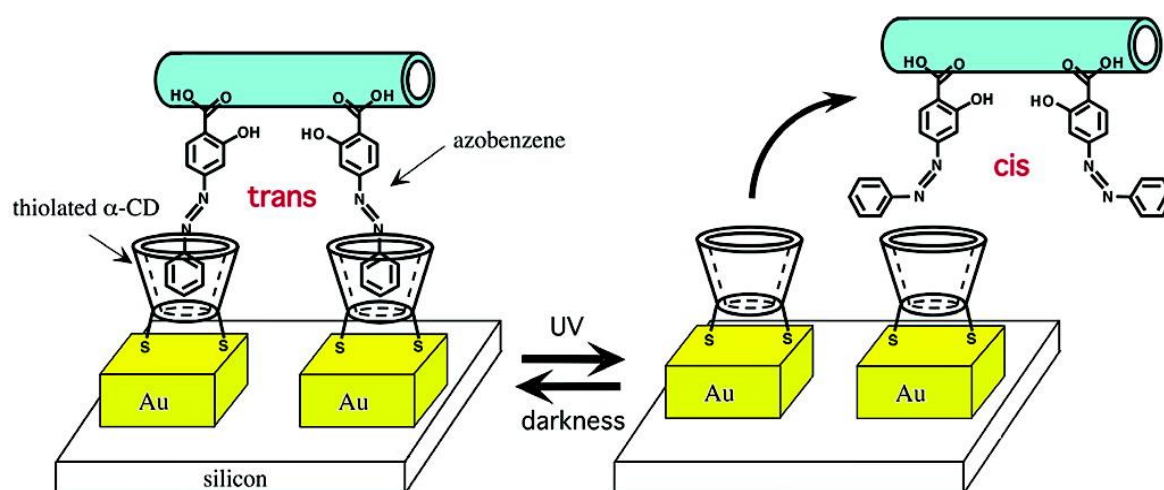


Figure 46: Schematic representation of the azobenzene nanotube assembly on the complementary α -CD/Au substrates via host-guest molecular recognition and light-induced nanotube detachment/attachment on the α -CD surfaces. Reprinted with permission from I. A. Banerjee, L. Yu, H. Matsui, *J. Am. Chem. Soc.* **2003**, 125, 9542-9543. Copyright (2003) American Chemical Society.

In conclusion, there are several reported examples for stimuli-responsive supramolecular assemblies on solid supports. However, only a few reports on photoswitchable surface-bound mechanically interlocked molecules exist. The only reported example of switchable rotaxanes deposited in self-assembled multilayers on surfaces was published in 2015 by the Schalley group.^[15d] Up to today, there is no example on multilayers of photoswitchable rotaxanes on surfaces, which constituted a main motivation for this thesis.

3.3.4. Analytical methods for surfaces

The study of surfaces and interfaces in a detailed and specific way goes back more than hundred years, starting predominantly in the fields of catalysis and corrosion.^[127] The development of ultra high vacuum techniques around 1960 led to a quantum leap in the development of elaborate surface analysis methods. While photon-based techniques can be operated at ambient pressure, analysis methods involving electrons and ions usually require pressures lower than 10^{-8} mbar as these particles are scattered by molecules in the gas phase.^[89] With the rise of high-resolution microscopy techniques around 1980, a detailed analysis of surface topography became possible.

Modern surface analysis uses a variety of complementary techniques to gain a detailed understanding of the elemental and molecular composition, structural orientation, physical topography and interfacial properties of a surface. No single technique can provide all these different kinds of information, so that usually several methods are applied in a surface study. Today, there exist over 50 different methods for surface analysis. Some of the most common are summarised in Table 3 including the principal information they provide.^[128]

Table 3: Selection of common surface analysis techniques

Analysis Technique	Elemental composition	Molecular composition	Structural orientation of adsorbates	Physical topography
XPS	✓	(✓)		
AES	✓	(✓)		
NEXAFS		✓	✓	
SIMS	✓	(✓)		
LEED			✓	
ISS	✓		✓	
UV-Vis		✓		
IRRAS		✓	✓	
AFM				✓
STM				✓
TEM				✓

Within this thesis, transmission UV-Vis spectroscopy, X-ray photoelectron spectroscopy (XPS), near edge X-ray absorption fine structure spectroscopy (NEXAFS) and contact angle measurements were employed for the characterisation of functionalised surfaces. These methods will be introduced and discussed further below.

3.3.4.1. Transmission UV-Vis spectroscopy

Transmission UV-Vis spectroscopy is a variant of absorption spectroscopy using light in the ultraviolet and visible region, typically between $\lambda = 200$ nm and $\lambda = 800$ nm. The interaction of molecules with electromagnetic radiation in this wavelength range leads to the excitation of valence electrons. If the wavelength of the incident light matches the energy difference between an occupied and an unoccupied orbital, an excitation of an electron into the energetically higher unoccupied orbital occurs. The resulting absorbance can be detected. As valence electrons participate in covalent bonds, these absorbances give information about the binding situation and the molecular composition of the studied substance. Figure 47 gives an overview of possible transitions and the resulting absorbance range in an UV-Vis spectrum. $\pi \rightarrow \pi^*$ and $n \rightarrow \pi^*$ transitions can be nicely measured with UV-Vis spectroscopy, while $\sigma \rightarrow \sigma^*$ transitions are usually not detected due to the high energy required for these transitions.^[129]

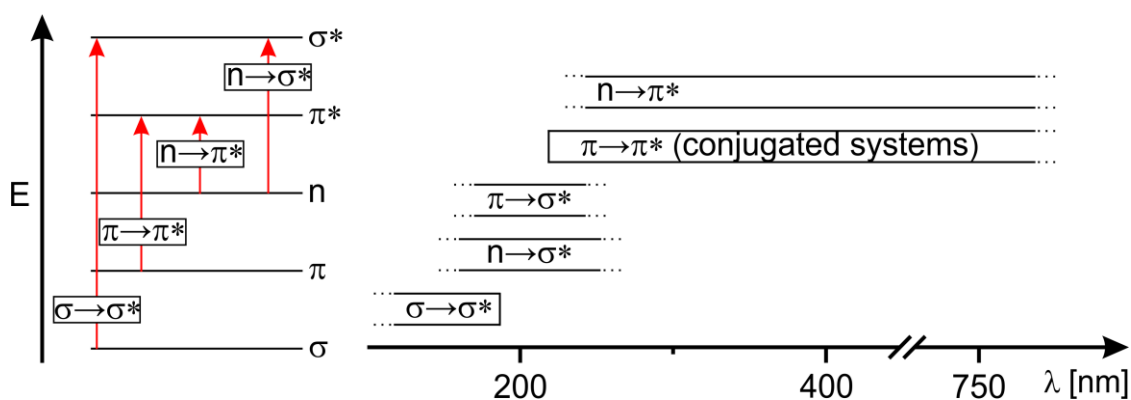


Figure 47: Molecular orbitals and electron transfers (left), absorption range of different electron transfers (right).^[129]

The attenuation of light by a material through which it is travelling can be described with the Lambert-Beer law (Equation 1). The absorbance is directly proportional to the molecular attenuation coefficient, the concentration of the absorbing substance and the path length and can therefore be used to determine the concentration of the absorbing substance in solution.

$$A = \lg\left(\frac{I}{I_0}\right) = \varepsilon * c * d$$

Equation 1: Lambert-Beer law. Absorbance (A), intensity of the incident light (I_0), transmitted intensity (I), molecular attenuation coefficient (ε), concentration (c), path length (d).

UV-Vis spectroscopy is usually employed for the measurement of solutions, but can also be utilised to examine transparent or semi-transparent solid materials. This has been used mostly for the analysis of functionalised glass surfaces. Thin gold films up to approximately 20 nm possess semi-transparent qualities and can therefore be analysed with UV-Vis spectroscopy as well.

Zharnikov and coworkers^[113f] for example used UV-Vis spectroscopy to follow the controlled growth of multilayers in multicomponent coordination-based oligomer films on siloxane-based templates on glass surfaces. Iron and ruthenium polypyridyl complexes with pendant pyridine groups and a coinage metal as linker were used as building blocks. UV-Vis measurements after each layer deposition step showed a good linear correlation between the optical absorption and the number of the metallo-ligand units (Figure 48).

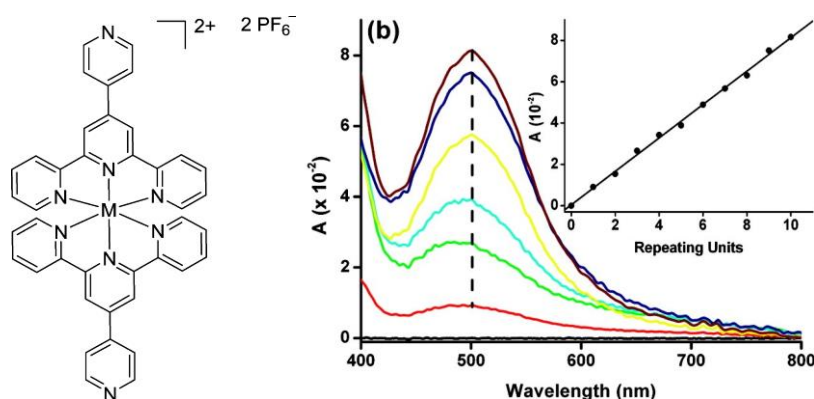


Figure 48: a) Metallo-ligands used for layer-by-layer self-assembly ($M = \text{Ru}, \text{Fe}$) and b) UV-Vis absorption spectra of Ag-based metallo-ligand terminated oligomer assemblies (1, 3, 5, 7, 9, and 10 repeating metal/metallo-ligand units) The oligomer films 1-9 comprise the Ru-based metallo-ligand, whereas the topmost 10th unit of the oligomers is the Fe-based metallo-ligand. Inset: Absorption at $\lambda_{\text{max}} = 498 \text{ nm}$ vs number of the repeating metal/metallo-ligand units (layers). Adapted with permission from P. C. Mondal, J. Yekkoni Lakshmanan, H. Hamoudi, M. Zharnikov, T. Gupta, *J. Phys. Chem. C* **2011**, 115, 16398-16404. Copyright (2011) American Chemical Society.

The detection of $\pi \rightarrow \pi^*$ transitions renders UV-Vis spectroscopy a valuable tool for the analysis of photoswitches, as they usually possess conjugated π -systems. Especially on surfaces, where only a limited range of analysis techniques is available in comparison to solution, UV-Vis spectroscopy often represents the method of choice for the analysis of photoresponsive systems.

Browne and coworkers^[130] used UV-Vis spectroscopy to follow the photoswitching of a spiropyran on gold substrates. They deposited a self-assembled monolayer of 6-nitro BIPS modified with a disulphide-terminated aliphatic chain on gold surfaces. The obtained SAMs were composed of the ring-closed spiropyran form (SP), which could be converted into the merocyanine form (MC) by irradiation with UV light. Back-switching was accomplished either thermally or by irradiation with visible light (Figure 49).

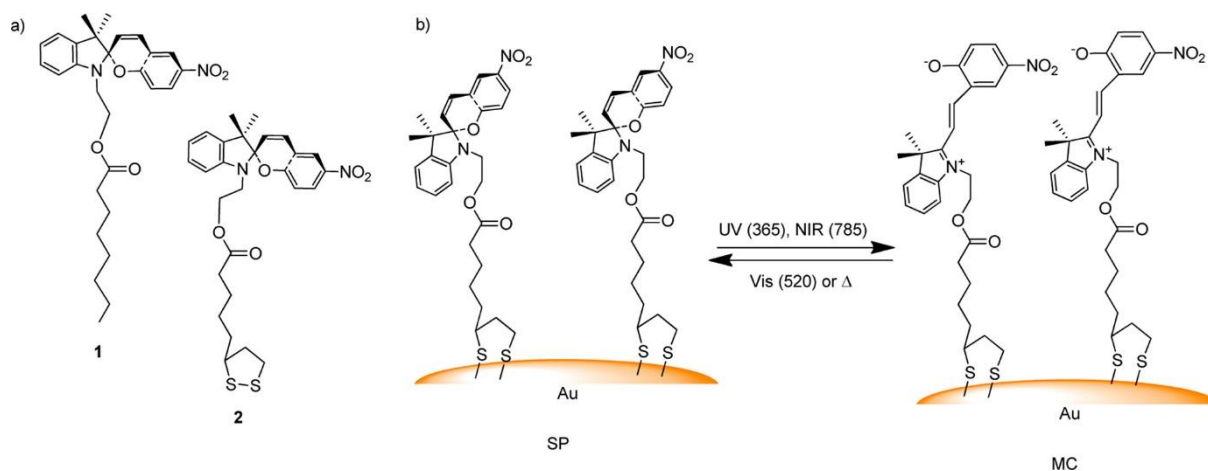


Figure 49: a) Structure of spiropyrans, b) photoswitching of spiropyran in a self-assembled monolayer on gold. Reprinted with permission from O. Ivashenko, J. T. van Herpt, B. L. Feringa, P. Rudolf, W. R. Browne, *Langmuir* **2013**, 29, 4290-4297. Copyright (2013) American Chemical Society.

With the use of semitransparent gold surfaces as substrates, absorption spectra of the SAM could be measured. The UV-Vis spectrum was dominated by gold plasmonic absorption in the range of 200 – 700 nm. After irradiation with UV light for 10 min, a decrease in absorption at 335 nm which can be associated to the $\pi \rightarrow \pi^*$ transition of spiropyran and an increase at 395 nm and 555 nm for the created merocyanine form were observed.

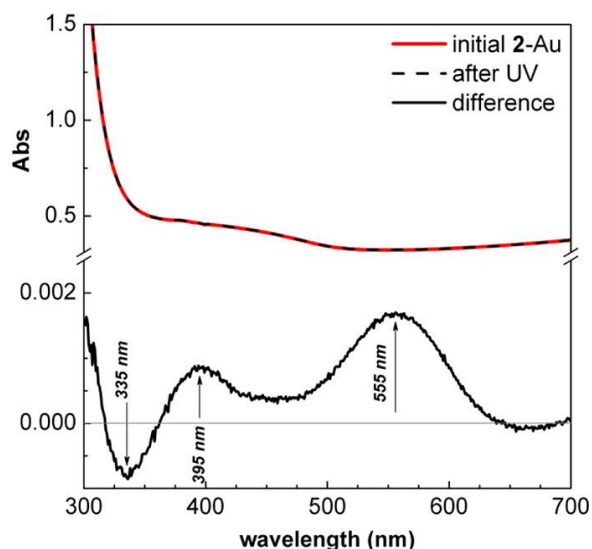


Figure 50: UV-Vis absorption spectra of a SAM on a semitransparent gold surface before (red) and after (dashed black) irradiation at 365 nm for 10 min. The difference spectrum is shown with arrows indicating the direction of the change in intensity upon irradiation. Reprinted with permission from O. Ivashenko, J. T. van Herpt, B. L. Feringa, P. Rudolf, W. R. Browne, *Langmuir* **2013**, 29, 4290-4297. Copyright (2013) American Chemical Society.

3.3.4.2. Contact angle measurement

The contact of a surface with a droplet of a liquid is characterised by the contact angle (CA). The contact angle is defined as the angle between the tangent to the liquid-fluid interface and the tangent to the solid surface at the contact line between the three phases and is usually measured on the liquid side (Figure 51).^[131] Ideal contact angles refer to a smooth, rigid, chemically homogeneous, insoluble and non-reactive surface. A distinction is made between dynamic and equilibrium CAs, of which only the latter are discussed in here.

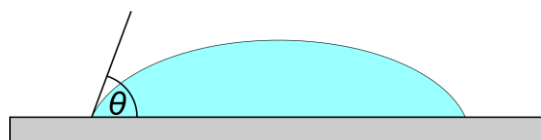


Figure 51: Schematic representation of a droplet on a surface with the contact angle θ .

Interfacial tensions exist between the liquid/fluid, the solid/liquid and the solid/fluid interface. The ratio of these tensions is expressed with the Young CA θ_Y (Equation 2).^[132] The Young CA therefore depends only on the physico-chemical properties of the fluid, liquid and solid phase. Besides the topography of a surface, the CA is in particular influenced by its chemical nature.

$$\cos \theta_Y = \frac{\sigma_{sf} - \sigma_{sl}}{\sigma_{lf}}$$

Equation 2: Young equation. Liquid-fluid interfacial tension (σ_{lf}), solid-liquid interfacial tension (σ_{sl}), solid-fluid interfacial tension (σ_{sf}).

Contact angle measurements provide perhaps the simplest way to monitor on-surface switching processes. Zhang and coworkers^[133] for example studied the influence of surface roughness on the surface wettability with functionalised gold surfaces. They deposited a molecular shuttle based on an azobenzene/cyclodextrin inclusion complex on smooth and rough gold surfaces. The azobenzene is functionalised with a trifluoromethane group at one end and an alkyl chain with a thiol endgroup at the other end. Photoswitching from *trans*- to *cis*-azobenzene induces the movement of the cyclodextrin from the azobenzene to the adjacent alkyl chain, while the trifluoromethyl group prevents deslipping of the cyclodextrin (Figure 52, top). Contact angle measurements revealed a change in surface wettability upon photoswitching of the molecular shuttle. For rough surfaces, the contact angle increased upon irradiation with UV light from 70° to 120° and was restored to its initial value upon irradiation with visible light. For flat surfaces, only a change in CA of about 2° upon photoswitching was measured (Figure 52, bottom).

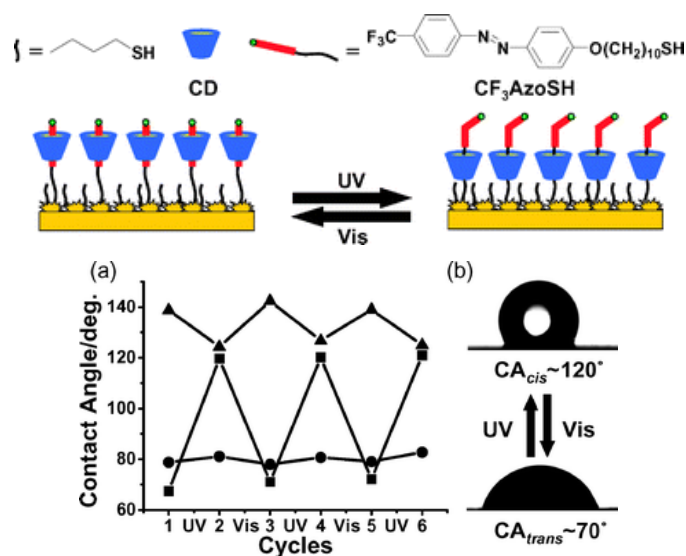


Figure 52: Photocontrolled reversible molecular shuttles on a rough surface (top). a) Reversible wettability changes of smooth surface functionalised with the molecular shuttle (circles), a functionalised rough surface (squares) and a functionalised rough surface without the cyclodextrin (triangles). b) The shapes of water droplets and corresponding contact angles on a functionalised rough surface. Reproduced from P. Wan, Y. Jiang, Y. Wang, Z. Wang, X. Zhang, *Chem. Commun.* **2008**, *44*, 5710-5712 with permission from The Royal Society of Chemistry.

3.3.4.3. X-ray photoelectron spectroscopy (XPS)

X-ray photoelectron spectroscopy is a common technique to determine the elemental and molecular composition of surfaces. The sample is irradiated under ultra-high vacuum conditions with high energy X-ray photons (> 100 eV). The impact of an X-ray photon to an atom can lead to three different events. In the first case, the photon passes through without interacting with the atom. The second case describes the scattering of the photon by an atomic orbital electron leading to partial energy loss, which is referred to as Compton scattering. In the third case, the photon transfers its total energy to a core level atomic orbital electron, leading to electron emission from the atom (Figure 53 left).^[128] The kinetic energy of the emitted electron is measured. Together with the energy of the X-ray source, the binding energy of the electron can be calculated using the Einstein equation (Equation 3). The binding energy of core electrons varies with the type of atom. As covalent or ionic bonds influence the electron distribution on the atom of interest, different binding situations can be analysed as well.

$$E_B = h\nu - KE$$

Equation 3: Einstein equation for the photoemission process. Binding energy of the electron in the atom (E_B), energy of the X-ray source ($h\nu$) and kinetic energy of the emitted electron (KE).^[134]

After the emission of a core level electron, an electron from a higher energy level of the atom drops to the vacant core hole. Since the electron dropped to a lower energy state, the atom

possesses excess energy, that is emitted either by ejecting an electron from a higher energy level (Auger electron) or by emitting an X-ray photon (X-ray fluorescence) (Figure 53 middle, right).

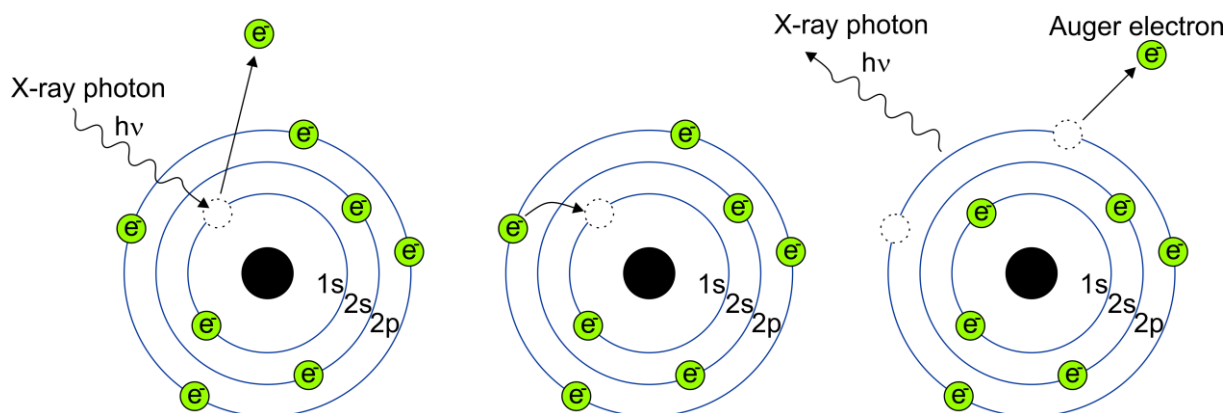


Figure 53: Schematic representation of the electronic processes in XPS. An X-ray photon transfers its energy to a core-level electron, leading to photoemission. An electron from a higher energy level drops to the vacant core hole. Excess energy in the atom can be emitted in as an Auger electron or as an X-ray photon.^[128]

Schalley and coworkers^[15a] used XPS for instance for the characterisation of SAMs. They deposited a self-assembled monolayer of 12-(pyridine-4-yl)dodecane-1-thiol (**PDT**) on gold surfaces. A survey XPS spectrum of the **PDT**-SAM on gold exhibited signals for C 1s, N 1s, S 2s and S 2p electrons and is thus confirming the deposition of the monolayer (Figure 54).

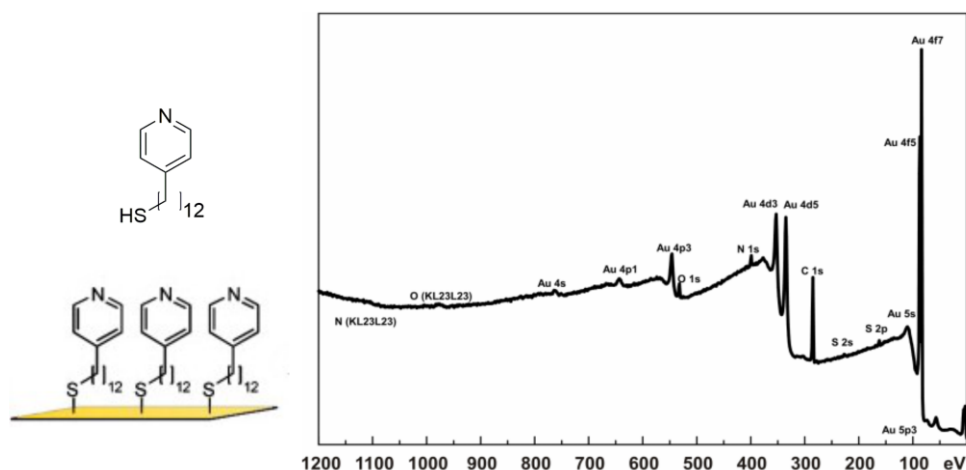


Figure 54: PDT and a SAM of PDT on a gold surface (left). Survey XPS spectrum of the **PDT**-SAM (right). Adapted with permission from J. Poppenberg, S. Richter, E. Darlatt, C. H. H. Traulsen, H. Min, W. E. S. Unger, C. A. Schalley, *Surf. Sci.* **2012**, 606, 367-377. Copyright (2011) Elsevier.

High resolution N 1s core-level spectra allowed to distinguish different binding modes of the pyridine nitrogen. The spectrum of the pristine **PDT**-SAM exhibited one large peak at 399.7 eV attributed to non-complexed pyridine nitrogen (Figure 55a). After treating the SAM with sulphuric acid, a significant shift in binding energy to 401.9 eV is observed, indicating the

protonation of the pyridine (Figure 55b). The pristine and protonated SAM were treated with a solution of $[\text{Pd}(\text{ACN})_4](\text{BF}_4)_2$ in acetonitrile to complex the pyridine with Pd(II) ions. In both XP spectra, an additional signal at 400.8 eV appeared, which is assigned to the pyridine nitrogen atoms coordinated to Pd(II) ions (Figure 55d, e).

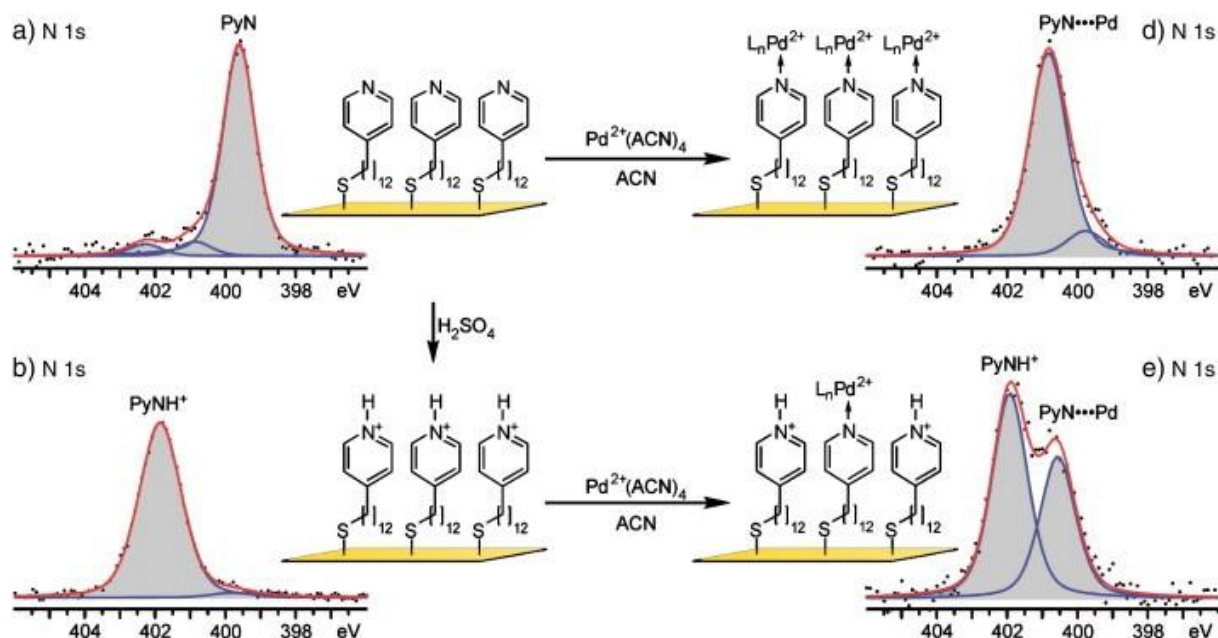


Figure 55: N 1s core level spectra of PDT SAMs in different states: a) pristine, b) protonated with H_2SO_4 , d) Pd(II)-coordinated, e) Pd(II)-coordinated after protonation. Adapted from reference ^[15a]. Copyright (2011) with permission from Elsevier.

The detailed analysis of binding states with XPS is of particular interest for the analysis of on-surface switching systems, as it can allow distinguishing between different switching states. This was for example shown by Browne and coworkers^[130] for a spiropyran based photoswitchable SAM (Figure 49). High resolution N 1s core-level spectra of the spiropyran SAM on gold exhibited two peaks at 405.9 eV and 339.4 eV, which were attributed to the nitro- and indoline-nitrogen of the spiropyran. Upon photoinduced spiropyran to merocyanine interconversion, a third peak at 400.8 eV appeared in the XP spectrum, which is assigned to the indoline nitrogen atom of the merocyanine (Figure 56).

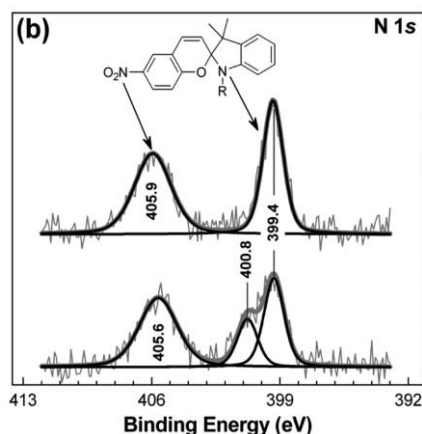


Figure 56: HR-XP spectra of the N 1s core level regions of a spiropyran-based SAM on gold before (top) and after irradiation with UV light (bottom). Reprinted with permission from O. Ivashenko, J. T. van Herpt, B. L. Feringa, P. Rudolf, W. R. Browne, *Langmuir* **2013**, 29, 4290-4297. Copyright (2013) American Chemical Society.

3.3.4.4. Near edge X-ray absorption fine structure (NEXAFS)

The near edge X-ray absorption fine structure (NEXAFS) technique was developed in the 1980s with the goal of analysing the structure of organic molecules on surfaces,^[135] while the underlying physical principles were described first in the 1920s.^[136] In X-ray absorption spectroscopy, electrons in inner-shell orbitals are excited to energetically higher unoccupied orbitals (π^* and σ^*). Relaxation of an energetically higher electron into the inner-shell orbital causes emission of energy in the form of Auger electrons or X-ray fluorescence (Figure 53). In contrast to XPS, not the initial photoelectron but a fluorescent photon, Auger electron or secondary electrons resulting from collision processes are detected. Depending on the excitation energy, a distinction is made between NEXAFS and EXAFS (extended X-ray absorption fine structure). NEXAFS spectroscopy is measured in the region of the absorption edge of an element, while in EXAFS electrons are excited far above this region (Figure 57).

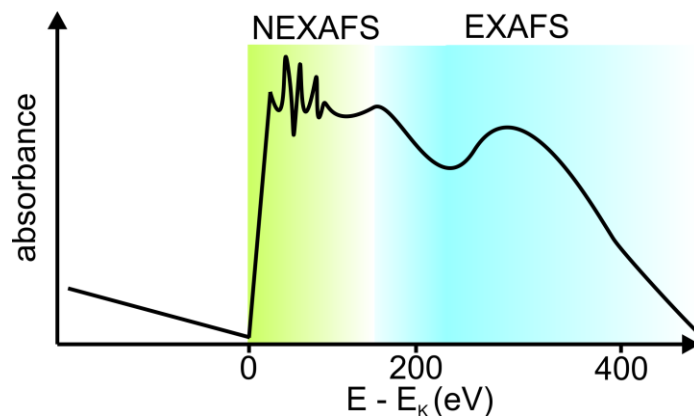


Figure 57: Schematic representation of an X-ray absorption spectrum with categorisation into NEXAFS and EXAFS areas.

NEXAFS spectroscopy requires monochromatic and linearly polarised X-radiation that can be varied in energy over a defined area. This is accomplished by the use of synchrotron radiation. Synchrotron radiation is emitted from charged particles that are accelerated radially and is usually generated from synchrotrons. In a synchrotron, electrons are accelerated close to light speed and forced on a circular path using magnets. The electrons tangentially emit photons, that are transmitted into a beam line through several optical elements resulting in linearly polarised monochromatic light available in a broad energy range from IR to X-ray. The NEXAFS measurements described in this thesis were conducted at the BESSY II synchrotron light source in Berlin-Adlershof (Figure 58).

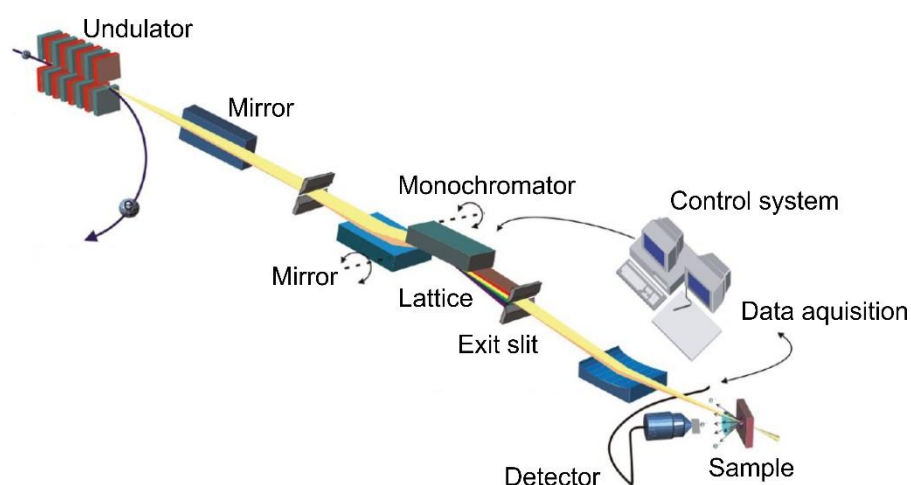


Figure 58: Path of radiation inside a beam line at BESSY II. ^[137]

The linearly polarised synchrotron radiation possesses an electric field vector vertical to the incident angle. Interaction with molecules only takes place, if the electric field vector overlaps with the transition dipole moment of the molecule. This can be explained exemplarily for benzene molecule laying flat on a surface (Figure 59).

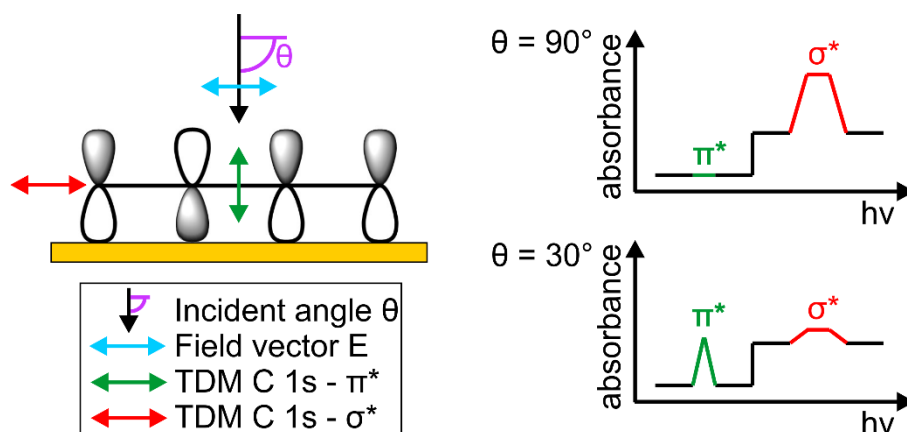


Figure 59: Schematic representation of the linear dichroism effect in NEXAFS on the example of a benzene molecule on a surface. ^[138]

If the synchrotron radiation is applied with an incident angle of 90° , the electric field vector is parallel to the transition dipole moment (TDM) of the σ^* -orbital and perpendicular to the TDM of the π^* orbital. In the resulting NEXAFS spectrum, a peak for the excitation of electrons to the σ^* -orbital is present, while no signal for the excitation of electrons to the π^* -orbital appears. If the incident angle of the synchrotron radiation is changed to 30° , an overlap of the electric field vector with both TDMs occurs, resulting in signals in the π^* and σ^* region. The signal for the excitation to the σ^* -orbital is smaller compared to an incident angle of 90° due to the more unfavourable overlap of the electric field and TDM vectors. This phenomenon is referred to as linear dichroism. With angle-resolved NEXAFS measurements, information about the orientation of molecules on a surface can be obtained.

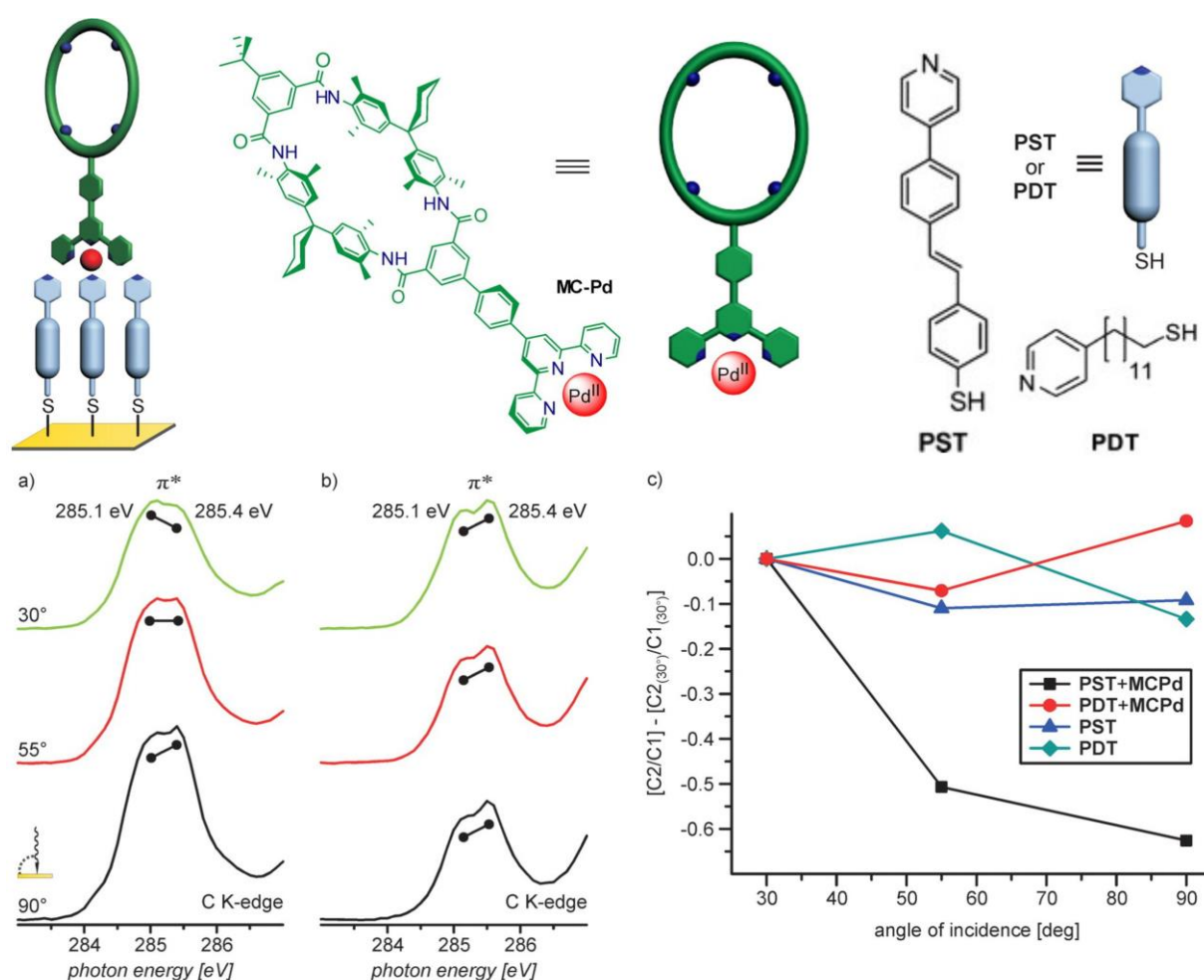


Figure 60: Monolayer of MC-Pd on a gold surface functionalised with a **PST** or **PDT** SAM (top). Angle-resolved NEXAFS C K-edge spectra of the π^* regions of the MC-Pd coordinated to a) the **PST**-SAM and b) the **PDT**-SAM. Differences of C2/C1 peak are ratios of π^* resonances between 281 and 286.5 eV at different incident angles of synchrotron light for **PST**, **PDT**, **PST+MC-Pd** and **PDT+MC-Pd** surfaces. Adapted with permission from S. Richter, J. Poppenberg, C. H. H. Traulsen, E. Darlatt, A. Sokolowski, D. Sattler, W. E. S. Unger, C. A. Schalley, *J. Am. Chem. Soc.* **2012**, 134, 16289-16297. Copyright (2012) American Chemical Society.

Angle-resolved NEXAFS measurements were applied by Schalley and coworkers^[139] to investigate the potential preferential orientation in a monolayer of a tetralactam macrocycle on two different SAMs on gold surfaces. The two SAMs **PST** and **PDT** differ with respect to the rigidity of the terminal pyridines with **PST** being more rigid. A monolayer of MC-Pd was deposited on the SAM using metal-ion/pyridine/terpyridine coordination chemistry (Figure 60, top). A higher coverage with macrocycles was observed on the more rigid **PST** SAM.

In the C K-edge NEXAFS spectra of the monolayer on a **PST**-SAM, two π^* resonance signals at 285.1 eV and 285.4 eV were observed that increase with increasing incident angle of the synchrotron irradiation. The same effect was observed for an uncomplexed **PST**-SAM, indicating that the preferential upright orientation of the **PST** molecules is not altered by the overlying monolayer of **MC**-Pd. The resonance at 285.1 eV (C1) is more intense at an incident angle of 30°, while the resonance at 285.4 eV (C2) has a greater intensity at an incident angle of 90° (Figure 60a). This specific linear dichroism effect was not observed in NEXAFS spectra of the pristine **PST**-SAM and can therefore be attributed to the monolayer of **MC**-Pd. The C K-edge NEXAFS spectra of the **MC**-Pd monolayer deposited on the more flexible **PDS**-SAM do not exhibit specific linear dichroism effects (Figure 60b). The change of the peak-area ratio of C1 and C2 is plotted over the incident angle to illustrate the effects (Figure 60c), showing no change for both SAMs and a monolayer of **MC**-Pd on **PDT**, but a significant change for a monolayer of **MC**-Pd on **PST**. The less pronounced linear dichroism effects do not necessarily indicate a low preferential orientation in the macrocycle layer, as the macrocycle comprises aromatic rings in different orientations. Even for a highly ordered layer, only small linear dichroism effects would be expected as the effects cancel each other out for differently orientated aromatic rings.

This leads to the conclusion that a preferential orientation in a layer of macrocycles is only achieved when the underlying SAM represents a rigid template, leading the macrocycles into an ordered arrangement. As a consequence of this finding, only the rigid monolayer **PST** for gold surfaces and the corresponding silane **PDS** for glass and silicon surfaces were used for the studies reported in this thesis.

The combination of angle dependent NEXAFS spectra and computational methods enables in principle the calculation of the structural orientation of molecules on a surface. Zharnikov and coworkers^[140] for instance were able to determine the tilt angle of SAMS of different nitrile-substituted oligo(phenylene ethynylene) thiols on gold surfaces to be between 33° and 36°. For more complex molecules like tetralactam macrocycles and rotaxanes, this is not straightforward. Besides the computational effort, the assignment of specific carbons or aromatic rings to single resonances in NEXAFS spectra is not easily possible for large systems.

3.4. Dynamic combinatorial libraries (DCLs)

The so far described systems included supramolecular host-guest assemblies and mechanically interlocked molecules consisting of a manageable number of individual components. The study of complex networks of molecular interactions within a large number of individual compounds started in the 1990s, when the research field of dynamic combinatorial chemistry (DCC) was initiated.^[141] Within this thesis, a dynamic combinatorial library (DCL) was investigated in a cooperation project with the group of Prof. Jonathan Nitschke.

A DCL is a thermodynamically controlled mixture of interconverting species that can respond to various stimuli.^[141a] In a DCL, molecular building blocks are connected by non-covalent or reversible covalent bonds to form a complex mixture of products. The reversible nature of the bonds allows a continuous interconversion of building blocks to minimize the total free energy of the system.

The thermodynamic control of the library composition can lead to the amplification of specific library members in the equilibrium that possess a higher stability. In a mixture of structures with different conformational properties for instance, the structure with the most favourable internal interactions is stabilised and amplified within the DCL (Figure 61a). The amplification of specific library members can also be achieved through the formation of stable assemblies or aggregates (Figure 61b). In addition, the distribution of the individual library members can be influenced through external templating. Adding a template that exhibits attractive interactions towards specific library members normally leads to a shift of the equilibrium and thus an increase in concentration of this library member. Both templates that act as guests or ligands (Figure 61c) and as host or receptors (Figure 61d) are possible.^[141b] Further possibilities to alter a library composition include electrochemical and photochemical stimuli or modifications of the environment (like temperature or pressure), if respective stimuli-responsive building blocks are used.

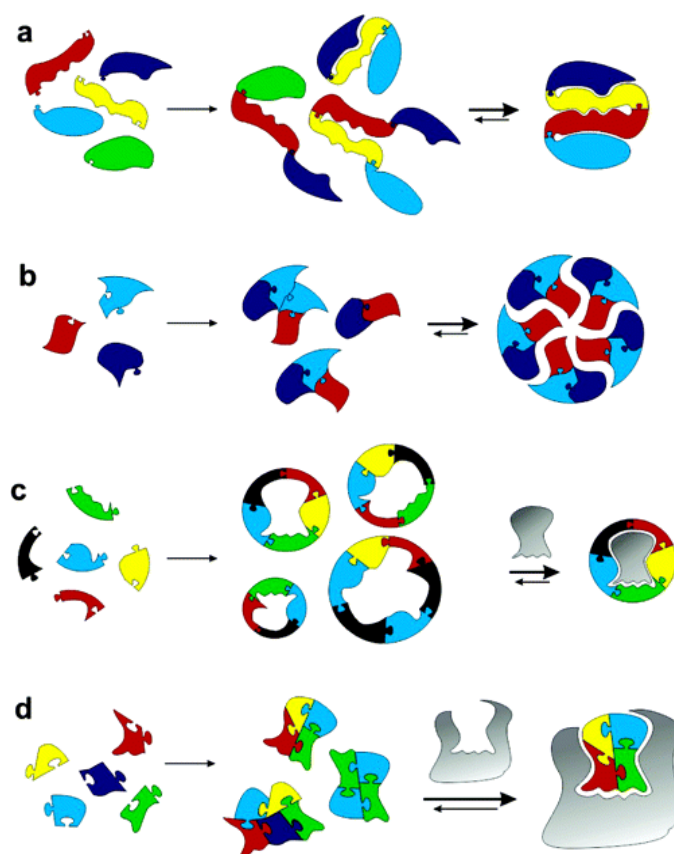


Figure 61: Different ways of selecting specific members of a dynamic combinatorial library on the basis of noncovalent interactions: (a) selection of foldamers driven by internal noncovalent interactions; (b) selection of self-assembling molecules on the basis of noncovalent interactions between different library members; (c) selection of a host by a separately introduced guest; (d) selection of a guest by a separately introduced host. Reprinted with permission from P. T. Corbett, J. Leclaire, L. Vial, K. R. West, J.-L. Wietor, J. K. M. Sanders, S. Otto, *Chem. Rev.* **2006**, *106*, 3652-3711. Copyright (2006) American Chemical Society.

An example for a DCL comprised of hydrogen-bonded nanotubes was reported by Sanders and coworkers (Figure 62).^[142] 1,4,5,8-Naphthalenetetracarboxylic diimide functionalised with amino acids forms a library of organic nanotubes of different sizes through carboxylic acid dimerization. A statistical distribution of chain length with an average degree of polymerisation of 5.3 was observed in solution as a result of similar free energies of shorter and longer helical oligomers. Incorporation of C₆₀ in the cavity of the nanotubes stabilizes longer oligomers. The addition of C₆₀ therefore led to an amplification of longer oligomers and a shift of the average degree of polymerisation to 15.7. In contrast, addition of C₇₀, which is too big to be incorporated in the nanotubes, led to a complete restructuring of the library from nanotubes to a hexameric capsule wrapped around C₇₀.

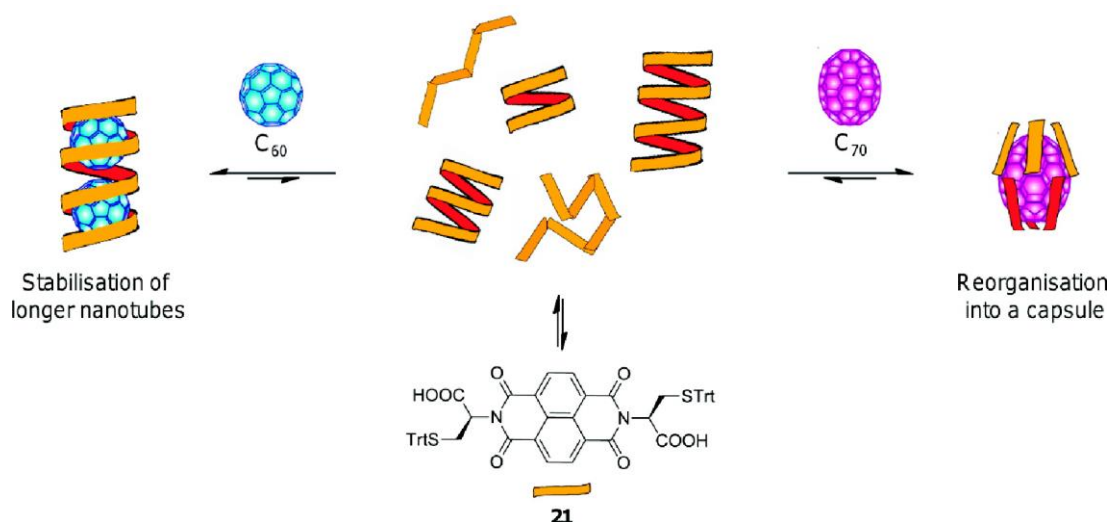


Figure 62: Library of hydrogen-bonded helical nanotubes. Templatation in the presence of C_{60} or C_{70} allows amplification of longer nanotubes or of a hexameric capsule, respectively. Reprinted with permission from F. B. L. Cougnon, J. K. M. Sanders, *Acc. Chem. Res.* **2012**, *45*, 2211-2221. Copyright (2012) American Chemical Society.

Nitschke and coworkers^[143] reported a DCL of tetrahedral metallocsupramolecular cages that can incorporate different aniline residues. The cages were prepared in a subcomponent self-assembly^[144] approach out of 3,3'-bipyridine-6,6'-dicarboxaldehyde, p-chloroaniline, p-bromoaniline, and p-iodoaniline and a Fe(II) salt (Figure 63).

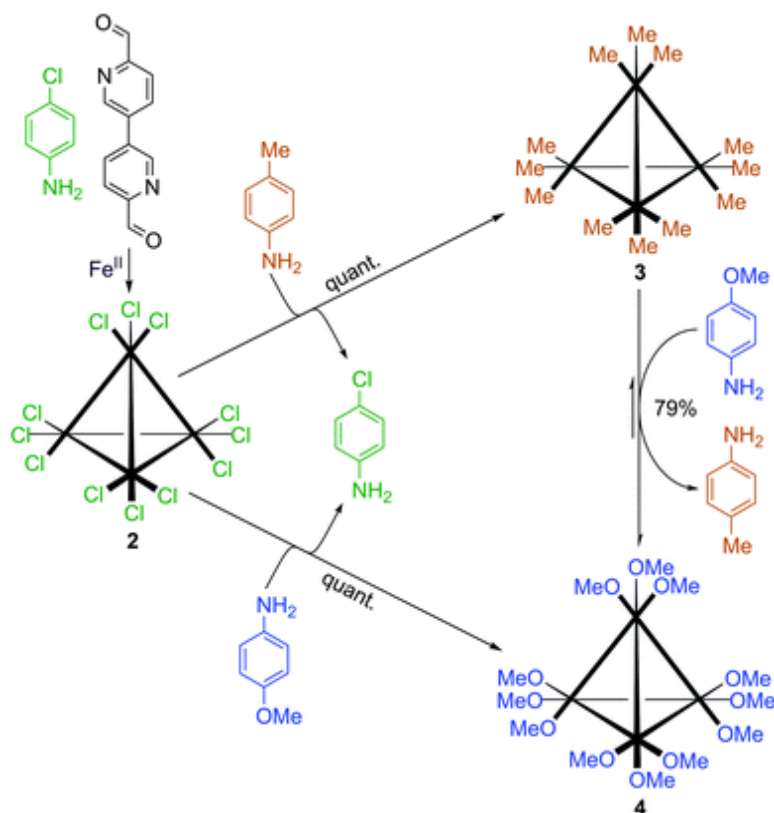


Figure 63: Subcomponent substitution driven by electronic effects: more electron-rich anilines are able to displace more electron-poor anilines. Reprinted from Y. R. Hristova, M. M. J. Smulders, J. K. Clegg, B. Breiner, J. R. Nitschke, *Chem. Sci.* **2011**, *2*, 638-641 with permission from The Royal Society of Chemistry.

The cages comprise six ligands that are connected by four metal centers. The ligands are formed in an imine condensation out of carboxaldehyde and aniline. The simultaneous reaction of three different substituted anilines gives rise to three homotopic and three heterotopic ligands, that can form up to 91 different cages by molecular composition and hundreds of thousands more if all possible structural isomers are taken into account. Addition of the more electron rich p-methoxyaniline resulted in the collapse of the library into the single homoleptic cage that only bears methoxysubstituted ligands.

3.4.1. ESI-FTICR MS as analytical tool for the analysis of complex systems

Analysing and characterizing the members of a complex DCL is a quite difficult task. NMR spectroscopic investigations of a DCL usually result in many overlapping resonances due to the numerous magnetically distinct environments of the different DCL members. The presence of resonances for different regio- and stereoisomers that occur in many complex systems further hamper NMR analysis so that even two-dimensional and diffusion-ordered NMR experiments cannot provide the necessary information about structures and abundances. In addition, the dynamic nature of complex formation and the high dependency of supramolecular interactions on the environment complicate the analysis.^[145]

Electrospray-ionisation Fourier-transform ion-cyclotron-resonance mass spectrometry (ESI-FTICR MS) is a powerful tool for the analysis of complex mixtures and was used within this thesis for the detailed examination of a mixed-ligand DCL.^[146] Electrospray ionisation (ESI) represents a soft-ionisation technique that produces ions with a relatively low internal energy and therefore enables the transfer of intact non-covalent complexes into the gas phase, including species with a high charge state.^[147] ESI is routinely available since the 1990s and represents nowadays besides matrix-assisted laser desorption ionization (MALDI) one of the favoured ionisation techniques in supramolecular chemistry.^[148] In an ESI source, a dilute sample of the analyte solution is pumped through a steel capillary to which a high voltage is applied (Figure 64). If the ESI capillary represents the anode (positive mode), positively charged ions and solvent molecules pass through the capillary, while negatively charged ions are neutralised, and vice versa if the ESI capillary represents the cathode (negative mode). Ionization occurs in the positive mode through protonation by protic solvents, complexation with ions (typically Na^+ , K^+ , NH_4^+) or oxidation and in the negative mode through deprotonation, reduction or complexation (e.g. Cl^-). In case that salts are measured, the respective oppositely charged counterions are stripped off in the capillary. At the tip of the capillary, the so-called Taylor cone is formed as a result of solvent flow and potential difference. From the tip of the Taylor cone, a jet of charged droplets is ejected.^[147a, 149] The droplets shrink through solvent

evaporation until the Rayleigh limit is reached, at which they undergo ion evaporation^[149-150] or Coulomb fission,^[151] finally yielding the bare desolvated ions.

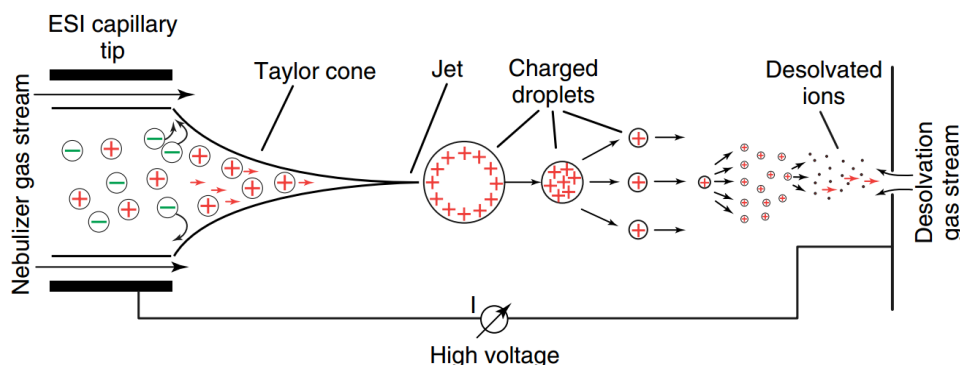


Figure 64: The principle of electrospray ionization (ESI). Reproduced with permission from C. A. Schalley, A. Springer, *Mass Spectrometry and Gas-Phase Chemistry of Non-Covalent Complexes*, Wiley, New York, **2009**. Copyright (2009) John Wiley & Sons.

A schematic representation of an ESI-FTICR MS instrument is shown in Figure 65. The ions are transferred from the ESI source through sample cone and extractor cone into the high vacuum area. They are guided through a quadrupole that enables mass selection to a hexapole collision cell, where ions are accumulated. In the collision cell, gases can be introduced through a pulsed valve to conduct for instance fragmentation or H/D exchange experiments. From the hexapole, ion packages are ejected into an ion guide to the ICR cell that is surrounded by a strong magnet.

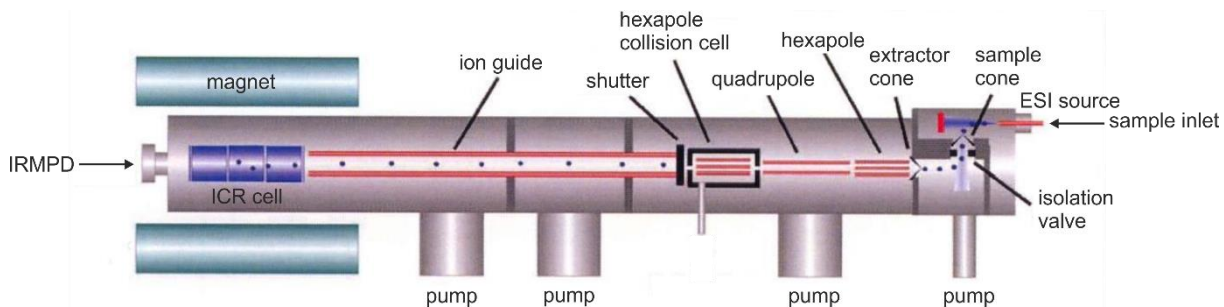


Figure 65: Schematic representation of an ESI-FTICR MS instrument.^[152]

In the ICR cell (Figure 66), ions are trapped in the middle of the cell through electrostatic repulsion with the cell walls, to which a voltage with the same polarity as the ions is applied. The ions move on a circular path perpendicular to the magnetic field on cyclotron orbits, whose radius is determined by the Lorentz force and the centrifugal force (Equation 4).^[153]

$$r = \frac{mv}{zeB}$$

Equation 4: Radius of ions (r), mass of ions (m), velocity (v), charge number (z), elemental charge (e) and magnetic field (B).

By describing the velocity as the product of radius and cyclotron frequency (Equation 5), it is shown that the m/z value of an ion is only related to the cyclotron frequency and the magnetic field.

$$\frac{m}{z} = \frac{eB}{\omega}$$

Equation 5: Dependency of the m/z value from the cyclotron frequency (ω).

A broadband radiofrequency pulse is applied to the two excitation plates to accelerate the ions to a higher cyclotron orbit, where they pass by the detection plates and induce a small current that is amplified and measured.^[154] The ions afterwards relaxate to their original orbit. All frequencies induced by different ions are measured simultaneously and transformed through Fourier transformation to the corresponding m/z values. In one detection sequence, 10^4 - 10^8 turns are recorded, whereby the accuracy of obtained m/z values increases with the number of measured turns.^[155]

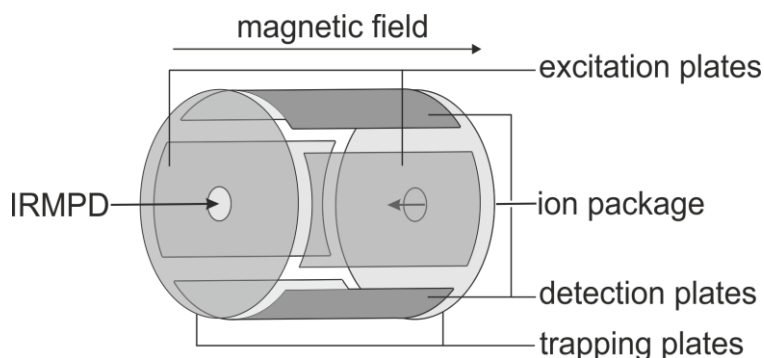


Figure 66: Schematic representation of an ICR cell.

A great advantage of FT-ICR MS is the possibility to perform tandem MS experiments, in which one or more mass-selection steps followed by gas-phase experiments prior to product ion detection are performed. Within this thesis, infrared multiphoton dissociation (IRMPD) experiments are performed within the ICR cell. In an IRMPD experiment, an infrared laser is used to induce fragmentation reactions of ions.^[156] Fragmentation with IRMPD requires that ions have at least one vibrational mode that is excited through absorption at the wavelength of the IR laser.^[157] The internal energy is distributed over the molecule and usually leads to the

cleavage of the weakest bond. In case of supramolecular structures, IRMPD leads in most cases to a cleavage of non-covalent bonds before also covalent bonds are broken with increasing laser energy or duration. Besides the m/z value, tandem MS experiments can provide detailed information about the structure and reactivity of non-covalent complexes in solution and gas phase.^[148, 155]

4. Photoswitchable (pseudo-)rotaxanes in solution and on surfaces

4.1. Spiropyran-based rotaxanes

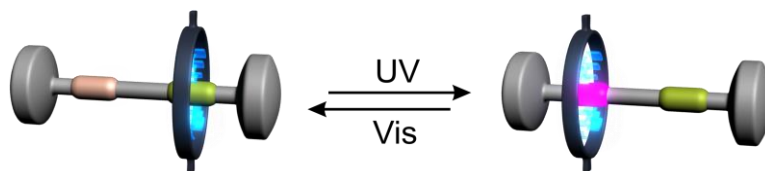


Figure 67: Graphical abstract.

4.1.1. Abstract

A photocontrolled binding site on the basis of spiropyran was designed and synthesised. The binding site reversibly binds to different tetralactam macrocycles in one switching state, while it does not exhibit attractive interactions in the other. Different spiropyran-based rotaxanes were synthesised on the basis of this binding motif and their switching behaviour was analysed in solution.

4.1.2. Results and discussion

To construct a photoswitchable rotaxane on the basis of spiropyran, preliminary experiments were conducted to investigate the photochemical properties of spiropyran and explore its suitability as a photoswitchable binding site. A well analysed spiropyran, 1',3'-dihydro-1',3',3'-trimethyl-6-nitrospiro[2*H*-1-benzopyran-2,2'-(2*H*)-indole] (6-Nitro-BIPS),^[50, 73, 158] was chosen as model compound for first feasibility tests. 6-Nitro-BIPS can be switched photochemically between two distinct states, the closed colourless spiropyran **1** and the open coloured merocyanine **2**. Irradiation of spiropyran at a wavelength of $\lambda_1 = 365$ nm induces ring opening to form the merocyanine. Back-switching to the closed spiropyran occurs thermally and can be accelerated by irradiation at $\lambda > 500$ nm. The merocyanine can be protonated by adding acid. All three states have different absorption properties and can be easily distinguished by UV-Vis spectroscopy (Figure 68).

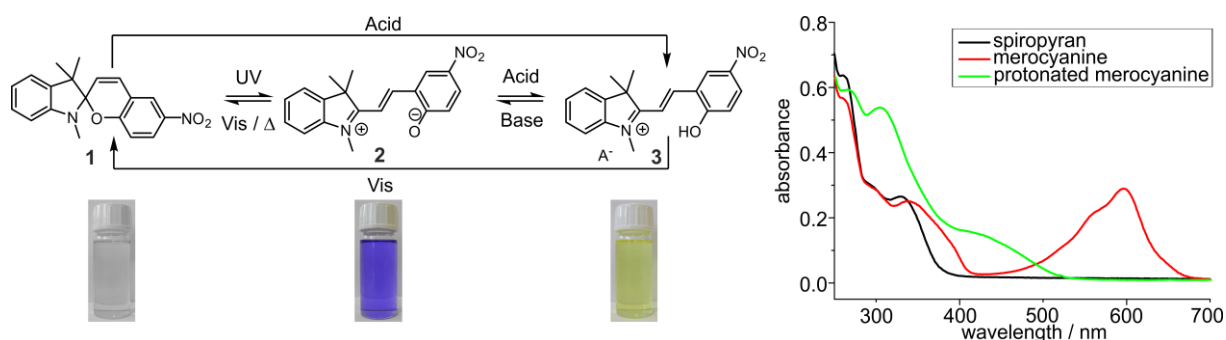


Figure 68: Switching states of 6-nitro-BIPS: spiropyran, merocyanine, protonated merocyanine and solution of all switching states in acetone (left) and corresponding UV-Vis spectra (right).

The merocyanine bears an oxo-anion, which can act as binding site for TLM.^[25b, 86] An ester group is used as second half of the binding site to strengthen the binding of the merocyanine, although it only represents a weak binding site by itself. The closed spiropyran does not bear any strong hydrogen bond acceptors and should therefore not exhibit significant attractive interactions towards TLM. MM2 force-field modelling^[159] shows the merocyanine **5** to nicely fit into the cavity of TLM **4** (Figure 69).

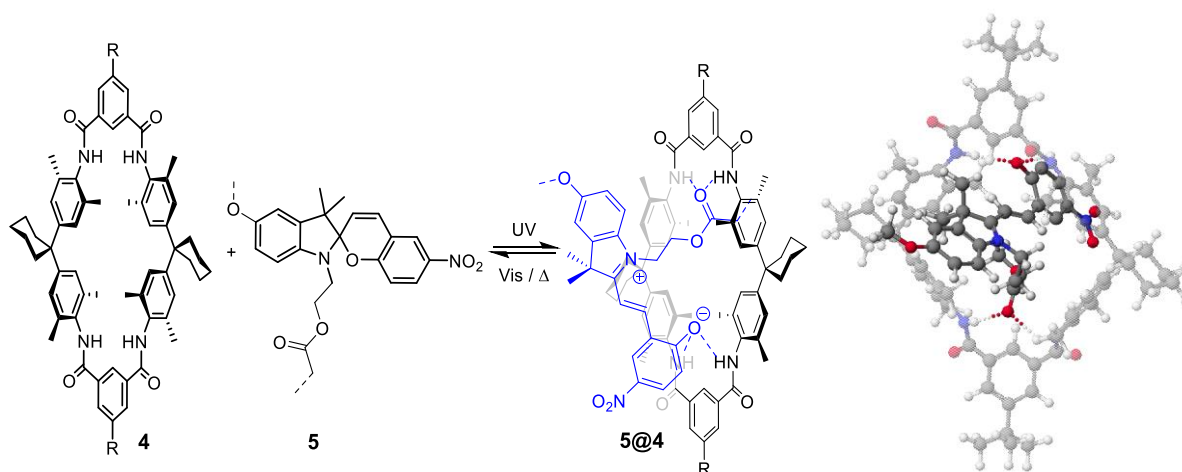


Figure 69: Binding of a merocyanine to a TLM (left), MM2 molecular modelling of the binding mode.

The merocyanine typically undergoes fast reversion to the closed spiropyran under standard ambient conditions. For the application as binding site in a photoswitchable rotaxane, a stabilised merocyanine state with an elongated lifetime is desired to ensure two distinct switching states of the rotaxane. The substitution pattern of the spiropyran has a great influence on the kinetics of this reaction. The ring closing reaction can be seen as nucleophilic attack of the oxo-anion towards the positively polarised carbon atom, creating the spirocenter. The reaction is therefore slowed down if the electron density is enriched on the indoline part and lowered on the chromene part of the merocyanine. This can be achieved by functionalisation with electron donating and withdrawing groups at the respective parts of the

molecule. For all further studies, a spiroopyran functionalised with an alkoxy group at the indoline and a nitro group at the chromene part was used (Figure 70).

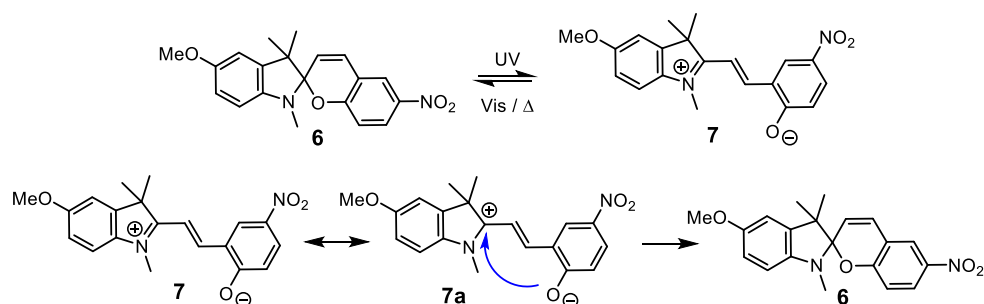


Figure 70: Influence of the substitution pattern on the merocyanine to spiroopyran interconversion.

The rate of the ring closing reaction of a merocyanine is also influenced by the solvent. The higher the polarity of a solvent, the longer is the lifetime of the open form. For the use as binding site in rotaxanes, only solvents which do not form strong hydrogen bonds are suitable, as they would otherwise disturb the interaction between binding site and TLM.

The ring closing reaction of merocyanine **7** in different solvents was investigated with UV-Vis spectroscopy. The UV-Vis spectrum of a solution of spiroopyran **6** in acetone shows absorption bands for the π - π^* transitions of the indoline part around 350 nm and of the chromene part around 410 nm (Figure 71 left, black line).^[80] Upon irradiation at $\lambda_1 = 365$ nm for 5 min, a strong absorption band around 570 nm appears, which is characteristic for merocyanine. The thermal reversion occurs within 15 min and was followed by UV-Vis (Figure 71 left). The spiroopyran to merocyanine interconversion was investigated in different solvents by measuring the change in absorbance at 570 nm over time (Figure 71, right). The rate of the reaction is slow in DMSO, DMF and ethanol. As these solvents all form strong hydrogen bonds, they cannot be used for studies with a TLM rotaxane. Acetonitrile and acetone yield intermediate

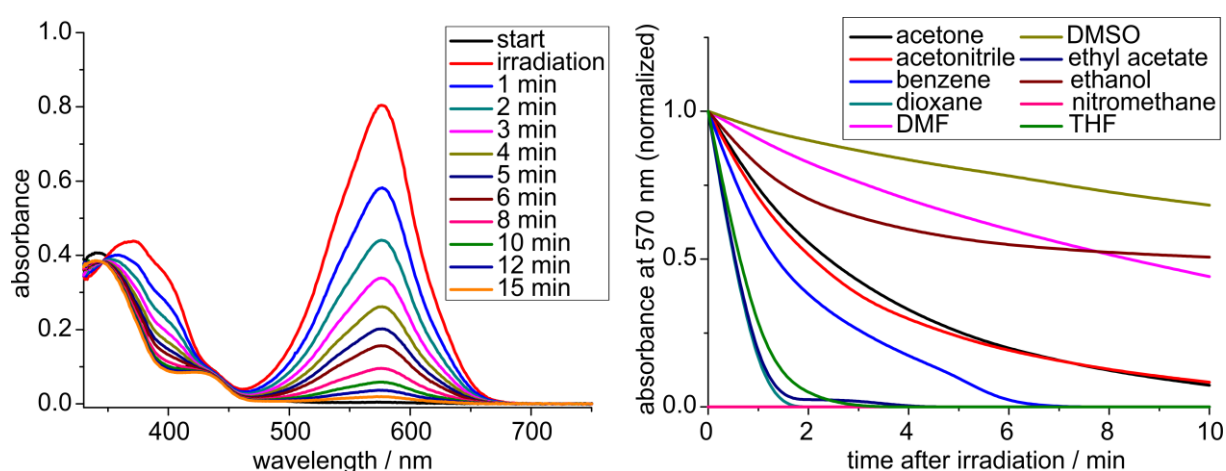


Figure 71: UV-Vis spectra of spiroopyran **6** in acetone before (black line) and after irradiation (left) and change in absorbance at 570 nm over time after irradiation of a solution of spiroopyran **6** in different solvents (right).

reaction rates. They both form only very weak hydrogen bonds which do not noticeably disturb the axle-macrocycle interactions and therefore represent a good compromise. All other tested solvents lead to too fast ring closing reactions and are therefore not appropriate for this study. Halogenated solvents like DCM or chloroform decompose under UV light to HCl which leads to protonation of the merocyanine and are therefore unsuitable.

Photoswitchable rotaxanes were designed to be integrated in surface bound multilayer systems of chemically switchable rotaxanes, that were developed before in the Schalley group.^[15d] Hunter-Vögtle-type TLM were used as macrocycles, that can be functionalised with pyridine or terpyridine groups for the construction of metal-coordinated multilayer. The rotaxane was designed as a two state switch with spiropyran as photoswitchable binding site and a diamide^[160] as second binding site.

To use spiropyran as central element in a photoswitchable rotaxane, it must be functionalised with electron donating and withdrawing groups as discussed above and furthermore comprise a suitable linker for the attachment of the second part of the axle. It was found that an unsubstituted spiropyran is not sufficiently sterically demanding to prevent deslipping of a TLM, but in addition a bulky stopper group needs to be attached. Spiropyran synthesis was accomplished by adapting literature known procedures.^[161] As stopper group, 4-tritylphenol was used, which was attached by an alkoxy chain to the indoline part.

The synthesis of spiropyran **15** started with commercially available 4-methoxyaniline **8**, which was converted in three steps to 5-methoxy-2,3,3-trimethyl-3*H*-indole **9** followed by deprotection of the hydroxyl group to 5-hydroxy-2,3,3-trimethyl-3*H*-indole **10**. 1,3-dibromopropane **12** was attached to 4-tritylphenol **11** and subsequently to indole **10**, yielding the stoppered indole **14**. Alkylation of **14** with 2-bromoethanol gave an intermediate indoline bromide salt, which was treated with 5-nitrosalicylaldehyde and piperidine to afford spiropyran **15** (Figure 72).

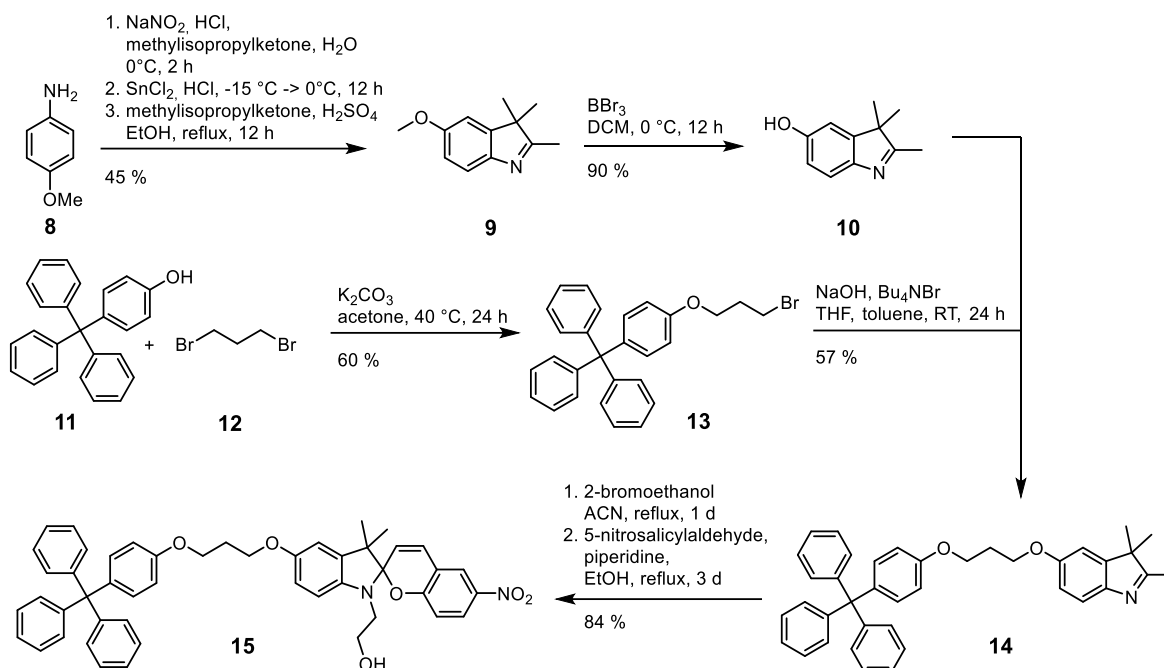


Figure 72: Synthesis of spiropyran **15**.

The second part of the axle **18** was comprised of the diamide binding site, a bulky trityl stopper and a linker unit for the rotaxane synthesis. Synthesis of **18** was carried out starting from tritylphenol **11**, which was reacted with ethyl bromoacetate to give carboxylic acid **16**. Mono-BOC protected ethylenediamine was attached to **16** in an amide synthesis, subsequently deprotected to amine **17**, which was again reacted in an amide synthesis with 2-(4-hydroxyphenyl)acetic acid to give the axle building block **18** (Figure 73).

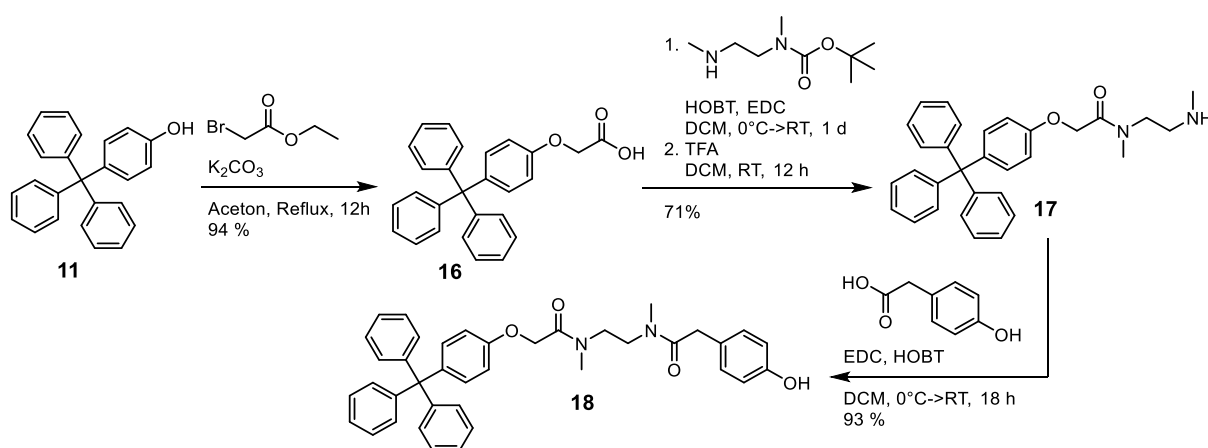


Figure 73: Synthesis of axle building block **18**.

The binding behaviour between the axle building block **18** containing the diamine site and the di-tert-butyl-substituted TLM **19** was investigated with NMR experiments. Since there is a fast exchange on the NMR timescale, the binding constants were evaluated by NMR titration analysis.^[162] A solution of TLM **19** in CDCl_3 was placed in an NMR tube and treated with

different amounts of **18**. A ^1H NMR spectrum was measured after each injection and the guest concentrations were determined by integration of the signals. The binding constant was calculated based on a 1:1 binding model and a binding constant of $1,400 \pm 140 \text{ M}^{-1}$ was obtained (Figure 74).

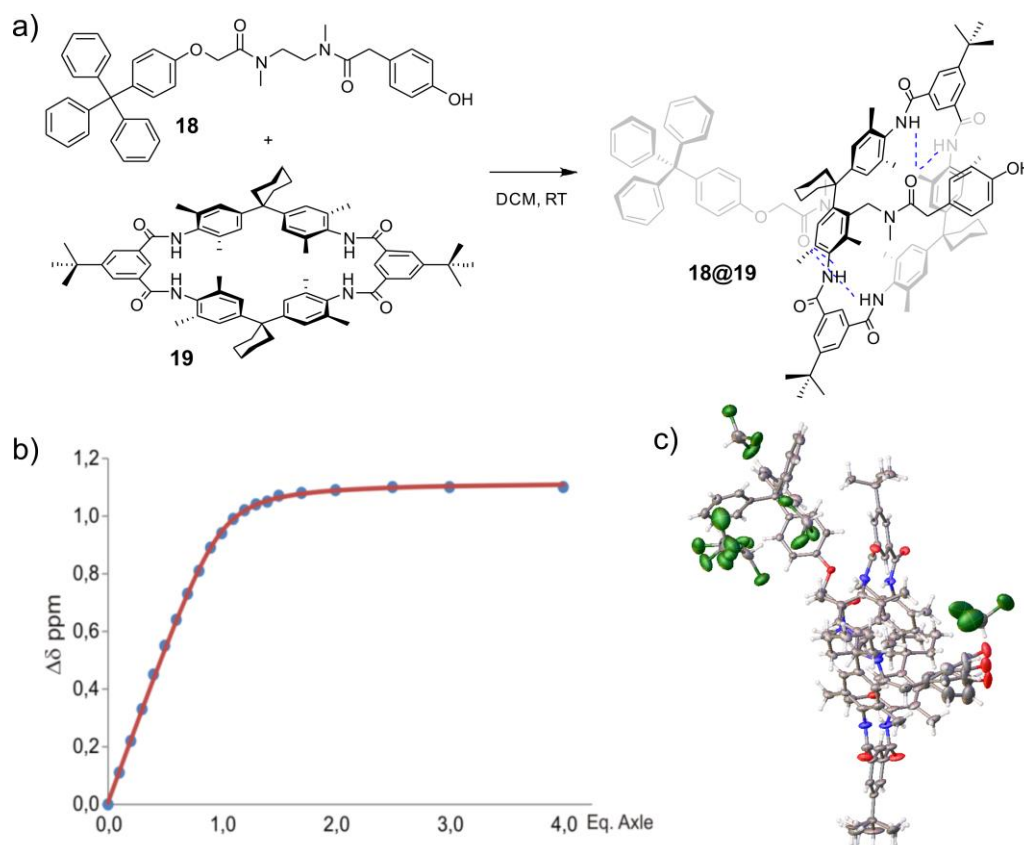


Figure 74: a) Pseudorotaxane **18@19**, b) NMR-Titration, $K=1400 \pm 140 \text{ M}^{-1}$, c) crystal structure of the pseudorotaxane.

Single crystals of pseudorotaxane **18@19** suitable for X-ray analysis were obtained by diffusion of diethyl ether in an equimolar solution of **18** and **19** in chloroform. The crystal structure (Figure 74c) confirms the threaded arrangement.

Spiropyran **15** was reacted with chloroacetic acid chloride followed by a Finkelstein reaction to give the corresponding iodoalkane **20** as linker unit for the following rotaxane synthesis. Rotaxanes **Rot1** and **Rot2** were obtained in a one-step ether-rotaxane synthesis out of the two axle building blocks **18** and **20** and the respective TLM **19** or **21** (Figure 75). The phenol linker unit of **18** is crucial for the reaction, as previous experiments with alkyl-hydroxy or carboxylic acid linkers did not lead to the desired axle formation reaction. Rotaxane **Rot1** with the di-*tert*-butyl TLM **19** was used for solution studies, while the di-iodo-functionalised **Rot2** opens up the path for further functionalisation with pyridine or terpyridine units for surface deposition.

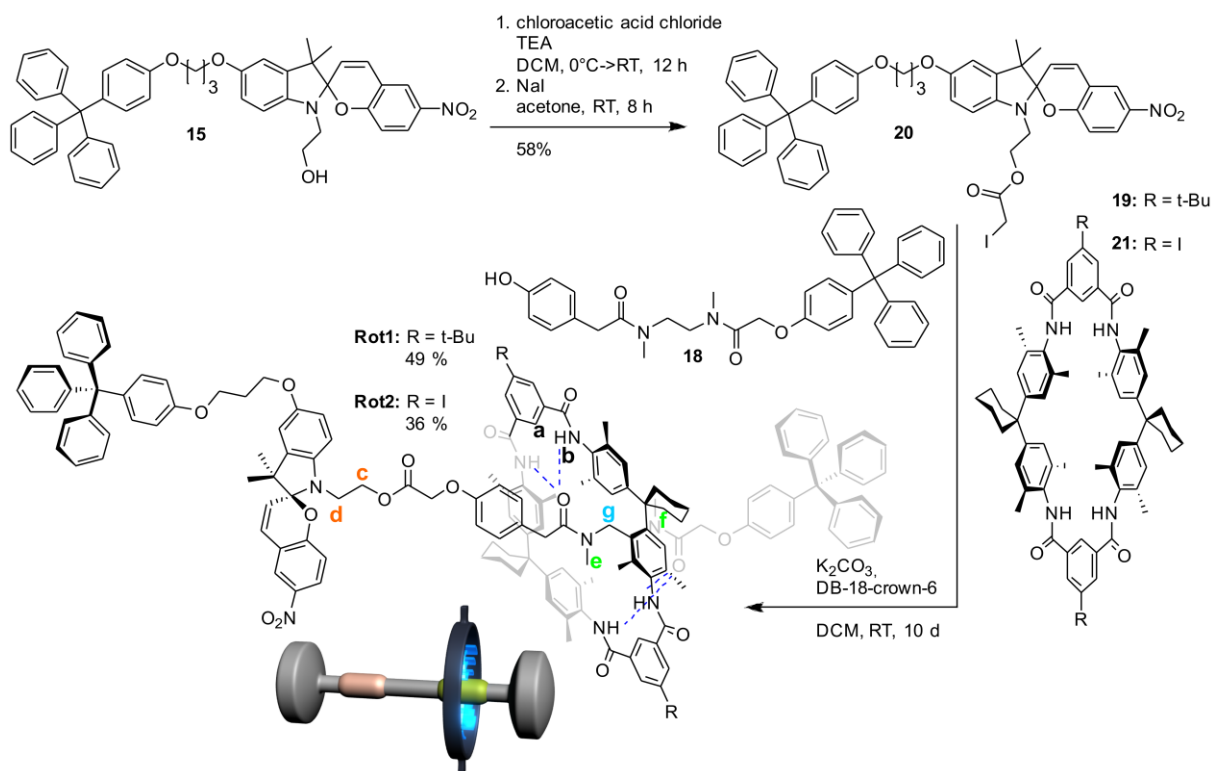


Figure 75 Synthesis of Rot1 and Rot2

The formation of **Rot1** was followed by ¹H NMR spectroscopy (Figure 76). The ¹H NMR spectrum of TLM **19** shows the signals for the macrocycle inner isophthalic and amide protons **a** and **b** at 7.33 respectively 7.96 ppm, which are shifted downfield by 0.97 and 0.47 ppm in the rotaxane spectrum due to hydrogen bonding to the axle.

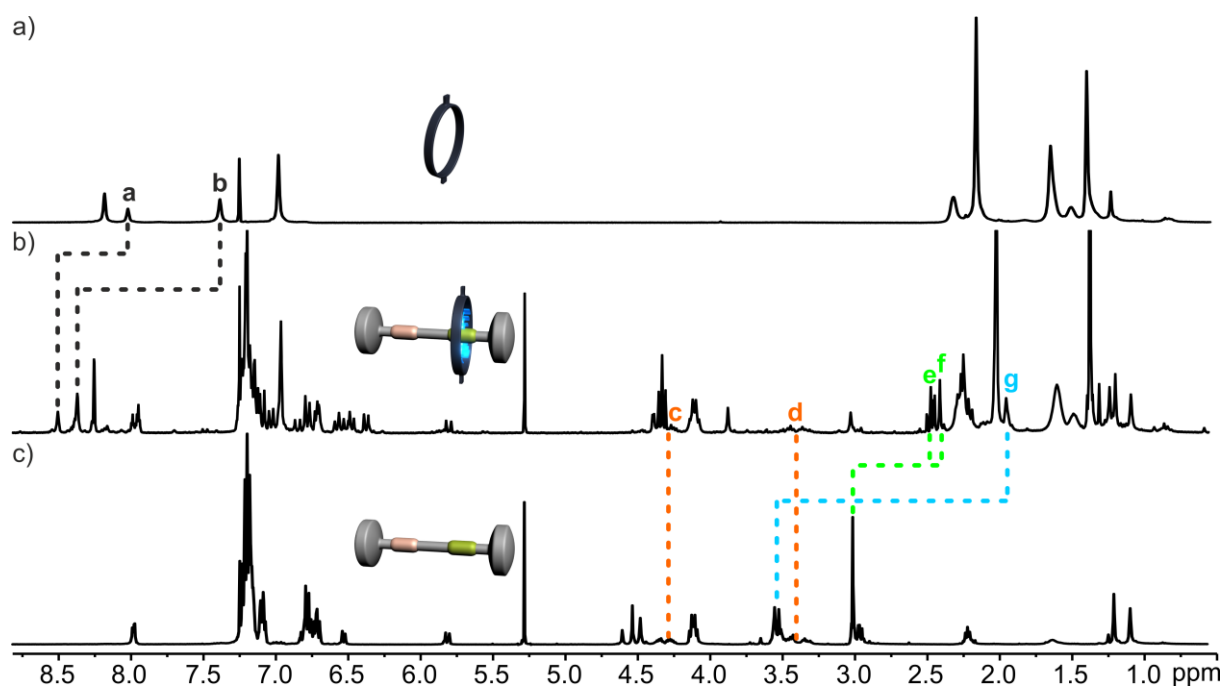


Figure 76: ¹H NMR spectra (CDCl₃, RT) of a) TLM **19**, b) **Rot1** and c) the free axle of **Rot1**.

Comparison of the NMR spectra of free axle and rotaxane reveals significant upfield shifts of the diamide methyl and methylene protons **e**, **f** and **g** of 0.54, 0.60 and 1.59 ppm, while the signals for the methylene protons **c** and **d** adjacent to the spiropyran remain almost unaffected at 4.23 and 3.35 ppm. This is clear evidence for the macrocycle being located at the diamide binding site.

Photoswitching of **Rot1** from the spiropyran to merocyanine state was performed by irradiation at $\lambda_1 = 365$ nm with a common TLC UV-lamp equipped with a long wave 365 nm tube. The formation of **Rot1-MC** could be easily detected with the naked eye due to the colour change of the solution from colourless to deep purple. Back-switching to **Rot1-SP** was carried out by thermal equilibration or irradiation with visible light with a halogen lamp equipped with filter cutting of light below 500 nm. In the spiropyran state, the macrocycle of **Rot1** binds to the diamide site of the axle. Upon photoinduced ring opening of the spiropyran, the oxo-anion of the merocyanine represents the better hydrogen bond acceptor, which makes it the preferred binding site for the TLM and therefore leads to a movement of the ring along the axle (Figure 77).

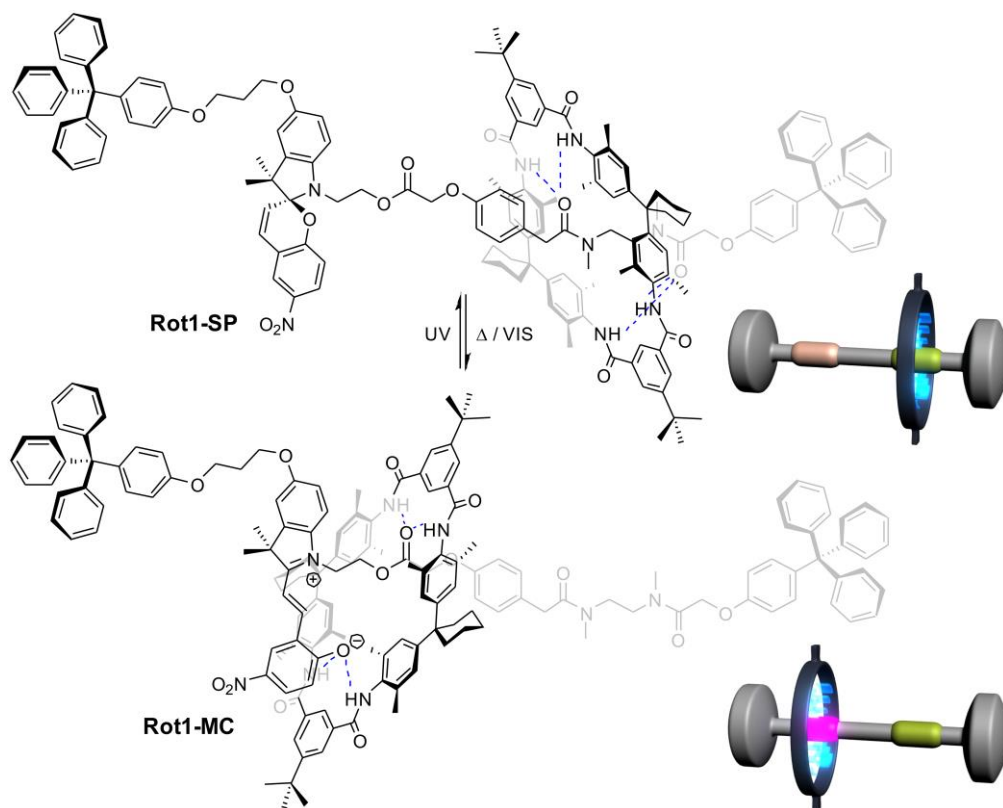


Figure 77: Photoswitching of **Rot1**.

The photoswitching of **Rot1** was followed by UV-Vis spectroscopy. The spectrum of **Rot1** in its spiropyran state (**Rot1-SP**) in acetonitrile shows absorbance up to 400 nm for the π - π^* resonances. Upon irradiation at $\lambda_1 = 365$ nm for 90 s, an intense band at 570 nm appeared,

which is characteristic for the merocyanine and therefore indicates the formation of the rotaxane in its merocyanine state (**Rot1-MC**) (Figure 78a). Thermal back-isomerisation to **Rot1-SP** occurred within 30 min at room temperature or was accelerated by irradiation with visible light for 90 s. In both photoreactions, a photostationary state was reached after 90 s. Reversibility of photoswitching was tested by alternating irradiations at $\lambda_1 = 365$ nm and visible light at $\lambda > 500$ nm. The changes in absorbance at 570 nm were monitored and did not reveal any fatigue effects over five cycles (Figure 78b).

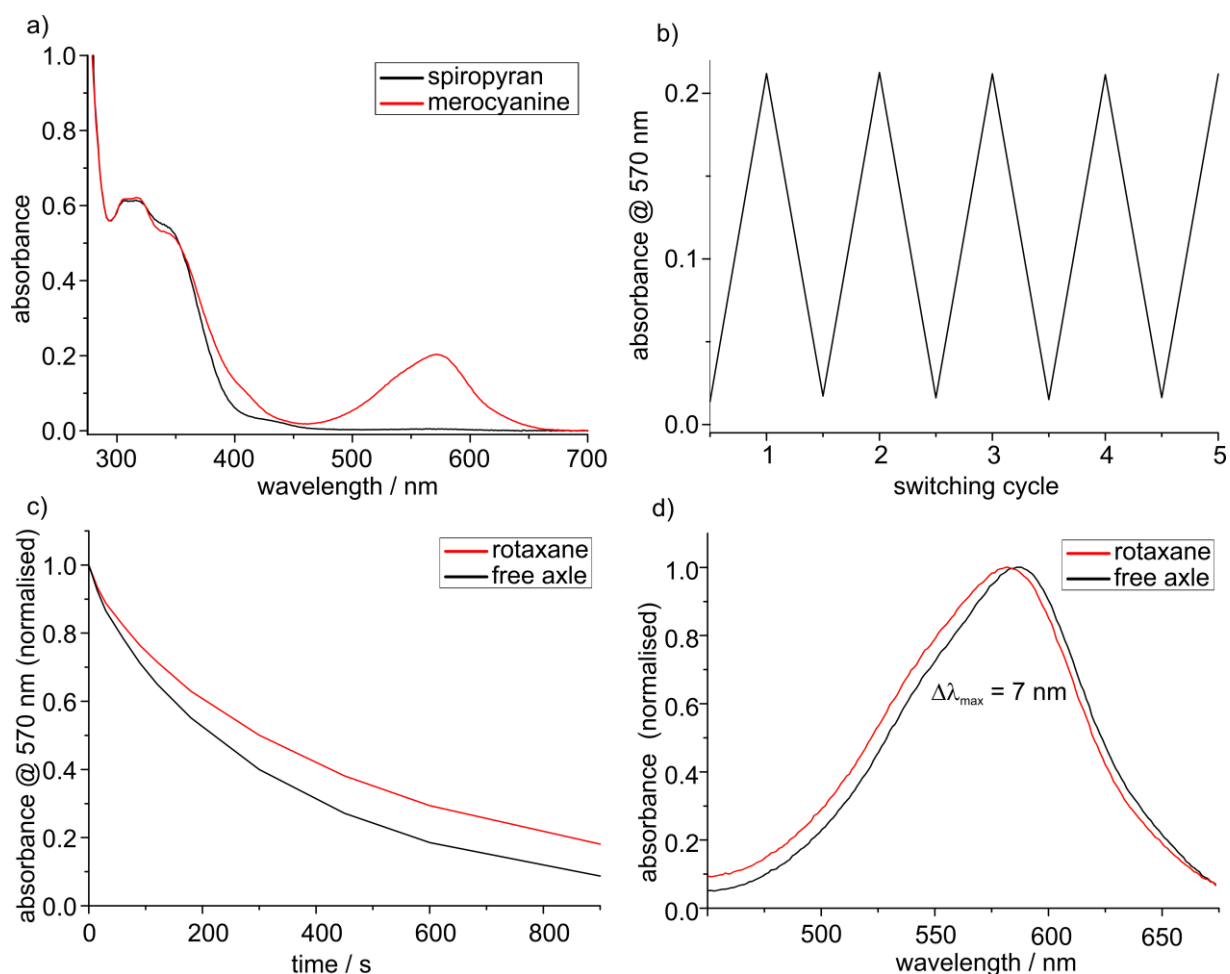


Figure 78: a) UV-Vis spectra of **Rot1-SP** and **Rot1-MC** in ACN, b) reversibility of SP-MC interconversion over five cycles, c) kinetics of the thermal back reaction of **Rot1-MC** and the corresponding free axle, d) absorption maximum of MC-Rotx and the free axle.

The kinetics of the thermal back isomerisation from spiropyran to merocyanine were analysed for **Rot1** and the corresponding free axle by following the absorbance of the merocyanine band at 570 nm for solutions of the particular substance in acetonitrile with UV-Vis spectroscopy. It was determined that the reaction rate is significantly slower for the rotaxane in comparison with the free axle (Figure 78c). While this effect was present in an acetonitrile solution, the reaction rates were similar for both molecules in DMF. This can be explained by stabilisation of the merocyanine in **Rot1-MC** through hydrogen bonds of the merocyanine's oxo-anion to

the TLM. The argument is supported by the observed shift for the absorption maxima of the merocyanine band of $\Delta\lambda_{\text{max}} = 7$ nm between free axle and rotaxane (Figure 78c), which can be explained as well with hydrogen bonding between TLM and merocyanine. This is clear evidence for the TLM being located at the merocyanine binding site in **Rot1-MC**.

The measurement of conclusive ^1H NMR spectra of **Rot1-MC** turned out to be very difficult. The short lifetime of the switched state complicated the measurement process as the time between irradiation and measurement has to be as short as possible. The transfer of the solution to an NMR tube and the measurement setup of the spectrometer required at least two minutes until the first acquisition. Within all measured NMR spectra, the signals for **Rot1-MC** were very low in intensity and hardly to distinguish from noise, so that a detailed analysis was not possible. Overall, the interconversion from **Rot1-SP** to **Rot-MC** was estimated to be approximately 5%.

For transferring the concept to surfaces, the iodo-substituted **Rot2** was functionalised with terpyridine groups to enable the deposition in multilayers by metal-ion based coordination chemistry. Reaction of **Rot2** with terpyridine boronic ester **22** in a Suzuki coupling reaction after a procedure developed in the Schalley group for the functionalisation of macrocycles^[139] and chemically switchable rotaxanes^[15d] lead to decomposition of the rotaxane axle at the ester group adjacent to the spiropyran as measured with ESI-MS and NMR. Alkyne functionalised terpyrine **23** was synthesised to repeat the functionalisation with a Sonogashira coupling reaction under milder conditions (Figure 79). The reaction of **Rot2** with **23** was monitored with ESI-MS. After two days, mono- and di-terpyridine substituted rotaxanes were detected in solution and after seven days, only the desired disubstituted product **Rot4** was present in the reaction mixture. All attempts to isolate **Rot4** failed and led to decomposition and overall a non-detectability of **Rot4** in all isolated fractions with ESI-MS and NMR. Also a strict exclusion of water while processing the reaction mixture did not lead to a stable product. A second possibility could be a total insolubility of **Rot4** once it is isolated, which is unlikely though as it could be detected with ESI-MS in the reaction mixture.

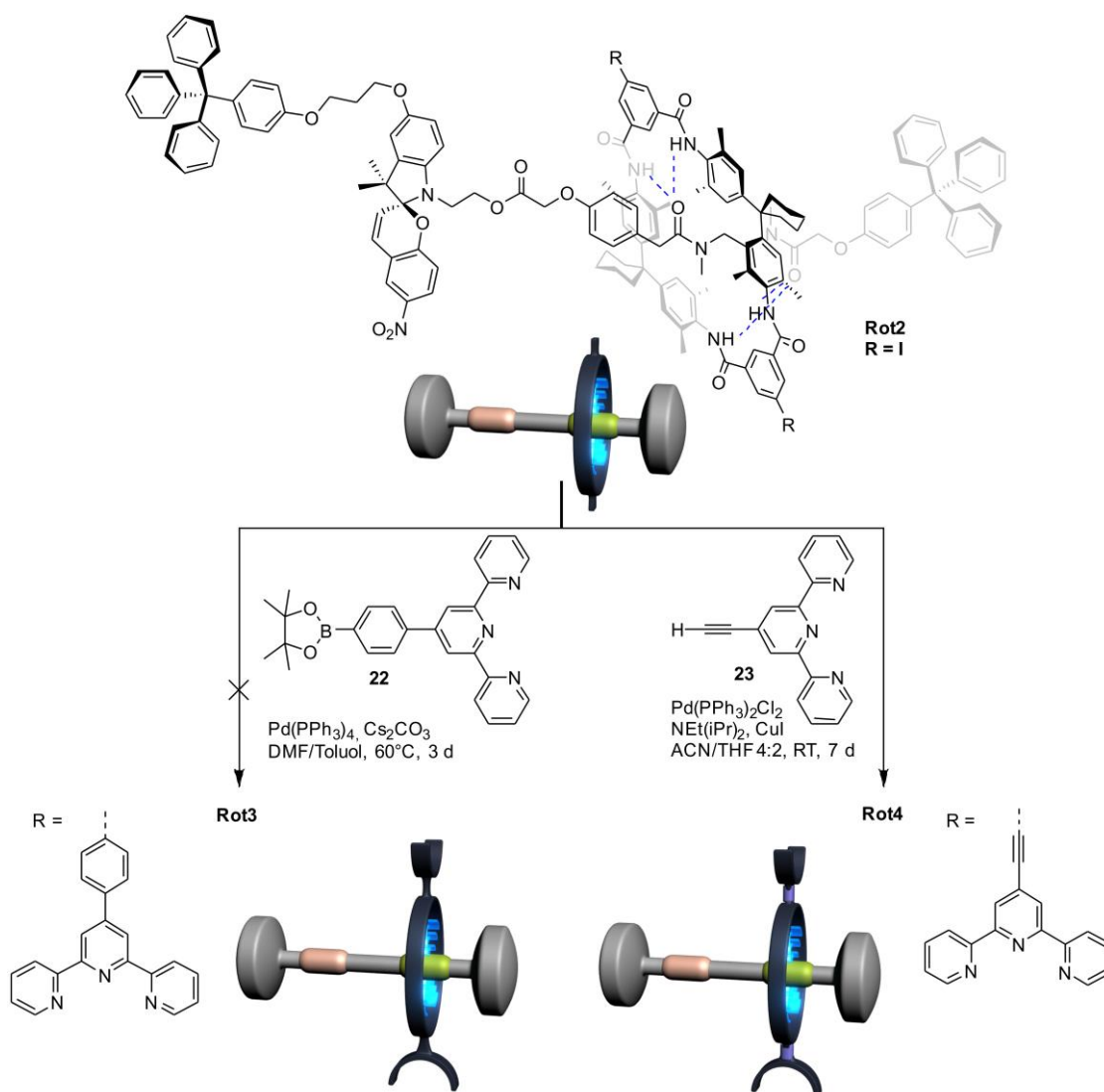


Figure 79: Synthesis of terpyridine functionalised rotaxanes **Rot3** and **Rot4**.

In a second approach, a literature known spiropyran rotaxane was modified to enable integration in the on-surface multilayer systems of switchable rotaxanes. The system published by Zhou and coworkers^[86] is comprised of a small unsubstituted tetralactam macrocycle^[163] and an axle bearing a spiropyran and a dipeptide binding site. The rotaxane is capable to switch the movement of the macrocycle between the two binding sites upon a light stimulus. In here, the rotaxane axle **27** was adopted and the rotaxane **Rot5** was synthesised with a iodo-substituted macrocycle to enable further functionalisation. The synthesis of the axle was thereby slightly modified and optimised.

Starting from 5-methoxy-2,3,3-trimethyl-3*H*-indole **9** which was synthesised as described in the previous chapter, the spiropyran **24** was prepared in three steps. Reaction with chloroacetylchloride led to the substituted spiropyran **25**. The second axle building block **26** was constructed out of 2-(4-tritylphenoxy)acetic acid **16** and ethyl glycyglycinate hydrochloride. Reaction of **25** and **26** gave the free axle **27**. Cyclisation of 5-iodoisophthaloyl

dichloride and 1,4-phenylenedimethanamine in the presence of axle **27** gave the rotaxane **Rot5** (Figure 80).

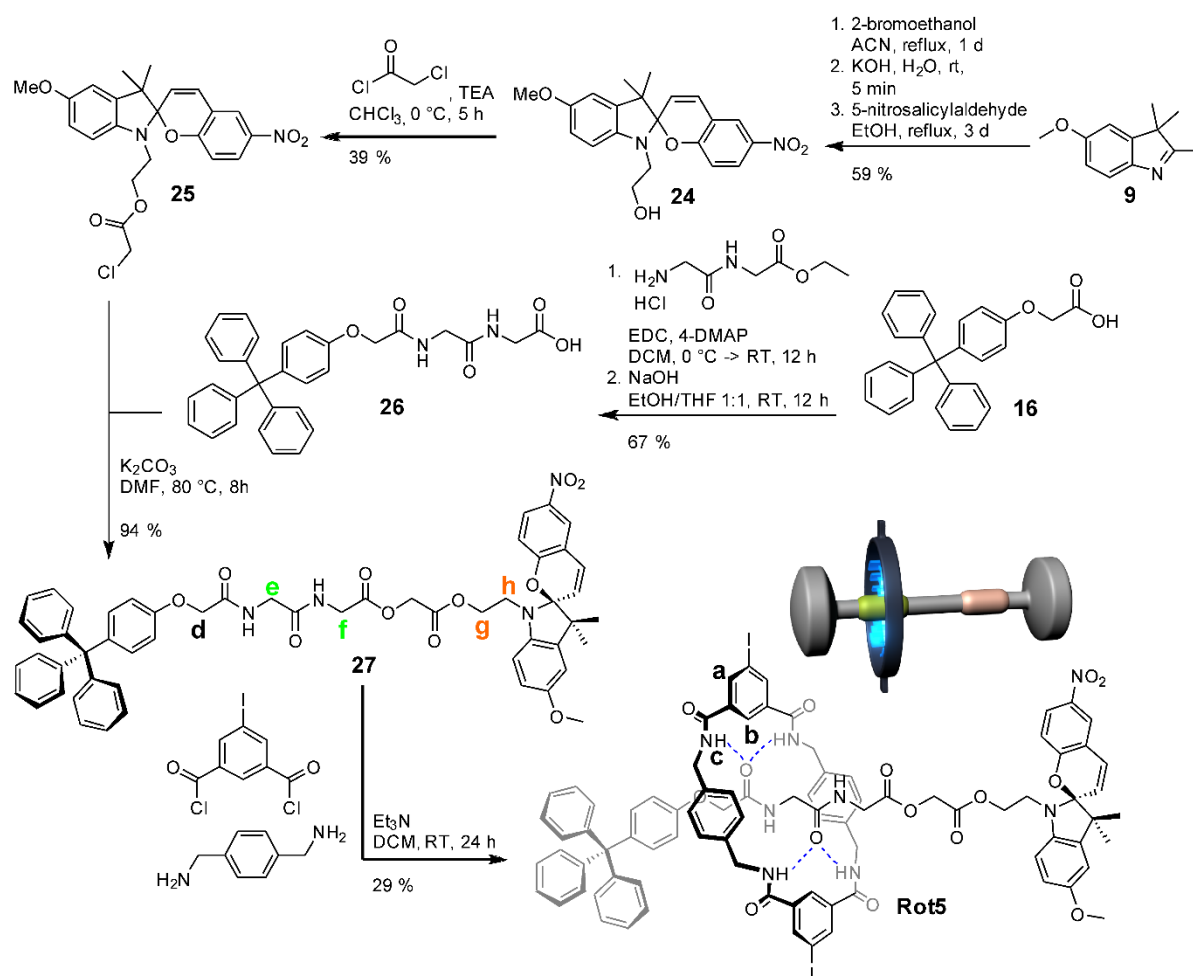


Figure 80: Synthesis of **Rot5**.

The formation of **Rot5** was followed by ¹H NMR spectroscopy. Comparison of the NMR spectra of the free axle (Figure 81a) and the rotaxane (Figure 81a) reveals significant upfield shifts of the diamide methylene protons **e** and **f** of 1.21 and 0.39 ppm and the adjacent methylene group **d** of 0.51 ppm due to the shielding effect of the macrocycle. The signals for protons **g** and **h** adjacent to the spiropyran remain unaffected at 4.25 and 3.37 ppm. This is clear evidence for the macrocycle being located at the diamide site. A spectrum of the free macrocycle could not be obtained due to its insolubility in all tested solvents.

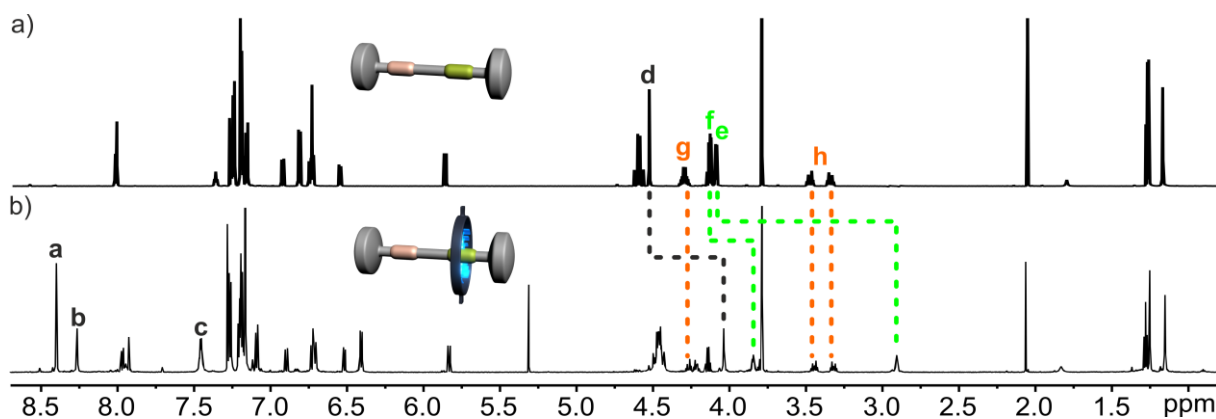


Figure 81: ^1H NMR spectra of a) free axle **27** and b) **Rot5**.

Photoswitching of **Rot5** was carried out analogously to the procedures described before for **Rot1**. Irradiation of a solution of **Rot5-SP** in acetonitrile at $\lambda_1 = 365$ nm for 90 s induced the isomerisation to **Rot5-MC**, as followed by UV-Vis spectroscopy. Irradiation with $\lambda > 500$ nm for 90 s or thermal equilibration for approximately 30 min lead to back switching to **Rot5-SP** (Figure 82).

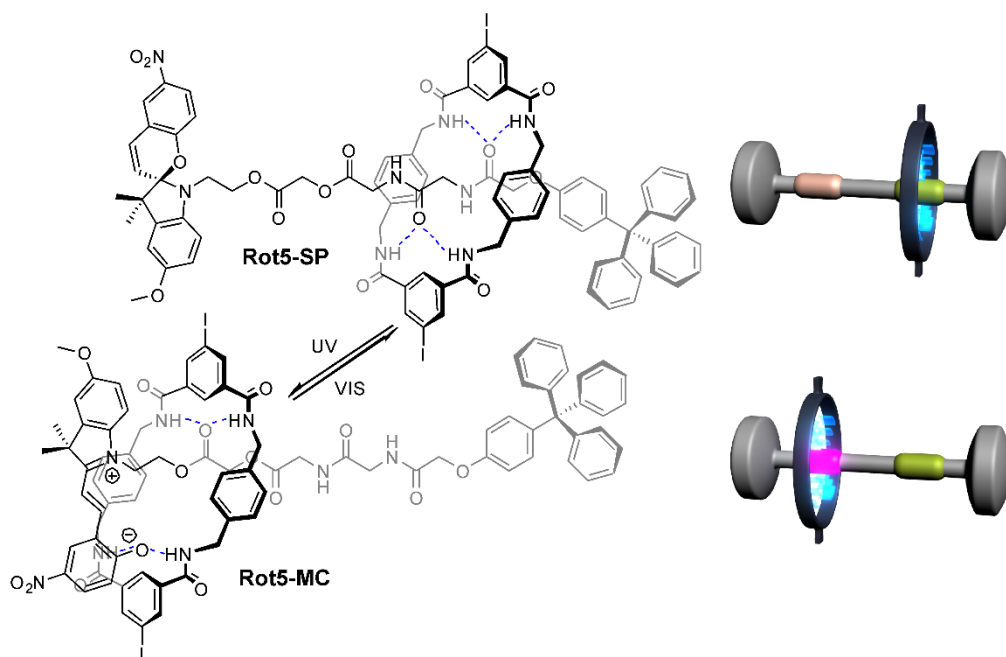


Figure 82: Photoswitching of **Rot5**.

To further functionalise **Rot5** with terpyridine units at the macrocycle, it was reacted with terpyridine **23** in a Sonogashira coupling reaction (Figure 83). Reaction conditions were optimised to be as mild as possible under strict exclusion of air and moisture and different solvents, catalysts, and bases were tested. Best results were achieved in a mixture of

acetonitrile and THF at room temperature with catalytic bis(triphenylphosphine)palladium(II) dichloride and copper(I) iodide and diisopropylethylamine, in which a complete conversion of the starting material to **Rot6** was shown in ESI-MS spectra of the reaction mixture. A fraction containing **Rot6** could be isolated. ESI-MS analysis revealed that significant amounts of starting material and monosubstituted product are still present, which have not been detected out of the crude reaction mixture. All attempts to achieve complete conversion by modifying the synthetic procedure by elongated reaction times, addition of more catalyst and terpyridine **23**, or raising the reaction temperature were not successful or led to decomposition of the product. Neither the attempt to isolate **Rot6** with preparative TLC or column chromatography nor dialysis led to a separation of mono- and disubstituted product and in some attempts resulted in decomposition of the product.

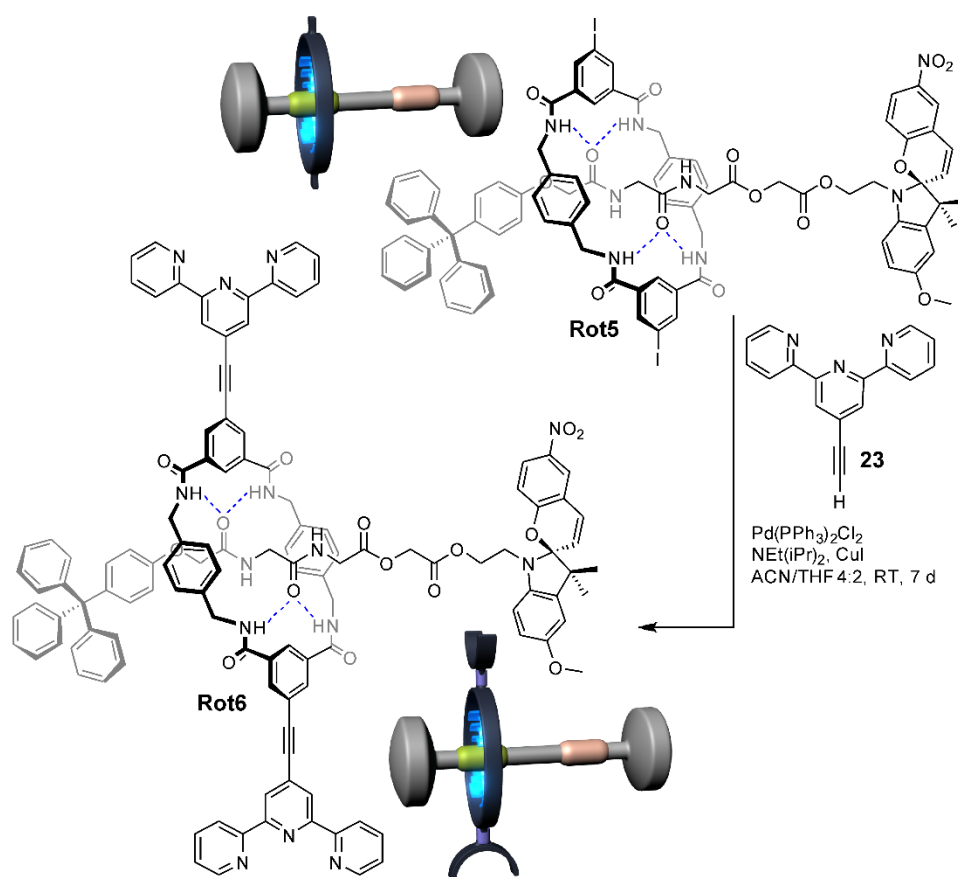


Figure 83: Synthesis of the terpyridine-substituted **Rot6**.

It is assumed that the ester group in the rotaxane axle represents the weak point of the structure, that can easily break during cross-coupling conditions with lewis acid catalysts or during workup procedures. As the ester's carboxyl group represents a necessary structural feature for the merocyanine binding station, it can not easily be exchanged.

4.1.3. Conclusions

Novel photoswitchable rotaxanes **Rot1** and **Rot2** comprised of *tert*-butyl or iodine-substituted Hunter-Vögtle-type TLM and a photoswitchable axle with spiropyran as central element were designed and synthesised. The rotaxane **Rot5** comprised of a Leigh-type TLM was synthesised inspired by a literature-known example with a modified substitution pattern of the macrocycle to enable further functionalisation. Photoswitching of **SP-Rot1** and **SP-Rot5** to their corresponding merocyanine forms could be performed and verified with UV-Vis spectroscopy, which also provided evidence for a photoinduced macrocycle movement. As the measurement of conclusive NMR spectra of the switched state turned out to be not straight forward, a degree of uncertainty remains. The terpyridine-functionalised rotaxanes for surface deposition could not be obtained for both Hunter-Vögtle-type TLM and Leigh-type TLM rotaxanes.

To overcome the mentioned difficulties, a second path towards towards photoswitchable rotaxanes on surfaces was followed by changing the photosystem to the more robust azobenzenes and developing a different type of photoswitchable rotaxane.

4.2. Azobenzene-based (pseudo-)rotaxanes

4.2.1. Photocontrolled on-surface pseudorotaxane formation with well-ordered macrocycle multilayers[†]

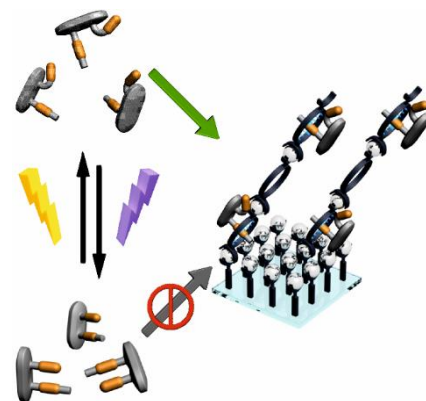


Figure 84: Graphical abstract.

4.2.1.1. Abstract

The photoinduced pseudorotaxane formation between a photoresponsive axle and a tetralactam macrocycle was investigated in solution and on glass surfaces with immobilised multilayers of macrocycles. In the course of this reaction, a novel photoswitchable binding station with azobenzene as the photoswitchable unit and diketopiperazine as the binding station was synthesised and studied by NMR and UV-Vis spectroscopy. Glass surfaces have been functionalised with pyridine-terminated SAMs and subsequently with multilayers of macrocycles through layer-by-layer self-assembly. A preferred orientation of the macrocycles could be confirmed by NEXAFS spectroscopy. The photocontrolled deposition of the axle into

[†] Parts of this chapter have been published and are reproduced in here with the kind permission of John Wiley and Sons, Inc.

F. B. Schwarz, T. Heinrich, J. O. Kaufmann, A. Lippitz, R. Puttreddy, K. Rissanen, W. E. S. Unger, C. A. Schalley, *Chem. Eur. J.* **2016**, *22*, 14383-14389.

The design, synthesis and analysis in solution of the photoswitchable pseudorotaxane, NMR titrations, crystal growing and surface UV-measurements were conducted by the author. Surface experiments were performed together with T. Heinrich. T. Heinrich conducted XPS and NEXAFS measurements together with A. Lippitz and synthesised the di-terpyridine macrocycles. J. O. Kaufmann contributed to the synthesis of precursor molecules. R. Puttreddy and K. Rissanen measured and solved the crystal structures. The manuscript was written mainly by the author together with T. Heinrich. All authors contributed to the final version of the manuscript.

the surface-bound macrocycle-multilayers was monitored by UV-Vis spectroscopy and led to an increase of the molecular order, as indicated by more substantial linear dichroism effects in angle-resolved NEXAFS spectra.

4.2.1.2. Introduction

Stimuli-responsive chemical systems capable of performing molecular motion are of great interest for the development of functional materials and molecular machines.^[38] Immobilizing such molecules on surfaces allows the concerted action of molecular switches and shuttles.^[5, 12-13, 164] Especially, surfaces functionalised with photoresponsive units have been of great interest in recent research.^[42a, 118a, 120] Mostly, gold and silicon substrates have been used as they can be easily functionalised with well-studied monolayers and due to the technological importance of these substrates.^[96, 165] Photochromic molecules like azobenzenes, spiropyrans or dithienylethenes bound to surfaces have for example been used to control the surface wettability,^[166] to change their electrical properties,^[167] or to control the adsorption of molecules on surfaces.^[168] Furthermore, photoresponsive units were utilised to actuate and control the molecular motion in molecular rotary motors^[11] and linear molecular muscles^[169].

Recently, we reported the deposition of ordered multilayers of Hunter-Vögtle-type tetralactam macrocycles^[24] (TLM) and TLM-based rotaxanes^[25c] on different substrates through layer-by-layer self-assembly^[113a-g] using metal-ion/pyridine/ terpyridine coordination chemistry.^[113h-k] This included the implementation of chemically switchable rotaxanes that change the macrocycle position in a cooperative manner when adding or removing chloride ions.^[15d] Although these systems work nicely, addressing responsive surfaces by inducing a chemical stimulus has some limitations. It unavoidably brings impurities into the system and therefore hampers an unambiguous analysis of structural changes on the surface. Another problem could be to address the lower layers in densely packed systems, which bulky molecules cannot reach easily by diffusion. In order to overcome these limitations, we aim to implement photoswitchable molecules in these previously realised macrocycle multilayer surfaces.

In this study, we start with a photoswitchable pseudorotaxane as the precursor for further studies with rotaxanes. Azobenzene, one of the most studied photochromic molecules, was chosen as the photoswitchable unit due to its fast and clean photoisomerization associated with different geometric and physico-chemical properties of the two switching states.^[47] The outstanding optomechanical properties make azobenzene a key-compound in switchable molecular and supramolecular functional systems, which is reflected in various reported examples in solution,^[65a, 65b] on nanoparticles,^[119] and on surfaces^[170]. However, there are only

a few reports on surface-^[124, 125b, 133] or nanoparticle-bound^[171] azobenzene-based (pseudo-)rotaxanes.

To utilize the *cis-trans* photoisomerization of azobenzene for controlling the threading and dethreading of a pseudorotaxane with a Hunter/Vögtle-type TLM, the photoswitch was attached to a rigid xanthene backbone resulting in a fixed position relative to the diketopiperazine binding station to influence its binding strength by steric hindrance. While the azobenzene blocks the binding station in its *trans*-configuration, the binding site becomes available upon switching to the *cis*-isomer. In solution studies by Jeong at al.^[67], a similar photoswitchable diamide station exhibited binding to nitro-substituted macrocycles. For our purposes, such a substitution on the macrocycles isophthaloyl diamide units is not suitable as it would block the functionalization necessary for surface binding. To design a suitable molecule for binding in our TLM multilayer surfaces, we have introduced diketopiperazine as the binding station, which exhibits a higher binding affinity towards TLM.^[172]

4.2.1.3. Results and Discussion

The photoswitchable binding site **36** was synthesised starting from commercially available xanthene **28** by following literature known procedures^[67b, 173] to give the azobenzene-substituted xantheneamine **32**. The synthesis was optimised to achieve higher product yields (see experimental section for details). The diketopiperazine binding station was attached to amine **32** in four steps^[174] starting with the reaction of **32** with bromoacetic acid ethyl ester to give secondary amine **33**. Compound **33** was then acetylated with chloroacetyl chloride and subsequently converted to iodide **34** in a Finkelstein reaction. Treatment of **34** with methanolic ammonia induced ring closure and afforded the diketopiperazine **35**. Methylation of **35** yielded the final product **36** with an overall yield of 14% over ten steps (Scheme 1). Tetralactam macrocycles were synthesised according to literature known procedures.^[26]

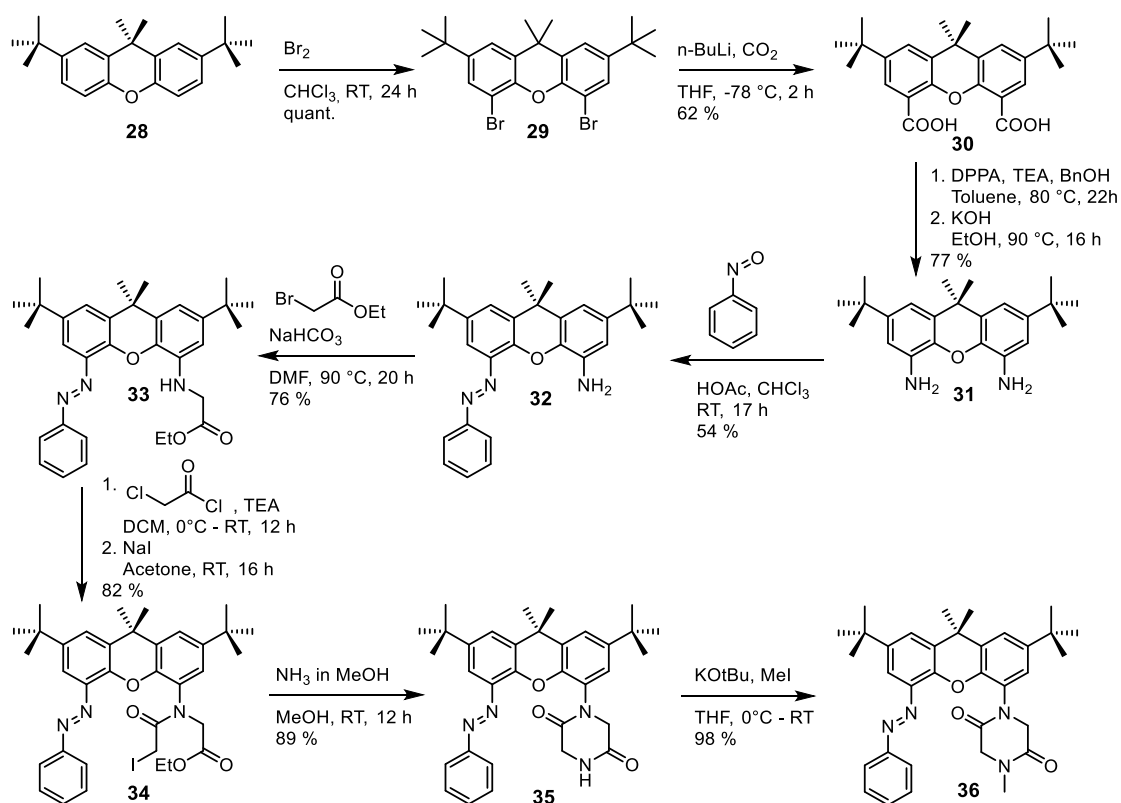


Figure 85: Synthesis of photoswitchable binding station **36**: a) 1. Br_2 , CHCl_3 , r.t., 24 h, quant., 2. $n\text{-BuLi}$, CO_2 , THF, -78°C , 2 h, 62%. b) 1. DPPA, TEA, BnOH, toluene, 80°C , 22 h, 79%, 2. KOH, EtOH, 90°C , 16 h, 98%. c) Nitrosobenzene, HOAc, CHCl_3 , r.t., 17 h, 54%. d) Ethyl bromoacetate, NaHCO_3 , DMF, 90°C , 20 h, 76%. e) 1. Chloroacetyl chloride, TEA, CH_2Cl_2 , $0^\circ\text{C} \rightarrow \text{r.t.}$, 12 h, 83%, 2. NaI, acetone, r.t., 16 h, 99%. f) NH_3 in MeOH, MeOH, r.t., 12 h, 89%. g) KOtBu, MeI, THF, $0^\circ\text{C} \rightarrow \text{r.t.}$, 98%.

Single crystals of *trans*-**35** suitable for X-ray analysis (SI) were obtained by the slow evaporation of a solution of *trans*-**35** in methanol. Figure 86a shows the section of the asymmetric unit of *trans*-**35**, crystallised in the triclinic space group *P*-1 with selected atom labelling. The asymmetric unit contains two *trans*-**35** and two water molecules. The restricted rotation of the diketopiperazine due to steric hindrance with the xanthene-substituted azobenzene favours the keto-groups as binding stations in **36**@**19**. The azobenzene is in its *trans*-configuration with the phenyl ring, and is nearly coplanar to the xanthene-backbone with a Root Mean Square Deviation (RMSD) of 0.140 \AA . The angle between the mean planes of these rings is 86.7° . The diketopiperazine rings in two crystallographically independent molecules constitutes RMSD of 0.132 and 0.58 , and are perpendicular to the xanthene backbone. All the bond parameters in the xanthene backbone of **35**, and C55-N5 [$1.440(4) \text{ \AA}$] are close to the reported values,^[175] while the C40-N7 [$1.423(4) \text{ \AA}$], N7-N8 [$1.261(4) \text{ \AA}$], N8-C37 [$1.429(4) \text{ \AA}$] are similar to *trans*-azobenzene.^[176]

MM2 force-field modeling shows *cis*-**36** to nicely fit into the cavity of the TLM (Figure 86b). The modelled structure is in good agreement with the crystal structure of **35** where the xanthene unit is almost planar, while the diketopiperazine unit is turned out of plane.

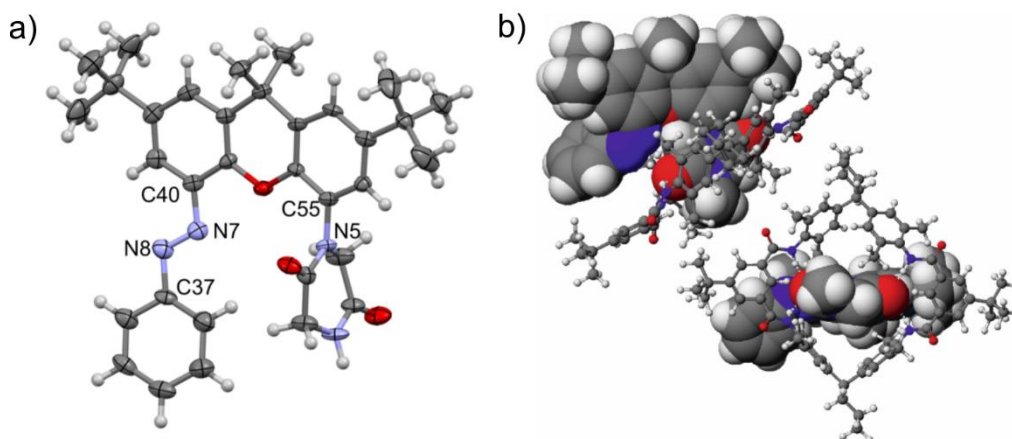


Figure 86: a) Crystal structure of **35** (thermal ellipsoids shown at the 50% probability level) and b) MM2 force-field model of the pseudorotaxane **36@19** with axle **35** displayed in space-filling mode and macrocycle **19** in ball and stick model (top left: side view, bottom right: top view). See experimental section for a crystal structure of **19**.

The photoisomerization of **36** and subsequent pseudorotaxane formation (Figure 87a) was studied first in solution by UV-Vis and NMR spectroscopy. The di-*tert*-butyl-substituted TLM **19** (for an X-ray structure, see experimental section) was used for solution studies due to its good solubility. Photoisomerization of **36** from *trans* to *cis* was carried out by irradiating a solution of *trans*-**36** in CH₂Cl₂ with an LED lamp at a wavelength of $\lambda_1 = 365$ nm. The back isomerization to the *trans* configuration was performed by either irradiation with an LED lamp at $\lambda_2 = 470$ nm or by equilibration in the dark at room temperature for 24 hours.

The UV-Vis spectrum of *trans*-**36** in CH₂Cl₂ (Figure 87b) shows the characteristic absorption band for the $\pi \rightarrow \pi^*$ transition of the azobenzene at 323 nm,^[58] which decreases upon irradiation with $\lambda_1 = 365$ nm, indicating the formation of *cis*-**36**. The photostationary state with a *cis*- to *trans*-**36** ratio of 2:1 was reached after approx. 10 minutes. After irradiation with $\lambda_2 = 470$ nm for 10 minutes or equilibration in the dark over 24 h, the UV-Vis spectrum was hardly different from the initial one. Reversibility was tested by alternating irradiation over five cycles (Figure 87c). UV-Vis analysis of **36** was also carried out with a 1:1 mixture of **36** and TLM **19**, in which, as expected, no shifts of absorption maxima could be observed since the binding mode does not significantly influence the chromophor's electronic properties.

Besides investigating the switching process and its reversibility by UV-Vis spectroscopy, NMR spectroscopy was applied to gain structural information and evidence for switchable pseudorotaxane formation. The NMR spectrum of TLM **19** (Figure 87d, I) shows the signals for the inner isophthalic acid protons **a** at 7.98 ppm and the amide protons **b** at 7.29 ppm. Upon addition of one equivalent *trans*-**36** (Figure 87d, II), the amide protons undergo only a very small shift of $\Delta\delta = 0.04$ ppm. After 10 minutes irradiation at $\lambda_1 = 365$ nm (Figure 87d, III), a second set of signals for *cis*-**36** appears with a ratio of *cis*- to *trans*-**36** of approx. 2:1. Due to a fast exchange of axle **36** and macrocycle **19**, no second set of signals for the free macrocycle

19 but time-averaged signals are present. The macrocycle protons **a** and **b** are now significantly shifted downfield by $\Delta\delta = 0.21$ ppm and $\Delta\delta = 0.86$ ppm due to hydrogen bonding to *cis*-**36**. The axle protons **c**, **d** and **e** are shifted upfield by $\Delta\delta = 0.44$ ppm, $\Delta\delta = 0.88$ ppm and $\Delta\delta = 0.49$ ppm due to the shielding effect of TLM **19**, clearly evidencing pseudorotaxane formation. After leaving the sample for 24 h in the dark, the spectrum was virtual undistinguishable from the initial one (Figure 87d, IV). When the back isomerization was carried out photochemically by irradiation at $\lambda_2 = 470$ nm, the photostationary state with a *cis*- to *trans*-**36** ratio of 1:9 was reached after approx. 10 minutes, as determined by NMR.

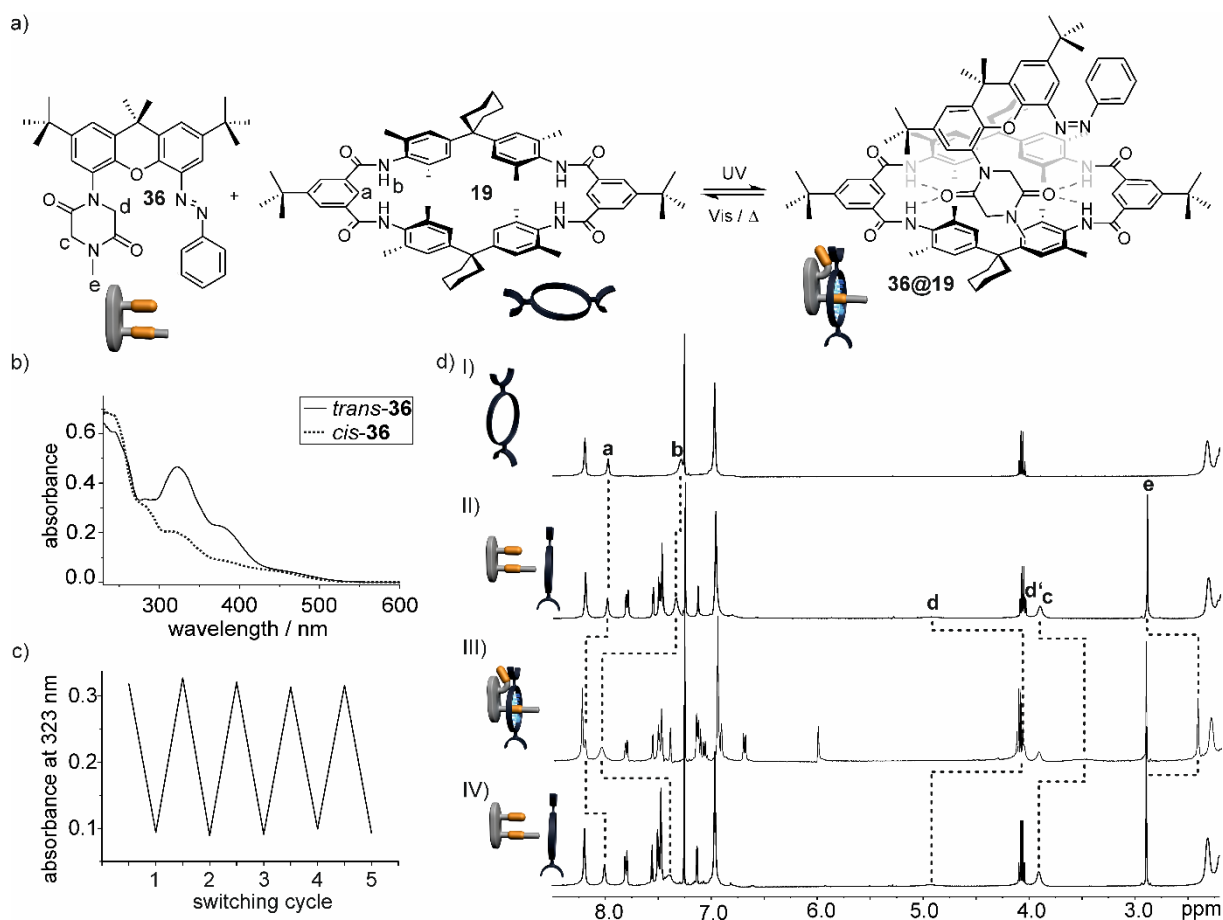


Figure 87: a) Photoswitchable pseudorotaxane formation. b) UV-Vis spectra of *cis*- and *trans*-**36** in CH_2Cl_2 . c) Reversibility of photoswitching in CH_2Cl_2 tested by alternating irradiation at $\lambda_1 = 365$ nm and $\lambda_2 = 470$ for 10 min in each step. d) NMR analysis (400 MHz, 298 K, CDCl_3) of pseudorotaxane switching. I: TLM **19**. II: **19** + *trans*-**36**, 1:1. III: **19** + **36** after 10 min irradiation at $\lambda_1 = 365$ nm. IV: **19** + **36** after 24 h in the dark at r.t.

To study the binding behavior of *cis*- and *trans*-**36** to the TLM **19**, NMR experiments have been performed. Since there is a fast exchange on the NMR timescale, the binding constants were evaluated by NMR titration analysis.^[162b, 177] A solution of TLM **19** (5.00 mg) in CDCl_3 (0.65 mL) was placed in an NMR tube and treated with different amounts of *cis*-**36** or *trans*-**36**, respectively. In case of *cis*-**36**, the solution of the axle was irradiated during the titration. A ^1H NMR spectrum was measured after each injection and the real guest concentrations were

determined by integration of the signals. The binding constants were determined based on a 1:1 binding model. For *trans*-**36**, a very small binding constant of $< 15 \text{ M}^{-1}$ was obtained, while *cis*-**36** has a binding constant of $1,650 \pm 165 \text{ M}^{-1}$ (Figure 88).

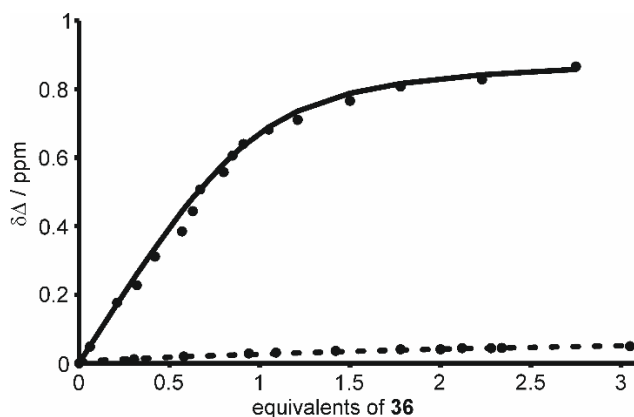


Figure 88: NMR titration of TLM **19** with *trans*-**36** (dashed) and *cis*-**36** (solid) in CDCl_3 at room temperature.

After studying pseudorotaxane formation and its switchability in solution, the concept was transferred to surfaces. Multilayers of tetralactam macrocycles have been prepared by metal-coordination-based layer-by-layer self-assembly on glass substrates according to previously established procedures.^[15b, 139, 178]

As the template layer, a self-assembled monolayer of **PDS** (Figure 89a) was deposited on cleaned glass surfaces. The surfaces were then treated with a 1 mM solution of $\text{Pd}(\text{CH}_3\text{CN})_4(\text{BF}_4)_2$ in CH_2Cl_2 to coordinate the pyridyl endgroups of the SAM with Pd^{II} ions, enabling the attachment of the next organic layer. By alternating deposition of di-terpyridine-TLM **37** and $\text{Fe}(\text{BF}_4)_2 \cdot 6\text{H}_2\text{O}$, a controlled growth of macrocycle layers was achieved, monitored by UV-Vis spectra recorded after each deposition step (Figure 89b).

To show that *cis*-**36** binds to the cavity of the macrocycles on the surface while *trans*-**36** does not, surfaces with 1, 3 and 5 layers of TLM **37** have been prepared. A surface with only the SAM was used as control. The surfaces were immersed in a 1 mM solution of *trans*-**36** (large excess) in CH_2Cl_2 for 24 h, followed by washing the surface with CH_2Cl_2 for 10 minutes to remove any unspecifically bound molecules. For all four surfaces, no increase of the π - π^* band in the UV-Vis spectra before and after immersion to the solution of *trans*-**36** was observed, clearly showing that no additional chromophores are deposited on the surface and therefore that *trans*-**36** does not bind to the macrocycle multilayers (Figure 89c).

The experiment was then repeated with the same surfaces immersed into the same solution, but now under continuous irradiation with UV light of a wavelength of $\lambda_1 = 365 \text{ nm}$ to form *cis*-**36**.

To avoid light-induced damages on the surfaces, the irradiation was carried out in a way that no light reached the surfaces directly, but only the solution was irradiated. After washing the surfaces for 10 minutes with CH_2Cl_2 , UV-Vis spectra were recorded. The spectrum of the surface with only the **PDS-SAM** showed no change before and after deposition of **36**. The spectra of the surfaces with one, three and five layers of TLM **37** showed a substantial increase of the absorption around 350 nm, indicating the deposition of *cis*-**36** (Figure 89d).

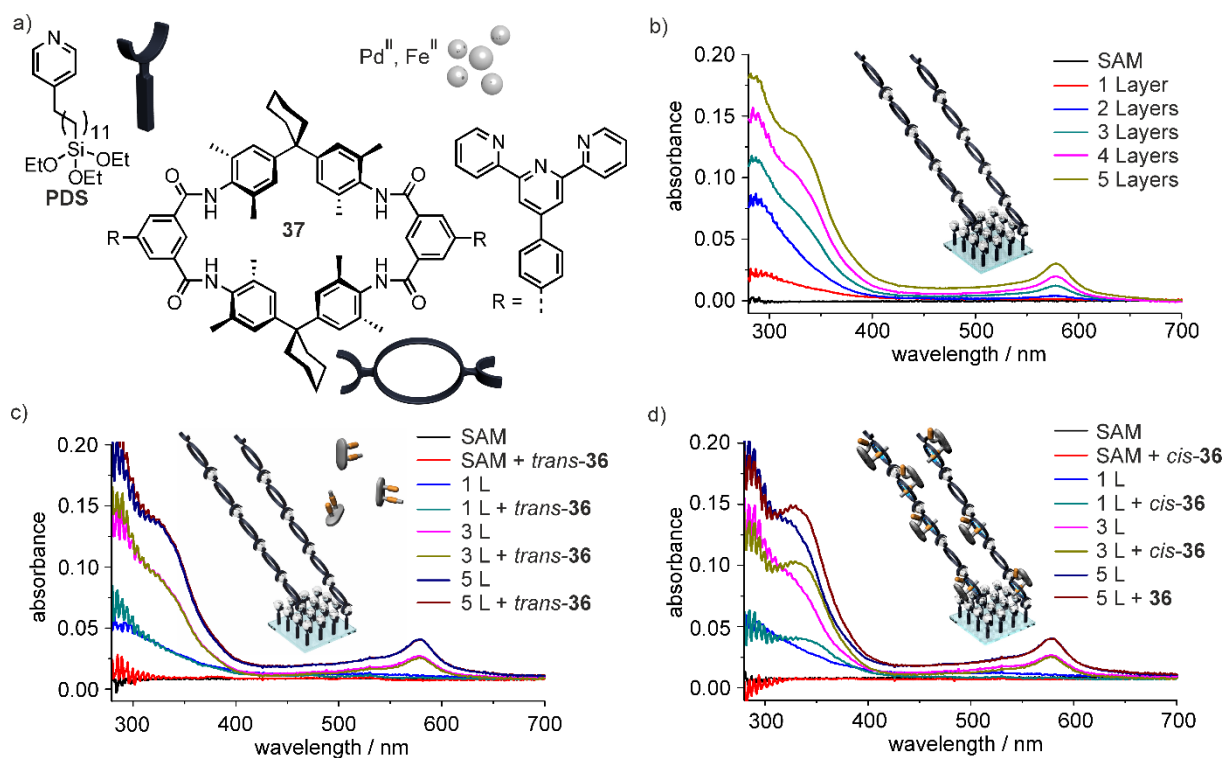


Figure 89: a) Di-terpyridine-TLM **37**, **PDS-SAM**, metal ions used for the self-assembly of macrocycle multilayers. b) Surface UV-Vis spectra showing multilayer deposition. c) UV-Vis spectra of surfaces before and after immersion in *trans*-**36** solution. d) UV-Vis spectra of surfaces before and after immersion in *cis*-**36** solution. The increase of absorption in 2d is in line with the solution UV-Vis spectra of *cis*-**36** in figure 87b.

Interestingly, the increase of absorption after the deposition of **36** on the surfaces does not linearly increase with a higher number of macrocycle layers. While the absorption increases for three layers relative to one layer, it does not increase any further for five layers (Figure 90). This indicates, that the multilayers are rather densely packed and that not all macrocycles are accessible for the binding of *cis*-**36**. In a previous study, we used a squaraine as the guest molecule that was bound to macrocycle multilayers and a linear increase of bound molecules with increasing number of layers was observed.^[179] This can be explained by the differences between the molecular structure of the guests. While the squaraine molecule used in the former study is relatively small, has a linear form without stopper-units and can therefore easily slip through the voids in the surface or the macrocycle cavities, guest molecule **36** used here is stoppered on one end through the xanthene unit, so that the accessibility of deeper macrocycle layers is significantly hampered.

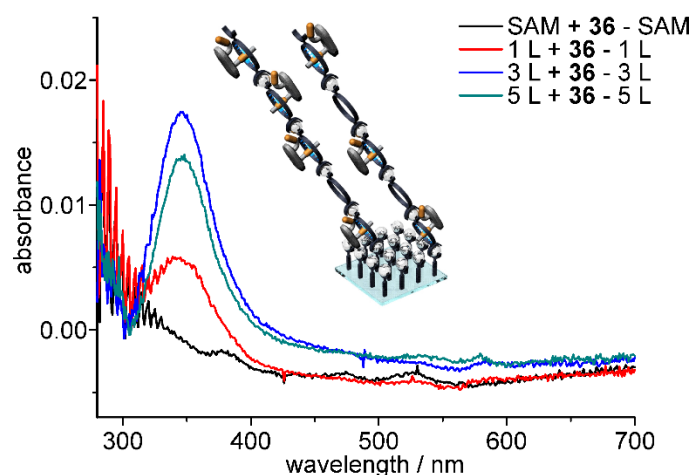


Figure 90: Difference spectra of glass surfaces with 1, 3 and 5 multilayer of macrocycle and the SAM before and after deposition of *cis*-**36**.

The same experiments with glass surfaces have been repeated with semitransparent gold substrates. As template layer, a self-assembled monolayer of **PST** (Figure 91a) was deposited on cleaned gold surfaces. The surfaces were then functionalised with multilayers of TLM **37** analogously to the glass surfaces described before. Due to the lower transmission of semitransparent gold surfaces compared to the glass substrates, surfaces with five and ten

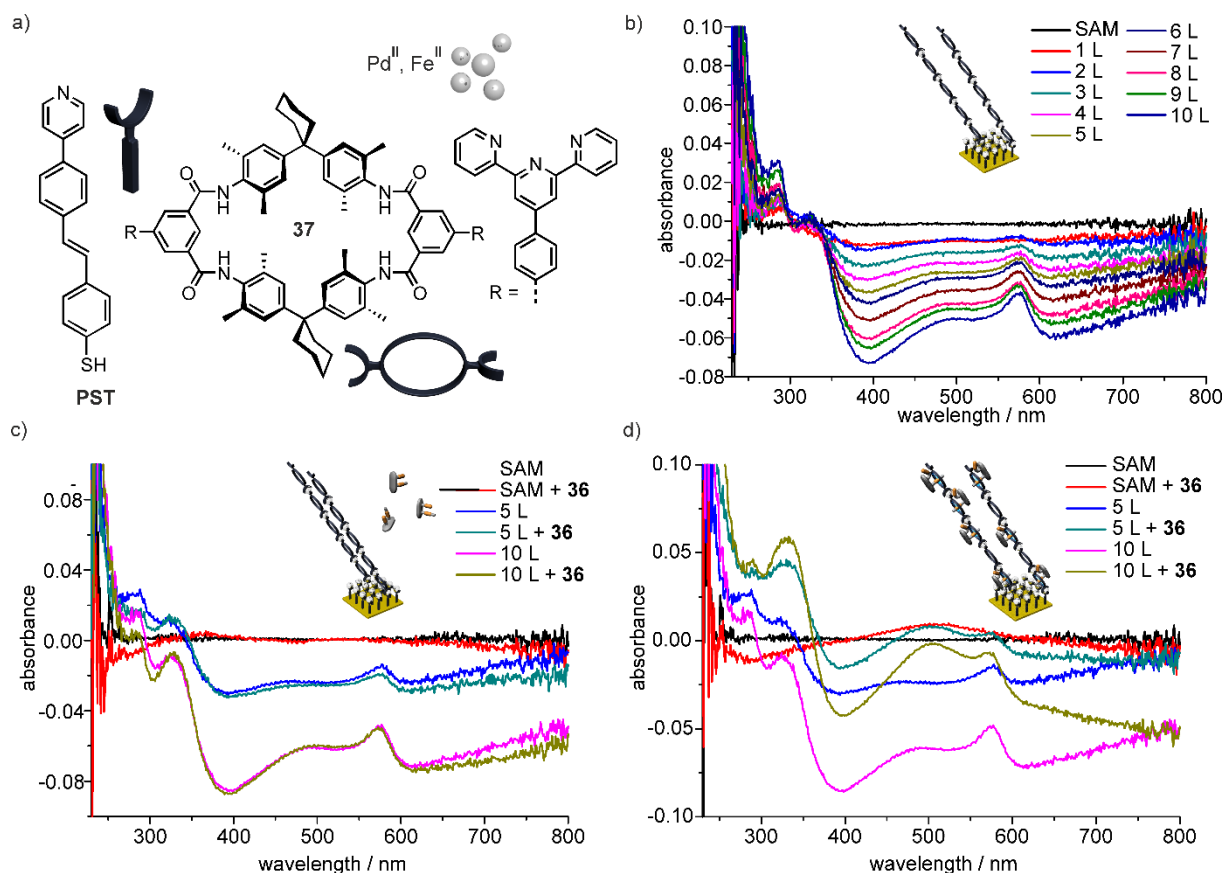


Figure 91: a) Materials used for surface experiments, b) UV spectra of the multilayer deposition of 10 Layers TLM **37** on a gold surface, c) UV-Vis spectra of surfaces before and after immersion in *trans*-**36** solution, d) UV-Vis spectra of surfaces before and after immersion in *cis*-**36** solution.

instead of one, three and five layers of macrocycle have been investigated. Similar to the glass surfaces, a controlled growth of macrocycle layers was achieved (Figure 91b). As organic material adsorbed on gold surfaces lowers the reflectance of the substrate, the absorption decreases with increasing number of multilayer. The UV-Vis spectra of gold surfaces with five and ten multilayers of macrocycle and the SAM as control experiment before and after immersion for 24 h in a solution of *trans*-**36** are displayed in Figure 91c. Almost no changes in the UV spectra occurred after the deposition step, clearly showing that *trans*-**36** does not bind to the gold surfaces. In contrast, the UV-Vis spectra of the surfaces with five and ten multilayers after 24 h immersion in a solution of *cis*-**36** show an increased absorption around 350 nm for the deposited azobenzene and around 500 nm for the surface plasmon resonance, clearly indicating the deposition of *cis*-**36** on the gold surfaces.

Both glass and gold surfaces showed similar results for macrocycle multilayer formation and photocontrolled pseudorotaxane deposition. As glass surfaces are better analyzable with UV-Vis due to their higher transparency compared to semitransparent gold surfaces, all further experiments were only conducted with glass surfaces.

In addition to UV-Vis spectroscopy, the surfaces have been analysed with XPS and NEXAFS spectroscopy. As glass slides are not suitable for these methods, silicon surfaces have been used that have been prepared in the same way as the glass slides used before. Surfaces with three layers of macrocycle with and without incorporated *cis*-**36** have been prepared and analysed. In addition, a thin film of **36** was deposited on a cleaned silicon surface via drop-coating from CH₂Cl₂. Survey XP spectra of surfaces with three layers of macrocycle with and without incorporated *cis*-**36** have been measured, showing oxygen 1s, carbon 1s, nitrogen 1s and silicon 2p signals (see experimental section). Synchrotron radiation (SR) XP spectra for the N 1s and C 1s core level regions have been measured to analyse the different species present on the surface (Figure 92).

The C 1s core level spectra exhibits the expected signals for amide (~288 eV), nitrogen-bound (~287 eV), aliphatic (~285 eV) and aromatic (284.5 eV) carbon,^[15d] where only small differences are visible before and after treatment of the surfaces with a *cis*-**36** solution. In the N 1s core level spectra, the component at 400.9 eV can be assigned to complexed pyridine and terpyridine nitrogen, whereas the component at 399.8 eV is assigned non-complexed (ter-)pyridine and amide nitrogen atoms.^[15a, 179] The nitrogen atoms of azobenzene give rise to peaks around 399.5 – 400.1 eV and are thus overlapping with the signal for non complexed (ter-)pyridine and amide nitrogens.^[180] The amide nitrogen atoms of the diketopiperazine exhibit a signal at 400.9 eV which is overlapping with the signal of complexed (ter-)pyridine nitrogens.^[181] The increase of this peak after treatment of the surface with a solution of *cis*-**36** indicates a successful deposition in the multilayers.

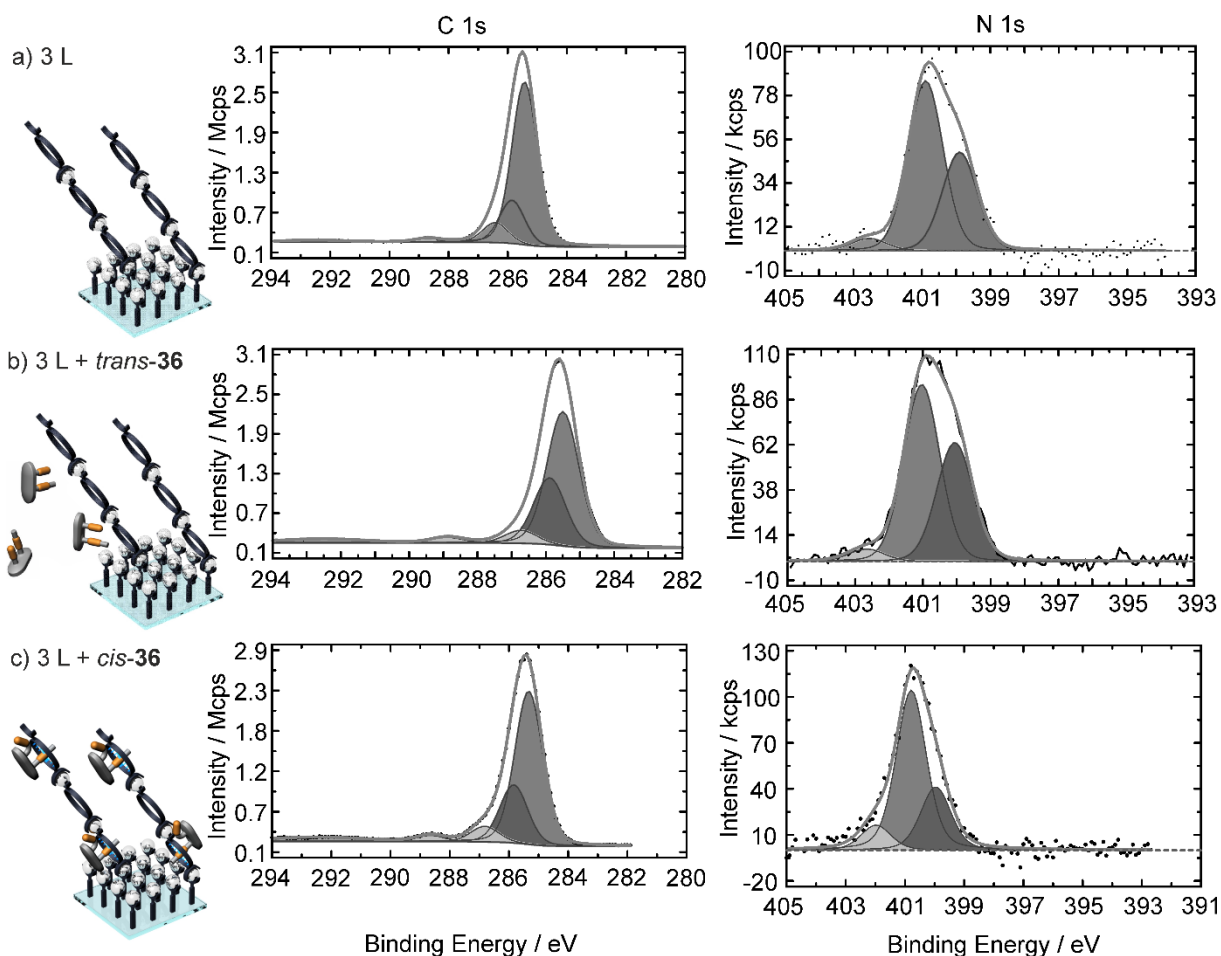


Figure 92: SR-XP C 1s (left, $h\nu = 385$ eV) and N 1s (right, $h\nu = 500$ eV) core level spectra of a) a three-layered macrocycle multilayer, (b) the multilayer treated with a solution of *trans*-**36**, (c) the multilayer treated with a solution of *cis*-**36**.

The N K-edge NEXAFS spectrum of the macrocycle multilayer shows three clearly visible peaks which are assigned to the terpyridine moiety (398.7 and 399.3 eV) as well as to the amide nitrogens of the macrocycle (400.6 eV) (Figure 93a). In the spectrum of dropcoated **36** (Figure 93d), two resonances for the excitation into π^* orbitals at 398.6 eV and 401.9 eV are found that can be assigned to the azobenzene- and diketopiperazine-nitrogen atoms. While these resonances are absent in the N K-edge NEXAFS spectra of the pristine macrocycle multilayers and those treated with *trans*-**36** (Figure 93b), they are present in the spectra of the multilayers treated with *cis*-**36** (Figure 93c), clearly showing the presence of *cis*-**8** on the surface and indicating the incorporation of the guest into the macrocycle multilayers.

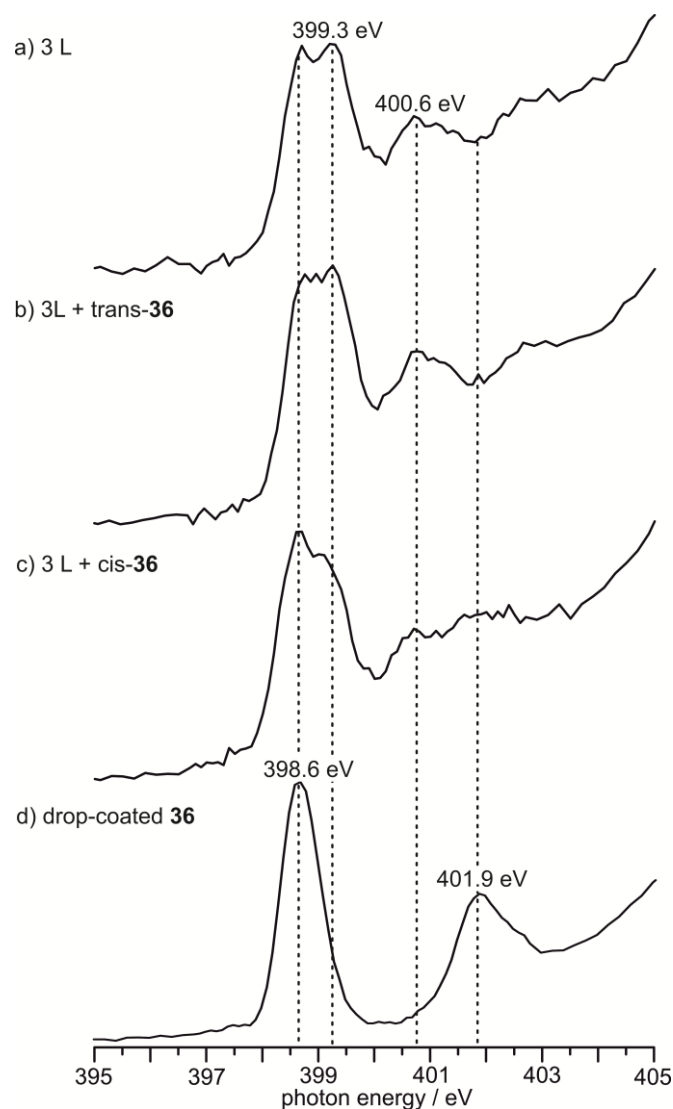


Figure 93: N K-edge NEXAFS spectra of (a) a three-layered macrocycle multilayer, (b) the multilayer treated with a solution of *trans*-**36** to the exclusion of light, (c) the multilayer treated with a solution of *cis*-**36**, and (d) the dropcoated **36**. Spectra were taken at an incidence angle of the linearly polarised synchrotron light of 55°.

To get a more detailed insight to the packing of macrocycles with and without *cis*-**36**, angle-dependent C K-edge NEXAFS spectra have been recorded (Figure 94). The pristine macrocycle multilayer (Figure 94a) shows effects analogous to those observed in earlier studies of macrocycles on a terpyridine-terminated template with gold as the substrate.^[179] The π^* resonance exhibits splitting into two characteristic peaks at 285.1 eV and 285.4 eV which show a clear linear dichroism in the 90°-30° difference spectrum in line with the earlier results. This also includes a significant change of the relative heights of the two peaks. When the multilayer is treated with *trans*-**36** solution (Figure 94b), the spectra closely resemble those of the pristine multilayer with comparable effects. In contrast, the surface treated with *cis*-**36** is different (Figure 94c). The signal at 285.4 eV seems to be superimposed by a second one and, furthermore, a signal at 288.3 eV shows-up. When we look at the C-K edge of dropcoated **36** (Figure 94d), we can observe three characteristic signals at photon energies of 285.4 eV,

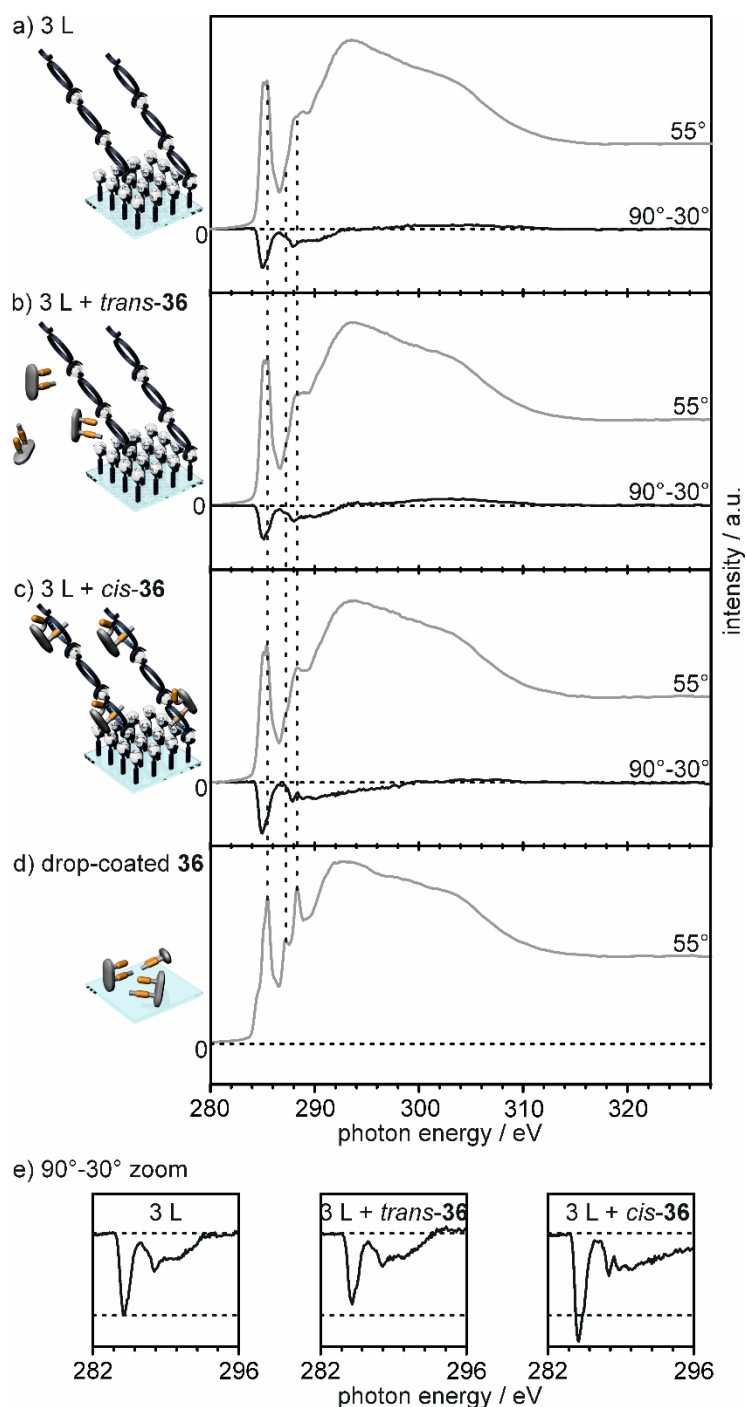


Figure 94: C K-edge NEXAFS spectra acquired at an incidence angle of the linearly polarised synchrotron light of (grey) 55° and (black) the difference between the spectra acquired at 90° and 30° of (a) a three-layered macrocycle multilayer, (b) the multilayer treated with a solution of *trans*-**36**, (c) the multilayer treated with a solution of *cis*-**36** and (d) a cleaned surface dropcoated with a solution of **36**. e) displays an enhanced section of the 90° - 30° difference spectra.

287.2 eV, and 288.3 eV, two of which can be assigned to the ‘new’ signals in the spectrum of the multilayer treated with a solution of *cis*-**36**. That we do not observe the third peak at 287.2 eV in this spectrum can be explained by its relatively low intensity and that it is therefore superimposed by the spectral contributions of the macrocycle multilayer. Together with the results from the N-K edge spectra, this is a clear evidence for the presence of the guest **36** on

the surface. If we look at the 90°-30° difference spectrum of this sample, an increase – when compared to the one of the original multilayer – of the linear dichroism in the area where the π^* resonances appear becomes apparent which indicates the incorporation of the guest into the cavity of the macrocycles.

To study on-surface switching, surfaces with 1, 3 and 5 layers of macrocycles with bound *cis*-**36** have been irradiated first with light of $\lambda_2 = 470$ nm and then $\lambda_1 = 365$ nm over different times (1-30 min). None of these irradiations induced any changes in the absorption spectra of the surfaces, showing that the bound azobenzenes do not undergo *cis*-to-*trans* photoisomerization on the surface. Additionally, we tried to remove *cis*-**36** from the multilayer by washing the surfaces with different solvents. Immersing the surfaces in CH₂Cl₂ over 24 h had no effect on the surface, showing that **36** is quite strongly bound in the macrocycles. Next, the surfaces were irradiated in CH₂Cl₂ with visible light of $\lambda_2 = 470$ nm to find out if the back isomerization to *trans*-**36** is facilitated in a solution environment, but even after 48 h no change in the UV-Vis spectra was achieved. Guest *cis*-**36** could finally be removed from the multilayers by treating the surfaces with DMF, which acts as a competitive binder to the macrocycle. After 1 h in DMF, *cis*-**36** was completely removed from the multilayers, as followed by UV-Vis spectroscopy (Figure 95a). Reversibility was tested by alternating deposition and removal of **36** via 24 h immersion in a solution of **36** under UV irradiation and 1 h washing with DMF (Figure 95b).

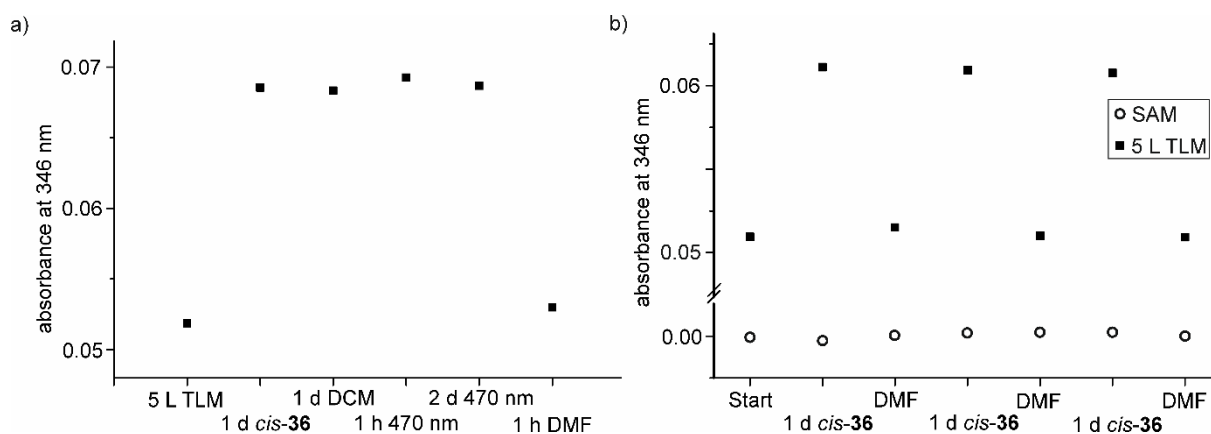


Figure 95: UV-Vis absorbance at 346 nm of surfaces. a) Removing **36** from 5-layer surface. b) Reversibility of *cis*-**36** deposition on a 5 layer surface vs. no deposition on a SAM surface.

Although *cis*-to-*trans* isomerization of **36** occurs easily in solution by both equilibration in the dark or irradiation with visible light at $\lambda_2 = 470$ nm, it does not happen when *cis*-**36** is incorporated in macrocycle multilayers on a solid support. It appears that in the densely packed multilayers, the freedom of *cis*-**36** to change its structure is too limited, thus blocking the *cis*-to-*trans* backswitching. This is in line with solid state studies, showing the (photo-)isomerization of azobenzenes not to take place unless the molecules are specially

designed to do so,^[57, 182] as the isomerization reaction requires a relatively large free volume^[183] and is therefore hindered in densely packed structures.

4.2.1.4. Conclusions

A photoswitchable binding station for tetralactam macrocycles based on azobenzene as the photoswitchable element and diketopiperazine as the binding station has been developed. The *cis-trans* isomerization of the molecule and subsequent pseudorotaxane formation with a TLM was analysed by UV-Vis and NMR spectroscopy. By using glass and gold surfaces with multilayers of tetralactam macrocycles, a photocontrolled on-surface pseudorotaxane formation could be achieved on both substrates, confirmed by UV-Vis, XPS and NEXAFS spectroscopy. Additionally, NEXAFS spectra revealed an increase in the molecular order on the surface after pseudorotaxane formation. The ordered and densely packed nature of the multilayers on the surface prevents isomerization of the incorporated azobenzene guest molecules, illustrating the significant differences between solution and surface.

As pseudorotaxanes are precursors of mechanical interlocked molecules like rotaxanes, this work opens a path towards photoswitchable rotaxanes embedded in multilayers on surfaces leading in combination with chemically switchable rotaxanes to multi-stimuli responsive surface systems. The quite densely packed and oriented nature of the multilayers on the surface may result in concerted movement and potential macroscopic effects.

4.2.2. A photoswitchable rotaxane operating in monolayers on solid support[†]

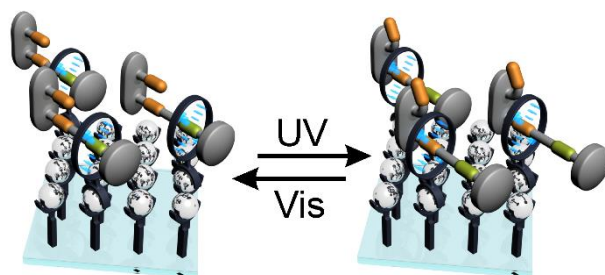


Figure 96: Graphical abstract.

4.2.2.1. Abstract

A novel photoswitchable rotaxane was synthesised and its switching behaviour in solution was analysed with NMR, MS and UV-Vis. A monolayer of rotaxanes was deposited on glass surfaces and the on-surface photoswitching was investigated. Angle-resolved NEXAFS spectra revealed a preferential orientation that reversibly changes upon switching.

4.2.2.2. Introduction

Photochromic molecules are widely used as key components in stimuli responsive molecular switches and machines. Common photoswitches like azobenzenes, spiropyrans and dithienylethenes offering a fast and clean photoisomerisation have been utilised in the development of complex functional systems and materials.^[42a, 65d, 118a, 120, 170b, 184] Especially, mechanically interlocked molecules (MIMs) like rotaxanes have been investigated intensely in this context. The transfer of MIMs from solution into ordered arrays at interfaces is of great interest in current research, as such order is the prerequisite for macroscopic effects through the concerted action of microscopic units.^[170a, 185] Several examples for the deposition of MIMs

[†] Parts of this chapter have been published and are reproduced in here with the kind permission The Royal Society of Chemistry.

Felix B. Schwarz, Thomas Heinrich, Andreas Lippitz, Wolfgang E. S. Unger, and Christoph A. Schalley, *Chem. Commun.* **2016**, Accepted Manuscript.

The design, synthesis and analysis in solution of the photoswitchable Rotaxane, NMR titrations, UV-Vis and contact angle measurements were conducted by the author. Surface experiments were performed together with T. Heinrich. T. Heinrich conducted XPS and NEXAFS measurements together with A. Lippitz. The manuscript was written mainly by the author together with T. Heinrich. All authors contributed to the final version of the manuscript.

on surfaces are reported in the literature.^[12, 13b, 186] However, there are only a few examples for surface-bound photoresponsive MIM-based systems.^[13a, 124, 133]

4.2.2.3. Results and discussion

Recently, we reported the photoinduced pseudorotaxane formation of a photoresponsive axle and a tetralactam macrocycle carried out in solution and on surfaces with immobilised multilayers of macrocycles.^[187] Here, we report a photoswitchable rotaxane, consisting of a tetralactam macrocycle (TLM) and a photoswitchable axle. The axle is comprised of an azobenzene photoswitch and a diketopiperazine binding site, which are both attached to a rigid xanthene backbone in a way that the azobenzene photoisomerisation influences the binding strength of the adjacent site by steric hindrance. By substitution with a suitable linker, this photoswitchable axle was used as the central building block for rotaxanes, serving as photoswitch, first binding site and stopper. The second part of the axle was designed out of a diamide binding site,^[160] which bears a bulky trityl stopper on one end and a linker unit at the other end.

Rotaxanes **Rot7** and **Rot8** were obtained in a one-step ether-rotaxane synthesis out of axle building blocks **38** and **18** and TLM **19** or **39** (Figure 97). Compound **38** was synthesised in one step from azobenzene pseudorotaxane axle **35** described in chapter 4.2.1. Axle building block **18** containing the diamide binding site introduced in chapter 4.1 has proven to be well suited for rotaxane synthesis and is therefore used in here again. Tetralactam macrocycles were synthesised according to literature known procedures.^[26] **Rot7** containing the di-*tert*-butyl substituted TLM **19** was used for all solution studies due to its good solubility, while **Rot8** was used for surface experiments.

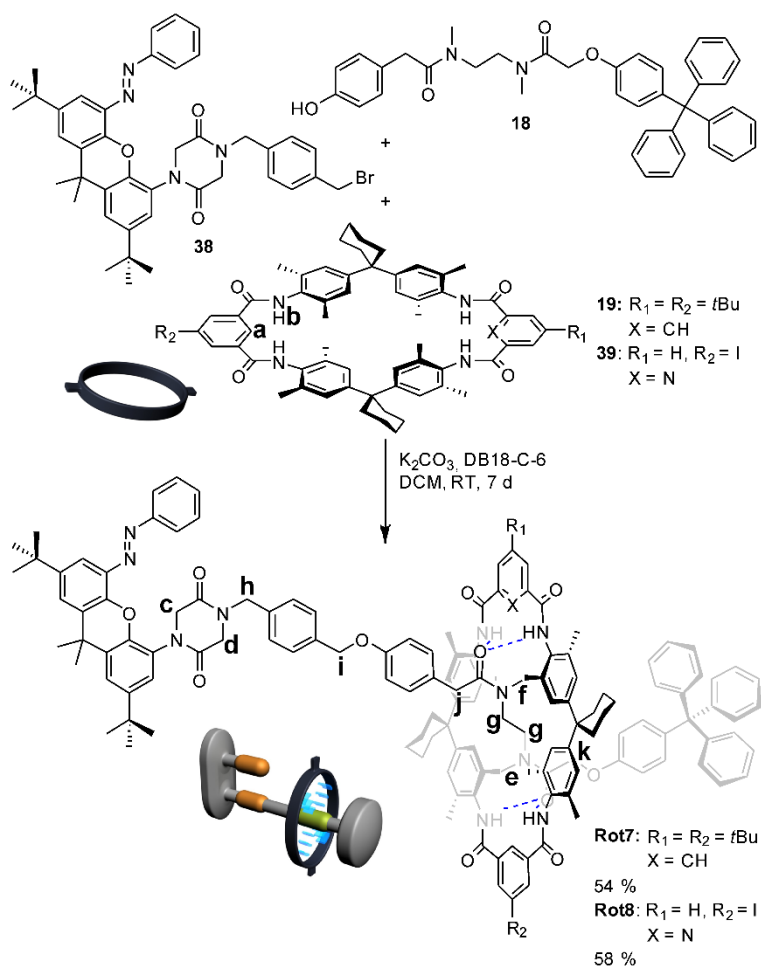


Figure 97: Synthesis of photoswitchable rotaxanes **Rot7** and **Rot8**.

The formation of **Rot7** was followed by 1H NMR spectroscopy (Figure 98). The 1H NMR spectrum of TLM **19** shows the macrocycle inner isophthalic and amide protons **a** and **b** at 7.30 respectively 7.98 ppm, which are shifted downfield by 1.15 and 0.62 ppm in the spectrum of the rotaxane due to hydrogen bonding to the axle. Comparison of the NMR spectra of free axle and rotaxane reveals significant upfield shifts of the diamide methyl and methylene protons **e, f** and **g** of 0.66, 0.75 and 1.56 ppm due to the shielding effect of TLM **19**, while the methylene protons **c** and **g** of the diketopiperazine binding site remain unaffected at 5.01 and 4.11 ppm. The methylene groups **h** and **i** next to the diketopiperazine binding site remain almost unaffected as well, while the methylene groups **j** and **k** adjacent to the diamide binding site are shifted upfield by 0.48 and 0.75 ppm. This is clear evidence for the TLM being located at the diamide and not at the diketopiperazine station.

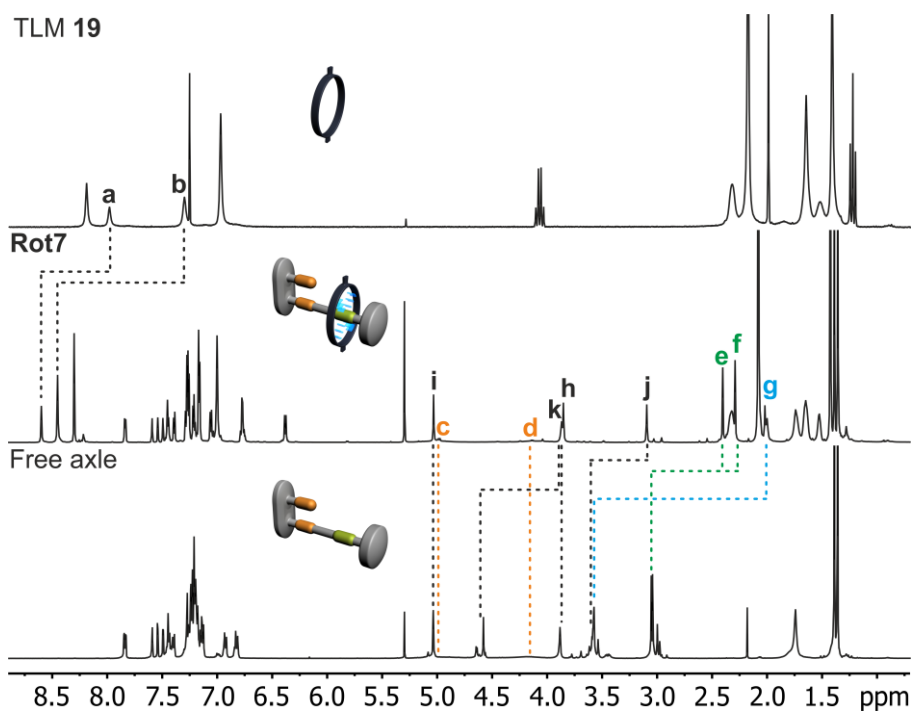


Figure 98: ^1H NMR spectra of TLM 19 (top), Rot7 (middle) and the free axle of the rotaxane (down)

The mechanically interlocked structure of **Rot7** was confirmed by IRMPD ESI-FTICR-MS experiments (Figure 99). The ESI-FTICR MS spectrum shows a peak for the rotaxane dication at m/z 1128, with the isotope pattern being in agreement with the calculated one. IRMPD fragmentation of this ion leads to fragmentation of the axle at the ether bond between the two phenyl rings, yielding two singly charged fragments at m/z 599 and 1658. Fragment 1658 consisting of the macrocycle and part of the axle further dissociates simultaneously (see experimental section for a detailed peak assignment). As no separation of axle and macrocycle without the fragmentation of a bond could be observed, it can be concluded that axle and macrocycle are mechanically interlocked.

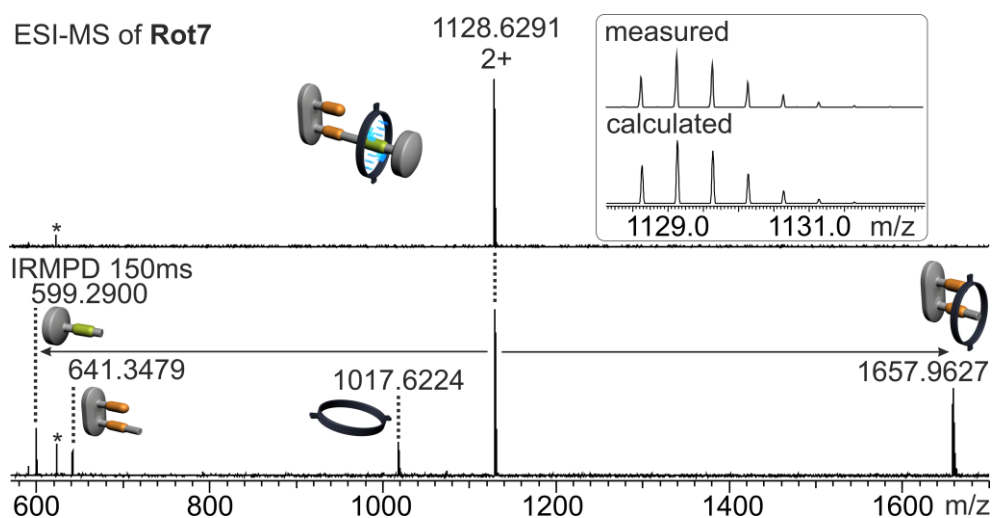


Figure 99: ESI-FTICR MS spectra and IRMPD fragmentation of Rot7.

As a control experiment, ^1H NMR and MS spectra of a 1:1 mixture of the free axle of **Rot7** and TLM **19** have been recorded (Figure 100). The mixture was equilibrated at room temperature over 24h prior to all measurements. The ^1H NMR spectrum of the 1:1 mixture of TLM **19** and the free axle of **Rot7** (black) clearly differs from the spectrum of **Rot7** (orange). The downfield shifts of the macrocycles amide and inner isophthalic protons indicate the formation of side-on complexes. The protons of the diamide binding site are not shifted upfield in the 1:1 mixture, which shows that they are not encapsulated by the macrocycle. The ESI-MS spectrum exhibits signals for the free macrocycle ($m/z = 1017$ $[\text{M}+\text{H}]^+$, 1039 $[\text{M}+\text{Na}]^+$, 1055 $[\text{M}+\text{K}]^+$, 2034 $[\text{2M}+\text{H}]^+$, 2034 $[\text{2M}+\text{Na}]^+$) and the free axle ($m/z = 1239$ $[\text{M}+\text{H}]^+$, 1261 $[\text{M}+\text{Na}]^+$, 1277 $[\text{M}+\text{K}]^+$), while no signals for an 1:1 complex of axle and macrocycle are present. The absence of any side-on complexes is not surprising, as side-on complexes with TLM usually are non-detectable in the gas phase. Both experiments confirm that in a 1:1 mixture of free axle and macrocycle, the macrocycle does not thread the axle.

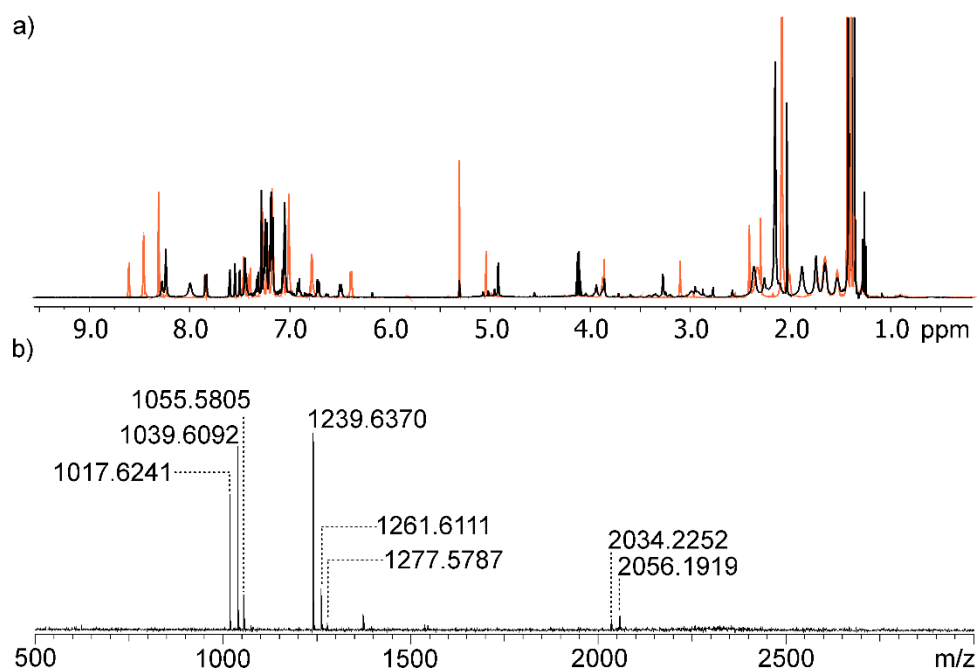


Figure 100: a) ^1H NMR spectra of **Rot7** (orange) and a 1:1 mixture of TLM **19** and the free axle of **Rot7** (black) in CDCl_3 at room temperature and b) ESI-MS spectrum of a 1:1 mixture of TLM **19** and the free axle of **Rot7**.

The photoswitching of **Rot7** was studied in solution by UV-Vis and NMR spectroscopy. Photoisomerisation of the azobenzene group in **Rot7** from *trans* to *cis* was carried out by irradiation with an LED lamp at a wavelength of $\lambda_1 = 365$ nm. Back switching was carried out by irradiation at $\lambda_2 = 470$ nm or thermal equilibration. The UV-Vis spectrum of **Rot7 trans** in CH_2Cl_2 displays a broad absorption band at approximately 520 nm with a characteristic absorption band for the $\pi \rightarrow \pi^*$ transition of azobenzene at 322 nm (Figure 101b).^[58] Irradiation at $\lambda_1 = 365$ nm lead to a decrease in intensity of the $\pi \rightarrow \pi^*$ absorption band, indicating the formation of **Rot7 cis**. Irradiating the sample at $\lambda_2 = 470$ nm induces back switching to

Rot7 *trans* up to approximately 90 %. In both cases, the photostationary state was reached after 10 minutes. Complete back isomerisation to **Rot7** *cis* was accomplished by equilibrating the sample in the dark at 35 °C over two days. Reversibility was investigated by alternating irradiation at $\lambda_1 = 365$ nm and $\lambda_2 = 470$ nm over five cycles (Figure 101c).

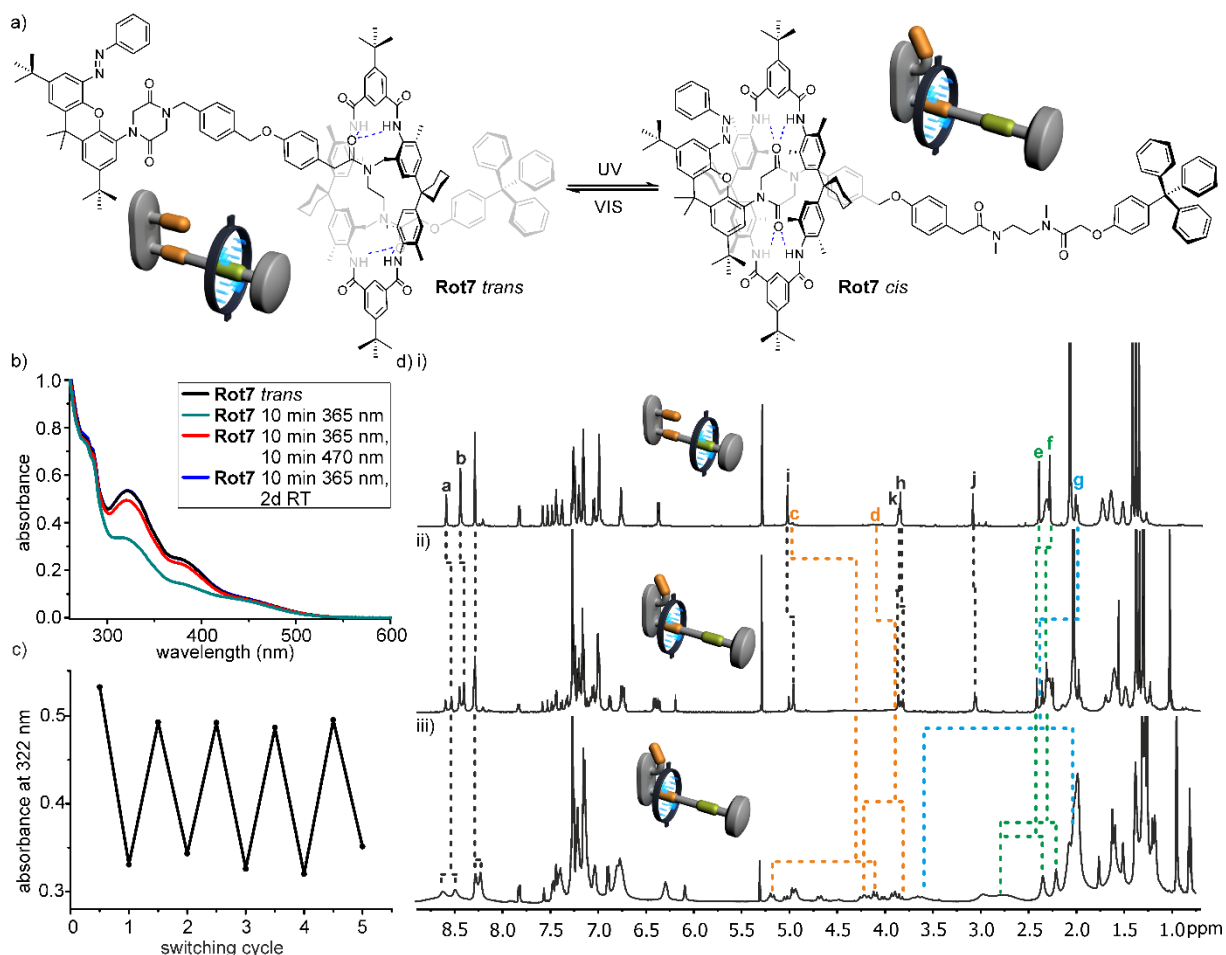


Figure 101: a) Photoswitching of **Rot7**. b) UV-Vis spectra of **Rot7** *trans* in CH_2Cl_2 (black), **Rot7** after 10 min irradiation at $\lambda_1 = 365$ nm (green), **Rot7** after irradiation at $\lambda_1 = 365$ nm and $\lambda_2 = 470$ nm for 10 min each (red), and **Rot7** after 10 min irradiation with 365 nm and subsequent equilibration for 2 d at 30 °C in the dark (blue, overlapping with black spectrum). c) Reversibility of photoswitching of **Rot7** in CH_2Cl_2 tested by alternating irradiation at $\lambda_1 = 365$ nm and $\lambda_2 = 470$ nm for 10 min in each step. d) ^1H NMR spectra **Rot7** *trans* in CDCl_3 at RT (i), *cis:trans* 2:1 at RT (ii) and *cis:trans* 2:1 at 228 K (iii).

^1H NMR spectra of **Rot7** were measured before and after irradiation at $\lambda_1 = 365$ nm for 10 min (Figure 101d, i, ii). In the spectrum after irradiation, a second set of signals for **Rot7** *cis* is observed with a ratio of **Rot7** *cis* : *trans* of approximately 2:1. The protons **a** and **b** of the macrocycle undergo a small shift upfield in **Rot7** *cis* relative to **Rot7** *trans*, indicating a different binding situation. The protons **c** and **d** of the diketopiperazine site are shifted upfield by 0.73 and 0.15 ppm, while the protons **e**, **f** and **g** of the diamide site are shifted downfield by 0.05, 0.06 and 0.42 ppm. This leads to the conclusion that the macrocycle is moving from the diamide towards the diketopiperazine binding site. In comparison with the ^1H NMR spectrum

of the free axle and the shifts observed in a previous binding study with the corresponding pseudorotaxane,^[187] the shifts of the binding site protons **c-g** upon switching of **Rot7** are smaller than expected. This leads to the assumption that the macrocycle undergoes a shuttling motion between the two binding sites which is fast on the NMR time scale and that therefore time-averaged signals are observed in the ¹H NMR spectrum.

The binding constants for both binding sites in **Rot7** were determined by NMR titrations using structurally analogous model compounds containing one binding site each. For the diketopiperazine site, binding constants of $1,650 \pm 170 \text{ M}^{-1}$ when the azobenzene is in *cis* configuration and $<15 \text{ M}^{-1}$ when the azobenzene is in *trans* configuration were obtained.^[187] For the diamide site, a binding constant of $1,400 \pm 140 \text{ M}^{-1}$ was obtained (experimental section). Although the diketopiperazine represents the favoured binding site, the small difference in binding energy will rather lead to a molecular shuttle than to a rotaxane-switch with two distinct positions of the macrocycle.

Temperature-dependent NMR spectra in a range between 300 K and 228 K have been recorded to investigate the shuttling of **Rot7** *cis* (see experimental section for the full set of spectra). The spectrum at 228 K (Figure 101d, iii) shows split or broadened signals, thus indicating a shuttling motion which is slow on the ¹H NMR timescale. Upon cooling the sample, the peak for the macrocycle protons **a** at 8.52 ppm in the ¹H NMR spectra gets broadened, undergoes coalescence at approx. 243 K and splits up upon further cooling into two signals at 8.63 and 8.50 ppm. At 228 K, the protons **c** and **d** for the diketopiperazine site split into two sets of signals at 5.20 and 4.12 ppm for **c** respectively 4.24 and 3.87 ppm for **d**. The signals for the protons **e**, **f**, and **g** for the diamide site split as well into signals at 2.93 and 2.86 ppm for **e**, 2.25 and 2.86 ppm for **f** and 2.11 and 3.59 ppm for **g**. This implies that three different species are present: **Rot7** *trans* with the macrocycle being located at the diamide site, **Rot7** *cis* with the macrocycle being located at the diketopiperazine site and **Rot7** *cis* with the macrocycle at the diamide site. Integration of the signals in the NMR spectrum at 228 K yields an overall ratio of **Rot7** with the macrocycle at the diketopiperazine site to **Rot7** with the macrocycle at the diamide site of approximately 1:3. Due to the very complex spectra and broad signals, a more detailed analysis of the shuttling behavior was not straightforward.

After the rotaxane switching was investigated in solution, the concept was transferred to surfaces by following previously established procedures for surface deposition.^[15c] To deposit a monolayer of rotaxanes on a surface, two different methods were applied: layer-by-layer self-assembly^[113a, 113c, 113e, 113f] using metal-ion/pyridine/terpyridine coordination chemistry^[113h, 113j] and covalent anchoring by click chemistry. Cleaned glass slides have been used as the substrates for UV surface experiments and contact angle measurements, while silicon substrates were used for XPS and NEXAFS experiments.

Rot9 functionalised with a terpyridine unit at the TLM was synthesised in one step starting from **Rot8** in a Sonogashira coupling reaction with acetylene functionalised terpyridine **23**. The alkyne functionalised **Rot10** was prepared likewise by Sonogashira reaction of **Rot8** with trimethylsilylacetylene **40** followed by deprotection of the alkyne group (Figure 102). Terpyridine **23** was prepared according to literature known procedures.^[188]

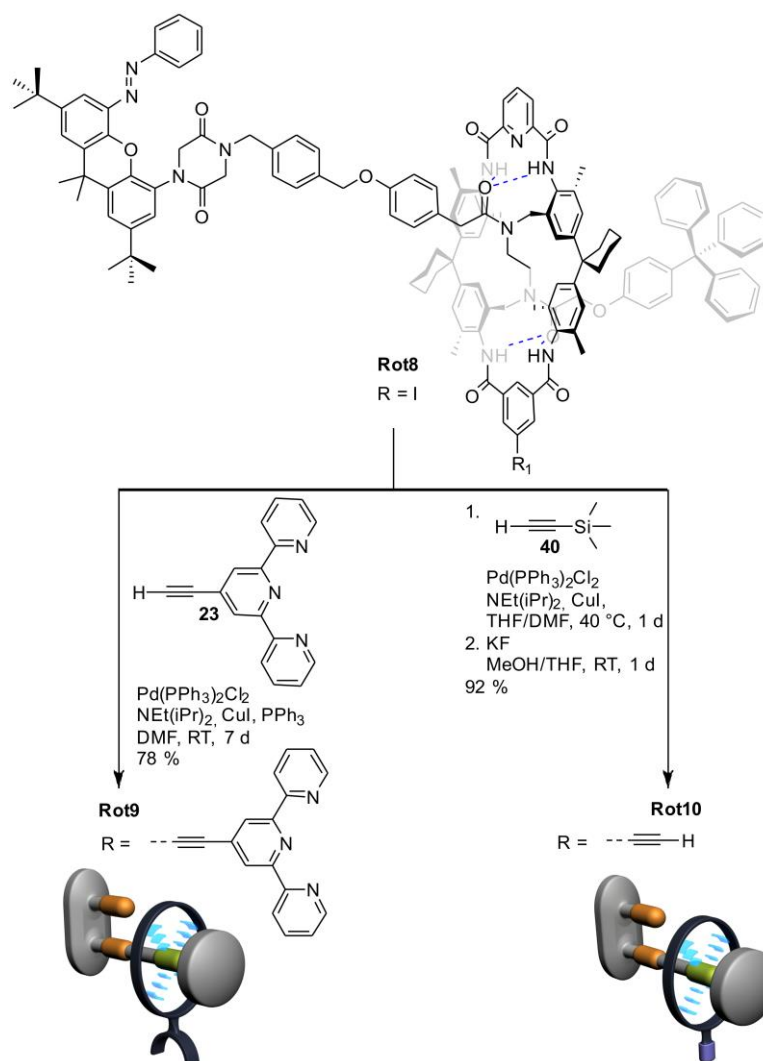


Figure 102: Synthesis of **Rot9** and **Rot10**.

For deposition of **Rot9**, a self-assembled monolayer of **PDS** was deposited on the surface by immersing the substrate in a 5 mM solution of **PDS**. The surfaces were then treated with a 1 mM solution of tetrakis(acetonitrile)palladium(II) tetrafluoroborate to coordinate the pyridyl endgroups of **PDS** with palladium(II) ions, followed by immersion in a 1 mM solution of **Rot9** to create a monolayer of rotaxanes on the surface (Figure 103a, top). To deposit **Rot10**, glass surfaces were functionalised with a self-assembled monolayer of **AUS** by immersing the substrate in a 5mM solution of **AUS**. Immersing these surfaces in a 1mM solution of **Rot10** in

the presence of a catalytic amount of catalyst **41**, **Rot10** was covalently attached to the SAM in an azide-alkyne click-reaction (Figure 103a, bottom).

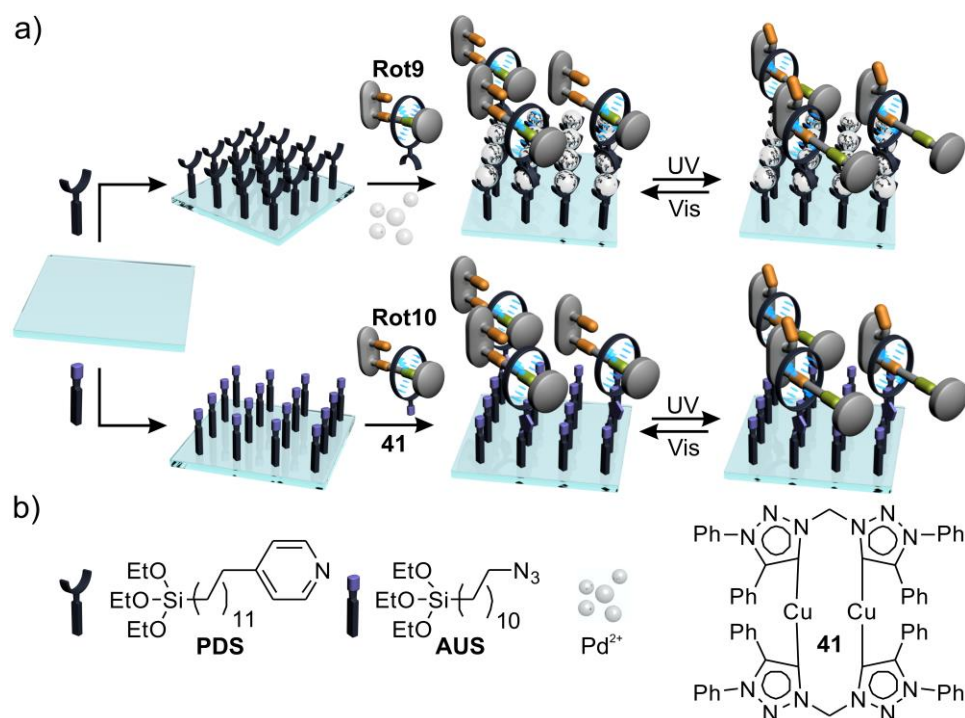


Figure 103: Schematic representation of surface deposition of **Rot9** (top) and **Rot10** (bottom) and on-surface photoswitching and b) materials used for surface experiments.

The deposition of **Rot9** and **Rot10** was followed by UV-Vis spectroscopy (Figure 104). As the glass slides absorb light below 300 nm, only the region above could be taken into account. The spectra of the surface with a **PDS**- respectively **AUS**-SAM were used as background and thus subtracted from all spectra. For both rotaxanes, a substantial increase in absorbance was detected after deposition, which resembles to the UV-Vis spectra of **Rot7** in solution and therefore indicates a successful monolayer formation. The stronger absorbance for the surface functionalised with **Rot9** in comparison to the surface with **Rot10** leads to the conclusion that a larger amount of **Rot9** than **Rot10** was deposited and thus the monolayer is packed more densely.

To investigate on-surface switching, surfaces functionalised with a monolayer of rotaxanes were irradiated with an LED-lamp at a wavelength of $\lambda_1 = 365$ nm or $\lambda_2 = 470$ nm from a distance of about 20 cm. Different irradiation times were investigated and it was found that in case of $\lambda_1 = 365$ nm, no further changes in the absorbance spectra occurred after an irradiation time of 1 h, while it took 1.5 h in case of $\lambda_2 = 470$ nm. After irradiation at $\lambda_1 = 365$ nm, the UV-Vis spectra of both type of surfaces showed a decrease in absorbance in the region between 300 and 500 nm, indicating the formation of **Rot9 cis** and **Rot10 cis**, respectively. After irradiation at $\lambda_2 = 470$ nm, the absorbance of both surfaces increased up to about 90 % of its

initial value, indicating almost complete back-switching to the *trans* configurations of **Rot9** and **Rot10**. The reversibility of the on-surface photoswitching was tested over five consecutive switching cycles for both types of monolayers.

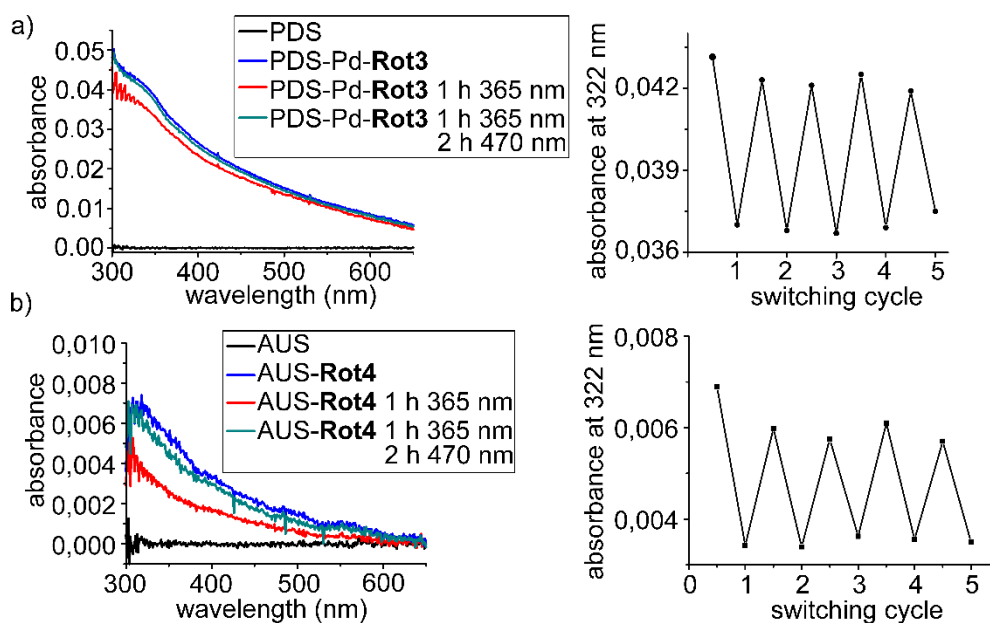


Figure 104: Transmission UV-Vis spectra of surfaces functionalised with a monolayer of a) **Rot9** and b) **Rot10** and the reversibility of the on-surface photoswitching tested over five cycles.

Contact angle measurements were conducted for a **PDS-Pd-Rot9** monolayer on a glass surface over five consecutive switching cycles (Figure 105). In each switching cycle, the monolayer was irradiated at $\lambda_1 = 365$ nm for 1 h and subsequently at $\lambda_2 = 470$ nm for 1.5 h. The experiments were repeated for every measurement point on two surfaces with three measurement spots on each surface. Averaged values of all measurements are reported. An error of 1° for inaccurate reading, differences in volume of the droplet and the measurement time is assumed. The contact angles display a strong and reversible change in polarity upon photoswitching of the rotaxane monolayer.

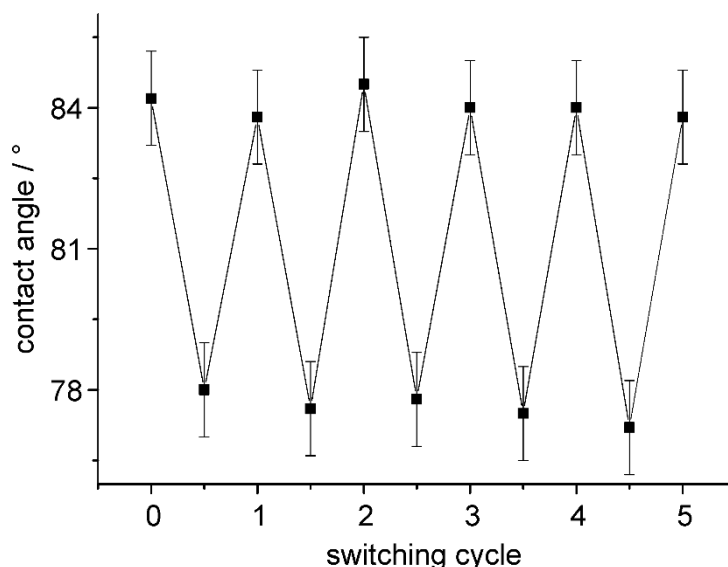


Figure 105: Contact angle measurements following the on-surface switching of a **PST-Rot9** monolayer over five consecutive switching cycles.

XP spectra have been measured on silicon surfaces functionalised with **PDS-Pd-Rot9** and **AUS-Rot10**, respectively (Figure 106). The C 1s core level spectra exhibits the expected signals for amide (~288 eV), nitrogen-bound (~287 eV), aliphatic (~285 eV) and aromatic (284.5 eV) carbon.^[15d] In the N 1s core level spectra of the **Rot9** monolayer, the component at 400.9 eV can be assigned to complexed pyridine and terpyridine nitrogen. Non-complexed (ter-)pyridine and amide nitrogen atoms give rise to a signal around 399.8 eV, which is overlapping with the adjacent peaks.^[15a, 179] The nitrogen atoms of azobenzene give rise to peaks around 399.5 – 400.1 eV.^[180] The amide nitrogen atoms of the diketopiperazine exhibit a signal around 400.0 eV.^[181] The triazol and amine nitrogen atoms in the **Rot10** monolayer contribute to the peak at 398.8 eV.^[15d]

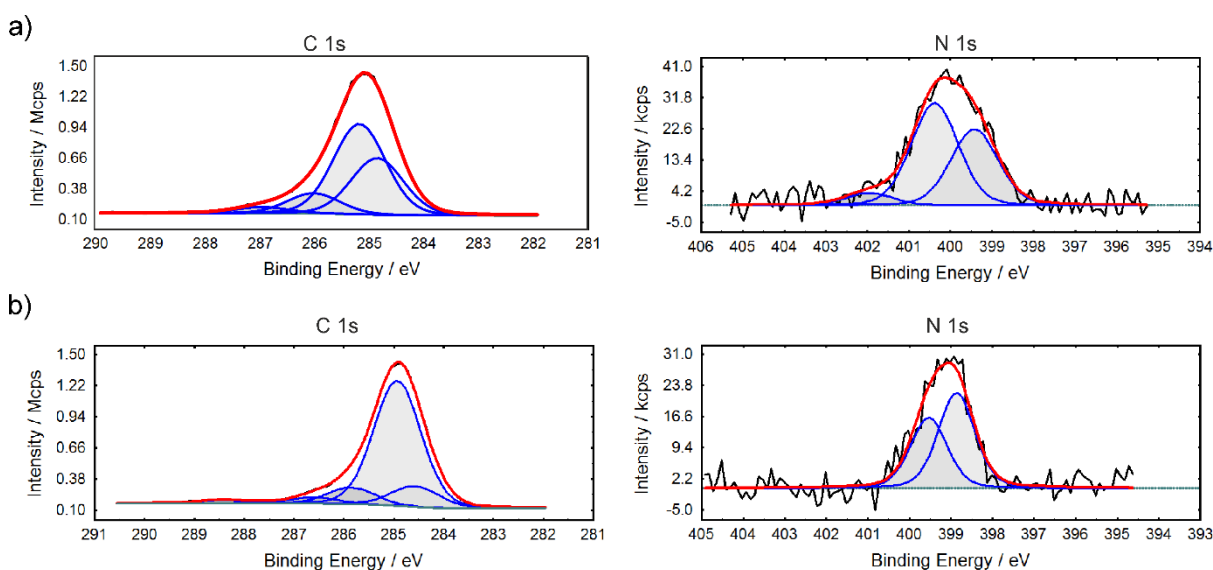


Figure 106: C 1s and N 1s core level XP spectra of a monolayer of a) **Rot9** and b) **Rot10**.

In order to estimate the amount of rotaxanes relative to the SAM deposited on the surfaces, peak fitting of the C 1s XP spectra was conducted for the two different monolayers. Theoretical peak areas for aromatic and aliphatic carbon atoms were calculated for different ratios of the rotaxane to the underlying monolayer. The best fit was obtained at a 1:15 ratio for **Rot9** and a 1:45 ratio for **Rot10**. The approximately three times higher value for the packing density of **Rot9** compared to **Rot10** is well in line with the surface UV-Vis spectra, where higher absorbances for the **Rot9** monolayer were obtained.

Table 4. Summary of the C 1s peak fits.

binding energy / eV	assigned atom	PDS-Pd-Rot9		AUS-Rot10	
		theor. Value (calc. for 1:15)	rel. peak area (exp.)	theor. Value (calc. for 1:45)	rel. peak area (exp.)
284.7	C _{sp2}	32	32	12	12
285.1	-CH ₂ -	50	52	70	73
286	CH ₂ -N, C _{sp2} -N	15	12	15	10
287	CNO	3	4	3	5

To prove successful rotaxane deposition and the structural effects of the rotaxane switching as well, angle-resolved C K-edge NEXAFS spectroscopy was conducted for the pristine rotaxane monolayer of **Rot9** on silicon, the monolayer after 1 h irradiation with $\lambda_1 = 365$ nm, and after 1 h light irradiation with $\lambda_1 = 365$ nm with subsequent 1.5 h irradiation at $\lambda_2 = 470$ nm as seen in Figure 4. In the 55° C-K edge spectrum of the pristine rotaxane layer, the characteristic π^* resonance-splitting for pyridines and benzene is visible.²⁷ Furthermore, the peak at 285.4 eV is significantly more intense than the peak at 284.9 eV. Together with the intense π^* resonance in the N-K edge spectrum (see experimental section) at 399.4 eV, which is characteristic for Pd-coordinated pyridine,^[139] a shoulder at 398.6 eV ($\pi^*_{\text{O=C-N}}$) characteristic for the axle molecule,^[187] and XPS data (see experimental section) this clearly indicates the successful deposition of the rotaxane. The pristine monolayer of **Rot9 trans** shows a relatively small linear dichroism for the C K-edge π^* and σ^* resonances when compared to the earlier examples,^[15d] but it is clearly visible. Irradiation with light at $\lambda_1 = 365$ nm results in a decrease of the linear dichroism in the C K-edge which is regained upon subsequent irradiation with $\lambda_2 = 470$ nm. In context of the solution study and the fact that the position of the macrocycle is fixed in **Rot9 trans**, but variable in **Rot9 cis**, a higher order in the monolayer when the rotaxane is switched to its *trans*-state can be assumed. The relatively small magnitude of the linear dichroism effect might be due to a rather sparse packing in the monolayer resulting in lower

preferential orientation of the immobilised molecules. Due to the exclusively photo-induced modification of the rotaxane states, the observed differences in linear dichroism can be associated with the switching states of **Rot9**.

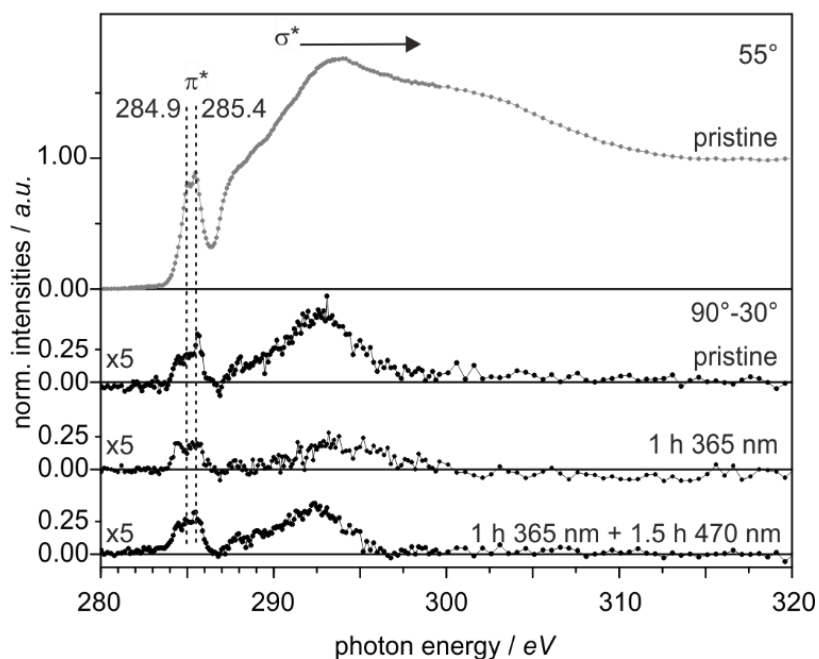


Figure **107**: 55° C K-edge NEXAFS spectrum of the pristine rotaxane monolayer and its 90°-30° difference spectrum. Difference spectra after 1 h irradiation with $\lambda = 365$ nm, and after 1 h irradiation with $\lambda = 365$ nm followed by 1.5 h irradiation with $\lambda = 470$ nm (peak assignments are given in eV).

4.2.2.4. Conclusions

In the present study, we developed a photoswitchable rotaxane and analysed its switching behavior in solution as well as in a monolayer of rotaxane molecules deposited on glass and silicon surfaces. NEXAFS spectroscopy revealed a preferential orientation in the monolayer, which reversibly changes upon photo switching of the rotaxane. In combination with chemically switchable rotaxanes we are aiming for multi-stimuli responsive surface systems capable of performing concerted switching of distinct layers resulting in potential macroscopic effects.

5. Stimuli responsive dynamic combinatorial libraries

5.1. Catenation and encapsulation induce distinct reconstitutions within a dynamic library of mixed-ligand Zn_4L_6 cages[†]

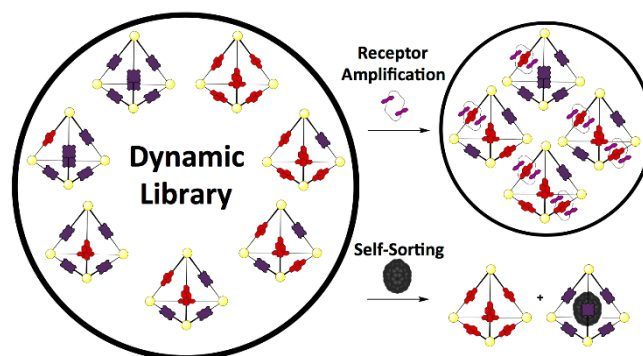


Figure 108: Graphical abstract.

5.1.1. Abstract

Two new Zn_4L_6 cages composed of diamine subcomponents containing either naphthalene diimide (NDI) or porphyrin moieties are described. Their structural differences allow these cages to exhibit distinct interactions with different chemical stimuli, yielding different supramolecular products. The electron-poor NDIs of the first cage were observed to thread through electron-rich aromatic crown ether macrocycles, forming mechanically interlocked species up to a [3]catenane, whereas the porphyrin ligands of the second cage interacted favourably with C_{70} , causing it to be bound as a guest. When mixed, the two cages were observed to form a dynamic combinatorial library (DCL) of seven constitutionally distinct mixed-ligand Zn_4L_6 cages. The DCL was observed to reconstitute in opposing ways when

[†] Parts of this chapter have been published and are reproduced in here with the kind permission The Royal Society of Chemistry.

S. P. Black, D. M. Wood, F. B. Schwarz, T. K. Ronson, J. J. Holstein, A. R. Stefankiewicz, C. A. Schalley, J. K. M. Sanders, J. R. Nitschke, *Chem. Sci.* **2016**, 7, 2614-2620.

The study on a dynamic library of mixed-ligand Zn_4L_6 cages was conducted in cooperation with the group of Prof. Jonathan Nitschke from the University of Cambridge. The synthesis of cages, NMR studies and crystal structure analysis has been done by the Nitschke and Sanders group. All mass spectrometric studies including sample preparation and processing of the results were conducted by the author. All authors contributed to the final version of the manuscript.

treated with either the crown ether or C₇₀: the electron-rich macrocycle templated the formation of heteroleptic catenanes, whereas C₇₀ caused the DCL to self-sort into homoleptic structures.

5.1.2. Introduction

Living systems respond in complex ways to different stimuli. The study of synthetic chemical systems that reconstitute and respond to different stimuli can offer insight into the signalling events that underpin biological systems,^[189] as well as identifying new means to synthesise useful stimuli-responsive systems^[190] and materials.^[191]

One approach to investigating stimuli-responsive behaviour is to design dynamic combinatorial libraries (DCLs)^[192] of molecules that exchange components under thermodynamic control, and thus are inherently responsive to changes in physical conditions and the addition of different stimuli.^[193] This approach has been used to identify protein inhibitors,^[194] design mixtures of compounds that self-sort into different host-guest complexes^[195] and to engineer separations of mixtures of molecules held together by dynamic covalent bonds.^[196] In some cases, the response of a DCL to a stimulus has led, through reconstitution of the system, to the promotion of library members that may otherwise not be observed.^[197]

As part of our investigations into stimuli responsive systems, we sought to design an adaptive library of different metallo-supramolecular cages that could respond to templates that are either bound inside the central cavity of a cage,^[198] or interact specifically with the edges of an assembly (i.e. catenation).^[199] To this end, it was necessary to design a library comprised of M₄L₆ cages containing two different kinds of diamine subcomponent, each of which engendered a response to a distinct kind of stimulus. It was also essential that the different ligands in such a library possess near-identical lengths to prevent sterically-driven self-sorting behaviour.^[200]

The DCL is based upon two similarly-sized Zn₄L₆ tetrahedral cages, built using ligands that contain naphthalene diimide (NDI) or Zn-porphyrin moieties, respectively. Combining these cages in solution yielded a DCL of seven different Zn₄L₆ cages, differing in their NDI:porphyrin ligand ratio. By utilizing different molecular recognition events, either the threading of the NDI components through a crown ether, or the encapsulation of the fullerene C₇₀, we explored the responsive nature of this DCL. The formation of either homoleptic or heteroleptic M₄L₆ structures was favoured, depending on the chemical stimulus that was employed. Our study thus represents a singular example of a multi-stimuli-responsive DCL of three-dimensional metallo-supramolecular assemblies. The challenge of analysing and characterizing the members of this complex DCL was met by employing Electrospray Ion Cyclotron Mass Spectrometry (ESI-FTICR MS).^[201]

5.1.3. Results and Discussion

NDI cage **N**₆ was synthesised through the subcomponent self-assembly^[202] of NDI-containing diamine **42** (6 equiv), 2-formylpyridine (12 equiv) and zinc triflimide (Zn(NTf₂)₂, 4 equiv) in MeCN (Figure 109). In similar fashion, Zn-porphyrin cage **P**₆ was prepared using Zn-porphyrin diamine **43** (6 equiv), 2-formylpyridine (12 equiv) and zinc triflimide (4 equiv) in MeCN:CHCl₃ (7:3). Both assemblies consisted of Zn₄L₆ tetrahedra, with the bis(imine) condensation products of 2-formylpyridine and the respective diamine acting as bis-bidentate ligands linking adjacent metal centres.

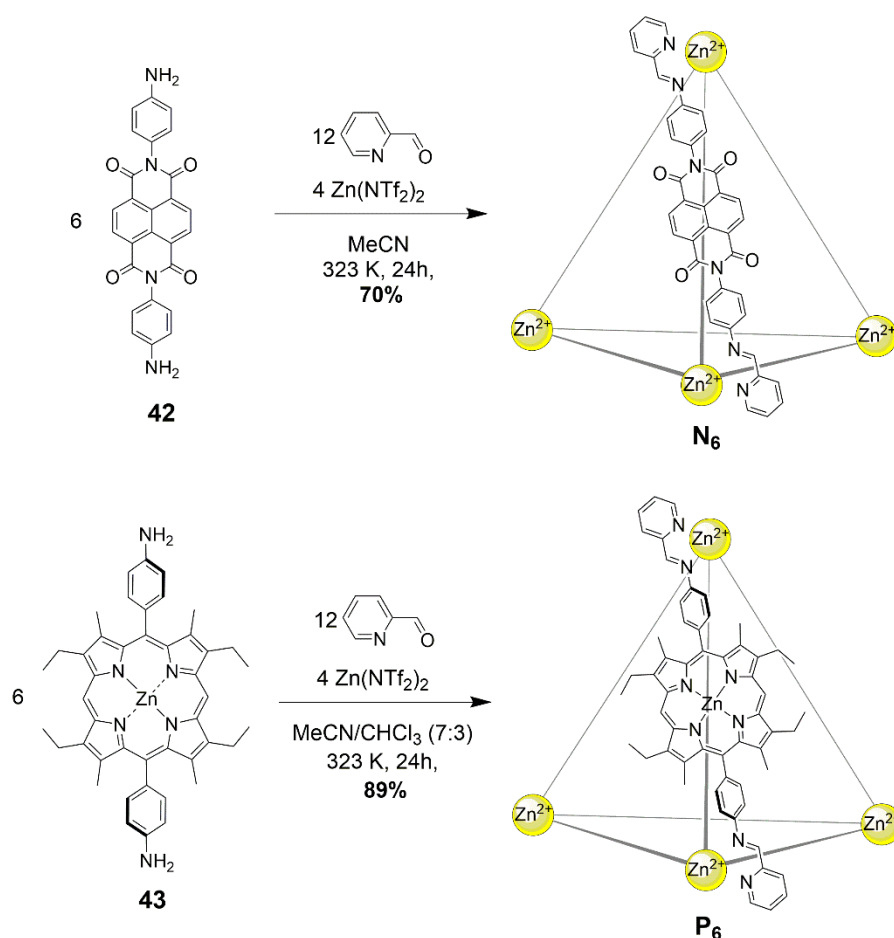


Figure 109 Synthesis of the Zn₄L₆ cages **N**₆ (top) from NDI-containing diamine **42**, and **P**₆ (bottom) from Zn porphyrin containing diamine **43**.

Cages **N**₆ and **P**₆ were characterised in solution using NMR spectroscopy and ESI-FTICR MS. In both cases, ¹H NMR spectra showed multiple resonances for each proton environment, consistent with the presence of the three possible diastereomers of tetrahedral Zn₄L₆ assemblies: homochiral *T*($\Delta\Delta\Delta\Delta/\Lambda\Lambda\Lambda\Lambda$), heterochiral *C*₃($\Delta\Delta\Delta\Lambda/\Lambda\Lambda\Lambda\Delta$), and achiral *S*₄($\Lambda\Lambda\Delta\Delta$).^[203] Analysis of the integrated signal intensities of the ¹H NMR spectrum of **P**₆ indicated a diastereomer distribution of 32 : 48 : 20 (*T* : *C*₃ : *S*₄) at 298 K (see experimental

section). The diastereomer distribution of **N**₆ could not be determined from its ¹H NMR spectrum (see experimental section) due to the greater degree of signal overlap.

The structures of **N**₆ and **P**₆ were confirmed in the solid state by single-crystal X-ray analysis (Figure 110). Crystals of **N**₆ were obtained by vapour diffusion of diethyl ether into a solution of **N**₆ in MeCN containing excess KPF₆ (10 equiv). The crystals were found to contain only the *S*₄-symmetric diastereomer. Of the six ligands that bridge the four octahedral zinc centres, four thus displayed a *syn*-conformation, bridging zinc centres of opposing handedness, and two adopted an *anti*-conformation, linking zinc centres of identical handedness. The metal-metal separations are 20.6-20.8 Å and 21.0 Å for the *syn*- and *anti*- ligands respectively.

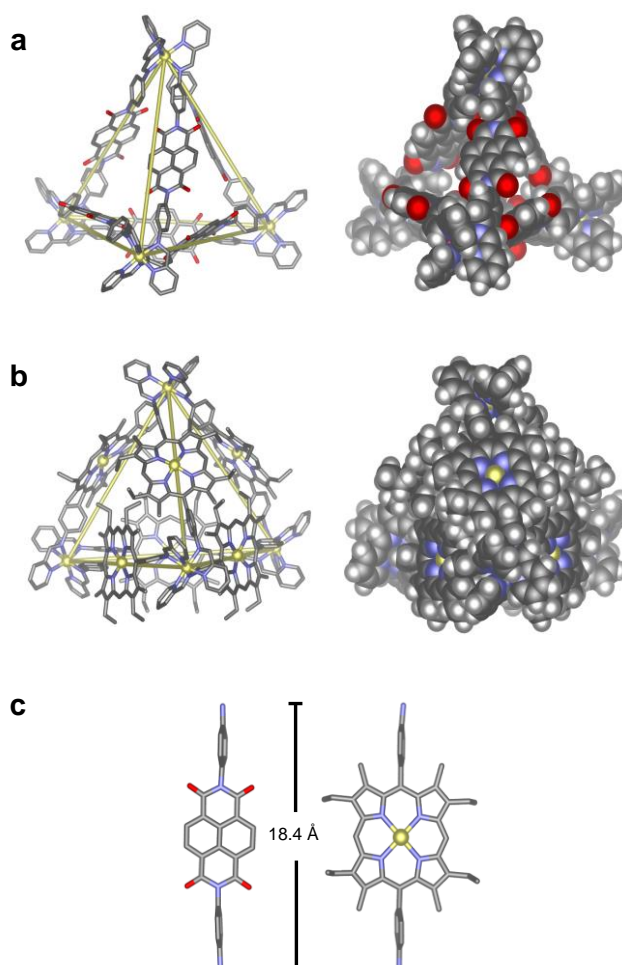


Figure 110: Crystal structures of Zn₄L₆ tetrahedra a) **N**₆ and b) **P**₆. Yellow lines connect Zn^{II} centres to highlight the tetrahedral frameworks. c) Comparison of the two diamine residues, highlighting their similar lengths. Hydrogen atoms, disorder, solvent molecules and anions are omitted for clarity. Zn = yellow, C = grey, H = white, N = blue, O = red.

Suitable crystals of **P**₆ were obtained through vapour diffusion of diethyl ether into a solution of its triflate salt in MeCN. In this case, only the *T*-symmetric diastereomer was observed, with both enantiomers ($\Delta\Delta\Delta\Delta/\Lambda\Lambda\Lambda\Lambda$) present in the unit cell. The metal-metal separations range from 20.7 – 21.4 Å, similar to those observed for **N**₆. Axial water ligands were observed to bind

to three porphyrin-Zn^{II} centres, with all three water ligands directed inside the tetrahedral cage (see experimental section). The remaining three porphyrin-Zn^{II} axial ligands were MeCN molecules that point outwards from the edges of the tetrahedron. Three of the faces of the Zn₄L₆ tetrahedron are almost completely enclosed by the Zn-porphyrin ligands that define the edges of the assembly. The remaining face is more open due to crystal packing effects, where a corner of each tetrahedron is observed to protrude slightly into the face of another.

Based upon the known affinity of electron-poor NDI moieties for the electron-rich macrocycle bis-1,5-(dinaphtho)-38-crown-10 (**C**),^[204] we anticipated that the NDI edges of cage **N**₆ would thread through **C** to yield a library of catenated cages. An excess of **C** (10 equiv) was thus added to a CD₃CN/CDCl₃ (1:1) solution of **N**₆, and the mixture left to equilibrate at 298 K for 24h. The resultant ¹H NMR spectrum showed the presence of new resonances consistent with **C** threaded around the NDI groups of **N**₆ (see experimental section), and the ESI-FTICR mass spectrum exhibited signals consistent with **N**₆ associated with up to four molecules of **C** (Figure 111b). In our previously studied system based on a larger NDI-edged tetrahedron, adducts of the cage with up to 12 molecules of **C** were detected by ESI-FTICR MS. However, infrared multiphoton dissociation (IRMPD) tandem MS analysis demonstrated that the higher adducts were the result of non-specific interactions in the gas phase.^[204]

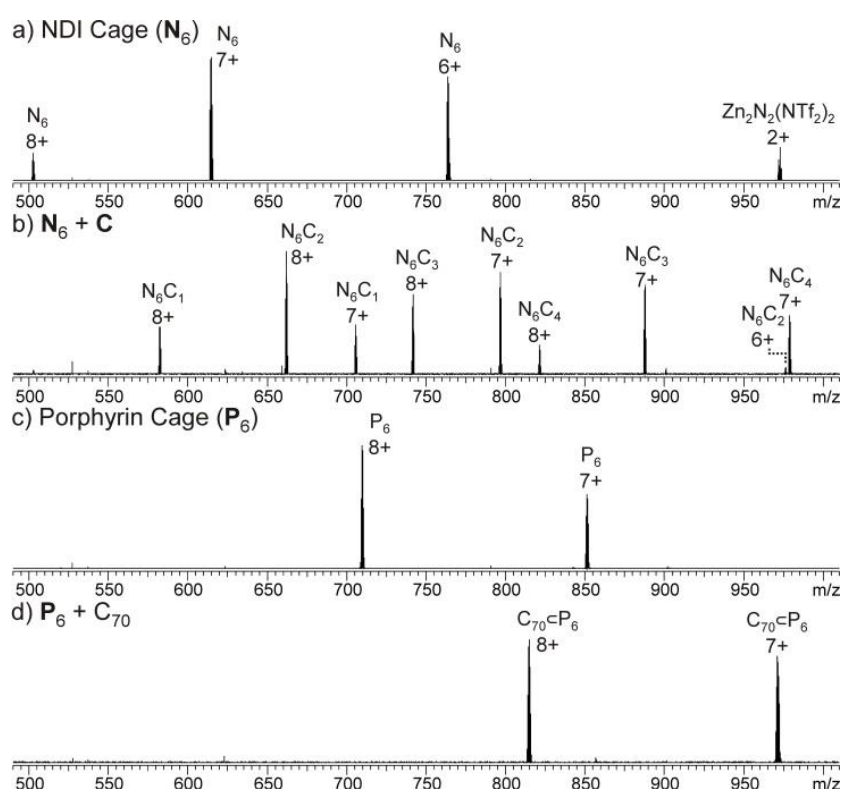


Figure 111: ESI-MS spectra of a) Zn₄L₆ NDI cage **N**₆, b) **N**₆ + **C** (4 equiv), yielding **N**₆C₂, c) Zn₄L₆ Porphyrin cage **P**₆ and d) **P**₆ + **C**₇₀ (5 equiv), yielding **C**₇₀-**P**₆.

Using a similar approach, the number of catenations per cage between **N₆** and **C** was investigated by IRMPD analysis, in which mass-selected parent ions were irradiated with a CO₂ laser to induce fragmentation (Figure 112). The [Zn₄**N₆C**(NTf₂)]⁷⁺ and [Zn₄**N₆C₂**(NTf₂)]⁷⁺ ions both underwent symmetrical fragmentation into 'half-cage' species [Zn₂**N₃**]⁴⁺ and [Zn₂**N₃C**]⁴⁺, which further decomposed into smaller fragments (e.g. [ZnN]²⁺ and [ZnNC]²⁺, Figure 4a-d). When [Zn₄**N₆C₃**(NTf₂)]⁷⁺ was isolated and irradiated, [Zn₄**N₆C₂**(NTf₂)]⁷⁺ (the product of the non-cage-destructive loss of C), [Zn₂**N₃**]⁴⁺ and [Zn₂**N₃C**]⁴⁺ were observed (Figure 112e-f).

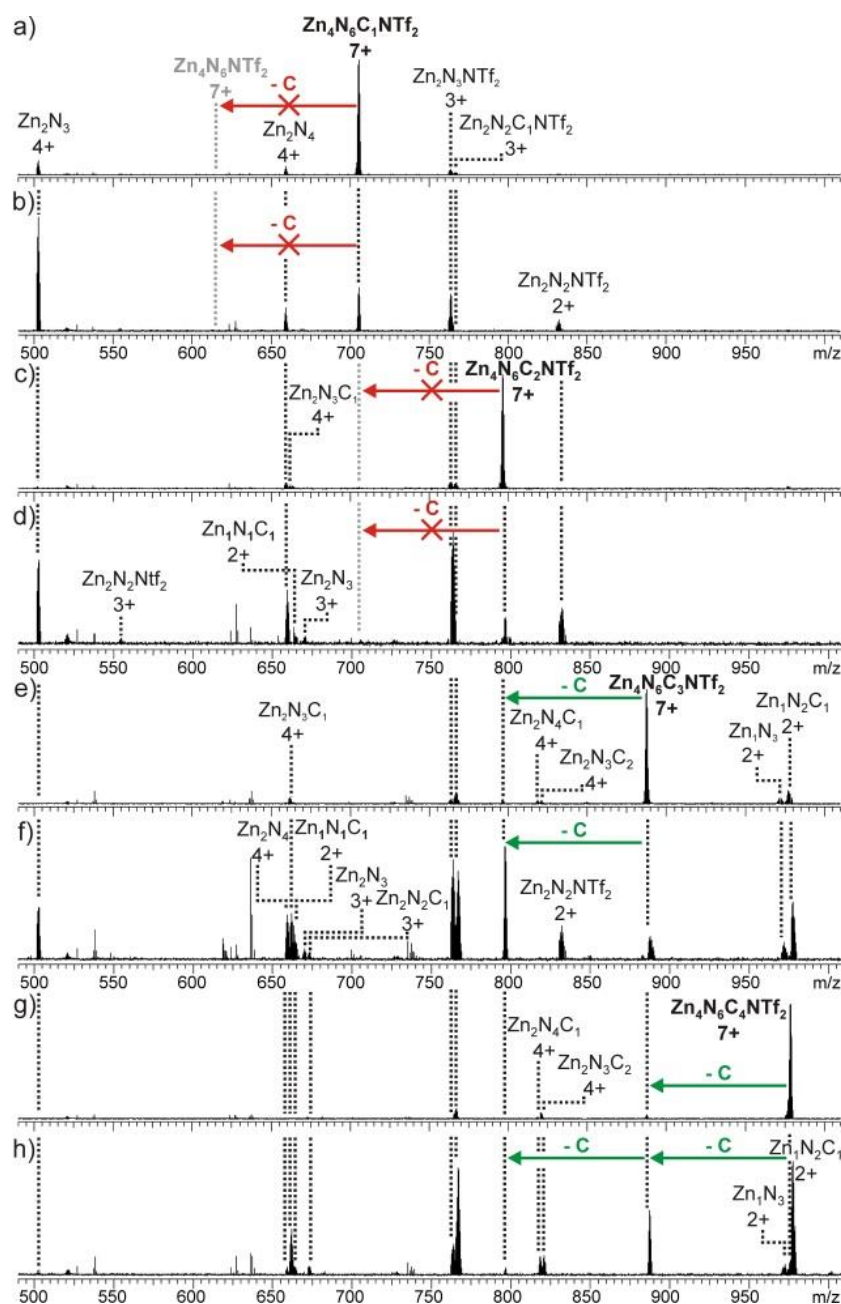


Figure 112: IRMPD ESI-MS spectra of [**N₆C₁₋₄**NTf₂]⁷⁺ ions. a) **N₆C₁**, 30% laser intensity b) **N₆C₁**, 70% c) **N₆C₂**, 30% d) **N₆C₂**, 50% e) **N₆C₃**, 25% f) **N₆C₃**, 35% g) **N₆C₄**, 20% h) **N₆C₄**, 28%.

Furthermore, the non-symmetric $[\text{Zn}_2\text{N}_3\text{C}_2]^{4+}$ fragment was not detected, indicating that the $[\text{Zn}_4\text{N}_6\text{C}_3(\text{NTf}_2)]^{7+}$ ion present in the ESI-FTICR mass spectrum does not correspond to a [4]catenane, but results from the non-specific gas-phase interactions between N_6C_2 and C . Similar conclusions can be drawn from the fragmentation of the $[\text{Zn}_4\text{N}_6\text{C}_4(\text{NTf}_2)]^{7+}$ ion, which shows successive loss of two molecules of C without destruction of the cage framework (Figure 112g-h).

The inhibition of further catenation once two equivalents of C have been threaded onto the N_6 framework contrasts with the statistical non-cooperative binding behaviour observed between C and our previously reported larger NDI-containing tetrahedron. In the larger system, a [7]catenane was obtained, in which up to six molecules of C were threaded onto a tetrahedral framework. The more limited catenation propensity of N_6 appears to arise from its smaller overall size, leading to a sterically-controlled, inhibitive binding process.^[205] We postulate that the degree of catenation is limited to two crown ethers, because the binding of a third molecule would require two macrocycles to thread around adjacent NDI ligands, generating steric strain within the resulting assembly.

C_{70} was identified as a potential guest molecule for both N_6 and P_6 due to their large internal cavities and the potential for π -interactions between C_{70} and the ligands of the hosts.^[206] C_{70} (5 equiv) was thus added to an MeCN solution of either N_6 or P_6 and the mixtures were heated to 323 K for 24 h. Analysis of the mixture of N_6 and C_{70} provided no evidence for host-guest interaction by either ^1H NMR or ESI-MS (Figure 113b). We infer that the large pores in the faces of N_6 provide limited screening of C_{70} from the bulk solvent; an inner phase is thus not differentiated, in contrast with more enclosed NDI-containing assemblies that have been shown to bind fullerenes.^[206a] In contrast, NMR analysis of P_6 after the addition of C_{70} provided clear evidence of guest binding (see experimental section).

The ^{13}C NMR spectrum of the solution showed resonances consistent with the presence of C_{70} , despite its limited solubility in MeCN. ESI-MS of the solution also showed signals corresponding to the C_{70} adduct of P_6 (Figure 111d). We infer from these observations that C_{70} is encapsulated within the cavity of P_6 (Figure 114). The behaviour of P_6 contrasted with the analogous porphyrinato- Ni^{II} assembly, which was found to rearrange into new architectures in the presence of C_{70} .^[207] We attribute this differing behaviour to the planar conformation adopted by Zn-porphyrin **2** (as observed in its crystal structure, Figure 110c), whereas the Ni-porphyrin congener adopts a saddled conformation.

Treatment of a solution of P_6 with excess C resulted in adducts of P_6 with up to four molecules of crown ether, which has been followed with ESI-MS (Figure 113a). As the size of the porphyrin ligand prevents threading of C as shown with ^1H NMR studies, these adducts are the result of non-specific interactions in the gas phase.

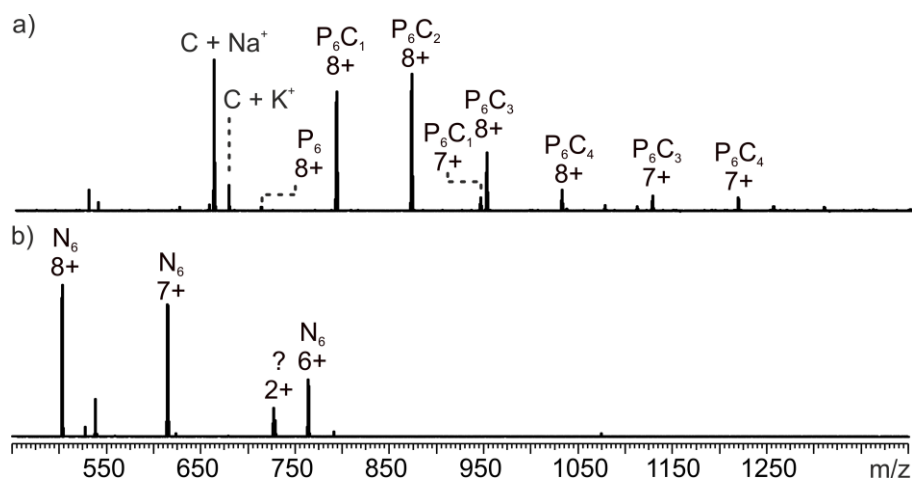


Figure 113: ESI-FTICR-MS spectra of a) $P_6 + C$ (10 equiv) and b) $N_6 + C_{70}$ (5 equiv).

Having established the responses of N_6 and P_6 to the chemical stimuli of crown C and fullerene C_{70} (Figure 114), the responses of a mixed-ligand DCL of tetrahedra were investigated. Separate solutions of pre-formed N_6 and P_6 ($CD_3CN/CDCl_3$, 1:1, 1.0 mM) were mixed in a 1:1 ratio at 298 K. Attempts to confirm the equilibrium state by an independent synthesis from a mixture of all building blocks failed due to incompatible solubilities. As no further changes were observed after 24 hours, we inferred that equilibrium had been reached.

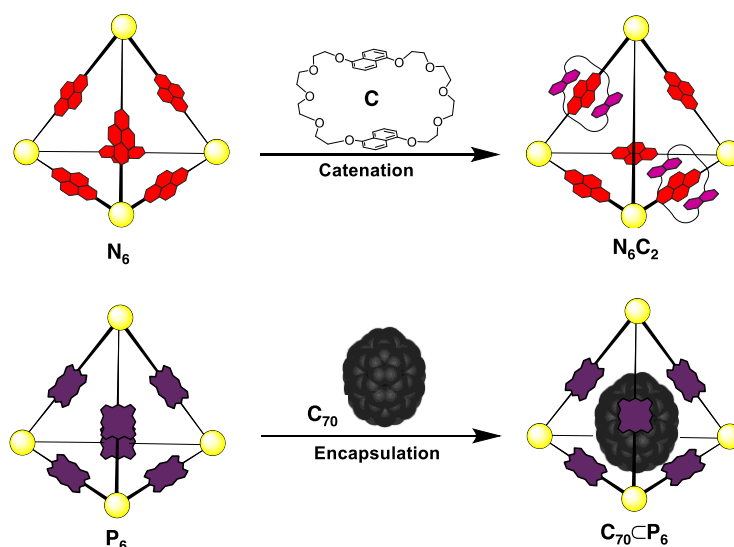


Figure 114: Summary of the host-guest of the homoleptic cages N_6 and P_6 : catenation of N_6 with crown C yielding N_6C_2 (top), encapsulation of fullerene C_{70} in porphyrin cage P_6 , yielding $C_{70} \subset P_6$.

1H NMR spectra of the mixture showed many resonances, corresponding to the numerous magnetically distinct environments of the mixed-ligand DCL members. The challenge of performing meaningful NMR analysis on this DCL was further complicated by the presence of resonances corresponding to the different regio- and stereo-isomers of the library members. The complicated nature of the spectra rendered DCL analysis by NMR impractical, even with

the use of two-dimensional and diffusion-ordered experiments. Therefore, ESI-FTICR MS analysis was employed to gain insight as to the composition of the library. Mass spectra revealed signals which corresponded to all seven of the possible Zn_4L_6 assemblies, hereby labelled $N_xP_{(6-x)}$ where **N** and **P** represent the NDI and porphyrin-based ligands (Figure 119a).

Solutions of N_6 and P_6 ($CD_3CN/CDCl_3$, 1:1, 1.0 mM) were mixed at 298 K and subjected to ESI-MS analysis. MS spectra were recorded directly after combining the cage solutions and subsequently after different time intervals to follow the exchange of ligands (Figure 115). No further changes were observed after an equilibration time of 24 h.

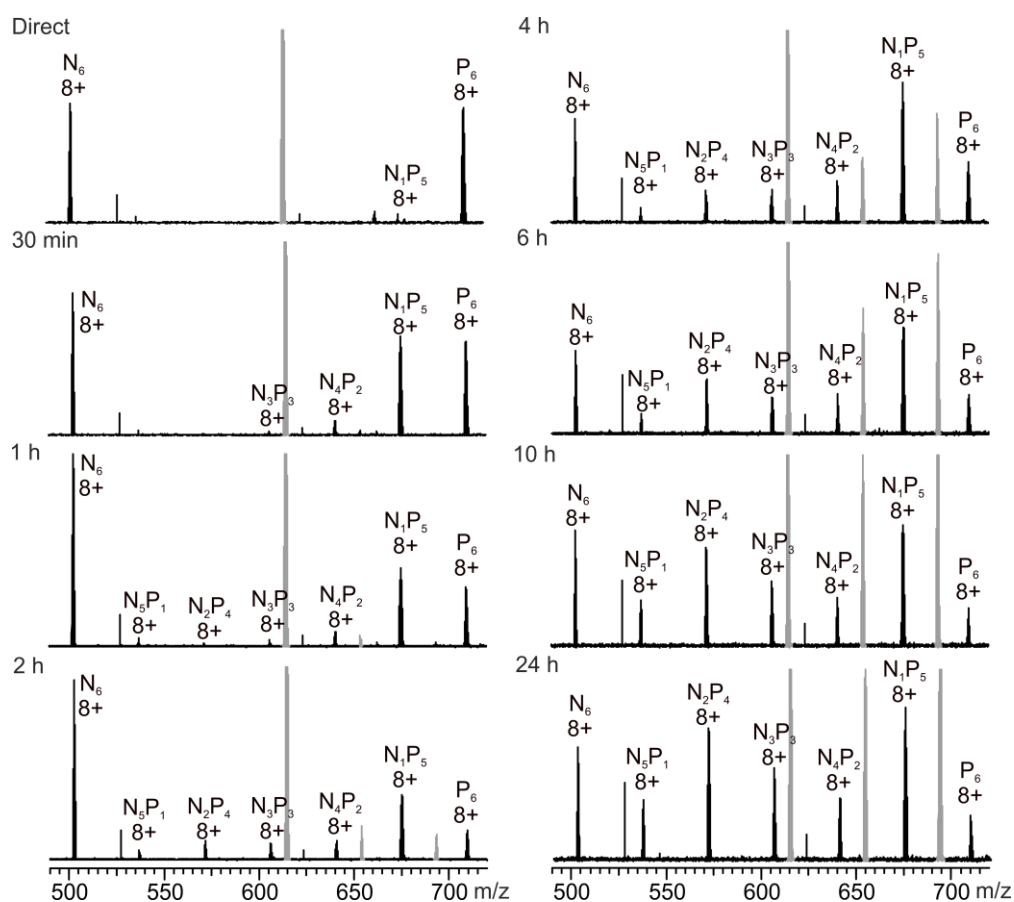


Figure 115: ESI-MS spectra of N_6 and P_6 after different equilibration times. Only +8 charges species are followed, peaks belonging to other charge states marked grey.

To confirm the thermodynamic equilibrium of the DCL, a solution of N_6 and P_6 ($CD_3CN/CDCl_3$, 1:1, 1.0 mM) was equilibrated for 24 h at 298 K, followed by 24 h at 348 K and again by 24 h at 298 K. ESI-MS spectra were recorded after each equilibration step (Figure 116). Slightly different signal intensities for the various cage species at 348 K compared to 298 K revealed a small temperature dependence of the library composition. Upon further equilibration at 298 K, the signal intensities were similar to the initial state, showing the reversibility of the library equilibrium.

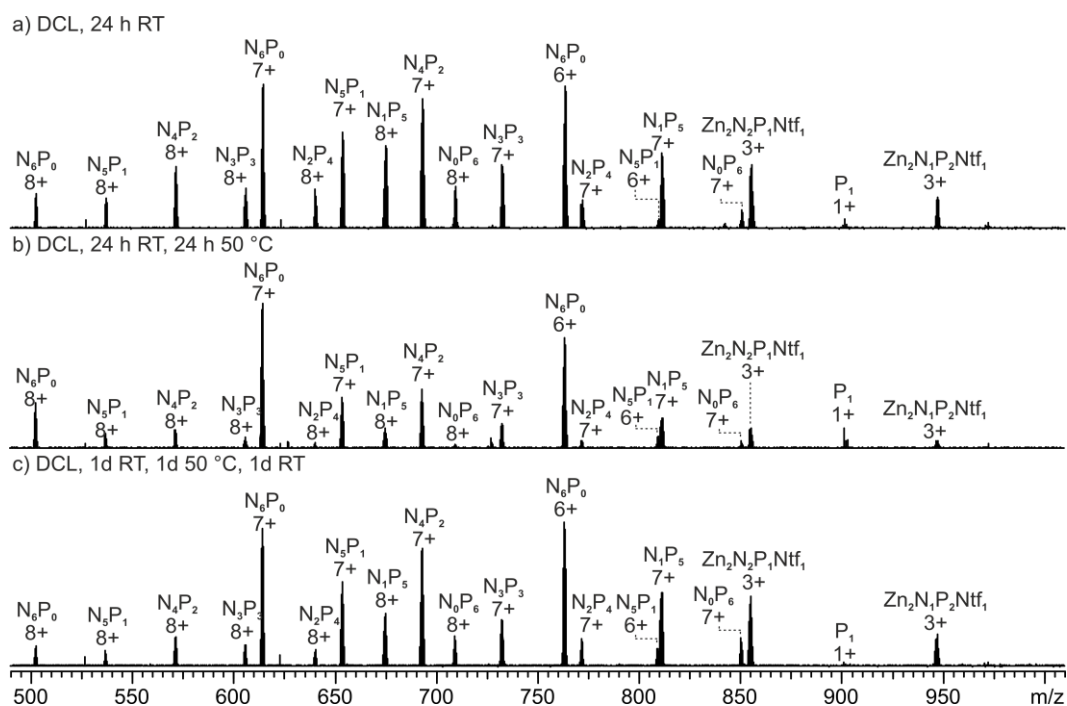


Figure 116: ESI-MS spectra of a DCL of **N₆** and **P₆** equilibrated for a) 24 h at 298 K, b) 24 h at 298 K and 24 h at 348 K and c) 24 h at 298 K, 24 h at 348 K and 24 h at 298 K.

Strictly speaking, a quantitative analysis of the changes in DCL composition using mass spectrometry requires that all species analysed possess similar ESI-response factors.^[208] As the homoleptic cages **N₆** and **P₆** appeared with similar intensities in the mass spectrum of the DCL (Figure 119a), we infer that this requirement is met to such a degree that changes in peak intensity between mixed ligand species correlate to the degree of change in their solution concentrations in the DCL.^[209]

All analysed DCLs were prepared under similar conditions, where solutions of **N₆** and **P₆** (CD₃CN/CDCl₃, 1:1, 1.0 mM) were allowed to equilibrate over 24 h at 298 K before template addition. The template (**C** or **C₇₀**) was added to DCLs in excess, at a ratio of 4 : 1 template/cage because this ratio was found to yield the strongest ESI-MS signals. The reaction of the DCL with **C** (Figure 117) and **C₇₀** (Figure 118) was followed with ESI-MS over 24 h, upon which no further changes of the library were observed. For all following experiments, the library was allowed to equilibrate at room temperature for a further 24 h after template addition.

DCL

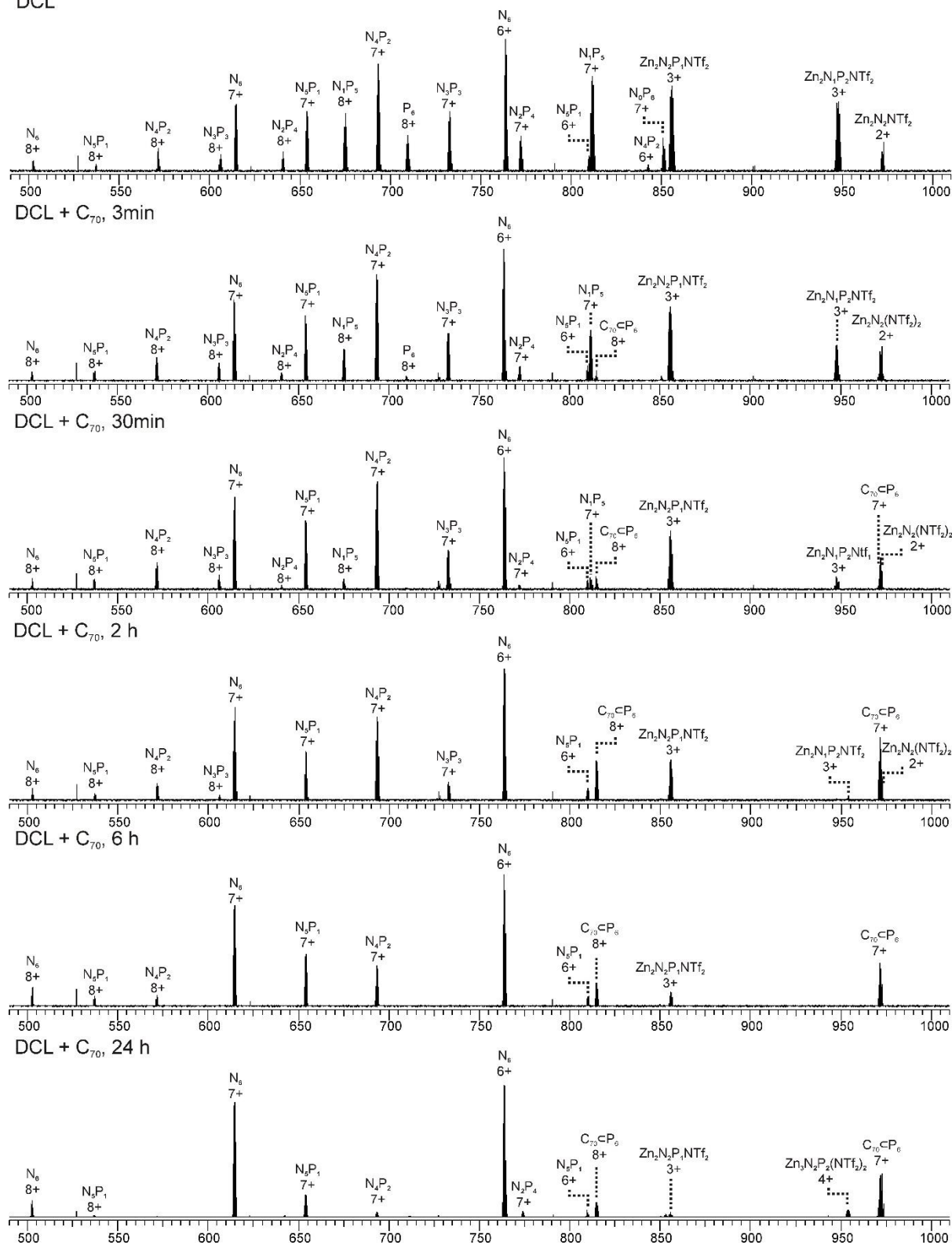


Figure 118: ESI-FTICR-MS spectra of DCL + C₇₀ (4 equiv.) at different time intervals.

The MS signals observed in each experiment were processed to establish the relative abundance of each $N_xP_{(6-x)}$ cage species (summing the detected m/z signal intensities of all charge states for each ligand ratio, including those signals that comprise additional **C** or **C**₇₀, see the Supporting Information). In the case of the non-templated DCL (Figure 119a), each one of the seven possible $N_xP_{(6-x)}$ species is observed, with **N**₄**P**₂ and **N**₁**P**₅ occurring in highest abundance.

This distribution deviates from a statistical ratio of species (which would follow the 7th level of Pascal's triangle – 1:6:15:20:15:6:1). We infer this deviation to result from a thermodynamic preference for the homoleptic cages **N**₆ and **P**₆. Minor differences between the lengths of subcomponents **1** and **2** could give rise to slight strain when both ligands are incorporated into the same assembly,^[210] thereby favouring the formation of homoleptic over heteroleptic assemblies.^[209]

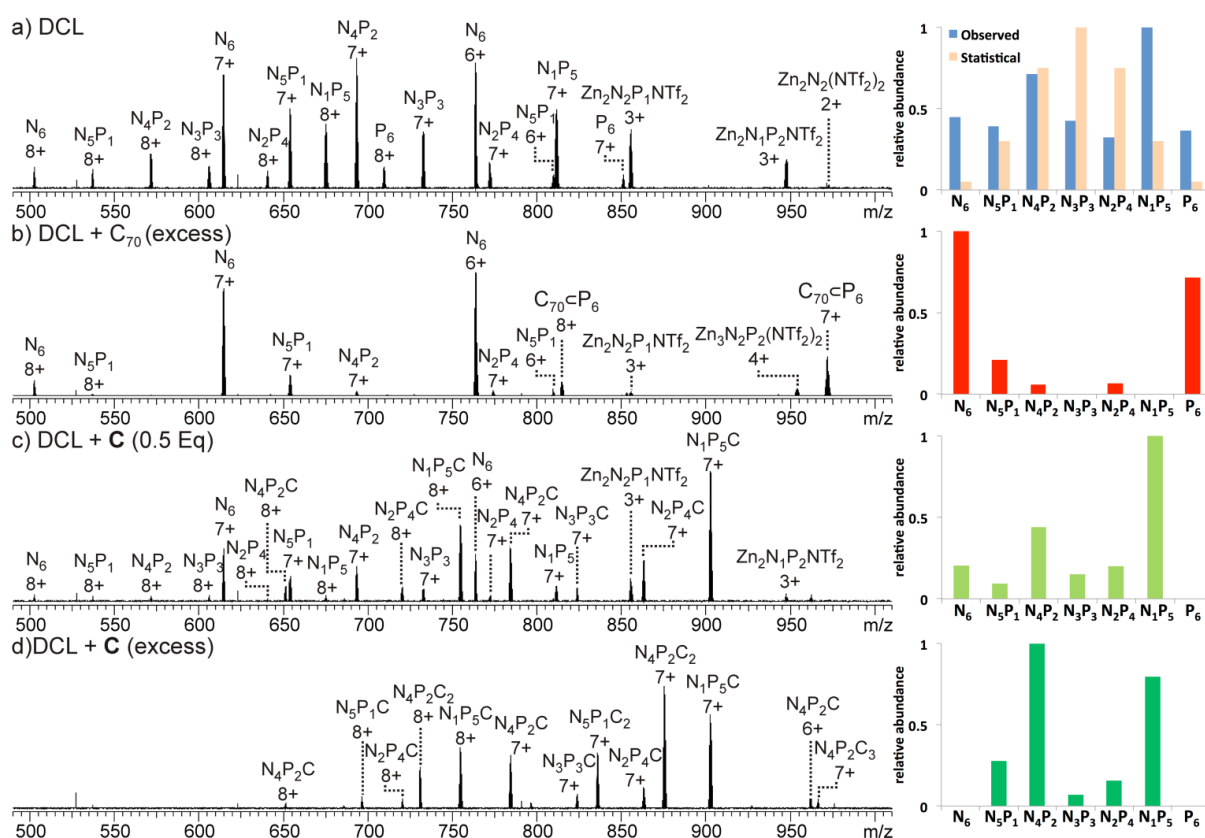


Figure 119: ESI-MS spectra (left) and corresponding charts (right) that show the relative abundances summed for all observed charge states: a) 1:1 DCL of **N**₆ and **P**₆ after 24 h of equilibration, no template, (blue) and statistical distribution (orange) b) 1:1 DCL of **N**₆ and **P**₆ containing C₇₀ (4 equiv), c) 1:1 DCL of **N**₆ and **P**₆ with **C** (0.5 equiv), and d) 1:1 DCL of **N**₆ and **P**₆ with **C** (4 equiv).

As a control experiment to confirm the equilibrium state, a DCL was prepared by an independent synthesis from a mixture of all building blocks and not as usual from the purified cages (see experimental section). A suspension of all building blocks was equilibrated for 7 d

at 50 °C and a sample of the mixture was filtered, diluted to 25 μM and subjected to MS analysis (Figure 120).

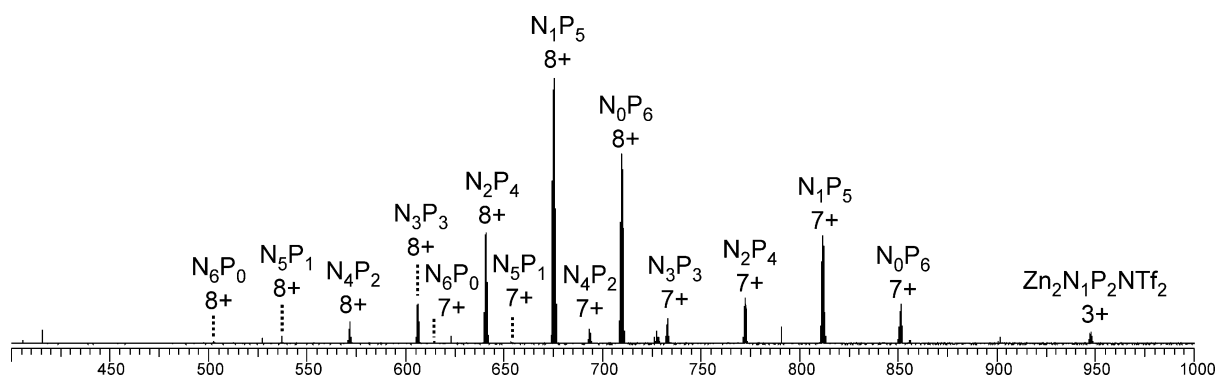


Figure 120: ESI-FTICR-MS spectrum of a DCL formed from ligands.

The distribution of mixed cages in this experiment is not in agreement with distribution in the DCL synthesised from pre-formed cages. Due to the very poor solubility of the NDI ligand, a strong excess of porphyrin-ligand is present in solution, leading to an excess of porphyrin-rich cages in the DCL.

Having generated a $N_xP_{(6-x)}$ DCL, we sought to investigate its response to **C** and fullerene C_{70} , which interacted with the individual homoleptic cages N_6 and P_6 , respectively. Following addition of C_{70} to the DCL and equilibration for 24 h at 298 K (Figure 119b), the composition shifted to give almost entirely N_6 and $C_{70} \subset P_6$. ESI-MS analysis of the library showed that only P_6 was interacting with C_{70} to form $C_{70} \subset P_6$, indicating that this self-sorting behaviour can be attributed to the thermodynamic stability of the $C_{70} \subset P_6$ host-guest complex, which removes the porphyrin ligands from the system.^[211] We observed no evidence for a mixed-ligand assembly that encapsulates C_{70} . We infer that the larger surface area of the porphyrin ligands relative to the NDIs (Figure 110c) renders P_6 , the most enclosed cage, uniquely capable of binding C_{70} .

While the addition of C_{70} causes the library distribution to shift almost completely towards the formation of the species with an optimised binding pocket for the template, we anticipated that the addition of **C** would have a less pronounced effect on DCL composition. The recognition events of **C** are limited to interactions with the NDI components and thus can be expected to affect the library distribution in a way that will maximize the favourable NDI-naphthalene π -interactions.

In the experiment where excess **C** (4 equiv) was added to the $N_xP_{(6-x)}$ DCL (Figure 119d), ESI-MS of the equilibrated library showed signals corresponding to mixed ligand assemblies N_5P_1 , N_4P_2 , N_3P_3 , N_2P_4 , and N_1P_5 . These mixed-ligand cages were observed to interact with 1 or 2 units of **C**.

No signals for the homoleptic assemblies \mathbf{N}_6 or \mathbf{P}_6 were observed. Only one signal in the ESI-MS is consistent with a species interacting with three units of \mathbf{C} ($\mathbf{N}_4\mathbf{P}_2\mathbf{C}_3$). Given that this stoichiometry exceeds the degree of catenation previously observed for \mathbf{N}_6 (Figure 112), we infer that the third crown ether is not likely to be catenated.^[204, 212]

In the similar experiment conducted with a sub-stoichiometric amount of \mathbf{C} (0.5 equiv, Figure 119c), the ESI-MS shows a distribution of all possible tetrahedral library members except \mathbf{P}_6 . In these experiments a maximum of one equivalent of \mathbf{C} was shown to interact with each tetrahedron, and signals were also observed for tetrahedra that are not associated with \mathbf{C} , as expected given the limited amount of \mathbf{C} added in the experiment.

Regardless of the amount of \mathbf{C} added, catenated cages with ligand ratios of $\mathbf{N}_4\mathbf{P}_2$ and $\mathbf{N}_1\mathbf{P}_5$ were the most abundant species observed in the DCL. This observation follows the trend of speciation in the non-templated DCL, where $\mathbf{N}_4\mathbf{P}_2$ and $\mathbf{N}_1\mathbf{P}_5$ were also the most abundant library members. However, the addition of \mathbf{C} significantly increases the preference for $\mathbf{N}_4\mathbf{P}_2$ and $\mathbf{N}_1\mathbf{P}_5$ at the expense of \mathbf{N}_6 and \mathbf{P}_6 (Figure 119c-d).

The most abundant catenated cages $\mathbf{N}_4\mathbf{P}_2\mathbf{C}_1$, $\mathbf{N}_4\mathbf{P}_2\mathbf{C}_2$, $\mathbf{N}_5\mathbf{P}_1\mathbf{C}_2$ and $\mathbf{N}_1\mathbf{P}_5\mathbf{C}_1$ were subjected to IRMPD MS/MS analysis to confirm the interlocked structure and rule out that \mathbf{C} is only unspecifically bound in the gas phase. For all four cages, no loss of \mathbf{C} without fragmentation of the cage could be observed.

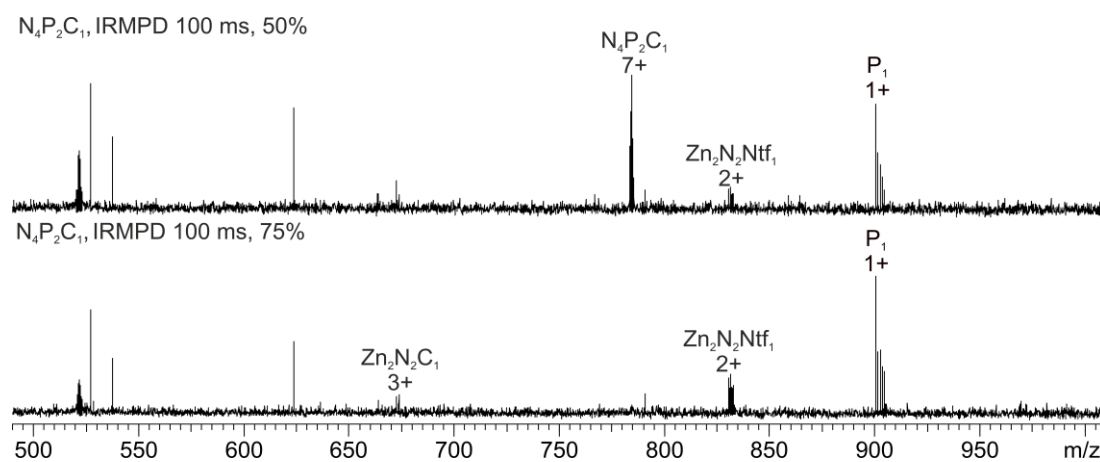


Figure 121: IRMPD ESI-MS spectra of $[\mathbf{N}_4\mathbf{P}_2\mathbf{C}_1\mathbf{NTf}_2]^{7+}$.

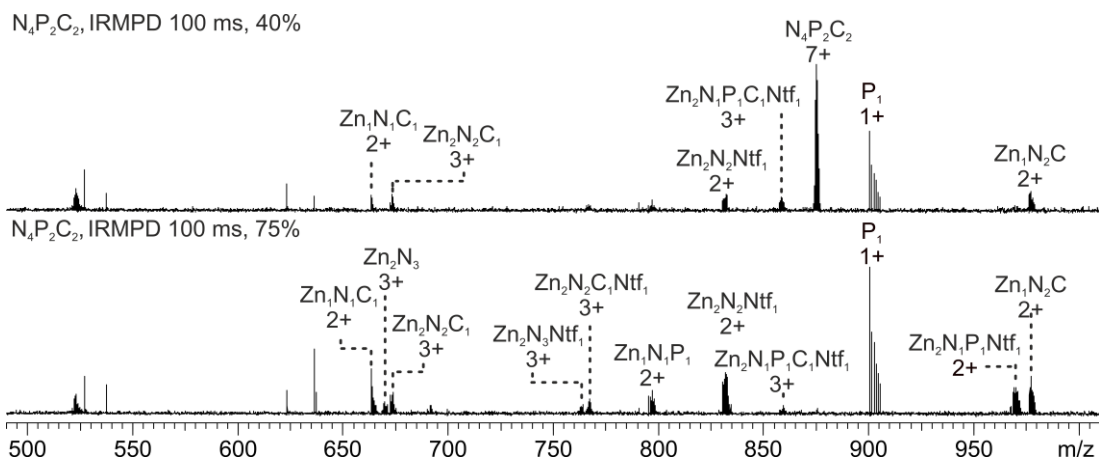


Figure 122: IRMPD ESI-MS spectra of $[\text{N}_4\text{P}_2\text{C}_2\text{NTf}_2]^{7+}$.

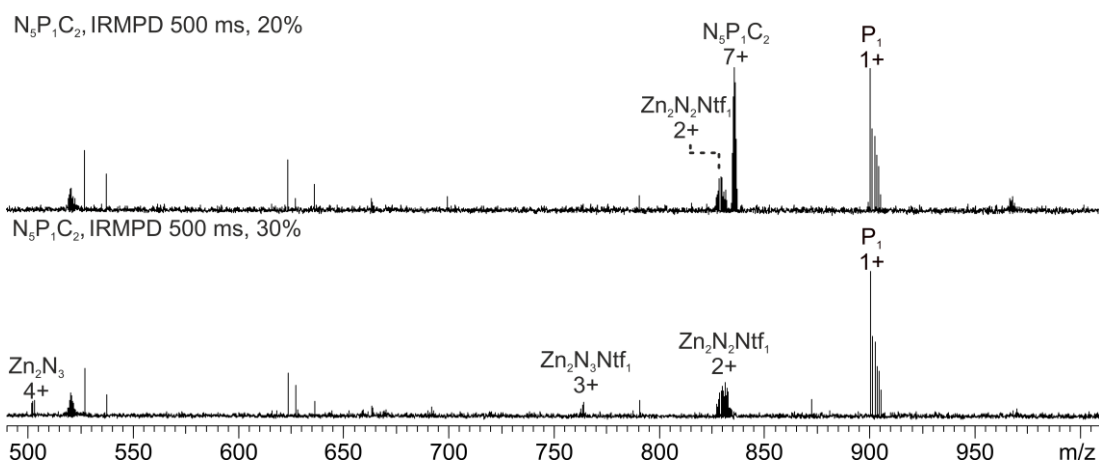


Figure 123: IRMPD ESI-MS spectra of $[\text{N}_5\text{P}_1\text{C}_2\text{NTf}_2]^{7+}$.

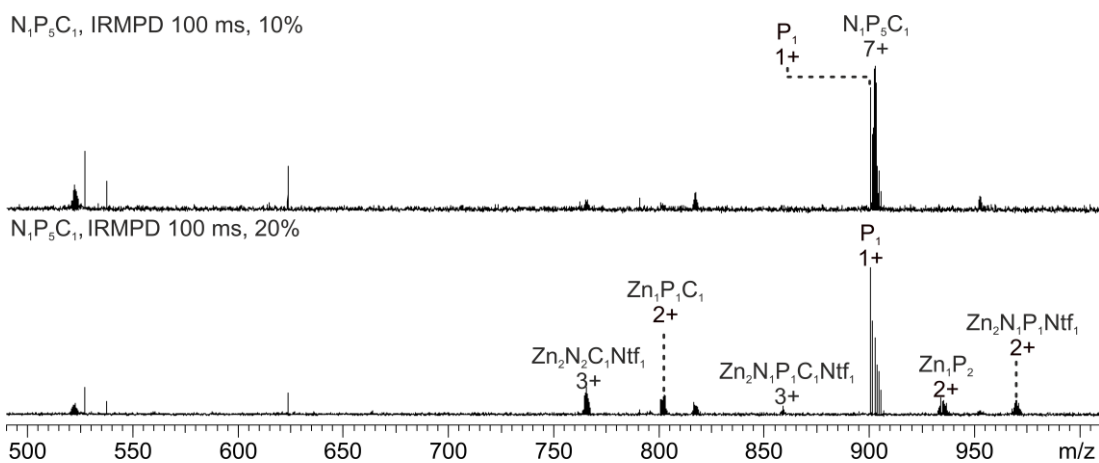


Figure 124: IRMPD ESI-MS spectra of $[\text{N}_1\text{P}_5\text{C}_1\text{NTf}_2]^{7+}$.

The shift in library composition towards mixed-ligand tetrahedra upon addition of **C** appears to maximize the number of interactions between the NDI ligands and **C**. In **N₆**, a maximum of two molecules of **C** can thread the six NDI ligands that are available. Therefore, shifting the library towards mixed-ligand assemblies increases the total number of NDI sites within the system that are available to thread through **C**. This hypothesis is supported by the absence of **N₆** in the DCL when an excess of **C** is present and the observation that all of the species observed by ESI-MS are catenated one or two times.

In order to achieve the maximum degree of catenation between the NDI ligands and **C**, the optimal tetrahedra to form are **N₄P₂**, **N₃P₃** and **N₂P₄** because these species are each able to accommodate two molecules of **C** and would thus maximize the number of NDI-naphthalene π -interactions. That **N₃P₃** and **N₂P₄** are only minor species in the DCL suggests that there are other factors influencing the distribution of the library. This inference is supported by the observation that the non-templated DCL also deviates from the purely statistical distribution, suggesting that the strain leading to a non-statistical distribution of the non-templated DCL also plays a role in controlling the DCL composition in the presence of **C**.

Experiments in which both templates, **C** and **C₇₀**, were added to the DCL either simultaneously or sequentially yielded poor ESI-MS data (Figure 125). The spectrum showed only peaks for **N₄P₂** and **N₅P₁** with up to three molecules of **C**, while no species with **C₇₀** were detected. We infer that aggregation may be occurring between **C** and **C₇₀**, which has been observed in other systems,^[213] precluding us from probing possible synergistic effects of these templates upon the DCL.

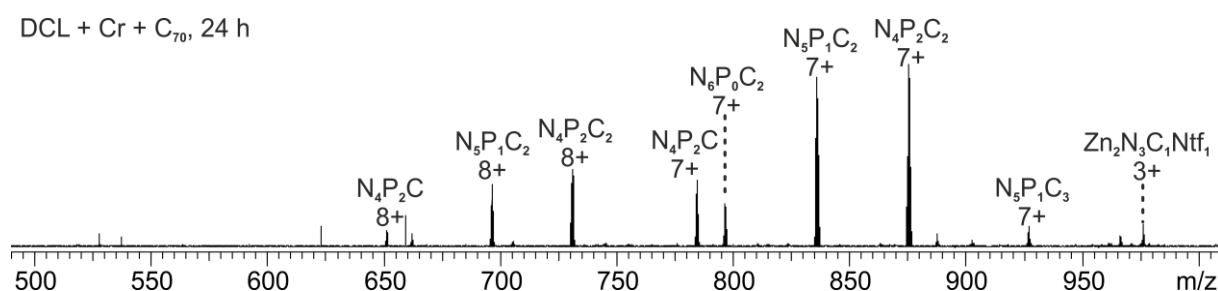


Figure 125: ESI-MS spectra of a 1:1 DCL of **N₆** and **P₆** with **C** (4 equiv) and **C₇₀** (4 equiv) after 24 h equilibration.

5.1.4. Conclusions

The difference in the shape and functionality of the NDI and porphyrin moieties of the ligands of \mathbf{N}_6 and \mathbf{P}_6 manifests in the form of distinct host-guest interactions with either \mathbf{C} or \mathbf{C}_{70} . The similarity in lengths of the edges of \mathbf{N}_6 and \mathbf{P}_6 allows for ligand exchange between the two assemblies, yielding a dynamic library of seven different tetrahedral cages $\mathbf{N}_x\mathbf{P}_{(6-x)}$. This DCL was shown to respond to the addition of \mathbf{C} or \mathbf{C}_{70} , with the different templates influencing the composition of the DCL in distinct ways. A point of interest in our study is the use of both encapsulation and catenation (Figure 126) as templation mechanisms within a DCL of three-dimensional receptors. Unlike systems derived from dynamic covalent species, the labile nature of these Zn_4L_6 tetrahedra precluded analysis by standard chromatographic separation^[192b] and instead a methodology was employed where information as to the distribution of the library could be extracted from ESI-MS. This approach allowed us to decipher the behaviour of a complex mixture of seven different cage species, each comprising 22 individual components, and each of which was shown to form additional host-guest interactions. The multiple-stimuli responsiveness thus engendered could be of use in modulating guest uptake within more complex chemical networks that include DCLs of cages.

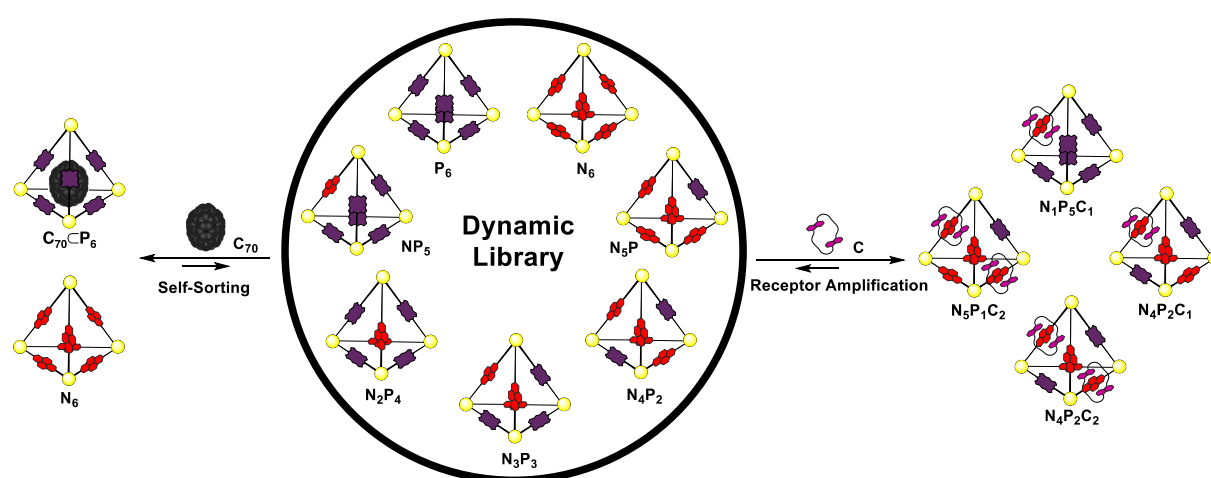


Figure 126: A schematic overview of the different templation effects observed in the 1:1 DCL formed upon mixing of \mathbf{N}_6 and \mathbf{P}_6 . Addition of \mathbf{C}_{70} leads to the self-sorting of ligands into their homoleptic cages, as the library shifts to form the \mathbf{C}_{70} receptor porphyrin cage \mathbf{P}_6 . Addition of macrocycle \mathbf{C} leads to the formation of heteroleptic cages, in which the total number of $\mathbf{N}\text{-}\mathbf{C}$ interactions is maximised, given that only two such interactions per cage are possible.

6. Conclusions and perspectives

Within this thesis, the layer-by-layer self-assembly project could be successfully advanced towards realising the long-term goals: The creation of multi-stimuli responsive multilayers of different rotaxanes that allow a distinct orthogonal addressing of individual layers and the realisation of coupled on-surface switching processes that can potentially result in macroscopic effects in more advanced systems in the future.

Two novel photoswitchable binding sites for Hunter-Vögtle-type TLMs based on spiropyran and azobenzene have been developed. They can both be reversibly switched with light of different wavelengths between two distinct states, one of which forms an inclusion complex with TLM, while the other one does not exhibit significant attractive interactions (Figure 127).

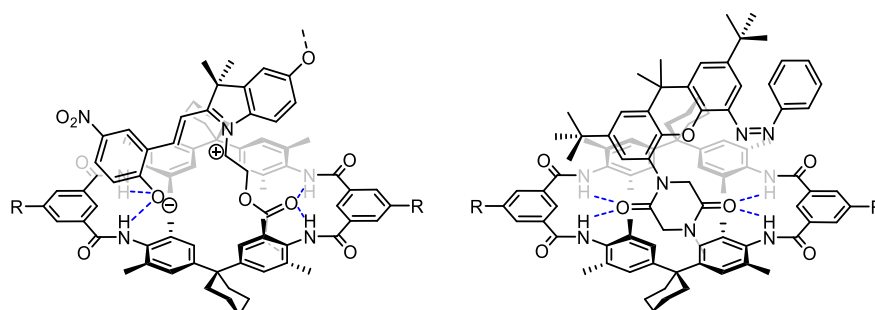


Figure 127: Photoswitchable binding sites based on spiropyran (left) and azobenzene (right).

Using the azobenzene binding site, a photocontrolled pseudorotaxane formation with well ordered multilayers of macrocycles on surfaces was demonstrated (Figure 128). Glass, silicon and gold surfaces have been functionalised with pyridine-terminated SAMs and subsequently with multilayers of macrocycles through layer-by-layer self-assembly. The photocontrolled deposition of the axle into the surface-bound macrocycle-multilayers was monitored by UV-Vis, XPS and NEXAFS spectroscopy. Angle-resolved NEXAFS spectra revealed a preferential orientation of the macrocycles with even more pronounced linear dichroism effects upon photoinduced binding of the axle. While the photoisomerisation of the binding site easily takes

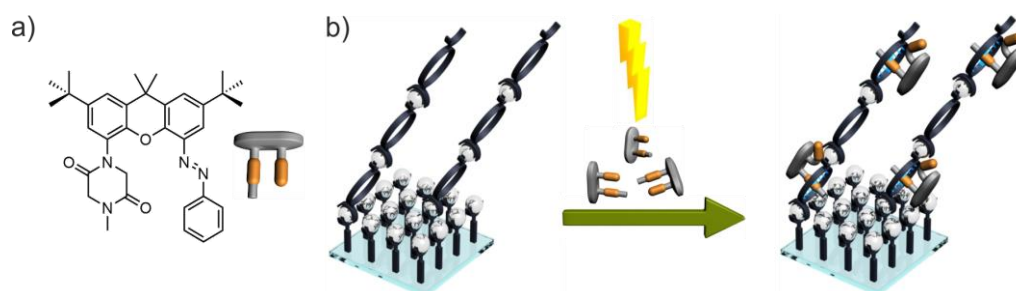


Figure 128: Photocontrolled on-surface pseudorotaxane formation.

place in solution, it was hampered when the axle is incorporated in the ordered and densely packed multilayers, illustrating the significant differences between solution and surface.

On the basis of the developed photoresponsive binding sites, different rotaxanes have been synthesised and extensively characterised in solution using UV-Vis and NMR spectroscopy (Figure 129). The rotaxanes could be reversibly switched between two distinct states, inducing a movement of the macrocycle along the axle. The different photophysical properties of azobenzene and spiropyran resulted in different switching characteristics of the respective rotaxanes.

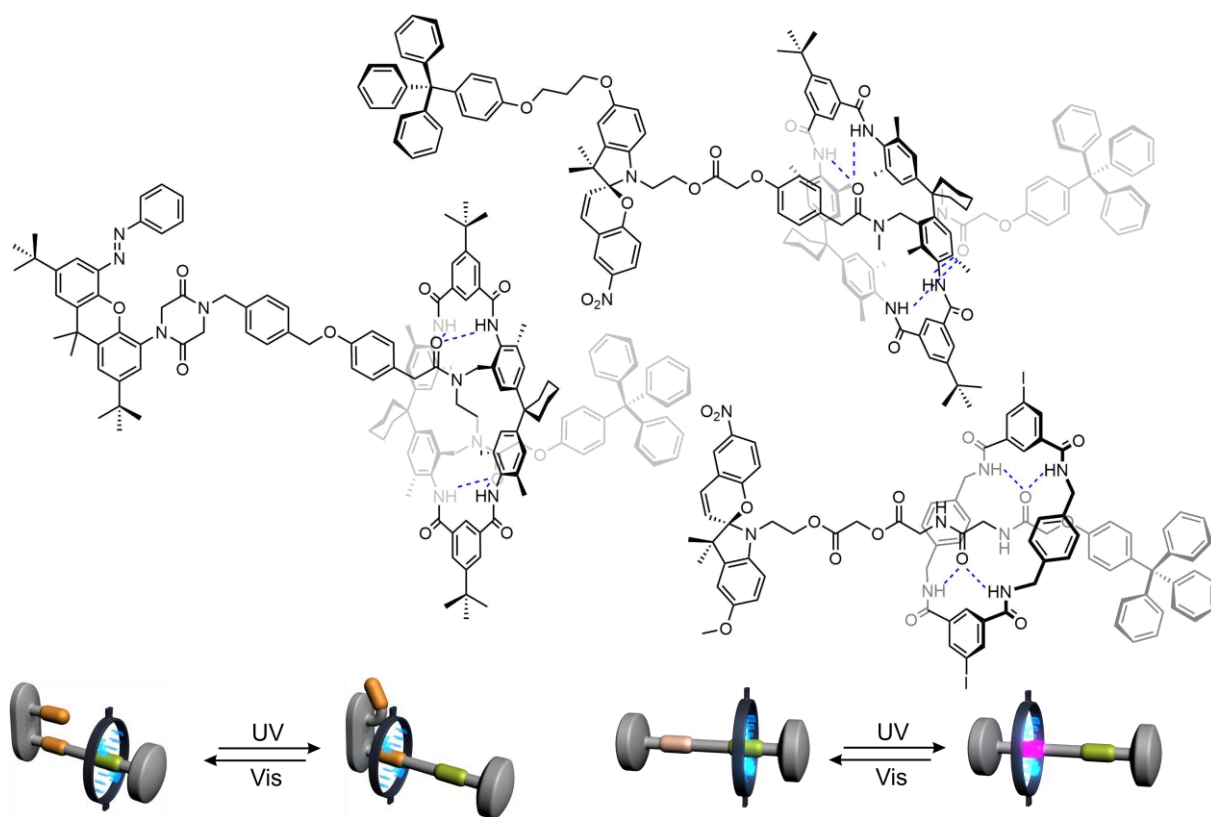


Figure 129: Structures of photoswitchable rotaxanes (top) and schematic representation of the photoinduced switching mode (bottom).

The azobenzene rotaxane was functionalised with either a terpyridine or an alkyne group and deposited in a monolayer on surfaces using layer-by-layer self-assembly or azide-alkyne click chemistry, respectively. A detailed study of the photoinduced on-surface switching processes was performed using contact angle measurements, UV-Vis, XPS and NEXAFS spectroscopy. It was shown that both the covalently and the coordinatively bound monolayer of rotaxanes can be reversibly switched between two distinct states on the surfaces. NEXAFS spectroscopy revealed a preferential orientation in the monolayers which reversibly changes upon photoswitching of the rotaxane.

The successful deposition of the photoswitchable rotaxane is of particular interest, as it allows a detailed and unambiguous analysis of the switching processes on the surface. Light stimuli can be delivered with a high temporal and spatial accuracy and, in contrast to chemical stimuli, do not bring in any impurities. The observed changes of the molecular orientation in the rotaxane monolayer could thus be clearly attributed to the photoinduced switching.

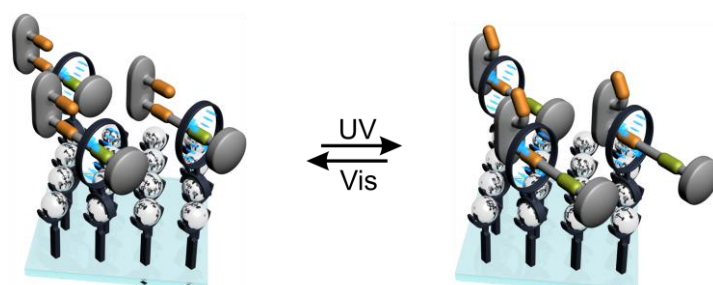


Figure 130: Reversible on-surface photoswitching of a rotaxane monolayer.

With this successful development of a photoswitchable rotaxane that can be deposited on surfaces, an important building block for the creation of multi-stimuli responsive surfaces that can be orthogonally addressed has been made available. The next step would be the systematic further development to a photoswitchable rotaxane that can be deposited in multilayers on surfaces, which should be straightforward on the basis of the achieved results. The following step would be the deposition of chemically and photochemically switchable rotaxanes in consecutive layers on surfaces (Figure 131). So far, neither an example for multilayers of photoswitchable rotaxanes nor multilayers of multi-stimuli responsive rotaxanes on surfaces has been reported in literature.

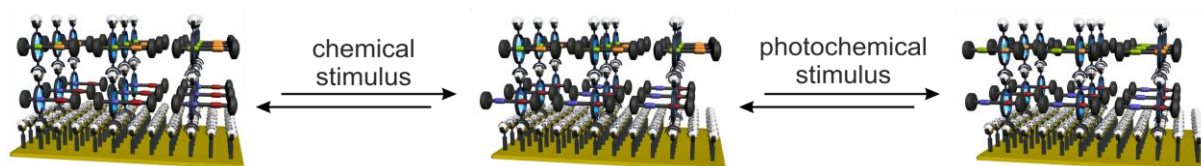


Figure 131: Schematic representation of a multi-stimuli responsive surface that can be addressed with chemical and photochemical stimuli.

Further studies should enhance the characterisation of the switching processes on the surface with special emphasis on the molecular orientation and the question if the molecules switch in a concerted fashion. The implementation of groups that exhibit attractive intramolecular non covalent interactions between the rotaxane axes might be an option to couple the switching processes of individual molecules into the synchronous switching of a whole layer. The addressability of lower layers for external stimuli in a densely packed multilayer system is of interest as well.

The integration of molecular switches in ordered arrays at interfaces is of great interest, as such order is the prerequisite for macroscopic effects through the concerted action of microscopic units. The layer-by-layer self-assembly project of the Schalley group, that allows the programmable deposition of macrocycles, metal ions and supramolecular switches in ordered multilayers on different solid supports has achieved a unique complexity, that is unparalleled in its depth and diversity. Today, these multilayer systems are the subject of academic basic research, as well as all other so far reported examples of molecular switches and machines are. However, this kind of academic research is of great interest and importance and offers numerous potential applications that could arise. This was also reflected in this year's Nobel price in chemistry, that was given to three of the pioneers of molecular switches, motors and machines. It remains exciting to see, whether and how this field of research has the potential to significantly influence our world in the future.

In the cooperation project with the group of Prof. Jonathan Nitschke, ESI-FTICR MS and IRMPD experiments could be successfully employed for the detailed characterisation of a complex dynamic combinatorial library of tetrahedral M_4L_6 cages. A qualitative and quantitative analysis of the DCL constitution was performed, whereby all constitutional isomers of cages and their relative abundances were measured. The responsiveness of the DCL towards different templates was investigated and the resulting constitutional changes of the library composition were determined (Figure 132).

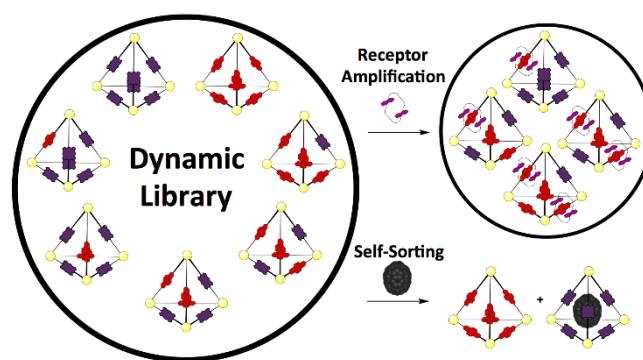


Figure 132: Schematic overview of the DCL and the different templation effects.

7. Experimental section

7.1. General methods

Reagents were purchased from Sigma-Aldrich, Alfa Aesar, ACROS or Fluka and used without further purification. Dry solvents were purchased from ACROS. Silica gel (0.04-0.063 mm; Machery-Nagel) was used for column chromatography. Ethanol (EtOH), dichloromethane (DCM), dimethylformamide (DMF), and acetonitrile (ACN) used for surface experiments were purchased from Carl Roth or VWR in HPLC grade and used as received. All reactions were carried out under argon protective atmosphere.

For XPS and NEXAFS experiments, layers were prepared on polished single-crystal Si(111) wafers purchased from CrysTec GmbH, stored under argon prior to use and cut into pieces (~1 cm²) with a diamond cutter. Microscope glass slides used for transmission UV-Vis spectroscopy were purchased from Thermo Scientific. All SAM, macrocycle and metal depositions were performed in gamma-sterilised tubes (Orange Scientific).

7.2. Instrumentation

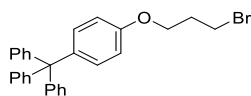
NMR spectra were recorded on a JEOL ECX 400, Bruker DRX-400, JEOL ECP 500, Bruker Avance 500 Cryo or Bruker Avance III 700 instrument. Unless otherwise stated, all spectra were recorded at 298K. All chemical shifts are reported in ppm with solvent signals taken as internal standards. Mass spectra were measured on an Ionspec QFT-7 FTICR mass spectrometer (Agilent Technologies, Lake Forest, CA, USA), equipped with a 7 T superconducting magnet and a Micromass Z-spray ESI source (Waters Co., Saint-Quentin, France) or an Agilent 6210 ESI-TOF instrument. UV-Vis spectra were measured on a Varian Cary 50 UV-Vis spectrometer. For surface UV-Vis spectra, a spectrum of the underlying SAM was used as background and subtracted from all multilayer spectra.

XPS and NEXAFS measurements were carried out at the HESGM CRG dipole magnet beamline at the synchrotron radiation source BESSY II (Berlin, Germany). SR XPS (synchrotron radiation XPS) O 1s, N 1s, Au 4f, S 2p, C 1s and F 1s data were acquired by a Scienta 3000 hemispherical electron analyzer (pass energy = 50 eV) at the HE-SGM dipole magnet CRG beamLine. The same beamLine was used for the acquisition of all NEXAFS spectra. An emission angle of 0° was used for all XPS measurements. The binding energy scale of the XP spectra was corrected for static charging using an electron binding energy BE of 83.95 eV for Au 4f_{7/2} photoemission of the gold substrate.^[214] Peak fitting of XP spectra was performed with a Lorentzian–Gaussian sum function peak shape model using the Unifit 2011

software (Unifit Scientific Software GmbH, Leipzig, Germany). Peak fits and integrated peak areas were obtained after subtraction of a polynomial backgrounds. If not otherwise denoted the FWHM for component peaks in N 1s and C 1s spectra were constrained to be identical. NEXAFS spectra were acquired in the PEY (partial electron yield) mode using a channel plate detector with a retarding field of -150 V and incident angles of linearly polarised synchrotron light of 30° (electric field vector upright to surface plane), 55° and 90° (electric field vector parallel to the surface plane).^[215] The resolution $E/\Delta E$ of the monochromator at the carbonyl π^* resonance ($h\nu = 287.4$ eV) of CO was in the order of 2500. Raw spectra were divided by ring current and monochromator transmission function. The latter was obtained with a freshly sputtered Au sample.^[215] Energy alignment of the energy scales was achieved by using an I_0 feature referenced to a C1s $\rightarrow \pi^*$ resonance measured with a fresh surface of HOPG (highly ordered pyrolytic graphite, Advanced Ceramic Corp., Cleveland, USA) at 285.4 eV. ^[216] Irradiation experiments were carried out with a Thorlabs DC2200 LED driver equipped with a M365LP1 (365 nm) or M470L3 (470 nm) mounted LED.

7.3. Experimental procedures for chapter 4.1

7.3.1. Synthesis of ((4-(3-bromopropoxy)phenyl)methanetriyl)tribenzene

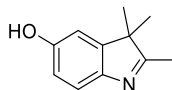


4-Tritylphenol (2.60 g, 7.73 mmol), 3-bromo-1-propanol (2.14 g, 15.4 mmol) and triphenylphosphine (4.04 g, 15.4 mmol) were dissolved in dry THF (70 mL) and cooled to 0 °C with an ice bath. DIAD (3.11 g, 15.4 mmol) was added dropwise and the mixture was stirred for 48 h while slowly warming up to RT. The solvent was removed and the residue purified by column chromatography (silica, DCM/*n*-hexane 1:1) which afforded the product as white solid (2.30 g, 5.02 mmol, 65 %).

$^1\text{H NMR}$ (400 MHz, CDCl_3) δ = 7.39 – 7.13 (m, 15H, H_{Ar}), 7.10 (d, J = 8.9 Hz, 2H, H_{Ar}), 6.77 (d, J = 8.9 Hz, 2H, H_{Ar}), 4.07 (t, J = 5.7 Hz, 2H, H_{CH_2}), 3.59 (t, J = 6.4 Hz, 2H, H_{CH_2}), 2.37 – 2.19 (m, 2H, H_{CH_2}) ppm.

The substance is literature-known and the $^1\text{H NMR}$ data corresponds to literature data.^[217]

7.3.2. Synthesis of 2,3,3-trimethyl-3H-indole-5-ol

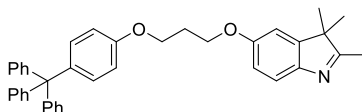


5-Methoxy-2,3,3-trimethyl-3H-indole (1.62 g, 8.50 mmol) was dissolved in dry DCM (10 mL) and cooled to 0 °C with an ice bath. Borontribromide (1M in DCM, 16.3 mL, 16.3 mmol) was added dropwise and the mixture was stirred for 12 h while slowly warming up to RT. Saturated aqueous NaHCO_3 solution (40 mL) and dest. water (100 mL) were added and the mixture was extracted with DCM (3 x 100 mL). The organic phases were combined, dried with magnesium sulfate, filtered and the solvent evaporated. The residue was purified by column chromatography (silica, DCM/MeOH 95:5), which afforded the product as brown solid (1.35 g, 7.70 mmol, 90 %).

$^1\text{H NMR}$ (400 MHz, CDCl_3) δ = 9.88 (s, 1H, OH), 7.30 (d, J = 8.2 Hz, 1H, H_{Ar}), 6.85 (dd, J = 2.4, 0.5 Hz, 1H, H_{Ar}), 6.78 (dd, J = 8.2, 2.4 Hz, 1H, H_{Ar}), 2.25 (s, 3H, H_{CH_3}), 1.27 (s, 6H, H_{CH_3}) ppm.

The substance is literature-known and the $^1\text{H NMR}$ data corresponds to literature data.^[218]

7.3.3. Synthesis of 2,3,3-trimethyl-5-(3-(4-tritylphenoxy)propoxy)-3H-indole



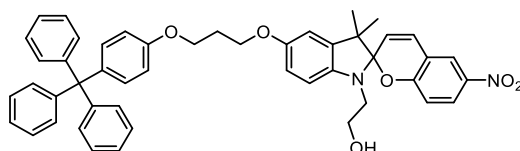
2,3,3-Trimethyl-3H-indole-5-ol (106 mg, 0.606 mmol) and tetrabutylammoniumbromide (20.0 mg, 0.062 mmol) were dissolved in THF (5 mL) and toluene (7 mL) and degassed with an argon stream for 10 min. Aqueous NaOH (50 %, 1 mL) was added and the mixture stirred for 15 min. ((4-(3-Bromopropoxy)phenyl)methanetriyl)tribenzene (388 mg, 0.848 mmol) was added and the mixture stirred for 12 h. The mixture was diluted with dest. Water (20 mL) and extracted with toluene (2 x 30 mL). The organic phases were combined, dried with sodium sulfate, filtrated and the solvent removed. The residue was purified by column chromatography (silica, DCM/EE 3:2), which afforded the product as white solid (115 mg, 0.208 mmol, 34 %).

$^1\text{H NMR}$ (400 MHz, CDCl_3) δ = 7.44 (d, J = 8.3 Hz, 1H, H_{Ar}), 7.34 – 7.08 (m, 17H, H_{Ar}), 6.90 – 6.76 (m, 4H, H_{Ar}), 4.27 – 4.07 (m, 4H, H_{CH_2}), 2.33 – 2.20 (m, 2H, H_{CH_2}), 2.26 (s, 3H, H_{CH_3}), 1.28 (s, 6H, H_{CH_3}).

$^{13}\text{C NMR}$ (101 MHz, CDCl_3) δ = 185.9, 157.3, 156.9, 147.6, 147.4, 147.1, 139.2, 132.3, 131.2, 127.6, 126.0, 120.2, 113.4, 112.9, 108.8, 65.0, 64.4, 64.3, 60.5, 53.89, 29.6, 23.4, 15.5 ppm.

MS (ESI, pos. Mode, MeOH/DCM): m/z calculated 552.2897 found 552.316 ($[\text{M}+\text{H}]^+$), calculated 574.2717 found 574.3014 ($[\text{M}+\text{Na}]^+$), calculated 590.2456 found 590.2779 ($[\text{M}+\text{K}]^+$).

7.3.4. Synthesis of 2-(3',3'-dimethyl-6-nitro-5'-(3-(4-tritylphenoxy)propoxy)spiro[chromene-2,2'-indolin]-1'-yl)ethan-1-ol



In a pressure tube, 2,3,3-trimethyl-5-(3-(4-tritylphenoxy)propoxy)-3H-indole (1.70 g; 3.10 mmol) and 2-bromoethanol (0.30 mL; 3.80 mmol) were dissolved in dry toluene (22 mL) and stirred for 2 d at 100 °C. The solvent was removed and the residue suspended in *n*-hexane, sonicated for 15 min and the solvent decanted off. The residue was dissolved in DCM (100 mL), washed with dest. water (100 mL), dried with magnesium sulfate, filtrated and the solvent

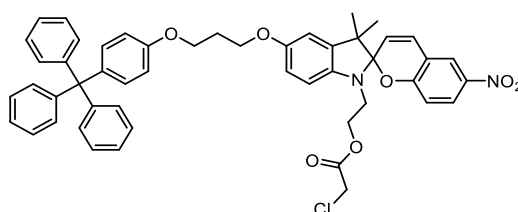
removed. The obtained solid was transferred into a pressure tube, dissolved in dry ethanol (70 mL), mixed with 2-hydroxy-5-nitrobenzaldehyde (0.70 g; 4.30 mmol) and stirred for 3 d at 65 °C. The solvent was removed and the residue was purified by column chromatography (silica, DCM -> DCM + 2 % MeOH -> DCM + 5 % MeOH), which afforded the product as violet solid (1.90 g; 2.55 mmol; 84 %).

^1H NMR (400 MHz, CDCl_3): δ = 1.17 (s, 3 H, H_{CH_3}), 1.24 (s, 3 H, H_{CH_3}), 1.55 (s, 1 H, OH), 2.23 (t, 2 H, H_{CH_2}), 3.31 (m, 2 H, H_{CH_2}), 3.71 (m, 2 H, H_{CH_2}), 4.12 (m, 4 H, H_{CH_2}), 5.86 (d, 1 H, $\text{H}_{\text{spiropyran}}$), 6.55 (d, 1 H, $\text{H}_{\text{spiropyran}}$), 6.76 (m, 6 H, H_{Ar}), 6.89 (d, 1 H, $\text{H}_{\text{spiropyran}}$), 7.10 (d, 2 H, $\text{H}_{\text{spiropyran}}$), 7.22 (m, 15 H, H_{trityl}), 8.00 (m, 2 H, $\text{H}_{\text{spiropyran}}$) ppm.

^{13}C NMR (126 MHz, CDCl_3): δ = 20.0, 29.6, 44.1, 53.7, 61.0, 64.4, 65.3, 100.0, 107.4, 110.4, 112.4, 113.3, 115.6, 121.2, 122.9, 123.9, 126.0, 127.5, 131.2, 131.8, 132.3, 137.6, 141.3, 141.5, 147.1, 153.7, 156.9, 159.5 ppm.

MS (ESI, pos. Mode, MeOH/DCM): m/z calculated 745.3278 found 745.3298 ($[\text{M}+\text{H}]^+$).

7.3.5. Synthesis of 2-(3',3'-dimethyl-6-nitro-5'-(3-(4-tritylphenoxy)propoxy)spiro[chromene-2,2'-indolin]-1'-yl)ethyl 2-chloroacetate



2-(3',3'-Dimethyl-6-nitro-5'-(3-(4-tritylphenoxy)propoxy)spiro[chromene-2,2'-indolin]-1'-yl)ethan-1-ol (1.9 g; 2.6 mmol) was dissolved in dry CHCl_3 (35 mL) and TEA (0.8 mL; 5.9 mmol) was added. The solution was cooled with an ice bath to 0 °C, mixed dropwise with chloroacetyl chloride (0.5 mL; 5.9 mmol) and stirred for 12 h while slowly warming up to RT. The solution was extracted with dest. water (2 x 20 mL), dried with magnesium sulfate, filtrated and the solvent evaporated. The residue was purified by column chromatography (silica, DCM + 0.1 % MeOH -> DCM + 2 % MeOH), which afforded the product as yellow solid (0.50 g; 0.61 mmol; 22 %).

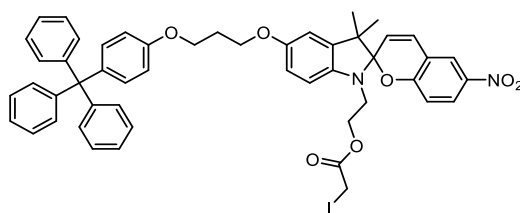
^1H NMR (400 MHz, CDCl_3): δ = 1.14 (s, 3 H, H_{CH_3}), 1.23 (s, 3 H, H_{CH_3}), 2.22 (m, 2 H, H_{CH_2}), 3.41 (m, 2 H, H_{CH_2}), 3.98 (s, 2 H, H_{CH_2}), 4.12 (m, 6

H, CH₂), 5.88 (d, 1 H, H_{spiropyran}), 6.54 (d, 1 H, H_{spiropyran}), 6.72 (m, 3 H, H_{spiropyran/Ar}), 6.75 (s, 1 H, H_{spiropyran}), 6.79 (m, 2 H, H_{Ar}), 6.90 (d, 2 H, H_{spiropyran}), 7.09 (d, 2 H, H_{Ar}), 7.20 (m, 15 H, H_{trityl}), 7.99 (m, 2 H, H_{Ar}), 8.02 (m, 1 H, H_{spiropyran}) ppm.

¹³C NMR (126 MHz, CDCl₃): δ = 20.2, 26.2, 29.9, 42.9, 53.7, 64.5, 64.7, 65.5, 107.2, 107.6, 110.7, 112.7, 113.6, 115.9, 118.8, 122.4, 123.2, 126.2, 127.8, 128.8, 131.5, 133.0, 137.7, 139.4, 141.3, 141.4, 147.4, 154.0, 157.2, 159.8, 169.0 ppm.

MS (ESI, pos. Mode, MeOH/DCM): m/z calculated 821.2994 found 821.3041 ([M+H]⁺); calculated 843.2813 found 843.2853 ([M+Na]⁺).

7.3.6. Synthesis of 2-(3',3'-dimethyl-6-nitro-5'-(3-(4-tritylphenoxy)propoxy)spiro[chromene-2,2'-indolin]-1'-yl)ethyl 2-iodoacetate



2-(3',3'-Dimethyl-6-nitro-5'-(3-(4-tritylphenoxy)propoxy)spiro[chromene-2,2'-indolin]-1'-yl)ethyl 2-chloroacetate (300 mg; 0.36 mmol) and sodium iodide (75 mg, 0.50 mmol) were dissolved in dry acetone (50 mL) and stirred for 2 h at RT. The solvent was removed and the residue dissolved in DCM (100 mL). The solution was washed with dest. water (2 x 50 mL), dried with magnesium sulfate, filtrated and the solvent evaporated. The product was obtained as orange solid (298 mg, 0.33 mmol, 92 %).

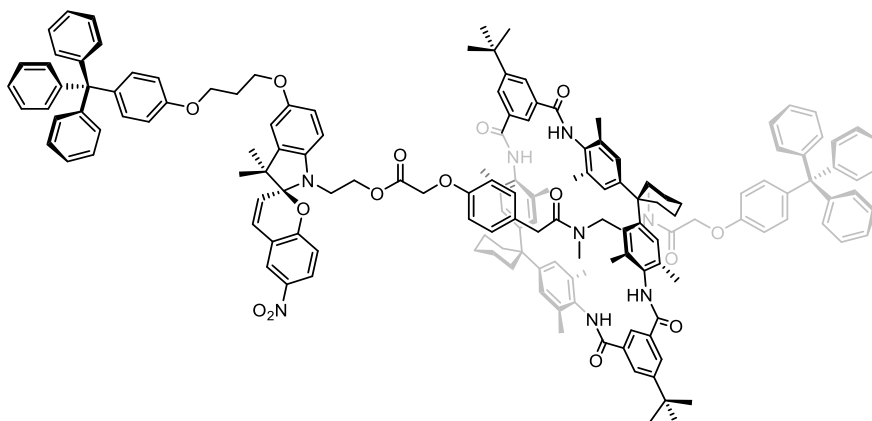
¹H NMR (400 MHz, CDCl₃): δ = 1.16 (s, 3 H, H_{CH3}), 1.24 (s, 3 H, H_{CH3}), 2.24 (m, 2 H, H_{CH2}), 3.42 (m, 2 H, H_{CH2}), 3.63 (s, 2 H, H_{CH2}), 4.13 (m, 4 H, H_{CH2}), 4.27 (m, 2 H, H_{CH2}), 5.92 (d, 1 H, H_{spiropyran}), 6.57 (d, 1 H, H_{spiropyran}), 6.74 (m, 2 H, H_{spiropyran}), 6.80 (s, 2 H, H_{Ar}), 6.92 (m, 1 H, H_{spiropyran}), 7.11 (d, 2 H, H_{Ar}), 7.22 (m, 15 H, H_{trityl}), 8.00 (m, 2 H, H_{Ar}), 8.02 (m, 1 H, H_{spiropyran}) ppm.

¹³C NMR (126 MHz, CDCl₃): δ = 20.2, 26.2, 29.9, 42.9, 53.7, 64.5, 64.7, 65.6, 107.3, 107.6, 110.8, 112.7, 113.7, 116.0, 118.9, 122.3, 123.2,

126.3, 127.9, 128.8, 131.5, 132.6, 137.8, 139.5, 141.0, 141.5, 147.4, 154.1, 157.4, 159.9, 169.1 ppm.

MS (ESI, pos. Mode, MeOH/DCM): [m/z] calculated 913.2350 found 913.2385 ([M+H]⁺); calculated 935.2169 found 935.2204 ([M+Na]⁺).

7.3.7. Synthesis of Rot1



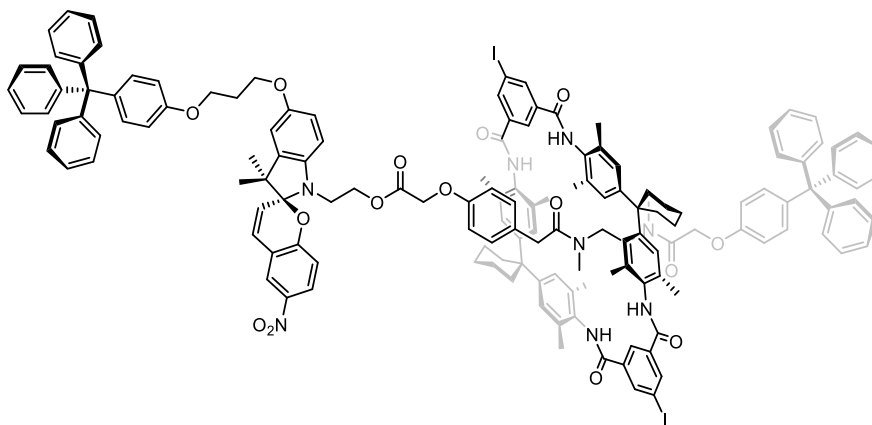
2-(4-Hydroxyphenyl)-*N*-methyl-*N*-(2-(*N*-methyl-2-(4-tritylphenoxy)acetamido)ethyl)acetamide (118 mg, 0.197 mmol), 2-(3',3'-dimethyl-6-nitro-5'-(3-(4-tritylphenoxy)propoxy)spiro[chromene-2,2'-indoline]-1'-yl)ethyl-2-iodoacetate (180 mg, 0.197 mmol), di-*tert*-butyl-TLM (100 mg, 0.098 mmol), dibenzo-18-crown-6 (32.0 g, 0.088 mmol) and potassium carbonate (136 mg, 0.0983 mmol) were dissolved in dry CHCl₃ (20 mL) and stirred at RT for 10 d. The mixture was diluted with DCM (100 mL), washed with dest. water (3 x 80 mL), dried with magnesium sulfate, filtrated and the solvent removed. The residue was purified by column chromatography (silica, DCM+5%MeOH), which afforded the product as yellow solid (50.0 mg, 0.021 mmol, 21 %).

¹H NMR (300 MHz, CDCl₃) δ = 8.44 (s, 2H, H_{isophthal}), 8.30 (s, 4H, H_{amide TLM}), 8.19 (s, 4H, H_{isophthal}), 7.95 – 7.86 (m, 2H, H_{spiropyran}), 7.17 – 7.09 (m, 30H, H_{trityl}), 7.08 – 6.98 (m, 6H, H_{Ar}), 6.90 (s, 8H, H_{Ar TLM}), 6.79 (d, *J* = 10.4 Hz, 1H, H_{spiropyran}), 6.72 (d, *J* = 8.9 Hz, 2H, H_{Ar}), 6.67 – 6.62 (m, 4H, H_{Ar}), 6.51 (d, *J* = 8.5 Hz, 2H, H_{Ar}), 6.41 (d, *J* = 8.7 Hz, 1H, H_{Ar}), 6.31 (d, *J* = 8.9 Hz, 1H, H_{spiropyran}), 5.74 (d, *J* = 10.3 Hz, 1H, H_{spiropyran}), 4.33 (d, *J* = 3.2 Hz, 2H, H_{CH2}), 4.30 – 4.15 (m, 2H, H_{CH2}), 4.11 – 3.98 (m, 6H, H_{CH2}), 3.82 (s, 2H, H_{CH2}), 3.45 – 3.25 (m, 2H, H_{CH2}), 2.97 (s, 2H, H_{CH2}), 2.46 – 2.34 (m, 8H, H_{Al}), 2.26 – 2.21 (m, 6H, H_{TLM}), 2.18 – 2.09 (m, 8H, H_{CH2}), 1.97 (s,

24H, H_{CH3 TLM}), 1.55 (bs, 12H, H_{TLM}), 1.43 (bs, 4H, H_{TLM}), 1.32 (s, 18H, H_{tBu TLM}), 1.15 (s, 3H, H_{CH3 spiropyran}), 1.04 (s, 3H, H_{CH3 spiropyran}) ppm.

MS (ESI, pos. Mode, DCM/ACN) m/z: calculated 1211.6062 found 1211.6027 ([M+H+Na]²⁺), m/z: calculated 1219.5932 found 1219.5900 ([M+H+K]²⁺), m/z: calculated 1222.5970 found 1222.5955 ([M+2Na]²⁺), m/z: calculated 1230.5842 found 1230.5817 ([M+Na+K]²⁺).

7.3.8. Synthesis of Rot2



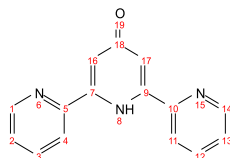
2-(4-Hydroxyphenyl)-*N*-methyl-*N*-(2-(*N*-methyl-2-(4-tritylphenoxy)acetamido)ethyl)acetamide (118 mg, 0.197 mmol), 2-(3',3'-dimethyl-6-nitro-5'-(3-(4-tritylphenoxy)propoxy)spiro[chromene-2,2'-indoline]-1'-yl)ethyl-2-iodoacetate (180 mg, 0.197 mmol), di-Iodo--TLM (114 mg, 0.098 mmol, 1 Eq), dibenzo-18-crown-6 (32.0 g, 0.088 mmol) and potassium carbonate (136 mg, 0.0983 mmol) were dissolved in dry CHCl₃ (20 mL) and stirred at RT for 10 d. The mixture was diluted with DCM (100 mL), washed with dest. water (3 x 80 mL), dried with magnesium sulfate, filtrated and the solvent removed. The residue was purified by column chromatography (silica, DCM+5%MeOH), which afforded the product as yellow solid (90.0 mg, 0.035 mmol, 36 %).

¹H NMR (300 MHz, CDCl₃) δ 8.64 = (s, 2H, H_{isophthal}), 8.52 (s, 4H, H_{isophthal}), 8.32 (s, 4H, H_{amide TLM}), 8.02 – 7.90 (m, 2H, H_{spiropyran}), 7.28 – 7.13 (m, 30H, H_{trityl}), 7.13 – 7.03 (m, 6H, H_{Ar}), 6.94 (s, 8H, H_{Ar TLM}), 6.78 (d, *J* = 8.9 Hz, 2H, H_{Ar}), 6.74 – 6.67 (m, 3H, H_{Ar}), 6.62 – 6.49 (m, 3H, H_{Ar}), 6.48 – 6.36 (m, 3H, H_{Ar}), 5.81 (d, *J* = 10.4 Hz, 1H, H_{spiropyran}), 4.40 (d, *J* = 3.2 Hz, 2H, H_{CH2}), 4.39 – 4.21 (m, 2H, H_{CH2}), 4.23 – 4.00 (m, 6H, H_{CH2}), 3.87 (s, 2H, H_{CH2}), 3.45 (s, 2H, H_{CH2}), 3.52 – 3.30 (m, 2H, H_{CH2}),

3.09 (s, 2H, H_{CH2}), 2.70 – 2.41 (m, 6H, H_{Al}), 2.37 – 2.21 (m, 6H, H_{TLM}), 2.23 – 2.15 (m, 8H, H_{Al}), 2.00 (s, 24H, H_{CH3 TLM}), 1.59 (s, 12H, H_{TLM}), 1.48 (s, 4H, H_{TLM}), 1.21 (s, 3H, H_{CH3 spiropyran}), 1.11 (s, 3H, H_{CH3 spiropyran}) ppm.

MS (ESI, pos. Mode, DCM/ACN) m/z: calculated 2539.8913 found 2539.8945 ([M+H]⁺),
m/z: calculated 2556.9179 found 2556.9207 ([M+NH₄]⁺),
m/z: calculated 2561.8733 found 2561.8759 ([M+Na]⁺),
m/z: calculated 2577.8472 found 2577.8502 ([M+K]⁺).

7.3.9. Synthesis of [2,2':6',2''-terpyridine]-4'(1'H)-one

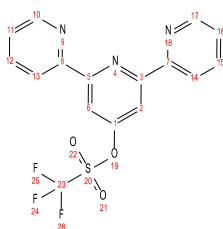


In a three necked flask, sodium hydride (60% in mineral oil, 13.2 g, 330.75 mmol) was suspended in dry THF (100 mL). A solution of ethyl picolinate (25.0 g, 165.38 mmol) in acetone (3.84 g, 66.2 mmol) in dry THF (100 mL) was placed in a dropping funnel and added over 1 h to the suspension of sodium hydride. The solution was stirred for 1 h and afterwards refluxed for 5.5 h. The solvents were removed and the residue was dissolved in dest. water (500 mL) and neutralised with 1N HCl_(aq). The yellow precipitate was filtered off, washed with dest. water (50 mL) and transferred to a pressure tube. Ammonium acetate (16.0 g, 207 mmol), aqueous ammonia (25%, 30 mL) and ethanol (50 mL) were added and the mixture was stirred for 24 h at 60 °C. Ethanol was removed and the aqueous residue was filtrated. The filtrate was reduced to half of its volume, cooled with an ice bath and filtered again. The obtained solid was dried in high vacuum, giving the product as white solid (9.81 g, 39,4 mmol, 59 %).

¹H NMR (400 MHz, DMSO-d₆) δ = 10.93 (s, 1H, H₈), 8.66 (d, J = 4.0 Hz, 2H, H_{1,14}), 8.55 (d, J = 7.9 Hz, 2H, H_{4,11}), 7.94 (td, J = 7.8, 1.7 Hz, 2H, H_{3,12}), 7.84 (s, 2H, H_{16,17}), 7.43 (ddd, J = 7.3, 4.9, 1.0 Hz, 2H, H_{2,13}) ppm.

The substance is literature-known and the ¹H NMR data corresponds to literature data.^[188]

7.3.10. Synthesis of [2,2':6',2'']-Terpyridine]-4'-yl-trifluoromethanesulfonate

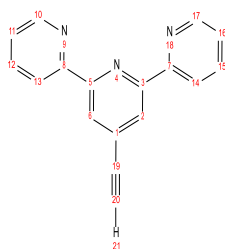


[2,2':6',2'']-Terpyridine]-4'(1'H)-on (9.50 g, 38.11 mmol) was dissolved in dry pyridine (40 mL) and cooled with an ice bath to 0 °C. Trifluoromethanesulfonic anhydride (16.13 g, 9.62 mL, 57.17 mmol) was added slowly and the mixture was stirred for 6 d at RT. Ice (400 g) was added, the mixture stirred for 30 min and filtrated. The obtained solid was dried and recrystallised from *n*-hexane, which afforded the product as a white solid (4.57 g, 11.98 mmol, 32 %).

¹H NMR (400 MHz, CDCl₃) δ = 8.73 (ddd, J = 4.7, 1.6, 0.8 Hz, 2H, H_{13,14}), 8.62 (d, J = 8.0 Hz, 2H, H_{10,17}), 8.43 (s, 2H, H_{2,6}), 7.89 (td, J = 7.7, 1.8 Hz, 2H, H_{12,15}), 7.40 (ddd, J = 7.5, 4.8, 1.1 Hz, 2H, H_{11,16}) ppm.

The substance is literature-known and the ¹H NMR data corresponds to literature data.^[188]

7.3.11. Synthesis of 4'-Ethynyl-2,2':6',2'']-terpyridin



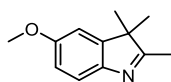
In a pressure tube, [2,2':6',2'']-terpyridine]-4'-yl-trifluoromethanesulfonate (2.50 g, 6.55 mmol) was dissolved in dry DMF (10 mL) and dry THF (40 mL). Pd(PPh₃)₂Cl₂ (230 mg, 0.328 mmol) was added and the mixture was degassed with an argon stream for 10 min. Ethynyltrimethylsilane (2.80 mL, 19.66 mmol), dry TEA (30 mL) and copper(I)-iodide (62.5 mg, 0.328 mmol) were added and the mixture stirred for 24 h at 60 °C. The solvents were removed and the residue was purified by column chromatography (basic alox, DCM/*n*-hex 1:1 + 2% TEA). The obtained white solid was dissolved in THF (80 mL) and methanol (60 mL), mixed with potassium fluoride (5.72 g, 98.25 mmol) and stirred for 12 h at RT. The solvents were removed and the residue was dissolved in DCM (100 mL). The solution was washed with dest. water (80 mL), dried with magnesium sulfate, filtrated and the solvent removed. The residue

was purified by column chromatography (basic alox, DCM/n-hexane 4:1 + 2% TEA), which afforded the product as white solid (1.48 g, 5.74 mmol, 87%).

$^1\text{H NMR}$ (400 MHz, CDCl_3): $\delta = 8.71$ (d, $J = 4.6$ Hz, 2H, $\text{H}_{13,14}$), 8.60 (d, $J = 8.0$ Hz, 2H, $\text{H}_{10,17}$), 8.54 (s, 2H, $\text{H}_{2,6}$), 7.87 (td, $J = 7.8, 1.7$ Hz, 2H, $\text{H}_{12,15}$), $7.38 - 7.33$ (m, 2H, $\text{H}_{11,16}$), 3.32 (s, 1H, H_{alkyne}) ppm.

The substance is literature known and the $^1\text{H NMR}$ data corresponds to literature data.^[188]

7.3.12. Synthesis of 5-methoxy-2,3,3-trimethyl-3H-indole

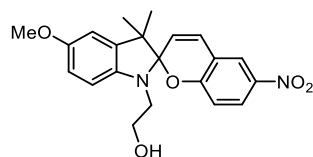


p-Anisidine (24.6 g, 200 mmol) was dissolved in methyl isopropyl ketone (100 mL) and cooled to 0°C with an ice bath. Conc. HCl (300 mL) was added and the solution stirred for 5 min. A solution of sodium nitrite (16.5 g, 240 mmol) in dest. water (30 mL) was added dropwise and the solution was stirred for further 2 h at 0°C . The mixture was cooled with an NaCl/ice bath to -15°C and a solution of tin(II)chloride (135 g, 600 mmol) in conc. HCl (100 mL) was added dropwise. The mixture was stirred for 12 h while slowly warming up to room temperature. The solution was neutralised with sodium hydroxide (approximately 135 g) and remaining methyl isopropyl ketone was removed in vacuum. The aqueous residue was extracted with diethyl ether (2 x 250 mL). The organic phases were combined, dried with magnesium sulfate, filtered and the solvent evaporated. The residue was dissolved in ethanol (300 mL). Methyl isopropyl ketone (34.1 mL, 400 mmol) and conc. sulphuric acid (10.7 mL, 200 mmol) were added and the solution refluxed for 12 h. The solvents were evaporated and the residue was dissolved in DCM (300 mL). The solution was washed with saturated aqueous sodium hydrogencarbonate solution (1 x 200 mL), dried with magnesium sulfate, filtered and the solvent evaporated. The residue was purified by column chromatography (silica, DCM/EE 12.5 :1), which afforded the product as a brown oil (18.2 g, 96.2 mmol, 48 %).

$^1\text{H NMR}$ (400 MHz, CDCl_3) $\delta = 7.40$ (d, $J = 8.2$ Hz, 1H, H_{Ar}), $6.86 - 6.75$ (m, 2H, H_{Ar}), 3.79 (s, 3H, H_{OCH_3}), 2.21 (s, 3H, H_{CH_3}), 1.25 (s, 6H, H_{CH_3}) ppm.

The substance is literature-known and the $^1\text{H NMR}$ data corresponds to literature data.^[218]

7.3.13. Synthesis of 2-(5'-methoxy-3',3'-dimethyl-6-nitrospiro[chromene-2,2'-indolin]-1'-yl)ethan-1-ol

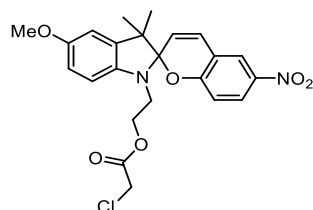


5-Methoxy-2,3,3-trimethyl-3H-indole (945 mg, 5.00 mmol) and 2-bromoethanol (0.440 mL, 6.25 mmol) was dissolved in dry toluene and refluxed for 2 d. The solvent was removed and the residue was suspended in *n*-hexane (40 mL), sonicated for 15 min and the solvent decanted off. The solid was dissolved in DCM (50 mL) and a solution of KOH (450 mg, 8.00 mmol) in dest. Water (10 mL) was added. The mixture was stirred for 15 min. The phases were separated and the aqueous phase extracted with DCM (1 x 50 mL). The organic phases were combined, dried with magnesium sulfate, filtered and the solvent evaporated. The residue and 2-hydroxy-5-nitrobenzaldehyde (1.25 g, 7.00 mmol) were dissolved in dry EtOH (25 mL) and refluxed for 2 d. The solvent was removed and the residue was purified by column chromatography (silica, DCM -> DCM/EE 9:1), which afforded the product as yellow solid (1.13 g; 2.95 mmol; 59 %).

$^1\text{H NMR}$ (400 MHz, CDCl_3) δ = 8.04 – 7.95 (m, 2H, H_{Ar}), 6.88 (d, J = 10.1 Hz, 1H, H_{CH}), 6.79 – 6.66 (m, 3H, H_{Ar}), 6.57 (d, J = 0.6 Hz, 1H, H_{Ar}), 5.86 (d, J = 10.3 Hz, 1H, H_{CH}), 3.78 (s, 3H, H_{OMe}), 3.84 – 3.66 (m, 2H, H_{CH_2}), 3.43 – 3.20 (m, 2H, H_{CH_2}), 1.26 (s, 3H, H_{CH_3}), 1.18 (s, 3H, H_{CH_3}) ppm.

The substance is literature-known and the $^1\text{H NMR}$ data corresponds to literature data.^[86]

7.3.14. Synthesis of 2-(5'-methoxy-3',3'-dimethyl-6-nitrospiro[chromene-2,2'-indolin]-1'-yl)ethan-1-ol



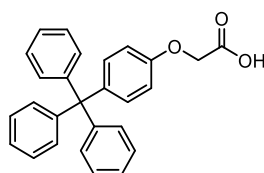
A solution of 2-(6'-methoxy-1',1'-dimethyl-6-nitro-1',3'-dihydrospiro[chromene-2,2'-inden]-3'-yl)ethan-1-ol (530 mg, 1.39 mmol) in dry CHCl_3 (20.0 mL) and TEA (0.800 mL, 3.20 mmol) was cooled with an ice bath to 0 °C. Chloroacetic acid chloride (0.250 mL, 3.20 mmol) was added dropwise. The solution was stirred for 10 min at 0°C and further 5 h at room temperature. The

solution was washed with dest. Water (2 x 20 mL), dried with magnesium sulfate, filtered and the solvent evaporated. The residue was purified by column chromatography (silica, DCM/*n*-hexane 19:1 -> DCM), which afforded the product as yellow solid (250 mg, 0.546 mmol, 39 %).

¹H NMR (400 MHz, CDCl₃) δ = 8.03 – 7.97 (m, 2H, H_{Ar}), 6.91 (d, J = 10.4 Hz, 1H, H_{CH}), 6.77 – 6.69 (m, 3H, H_{Ar}), 6.57 (d, J = 9.2 Hz, 1H, H_{Ar}), 5.90 (d, J = 10.4 Hz, 1H, H_{CH}), 4.43 – 4.24 (m, 2H, H_{CH2}), 4.00 (d, J = 2.9 Hz, 2H, H_{CH2}), 3.79 (s, 3H, H_{OMe}), 3.56 – 3.30 (m, 2H, H_{CH2}), 1.25 (s, 3H, H_{CH3}), 1.16 (s, 3H, H_{CH3}) ppm.

The substance is literature-known and the ¹H NMR data corresponds to literature data.^[86]

7.3.15. Synthesis of 2-(4-tritylphenoxy)acetic acid

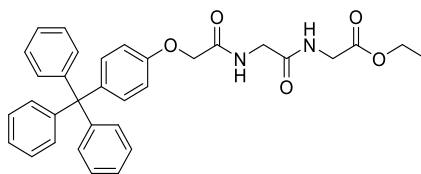


4-Tritylphenol (2.35 g, 7.00 mmol), bromoacetic acid ethyl ester (0.770 mL, 7.00 mmol) and potassium carbonate (2.90 g, 21.0 mmol) were dissolved in dry acetone (150 mL) and refluxed for 12 h. After cooling down to room temperature, the solution was filtrated and the solvent removed in vacuum. The residue was dissolved in DCM (100 mL), washed with dest. water (2 x 50 mL), dried with magnesium sulfate, filtered and the solvent evaporated. The residue was dissolved in THF (50 mL), LiOH (335 mg, 14.0 mmol) was added and the solution stirred for 3 d at room temperature. 1N HCl (100 mL) was added, the mixture filtrated and the obtained solid was dried in vacuum, which afforded the product as a white solid (1.80 g, 4.56 mmol, 65 %).

¹H NMR (400 MHz, DMSO-d₆) δ = 13.00 (s, 1H, H_{OH}), 7.39 – 7.08 (m, 15H, H_{Ar}), 7.03 (d, J = 9.0 Hz, 2H, H_{Ar}), 6.84 (d, J = 9.0 Hz, 2H, H_{Ar}), 4.63 (s, 2H, H_{CH2}) ppm.

The substance is literature-known and the ¹H NMR data corresponds to literature data.^[86]

7.3.16. Synthesis of (2-(4-tritylphenoxy)acetyl)glycylglycine ethyl ester

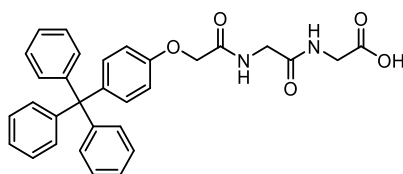


2-(4-Tritylphenoxy)acetic acid (788 mg, 2.00 mmol), glycylglycine ethyl ester hydrochloride (393 mg, 2.00 mmol) and DMAP (274 mg, 2.25 mmol) were dissolved in dry DCM (80 mL) and cooled with an ice bath to 0 °C. 1-Ethyl-3-(3-dimethylaminopropyl)carbodiimide (388 mg, 2.5 mmol) was added dropwise and the mixture was stirred for 12 h while slowly warming up to room temperature. The solution was washed with saturated aqueous NaHCO₃ solution (50 mL), dest. water (50 mL) and brine (50 mL), dried over magnesium sulfate, filtered and the solvent evaporated. The residue was purified by column chromatography (silica, DCM/EE 1:1), which afforded the product as white solid (820 mg, 1.53 mmol, 76 %).

¹H NMR (400 MHz, CDCl₃) δ = 7.30 (br, 1H, H_{NH}), 7.27 – 7.08 (m, 17H, H_{Ar}), 6.81 (d, J = 8.9 Hz, 2H, H_{Ar}), 6.54 (br, 1H, H_{NH}), 4.52 (s, 2H, H_{CH2}), 4.19 (q, J = 7.0 Hz, 2H, H_{CH2}), 4.08 (d, J = 5.7 Hz, 2H, H_{CH2}), 4.03 (d, J = 5.2 Hz, 2H, H_{CH2}), 1.27 (t, J = 7.0 Hz, 3H, H_{CH3}) ppm.

The substance is literature-known and the ¹H NMR data corresponds to literature data.^[86]

7.3.17. Synthesis of (2-(4-tritylphenoxy)acetyl)glycylglycine



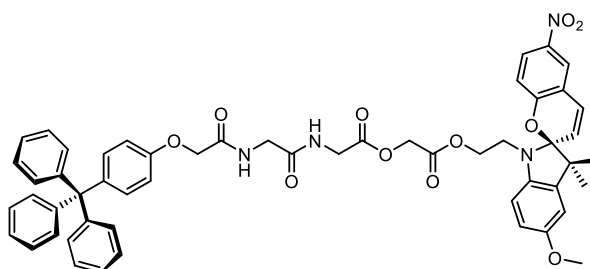
(2-(4-Tritylphenoxy)acetyl)glycylglycine ethyl ester (2.50 g, 4.66 mmol) was dissolved in EtOH/THF 1:1 (190 mL), cooled with an ice bath to 0 °C and mixed with aqueous NaOH (1 mol/L, 8 mL). The solution was stirred for 1.5 h at 0 °C and then neutralised with aqueous HCl (1 mol/L, approx. 8 mL). The organic solvents were removed and the aqueous residue was filtered. The solid was washed with dest. water (3 x 100 mL) and dried in high vacuum, which afforded the product as white solid (2.28 g, 4.48 mmol, 96 %).

¹H NMR (400 MHz, DMSO-d₆) δ = 8.29 (t, J = 5.9 Hz, 1H, H_{NH}), 8.17 (t, J = 5.9 Hz, 1H, H_{NH}), 7.25 (d, J = 8.0 Hz, 6H, H_{Ar}), 7.20 – 7.14 (m, 3H, H_{Ar}), 7.09 (d, J = 8.0 Hz, 6H, H_{Ar}), 7.01 (d, J = 9.0 Hz, 2H,

H_{Ar}), 6.89 (d, *J* = 9.0 Hz, 2H, H_{Ar}), 4.47 (s, 2H, H_{CH2}), 3.77 (d, *J* = 5.9 Hz, 2H, H_{CH2}), 3.72 (d, *J* = 5.9 Hz, 2H, H_{CH2}) ppm.

The substance is literature-known and the ¹H NMR data corresponds to literature data [86]

7.3.18. Synthesis of 2-(2-(5'-methoxy-3',3'-dimethyl-6-nitrospiro[chromene-2,2'-indolin]-1'-yl)ethoxy)-2-oxoethyl (2-(4-tritylphenoxy)acetyl)glycylglycinate



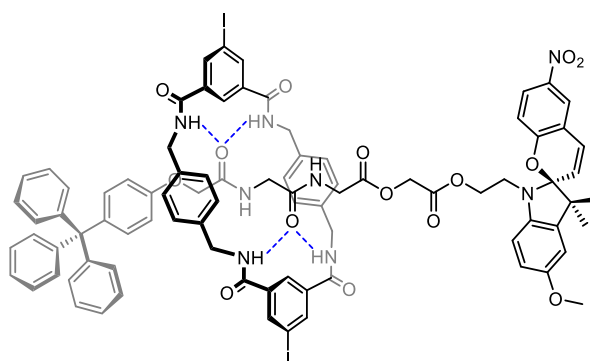
(2-(4-Tritylphenoxy)acetyl)glycylglycine (1.50 g, 2.95 mmol), 2-(5'-methoxy-3',3'-dimethyl-6-nitrospiro[chromene-2,2'-indolin]-1'-yl)ethyl-2-chloroacetate (1.35 g, 2.95 mmol) and potassium carbonate (815 mg, 5.90 mmol) were dissolved in dry DMF (120 mL) and stirred for 48 h at RT. The solvent was removed in vacuum without heating the mixture over RT. The residue was dissolved in DCM (200 mL) and dest. water (100 mL) was added. The mixture was neutralised with 1N aqueous HCl and the phases were separated. The organic phase was dried with sodium sulfate, filtrated and the solvent evaporated. The residue was purified by column chromatography (silica, DCM/EE 1:1), which afforded the product as light yellow solid (2.60 g, 2.79 mmol, 94%).

¹H NMR (400 MHz, CDCl₃): δ = 8.05 – 7.95 (m, 2H, H_{Ar}), 7.35 (t, *J* = 5.7 Hz, 1H, H_{Ar}), 7.27 – 7.11 (m, 15H, H_{Ar}), 6.91 (d, *J* = 10.4 Hz, 1H, H_{Ar}), 6.79 (d, *J* = 8.9 Hz, 2H, H_{Ar}), 6.76 – 6.67 (m, 4H, H_{Ar}), 6.53 (d, *J* = 9.3 Hz, 1H, H_{Ar}), 5.84 (d, *J* = 10.3 Hz, 1H, H_{Ar}), 4.58 (d, *J* = 4.4 Hz, 2H, H_{CH2}), 4.51 (s, 2H, H_{CH2}), 4.28 (tq, *J* = 9.3, 4.9 Hz, 2H, H_{CH2}), 4.18 – 4.02 (m, 4H, H_{CH2}), 3.77 (s, 3H, H_{OCH3}), 3.46 (dt, *J* = 15.3, 6.4 Hz, 1H, H_{CH2}), 3.32 (dt, *J* = 15.2, 6.1 Hz, 1H, H_{CH2}), 1.24 (s, 3H, H_{CH3}), 1.15 (s, 3H, H_{CH3}).

MS (ESI, pos. Mode, MeOH/DCM): m/z calculated 930.3470 found 931.3429 ($[M+H]^+$),
calculated 953.3368 found 953.3331 ($[M+Na]^+$),
calculated 969.3108 found 969.3069 ($[M+K]^+$).

The substance is literature-known and the 1H NMR data corresponds to literature data ^[86]

7.3.19. Synthesis of Rot5



2-(2-(5'-methoxy-3',3'-dimethyl-6-nitrospiro[chromene-2,2'-indolin]-1'-yl)ethoxy)-2-oxoethyl (2-(4-tritylphenoxy)acetyl)glycylglycinate (200 mg, 0.214 mmol) was dissolved in dry DCM (90 mL) and TEA (217 mg, 0.300 mL, 2.15 mmol) was added. 5-Iodoisophthalic acid chloride was dissolved in dry DCM (24 mL). 1,4-Phenylenedimethanamine was dissolved in dry DCM (24 mL) and TEA (217 mg, 0.300 mL, 2.15 mmol) was added. Both solutions were added simultaneously over 2 h with a syringe pump to the first solution, while stirring it. The solution was stirred for further 12 h. It was then diluted with $CHCl_3$ (100 mL) and filtered over celite. The solvent was evaporated and the residue purified by column chromatography (silica, $CHCl_3/EE$ 3:2). The product was dissolved in DCM and filtrated after 2 h. The solvent was removed, which afforded the pure product as yellow-brown solid (110 mg, 0.064 mmol, 29%).

1H NMR (400 MHz, $CDCl_3$): δ = 8.38 (d, J = 1.4 Hz, 4H, $H_{isophthal}$), 8.27 (s, 2H, $H_{isophthal}$), 7.97 – 7.88 (m, 3H, H_{Ar}), 7.49 (t, J = 4.8 Hz, 4H, $H_{amide\ TLM}$), 7.26 – 7.20 (m, 6H, H_{Ar}), 7.18 – 7.11 (m, 17H, H_{Ar}), 7.05 (d, J = 9.0 Hz, 2H, H_{Ar}), 6.87 (d, J = 10.3 Hz, 1H, $H_{spiropyran}$), 6.71 – 6.64 (m, 4H, H_{Ar}), 6.49 (dd, J = 7.6, 1.2 Hz, 1H, $H_{spiropyran}$), 6.36 (d, J = 9.0 Hz, 2H, $H_{spiropyran}$), 5.80 (d, J = 10.2 Hz, 1H, $H_{spiropyran}$), 4.42 (s, 8H, $H_{CH_2\ TLM}$), 4.30 – 4.12 (m, 2H, $H_{CH_2\ axle}$), 4.01 (s, 2H, $H_{CH_2\ axle}$), 3.81 (d, J = 5.6 Hz, 2H, $H_{CH_2\ axle}$), 3.75 (s, 3H, H_{OCH_3}), 3.72 – 3.63 (m, 2H, $H_{CH_2\ axle}$), 3.62 – 3.43 (m, 2H, $H_{CH_2\ axle}$), 3.43

– 3.24 (m, 2H, H_{CH₂ axle}), 1.24 (s, 3H, H_{CH₃}), 1.21 (s, 3H, H_{CH₃}) ppm.

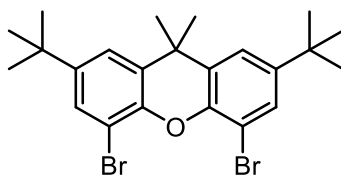
¹³C NMR (101 MHz, CDCl₃)

δ = 169.7, 169.1, 168.5, 167.0, 165.2, 165.1, 159.5, 154.4, 154.3, 146.7, 141.5, 141.0, 140.7, 140.2, 137.4, 135.7, 132.6, 131.1, 131.0, 129.2, 128.6, 127.7, 127.6, 126.1, 123.53, 122.9, 121.7, 118.5, 116.6, 115.6, 113.4, 111.6, 109.9, 107.0, 106.7, 94.8, 72.6, 71.3, 70.6, 70.2, 64.4, 63.8, 61.9, 61.1, 56.0, 53.1, 44.3, 42.7, 41.5, 41.0, 29.8, 19.9 ppm.

MS (ESI, pos. Mode, MeOH/DCM): m/z calculated 1715.3592 found 1715.3578 ([M+H]⁺),
calculated 1737.3412 found 1737.3384 ([M+Na]⁺),
calculated 1753.3151 found 1753.3130 ([M+K]⁺).

7.4. Experimental Procedures for chapter 4.2.1

7.4.1. Synthesis of 4,5-dibromo-2,7-di-*tert*-butyl-9,9-dimethyl-9H-xanthene

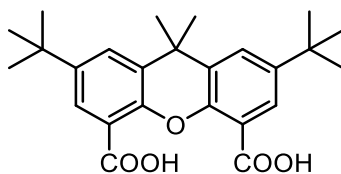


A solution of 2,7-di-*tert*-butyl-9,9-dimethyl-9H-xanthene (5.00 g, 15.5 mmol) in dry CHCl_3 (60 mL) was cooled to 0 °C with an ice bath. Bromine (1.80 mL, 35.1 mmol) was added dropwise and the solution was stirred for 2 h at 0 °C. A second portion of bromine (1.50 mL, 29.3 mmol) was added and the solution stirred for another 12 h while slowly warming up to room temperature. Saturated NaHSO_3 solution was added after complete decolouration of the mixture. Water (100 mL) and DCM (50 mL) were added, the phases separated and the aqueous phase extracted with DCM (50 mL). The organic phases were combined, dried with magnesium sulfate, filtered and the solvent evaporated, which afforded the product as a white solid (7.44 g, 15.5 mmol, quant.).

^1H NMR (400 MHz, CDCl_3): δ = 7.48 (d, J = 2.2 Hz, 2H, $\text{H}_{\text{xanthene}}$), 7.33 (d, J = 2.2 Hz, 2H, $\text{H}_{\text{xanthene}}$), 1.63 (s, 6H, H_{CH_3}), 1.32 (s, 18H, $\text{H}_{\text{t-Bu}}$) ppm.

The substance is literature-known and the ^1H NMR data corresponds to literature data.^[67b] The procedure was modified in comparison to the literature known one and is therefore described here.

7.4.2. Synthesis of 2,7-di-*tert*-butyl-9,9-dimethyl-9H-xanthene-4,5-dicarboxylic acid



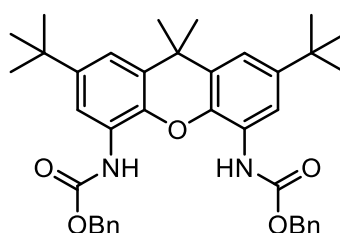
In a three-necked round flask, 4,5-dibromo-2,7-di-*tert*-butyl-9,9-dimethyl-9H-xanthene (7.4 g, 15.4 mmol) was dissolved in dry THF (200 mL) and cooled with an acetone/dry ice bath to -78 °C. A solution of *n*-butyllithium (1.6 M in *n*-hexane, 32.0 mL, 50.0 mmol) was slowly added and the mixture stirred for further 20 min at -78 °C. CO_2 was produced by evaporating dry ice (approximately 250 g, excess) in a round flask, bubbled through conc. H_2SO_4 and passed into the solution for approx. 2 h. The reaction was quenched with ice (50 g) and conc. HCl (20 mL).

Diethyl ether (100 mL) was added and the phases separated. The aqueous phase was extracted with diethyl ether (100 mL). The organic phases were combined, dried with magnesium sulfate, filtered and the solvent evaporated. The residue was suspended in *n*-hexane (50 mL), stirred and filtered and the solid was washed again with *n*-hexane, which afforded the product as white solid (3.93 g, 9.57 mmol, 62 %).

$^1\text{H NMR}$ (400 MHz, CDCl_3): $\delta = 8.17$ (d, $J = 2.5$ Hz, 2H, $\text{H}_{\text{xanthene}}$), 7.71 (d, $J = 2.5$ Hz, 2H, $\text{H}_{\text{xanthene}}$), 1.70 (s, 6H, H_{CH_3}), 1.38 (s, 18H, $\text{H}_{\text{t-Bu}}$) ppm.

The substance is literature-known and the $^1\text{H NMR}$ data corresponds to literature data. ^[67b] The procedure was modified in comparison to the literature known one and is therefore described here.

7.4.3. Synthesis of dibenzyl (2,7-di-*tert*-butyl-9,9-dimethyl-9H-xanthene-4,5-diyl)dicarbamate

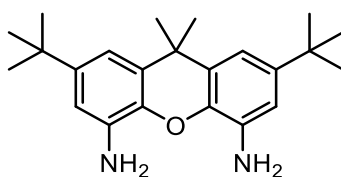


2,7-di-*tert*-butyl-9,9-dimethyl-9H-xanthene-4,5-dicarboxylic acid (3.92 g, 9.55 mmol) was suspended in dry toluene (50 mL) and diphenylphosphoryl azide (5.38 mL, 26.7 mmol) was slowly added and the solution stirred for 5 min at room temperature. Triethyl amine (3.70 mL, 26.7 mmol) was added, resulting in a clear yellow solution. After 15 min, benzyl alcohol (3.17 mL, 30.5 mmol) was added dropwise and the mixture stirred for 12 h at 80 °C. The solvent was evaporated and the residue purified by column chromatography (silica, DCM/*n*-hexane 4:1 -> 9:1 -> DCM) affording the pure product as a white solid (4.73 g, 7.62 mmol, 79 %).

$^1\text{H NMR}$ (400 MHz, CDCl_3): $\delta = 7.77$ (s, 2H, H_{NH}), 7.31 (m, 12 $\text{H}_{\text{xanthene, phenyl}}$), 7.16 (d, $J = 2.3$ Hz, 2H, $\text{H}_{\text{xanthene}}$), 5.16 (s, 4H, H_{CH_2}), 1.62 (s, 6H, H_{CH_3}), 1.32 (s, 18H, $\text{H}_{\text{t-Bu}}$) ppm.

The substance is literature-known and the $^1\text{H NMR}$ data corresponds to literature data. ^[219] The procedure was modified in comparison to the literature known one and is therefore described here.

7.4.4. Synthesis of 2,7-di-*tert*-butyl-9,9-dimethyl-9H-xanthene-4,5-diamine

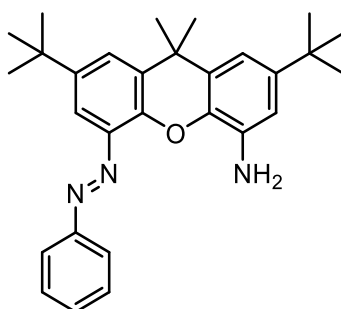


A solution of potassium hydroxide (6.2 g, 110 mmol) in water (40 mL) was added to a solution of dibenzyl-(2,7-di-*tert*-butyl-9,9-dimethyl-9H-xanthene-4,5-diyl)dicarbamate (4.73 g, 7.62 mmol) in ethanol (100 mL). The mixture was refluxed for 24 h. Ethanol was removed in vacuo and the aqueous residue was diluted with water (200 mL) and extracted with diethyl ether (2 x 150 mL). The organic phases were combined, dried with magnesium sulfate, filtered and the solvent evaporated. The residue was purified by column chromatography (silica, EE/*n*-hexane 1:1 + 1% triethyl amine) which afforded the pure product as a light-brown solid (2.63 g, 7.47 mmol, 98 %).

^1H NMR (400 MHz, CDCl_3): δ = 6.84 (d, J = 2.2 Hz, 2H, $\text{H}_{\text{xanthene}}$), 6.69 (d, J = 2.2 Hz, 2H, $\text{H}_{\text{xanthene}}$), 3.81 (s, 4H, H_{NH_2}), 1.62 (s, 6H, H_{CH_3}), 1.30 (s, 18H, $\text{H}_{\text{t-Bu}}$) ppm.

The substance is literature-known and the ^1H NMR data corresponds to literature data.^[67b] The procedure was modified in comparison to the literature known one and is therefore described here.

7.4.5. Synthesis of (*E*)-2,7-di-*tert*-butyl-9,9-dimethyl-5-(phenyldiazenyl)-9H-xanthene-4-amine



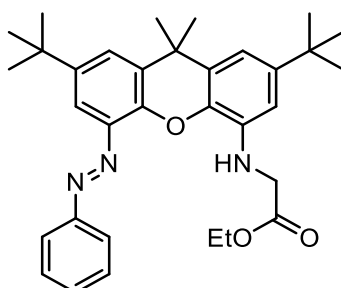
Acetic acid (2.5 mL) was added to a solution of 2,7-di-*tert*-butyl-9,9-dimethyl-9H-xanthene-4,5-diamine (3.48 g, 9.87 mmol) in dry CHCl_3 (150 mL). A solution of nitrosobenzene (1.05 g, 9.87 mmol) in dry CHCl_3 (15 mL) was added over 90 min via a syringe pump to the mixture which was afterwards stirred for further 18 h. The solution was diluted with DCM (100 mL), washed with saturated NaHCO_3 solution (1 x 100 mL) and brine (1 x 100 mL), dried with magnesium

sulfate, filtered and the solvent evaporated. The crude product was purified by column chromatography (silica, DCM/*n*-hexane 1:1 → DCM → DCM/EE 1:1 → DCM/EE 1:4) which afforded the product as an orange solid (2.35 g, 5.33 mmol, 54%).

¹H NMR (400 MHz, CDCl₃): δ = 7.97 (d, *J* = 7.4 Hz, 2H, H_{xanthene}), 7.59 (m, 2H, H_{azobenzene}), 7.53 (m, 2H, H_{azobenzene}), 7.47 (m, 1H, H_{azobenzene}), 6.85 (d, *J* = 2.0 Hz, 1H, H_{xanthene}), 6.73 (d, *J* = 2.0 Hz, 1H, H_{xanthene}), 4.03 (s, 2H, H_{NH2}), 1.69 (s, 6H, H_{CH3}), 1.38 (s, 9H, H_{*t*-Bu}), 1.32 (s, 9H, H_{*t*-Bu}) ppm.

The substance is literature-known and the ¹H NMR data corresponds to literature data.^[67b] The procedure was modified in comparison to the literature known one and is therefore described here.

7.4.6. Synthesis of ethyl (*E*)-(2,7-di-*tert*-butyl-9,9-dimethyl-5-(phenyldiazenyl)-9H-xanthen-4-yl)glycinate



(*E*)-2,7-di-*tert*-butyl-9,9-dimethyl-5-(phenyldiazenyl)-9H-xanthen-4-amine (2.37 g, 5.37 mmol) was dissolved in dry DMF (60 mL) and bromoacetic acid ethyl ester (1.12 g, 6.71 mmol, 0.74 mL) and NaHCO₃ (4.50 g, 53.7 mmol) were added. The reaction was stirred for 18 h at 95 °C. After cooling to room temperature, DCM (100 mL) was added and the solution was washed with water (2 x 60 mL). The organic phase was dried with magnesium sulfate, filtered and the solvent evaporated. The residue was purified by column chromatography (silica, DCM/*n*-hexane 7:3) which afforded the pure product as an orange solid (2.16 g, 4.09 mmol, 76%).

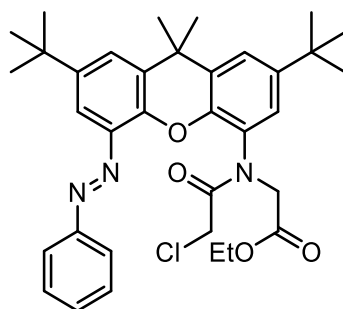
¹H NMR (400 MHz, CDCl₃): δ = 8.16 (m, 2H, H_{azobenzene}), 7.66 (d, *J* = 2.4 Hz, 1H, H_{xanthene}), 7.57 (d, *J* = 2.4 Hz, 1H, H_{xanthene}), 7.57 (m, 2H, H_{azobenzene}), 7.47 (m, 1H, H_{azobenzene}), 6.83 (d, *J* = 2.2 Hz, 1H, H_{xanthene}), 6.48 (d, *J* = 2.2 Hz, 1H, H_{xanthene}), 5.29 (s, 1H, H_{NH}), 4.31 (q, *J* = 7.2 Hz, 2H, H_{ethyl-CH2}), 4.02 (d, *J* =

4.4 Hz, 2H, H_{CH2}), 1.69 (s, 6H, H_{CH3}), 1.38 (s, 9H, H_{t-Bu}),
1.34 (s, 9H, H_{t-Bu}), 1.32 (t, *J* = 7.2 Hz, 3H, H_{ethyl-CH3}) ppm.

¹³C NMR (101 MHz, CDCl₃): δ = 170.9, 153.4, 146.4, 146.3, 145.3, 140.0, 136.2,
135.5, 132.0, 130.8, 129.2, 128.7, 126.1, 123.6, 111.5,
110.5, 106.2, 61.3, 46.0, 35.0, 34.9, 34.9, 32.1, 31.8,
31.6, 14.4 ppm.

HR-MS (ESI-TOF, pos. Mode, MeOH) m/z: calculated 528.3221, found 528.3242
([M+H]⁺); calculated 550.3040, found 550.3068
([M+Na]⁺); calculated 566.2780, found 566.2802
([M+K]⁺).

7.4.7. Synthesis of ethyl (*E*)-*N*-(2-chloroacetyl)-*N*-(2,7-di-*tert*-butyl-9,9-dimethyl-5-(phenyldiazenyl)-9H-xanthen-4-yl)glycinate



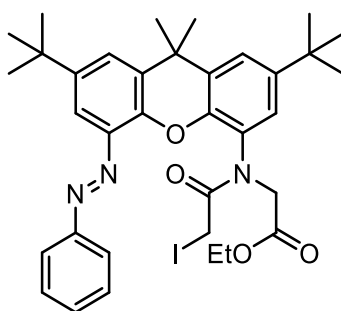
Diisopropylethylamine (3.16 g, 24.5 mmol, 4.16 mL) was added to a solution of ethyl (*E*)-(2,7-di-*tert*-butyl-9,9-dimethyl-5-(phenyldiazenyl)-9H-xanthen-4-yl)glycinate (2.16 g, 4.08 mmol) in dry DCM (60 mL). The solution was cooled with an ice bath to 0 °C followed by addition of chloroacetic acid chloride (2.77 g, 24.5 mmol, 1.95 mL). The solution was stirred for another 12 h, slowly warming to room temperature. The solution was washed with saturated NH₄Cl solution (1 x 30 mL) and water (1 x 30 mL), dried with magnesium sulfate, filtered and the solvent evaporated. The residue was purified by column chromatography (silica, DCM -> DCM/EE 9:1) which afforded the pure product as an orange solid (2.04 g, 3.38 mmol, 83%).

¹H NMR (400 MHz, CDCl₃): δ = 8.00 (m, 2H, H_{azobenzene}), 7.64 (d, *J* = 2.3 Hz, 1H, H_{xanthene}), 7.59 (m, 2H, H_{azobenzene}), 7.58 (m, 1H, H_{xanthene}), 7.51 (m, 2H, H_{xanthene}), 7.49 (m, 1H, H_{azobenzene}), 5.12 (d, *J* = 17.4 Hz, 1H, H_{CH2}), 4.17 (m, 2H, H_{CH2-CH3}), 4.01 (s, 2H, H_{CH2}), 3.92 (d, *J* = 17.4 Hz, 1H, H_{CH2}), 1.74 (s, 3H, H_{Me}), 1.72 (s, 3H, H_{CH3}), 1.39 (s, 9H, H_{t-Bu}), 1.36 (s, 9H, H_{t-Bu}), 1.24 (t, 3H, H_{CH2-CH3}) ppm.

^{13}C NMR (101 MHz, CDCl_3): $\delta = 169.2, 167.2, 153.1, 146.9, 146.6, 145.5, 143.9, 140.3, 131.7, 131.4, 131.3, 129.4, 128.4, 125.3, 123.5, 123.2, 120.8, 111.8, 61.3, 51.0, 41.9, 35.2, 35.0, 34.7, 32.1, 32.0, 31.6, 31.5, 14.3$ ppm.

HR-MS (ESI-TOF, pos. Mode, MeOH) m/z: calculated 604.2937, found 604.2935 ($[\text{M}+\text{H}]^+$); calculated 626.2756, found 626.2757 ($[\text{M}+\text{Na}]^+$); calculated 642.2495, found 642.2493 ($[\text{M}+\text{K}]^+$).

7.4.8. Synthesis of ethyl (*E*)-*N*-(2,7-di-*tert*-butyl-9,9-dimethyl-5-(phenyldiazenyl)-9H-xanthen-4-yl)-*N*-(2-iodoacetyl)glycinate



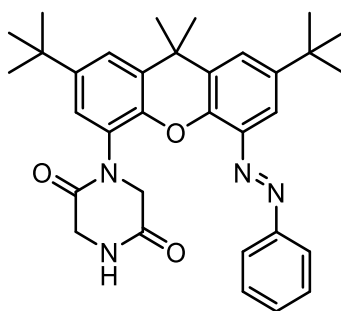
Sodium iodide (1.80 g, 11.9 mmol) was added to a solution of ethyl (*E*)-*N*-(2-chloroacetyl)-*N*-(2,7-di-*tert*-butyl-9,9-dimethyl-5-(phenyldiazenyl)-9H-xanthen-4-yl)glycinate (1.80 g, 2.98 mmol) in dry acetone (60 mL). After stirring for 18 hat room temperature, the solvent was evaporated. The residue was dissolved in DCM (50 mL) and washed with water (2 x 50 mL). The organic phase was dried with magnesium sulfate, filtered and the solvent evaporated to yield the product as an orange solid (2.05 g, 2.95 mmol, 99 %).

^1H NMR (400 MHz, CDCl_3): $\delta = 8.00$ (m, 2H, $\text{H}_{\text{azobenzene}}$), 7.64 (d, $J = 2.3$ Hz, 1H, $\text{H}_{\text{xanthene}}$), 7.61 (d, $J = 2.3$ Hz, 1H, $\text{H}_{\text{xanthene}}$), 7.58 (m, 2H, $\text{H}_{\text{azobenzene}}$), 7.58 (d, $J = 2.3$ Hz, 1H, $\text{H}_{\text{xanthene}}$), 7.50 (d, $J = 2.3$ Hz, 1H, $\text{H}_{\text{xanthene}}$), 7.48 (m, 1H, $\text{H}_{\text{azobenzene}}$), 5.12 (d, $J = 17.4$ Hz, 1H, H_{CH_2}), 4.17 (m, 2H, $\text{H}_{\text{CH}_2\text{-CH}_3}$), 3.87 (d, $J = 17.4$ Hz, 1H, H_{CH_2}), 3.73 (d, $J = 9.9$ Hz, 1H, H_{CH_2}), 3.57 (d, $J = 9.9$ Hz, 1H, H_{CH_2}), 1.75 (s, 3H, H_{CH_3}), 1.71 (s, 3H, H_{Me}), 1.38 (s, 9H, $\text{H}_{\text{t-Bu}}$), 1.38 (s, 9H, $\text{H}_{\text{t-Bu}}$), 1.26 (t, $J = 7.1$ Hz, 3H, $\text{H}_{\text{CH}_2\text{-CH}_3}$) ppm.

^{13}C NMR (101 MHz, CDCl_3) $\delta = 169.4, 168.8, 153.2, 146.6, 146.4, 145.6, 143.7, 140.2, 131.5, 131.4, 131.3, 129.4, 129.2, 125.5, 125.1, 123.5, 123.0, 111.7, 61.3, 50.9, 35.2, 35.0, 34.9, 32.2, 32.0, 31.6, 31.6, 14.3, -3.0$ ppm.

HR-MS (ESI-TOF, pos. Mode, MeOH/DCM) m/z : calculated 696.2293, found 696.2327
([M+H]⁺); calculated 718.2112, found 718.2155
([M+Na]⁺); calculated 734.1852, found 734.1893
([M+K]⁺).

7.4.9. Synthesis of (*E*)-1-(2,7-di-*tert*-butyl-9,9-dimethyl-5-(phenyldiazenyl)-9H-xanthen-4-yl)piperazine-2,5-dione



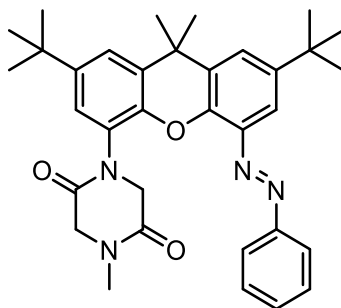
A solution of ammonia in methanol (7 M, 101 mL) was added to a solution of ethyl (*E*)-*N*-(2,7-di-*tert*-butyl-9,9-dimethyl-5-(phenyldiazenyl)-9H-xanthen-4-yl)-*N*-(2-iodoacetyl)glycinate (2.25 g, 3.23 mmol) in dry methanol (80 mL). After stirring for 24 h at room temperature, the solvent was evaporated. The crude product was cleaned via column chromatography (silica, DCM/MeOH 97:3) which afforded the pure product as an orange solid (1.55 g, 2.88 mmol, 89 %).

^1H NMR (500 MHz, CDCl_3): $\delta = 7.90 - 7.81$ (m, 2H, $\text{H}_{\text{azobenzene}}$), 7.58 (d, $J = 2.3$ Hz, 1H, $\text{H}_{\text{xanthene}}$), 7.54 (d, $J = 2.3$ Hz, 1H, $\text{H}_{\text{xanthene}}$), 7.53 – 7.49 (m, 2H, $\text{H}_{\text{azobenzene}}$), 7.49 (d, $J = 2.3$ Hz, 1H, $\text{H}_{\text{xanthene}}$), 7.51 – 7.41 (m, 1H, $\text{H}_{\text{azobenzene}}$), 7.17 (d, $J = 2.3$ Hz, 1H, $\text{H}_{\text{xanthene}}$), 6.12 (s, 1H, H_{NH}), 4.95 (bs, 1H, H_{CH_2}), 4.10 (bs, 1H, H_{CH_2}), 3.98 (s, 2H, H_{CH_2}), 1.73 (s, 6H, H_{CH_3}), 1.37 (s, 9H, H_{tBu}), 1.35 (s, 9H, H_{tBu}) ppm.

^{13}C NMR (126 MHz, CDCl_3): $\delta = 167.1, 164.5, 153.5, 146.6, 146.2, 145.5, 143.8, 140.4, 131.4, 131.4, 131.0, 127.0, 125.8, 123.7, 123.1, 122.7, 112.0, 52.5, 45.4, 35.1, 35.0, 34.8, 31.6, 31.6$ ppm.

HR-MS (ESI-TOF, pos. Mode, MeOH) m/z: calculated 539.3017, found 539.3038 ([M+H]⁺); caclcd. 561.2836, found 561.2861 ([M+Na]⁺); caclcd. 577.2576, found 577.2603 ([M+K]⁺).

7.4.10. Synthesis of (*E*)-1-(2,7-di-*tert*-butyl-9,9-dimethyl-5-(phenyldiazenyl)-9H-xanthen-4-yl)-4-methylpiperazine-2,5-dione



(*E*)-1-(2,7-di-*tert*-butyl-9,9-dimethyl-5-(phenyldiazenyl)-9H-xanthen-4-yl)piperazine-2,5-dione (250 mg, 0.464 mmol) was dissolved in dry THF (18 mL). The solution was cooled with an ice bath to 0 °C and potassium *tert*-butanolate (57.0 mg, 0.510 mmol) was added. After 10 min stirring and subsequent addition of methyl iodide (72.4 mmol, 0.032 mL, 0.510 mmol), the solution was stirred for further 2 h at 0 °C. It was then diluted with DCM (100 mL) and washed with water (1 x 50 mL). The organic phase was dried with magnesium sulfate, filtered and the solvent evaporated. The crude product was purified via column chromatography (silica, DCM/EE 9:1) which afforded the pure product as an orange solid (251 mg, 0.454 mmol, 98 %).

¹H NMR (500 MHz, CDCl₃) δ = 7.85 – 7.79 (m, 2H, H_{azobenzene}), 7.57 (d, J = 2.3 Hz, 1H, H_{xanthene}), 7.52 (d, J = 2.3 Hz, 1H, H_{xanthene}), 7.51 – 7.49 (m, 2H, H_{azobenzene}), 7.48 (d, J = 2.3 Hz, 1H, H_{xanthene}), 7.49 – 7.43 (m, 1H, H_{azobenzene}), 7.15 (d, J = 2.3 Hz, 1H, H_{xanthene}), 4.95 (bs, 1H, H_{CH2}), 4.07 (bs, 1H, H_{CH2}), 3.92 (s, 2H, H_{CH2}), 2.92 (s, 3H, H_{N-CH3}), 1.72 (s, 6H, H_{CH3}), 1.37 (s, 9H, H_{tBu}), 1.34 (s, 9H, H_{tBu}) ppm.

¹³C NMR (126 MHz, CDCl₃) δ = 164.3, 153.6, 146.6, 146.1, 145.1, 143.8, 140.6, 131.4, 131.3, 130.8, 129.2, 126.7, 125.7, 123.6, 123.1, 122.8, 112.5, 52.6, 52.1, 35.1, 35.0, 34.8, 33.4, 31.6, 31.6 ppm.

HR-MS (ESI-FTICR, pos. mode, DCM/MeOH) m/z: calculated 553.3173 found 553.3197
([M+H]⁺), m/z: calculated 575.2993 found 575.3021
([M+Na]⁺), m/z: calculated 591.2732 found 591.2762
([M+K]⁺).

7.4.11. Crystallographic data

Single crystal X-ray data for **35** were collected at 123 K using Agilent SuperNova single-source diffractometer with an Atlas EoS CCD detector using mirror-monochromated Mo-K α ($\lambda = 0.71073$ Å) radiation, and the data for **19** was measured at 100 K with Agilent Super-Nova dual source wavelength diffractometer with an Atlas CCD detector using multilayer optics monochromatised Cu-K α ($\lambda = 1.54184$ Å) radiation. The data collection and reduction for **35** and **19** were performed using the program *CrysAlisPro*^[220] and the intensities were corrected using Gaussian face index absorption correction method.^[220] All the structures were solved with direct methods (*SHELXS*^[221]) and refined by full-matrix least squares on F^2 using the *OLEX2*,^[222] which utilizes the *SHELXL-2013* module.^[221] Constraints and restraints are used where appropriate for disordered models.

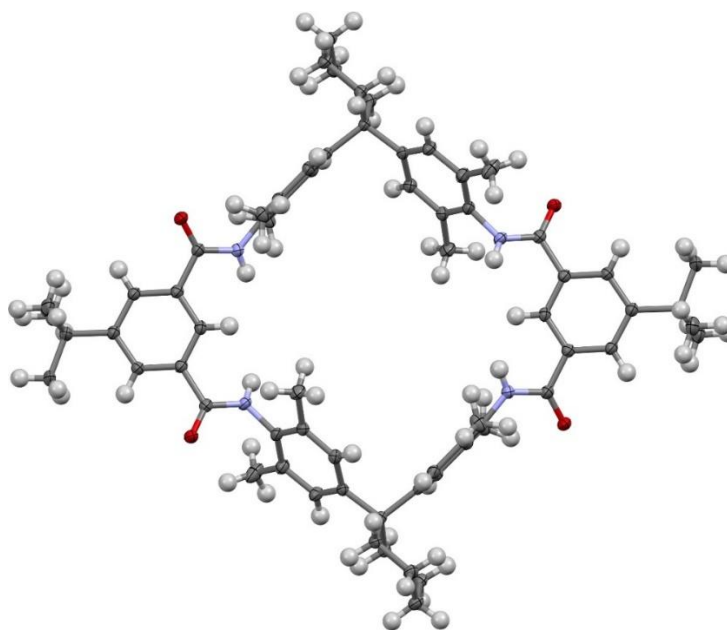


Figure 133: X-ray crystal structure of **19** with thermal ellipsoids with 50% probability level. The cavity-bound and lattice MeOH molecules are omitted for clarity.

Table 5: X-Ray crystal data details for compounds **35** and **19**.

Compound	35	19
CCDC deposition number	1479470	1479471
Empirical formula	C ₃₃ H ₄₀ N ₄ O ₄	C _{75.50} H _{111.50} N ₄ O _{12.50}
Formula weight	556.69	1275.18
Temperature (K)	123.0	100.0
Crystal system	Monoclinic	Triclinic
Space group	<i>P2₁/c</i>	<i>P</i> -1
Unit cell dimensions: a (Å)	11.1064(7)	11.4947(6)
b (Å)	22.1507(14)	12.7587(7)
c (Å)	25.3351(18)	14.2153(7)
α (°)	90	80.164(5)
β (°)	90.026(6)	78.561(5)
γ (°)	90	63.742(5)
Volume / Å ³	6232.8(7)	1824.32(19)
Z	8	1
Density (calculated) mg/m ³	1.187	1.161
Absorption Coefficient mm ⁻¹	0.079	0.622
F(000)	2384	692
Crystal size (mm ³)	0.24 x 0.12 x 0.10	0.19 x 0.17 x 0.11
θ range for data collection (°)	3.05 to 25.25	3.88 to 66.75
Reflections collected [R(int)]	35091 [0.0802]	10343 [0.0207]
Reflections [I>2σ(I)]	6470	5448
Data completeness (%)	99.7	98.7
Data/ restraints/ parameters	11247/0/765	6383/1/466
Goodness-of-fit on F ²	1.020	1.042
Final R ₁ indices [I>2σ(I)]	R ₁ = 0.0801, wR ₂ = 0.1648	R ₁ = 0.0490, wR ₂ = 0.1323
Final R indices [all data]	R ₁ = 0.1450, wR ₂ = 0.2002	R ₁ = 0.0570, wR ₂ = 0.1408
Largest diff. peak/hole (e.Å ⁻³)	0.305/ -0.362	0.717/ -0.907

7.4.12. Surface preparations

Glass and silicon surfaces were cleaned by immersing them for 30 min in piranha-solution (conc. H_2SO_4 / H_2O_2 30 % 3:1) followed by washing with deionised water. Gold surfaces were cleaned by immersing them for 10 min in conc HCl followed by washing with deionised water.

The self-assembled monolayer (SAM) **PDS** and **PST** were prepared as described before.^[178, 223] For the SAM deposition, cleaned surfaces were immersed in a 5 mM solution of **PDS** in DCM for 24 h respectively in a 1 mM solution of **PST** in DMF for 24 h. As the first layer of metal ions, Pd^{II} ions were used to connect the pyridyl endgroup of the SAM with the terpyridine group of the TLM. The deposition was carried out by immersing the surfaces in a 1 mM solution of tetrakis(acetonitrile)palladium(II) tetrafluoroborate in ACN for 30 min. Deposition of di-terpyridine-TLM **10** was carried out by immersing the surfaces in a 1 mM solution in DMF over 24 h. Following the first macrocycle layer, Fe^{II} ions deposited from a 1 mM solution of iron(II) tetrafluoroborate hexahydrate in ethanol over 30 min are used to connect the two terpyridines of subsequent macrocycle layers.

For pseudorotaxane formation, surfaces were immersed in a 1 mM solution of the axle **35** in DCM over 24 h. After each deposition step, the surfaces were immersed for 10 min in the pure solvent used in that deposition step to remove any unspecifically bound molecules. Prior to characterization, surfaces were dried under an argon stream.

7.4.13. Additional XPS data

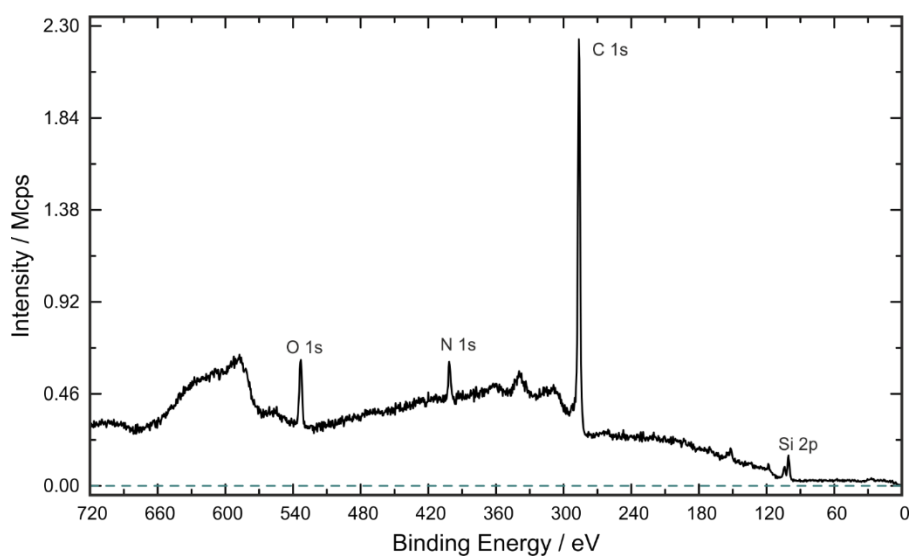


Figure 134: Survey XP spectrum of **PDS-PdMC-(FeMC)₂** (excitation energy: 849 eV, MC = compound 10).

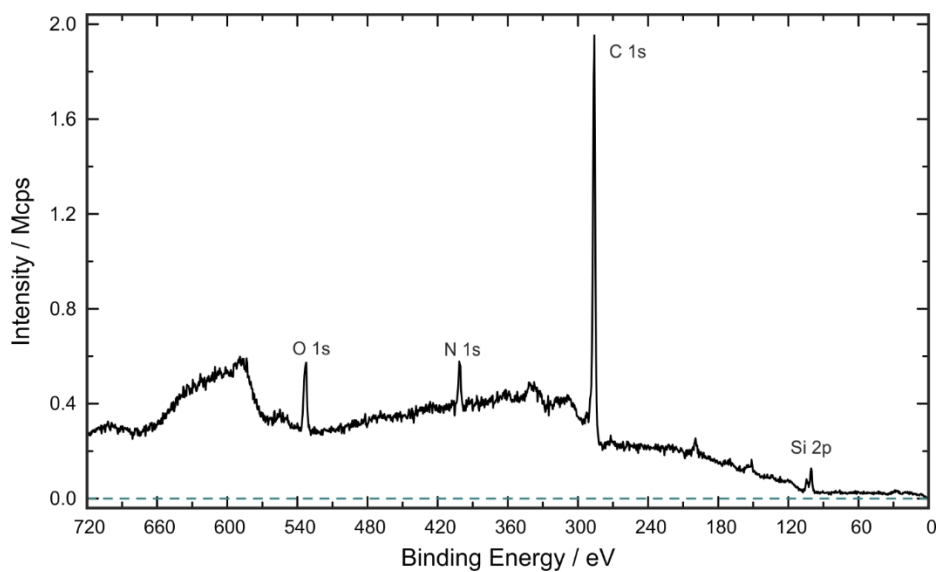


Figure 135: Survey XP spectrum of **PDS-PdMC-(FeMC)₂** treated with solution of **cis-8** (excitation energy: 849 eV, MC = compound 10).

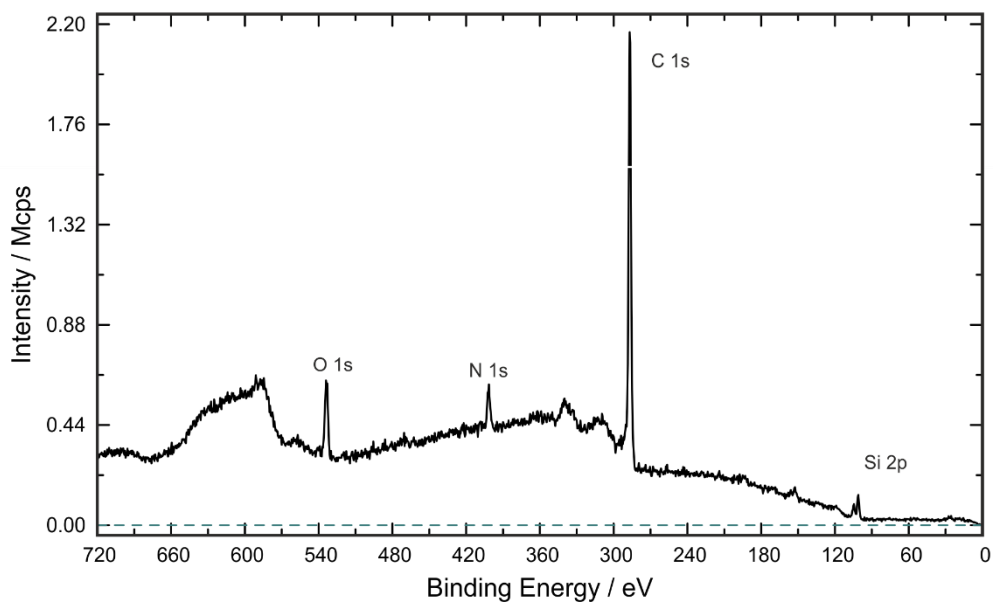
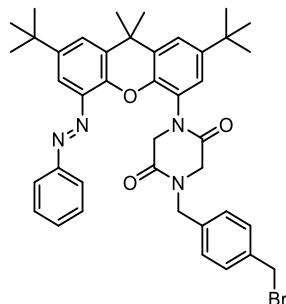


Figure 136: Survey XPS spectrum of PDS-PdMC-(FeMC)₂ treated with solution of trans-8 (excitation energy: 849 eV, MC = compound 10).

7.5. Experimental procedures for chapter 4.2.2

7.5.1. Synthesis of (*E*)-1-(4-(bromomethyl)benzyl)-4-(2,7-di-*tert*-butyl-9,9-dimethyl-5-(phenyldiazenyl)-9*H*-xanthen-4-yl)piperazine-2,5-dione



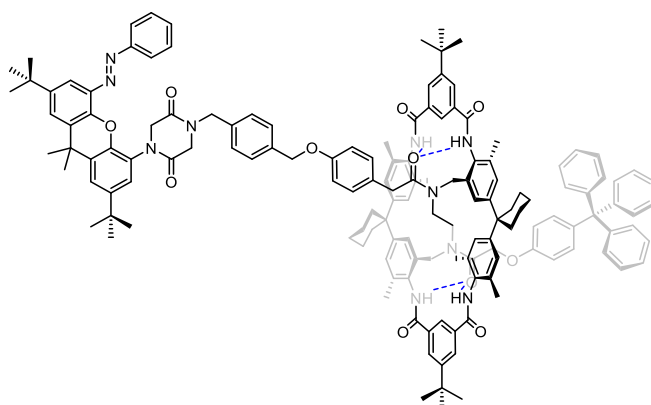
(*E*)-1-(2,7-Di-*tert*-butyl-9,9-dimethyl-5-(phenyldiazenyl)-9-xanthen-4-yl)piperazin-2,5-dion (50.0 mg, 0.093 mmol) and xylylene dibromide (245 mg, 0.930 mmol) were dissolved in dry THF (10 mL) and cooled with an ice bath to 0 °C. Potassium *tert*-butanolate (12.0 mg, 0.102 mmol) was added. The mixture was stirred for 1 h at 0 °C and for further 2.5 h at room temperature. After adding diethyl ether (50 mL), the solution was washed with distilled water (50 mL), dried over magnesium sulfate, filtered and the solvent evaporated. The residue was purified by column chromatography (silica, DCM/*n*-hexane 4:1 – DCM – DCM/EE 9:1), which afforded the product as an orange solid (55.0 mg, 0.0762 mmol, 82%).

¹H NMR (400 MHz, CDCl₃) δ = 7.85 – 7.79 (m, 2H, H_{azobenzene}), 7.57 – 7.56 (m, 1H, H_{xanthene}), 7.51 (dd, J = 2.3, 0.7 Hz, 1H, H_{xanthene}), 7.47 (m, 1H, H_{xanthene}), 7.45 (m, 3H, H_{azobenzene}) 7.36 (d, J = 7.9 Hz, 2H, H_{xylylene}), 7.22 (d, J = 7.9 Hz, 2H, H_{xylylene}), 7.15 (dd, J = 2.3, 0.7 Hz, 1H, H_{xanthene}), 4.94 (bs, 2H, H_{piperazine-2,5-dione}), 4.50 (s, 2H, H_{CH2}), 4.27 – 4.01 (bs, 2H, H_{piperazine-2,5-dione}), 3.85 (s, 2H, H_{CH2}), 1.71 (s, 6H, H_{CH3}), 1.36 (s, 9H, H_{t-bu}), 1.33 (s, 9H, H_{t-bu}) ppm.

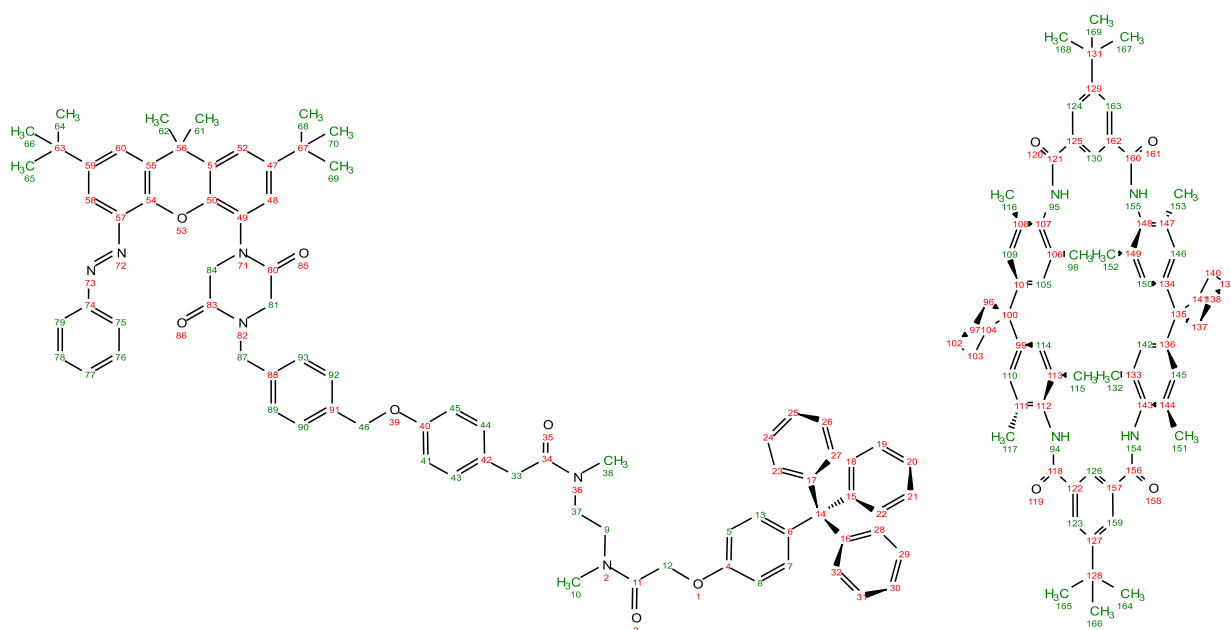
¹³C NMR (101 MHz, CDCl₃) δ = 164.6, 164.5, 153.7, 146.6, 146.1, 145.2, 143.7, 140.6, 137.8, 135.6, 131.3, 131.3, 130.8, 129.7, 129.2, 129.2, 126.5, 125.8, 123.8, 123.1, 122.7, 112.4, 60.5, 52.8, 49.7, 49.1, 35.0, 34.9, 34.8, 33.0, 31.6, 31.5, 21.2, 14.3 ppm.

MS (ESI, pos. Mode, DCM/MeOH) m/z: calculated 721.2748 found 721.2741 ([M+H]⁺), calculated 743.2567 found 743.2563 ([M+Na]⁺), calculated 759.2307 found 759.2296 ([M+K]⁺).

7.5.2. Synthesis of Rot7



(E)-1-(4-(Bromomethyl)benzyl)-4-(2,7-di-*tert*-butyl-9,9-dimethyl-5-(phenyldiazenyl)-9H-xanthene-4-yl)piperazine-2,5-dione (212 mg, 0.295 mmol), 2-(4-hydroxyphenyl)-*N*-methyl-*N*-(2-(*N*-methyl-2-(4-tritylphenoxy)acetamido)ethyl)acetamide (177 mg, 0.295 mmol), TLM 1 (100 mg, 0.098 mmol), potassium carbonate (203 mg, 1.47 mmol) and dibenzo-18-crown-6 (53.0 mg, 0.147 mmol) were dissolved in dry DCM (15 mL) and stirred for 7 d at room temperature. The solution was diluted with DCM (100 mL), washed with dest. water (2 x 50 mL), dried with magnesium sulfate, filtered and the solvent evaporated. The residue was purified by column chromatography (silica, toluene/ethyl acetate 7:3 – 1:4 – toluene + 6 % MeOH), which afforded a fraction containing the rotaxane followed by a fraction containing the free axle. The fraction containing the rotaxane was further purified by preparative TLC (Silica, ethyl acetate/cyclohexane 5:7), which afforded the pure compound as an orange solid (120 mg, 0.053 mmol, 54%).



^1H NMR (700 MHz, CDCl_3)

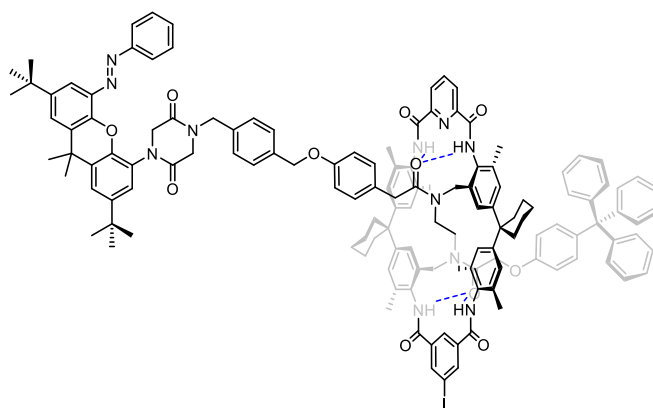
δ = 8.61 (s, 2H, $\text{H}_{126, 130}$), 8.46 (s, 4H, $\text{H}_{94, 95, 154, 155}$), 8.31 (s, 4H, $\text{H}_{123, 124, 159, 163}$), 7.85 (dd, J = 6.4, 1.8 Hz, 2H, $\text{H}_{75, 79}$), 7.60 (d, J = 2.4 Hz, 1H, $\text{H}_{\text{xanthene}}$), 7.55 (d, J = 2.3 Hz, 1H, $\text{H}_{\text{xanthene}}$), 7.50 (d, J = 2.3 Hz, 1H, $\text{H}_{\text{xanthene}}$), 7.49 – 7.43 (m, 3H, $\text{H}_{76, 77, 78}$), 7.40 (d, J = 8.0 Hz, 2H, $\text{H}_{90, 92}$), 7.29 (d, J = 9.7 Hz, 2H, $\text{H}_{89, 93}$), 7.28-7.17 (m, 15 H, H_{trityl}), 7.16 (s, d, J = 2.4 Hz, 1H, $\text{H}_{\text{xanthene}}$), 7.07 (d, J = 8.9 Hz, 2H, $\text{H}_{7, 13}$), 7.01 (s, 8H, $\text{H}_{105, 109, 110, 114, 142, 145, 146, 150}$), 6.79 (d, J = 8.9 Hz, 2H, $\text{H}_{43, 44}$), 6.77 (d, J = 8.9 Hz, 2H, $\text{H}_{41, 45}$), 6.39 (d, J = 9.1 Hz, 2H, $\text{H}_{5, 8}$), 5.04 (s, 2H, H_{46}), 5.01 (bs, 2H, H_{84}), 4.08 (bs, 2H, H_{81}), 3.88 (s, 2H, H_{12}), 3.86 (s, 2H, H_{87}), 3.10 (s, 2H, H_{33}), 2.41 (s, 3H, H_{10}), 2.33 (bs, 6H, $\text{H}_{\text{cyclohexyl}}$), 2.30 (s, 3H, H_{38}), 2.09 (s, 24H, $\text{H}_{98, 115, 116, 117, 132, 151, 152, 153}$), 2.05 – 1.97 (m, 4H, $\text{H}_{9, 37}$), 1.75 (bs, 6H, $\text{H}_{61, 62}$), 1.66 (bs, 10H, $\text{H}_{\text{cyclohexyl}}$), 1.53 (bs, 4H, $\text{H}_{\text{cyclohexyl}}$), 1.43 (s, 18H, $\text{H}_{164, 165, 166, 167, 168, 169}$), 1.40 (s, 9H, $\text{H}_{68, 69, 70}$), 1.37 (s, 9H, $\text{H}_{64, 65, 66}$) ppm.

^{13}C NMR (176 MHz, CDCl_3)

δ = 173.0, 168.5, 165.8, 164.6, 164.5, 158.0, 155.0, 153.7, 153.6, 148.1, 146.7, 146.6, 146.2, 145.2, 143.7, 141.3, 140.6, 136.7, 135.3, 134.3, 132.5, 131.9, 131.4, 131.3, 131.1, 130.8, 129.2, 129.1, 129.0, 128.1, 127.7, 126.6, 126.2, 125.8, 125.4, 123.8, 123.1, 123.1, 122.7, 115.4, 113.3, 112.4, 69.8, 65.8, 64.4, 52.8, 49.6, 49.1, 45.0, 43.4, 43.3, 39.6, 35.8, 35.6, 35.5, 35.1, 35.0, 34.8, 34.1, 31.6, 31.6, 31.4, 26.4, 22.9, 19.1 ppm.

MS (ESI, pos. Mode, DCM/MeOH) m/z : calculated 2256.2497 found 2256.2492 ($[\text{M}+\text{H}]^+$).

7.5.3. Synthesis of Rot8



(*E*)-1-(4-(Bromomethyl)benzyl)-4-(2,7-di-*tert*-butyl-9,9-dimethyl-5-(phenyldiazenyl)-9*H*-xanthene-4-yl)piperazine-2,5-dione (175 mg, 0.240 mmol), 2-(4-hydroxyphenyl)-*N*-methyl-*N*-(2-(*N*-methyl-2-(4-tritylphenoxy)acetamido)ethyl)acetamide (145 mg, 0.240 mmol), TLM **2** (100 mg, 0.097 mmol), potassium carbonate (134 mg, 0.97 mmol) and dibenzo-18-crown-6 (35.0 mg, 0.097 mmol) were dissolved in dry DCM (15 mL) and stirred for 7 d at room temperature. The solution was diluted with DCM (100 mL), washed with dest. water (2 x 50 mL), dried with magnesium sulfate, filtered and the solvent evaporated. The residue was purified by column chromatography (silica, -hexane/ethyl acetate 2:1 – ethyl acetate), which afforded a fraction containing the rotaxane followed by a fraction containing the free axle. The fraction containing the rotaxane was further purified by preparative TLC (silica, ethyl acetate/cyclohexane 5:7), which afforded the pure compound as an orange solid (128 mg, 0.056 mmol, 58%).

$^1\text{H NMR}$ (700 MHz, CDCl_3) δ = 10.38 (s, 2H, H_{NH}), 8.54 (s, 1H, $\text{H}_{\text{isophthal}}$), 8.46 (d, J = 1.5 Hz, 2H, $\text{H}_{\text{isophthal}}$), 8.45 (m, 2H, H_{NH}), 8.36 (s, 2H, $\text{H}_{\text{isophthal}}$), 8.10 (t, J = 7.8 Hz, 1H, $\text{H}_{\text{isophthal}}$), 7.82 (dd, J = 7.9, 1.8 Hz, 2H, $\text{H}_{\text{azobenzene}}$), 7.57 (d, J = 2.4 Hz, 1H, $\text{H}_{\text{xanthene}}$), 7.52 (d, J = 2.2 Hz, 1H, $\text{H}_{\text{xanthene}}$), 7.47 (d, J = 2.2 Hz, 1H, $\text{H}_{\text{xanthene}}$), 7.46 – 7.42 (m, 3H, $\text{H}_{\text{azobenzene}}$), 7.40 (d, J = 8.4 Hz, 2H, H_{phenyl}), 7.27 (d, J = 7.5 Hz, 2H, H_{phenyl}), 7.26 – 7.23 (m, 5H, H_{trityl}), 7.21 – 7.15 (m, 10H, H_{trityl}), 7.15 (d, J = 2.2 Hz, 1H, $\text{H}_{\text{xanthene}}$), 7.07 (d, J = 9.1 Hz, 2H, H_{phenyl}), 6.98 (s, 4H, $\text{H}_{\text{aryl TLM}}$), 6.95 (s, 4H, $\text{H}_{\text{aryl TLM}}$), 6.71 (d, J = 8.8 Hz, 2H, H_{phenyl}), 6.55 (d, J = 8.9 Hz, 2H, H_{phenyl}), 6.43 (d, J = 9.1 Hz, 2H, H_{phenyl}), 5.03 (s, 2H, H_{CH_2}), 5.13 – 4.87 (br, 2H, $\text{H}_{\text{diketopiperazine}}$), 4.17 (s, 2H, H_{CH_2}), 4.25 – 4.01 (br, 2H, $\text{H}_{\text{diketopiperazine}}$), 3.85 (s, 2H, H_{CH_2}), 3.28 (s, 2H, H_{CH_2}), 2.42 – 2.23 (m, 12H, H_{CH_3}), 2.16 (m, 2H, H_{CH_2} diamide), 2.12 (s, 12H, H_{CH_3} TLM), 2.08 – 2.03 (m, 2H, H_{CH_2}

diamide), 1.98 (s, 12H, H_{CH₂ TLM}), 1.78 – 1.70 (m, 10H, H_{cyclohexyl}), 1.62 – 1.56 (m, 6H, H_{cyclohexyl}), 1.54 – 1.48 (m, 4H, H_{cyclohexyl}), 1.37 (s, 9H, H_{t-Bu}), 1.34 (s, 9H, H_{t-Bu}) ppm.

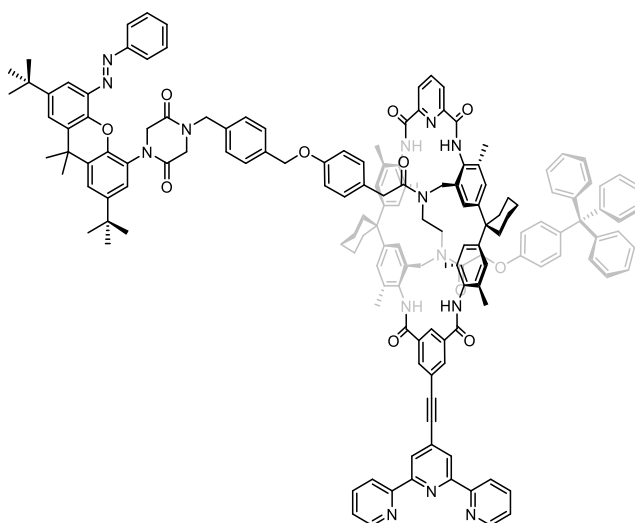
¹³C NMR (176 MHz, CDCl₃)

δ = 172.7, 168.8, 164.5, 164.5, 164.5, 162.0, 157.8, 155.2, 153.6, 148.9, 146.7, 146.6, 146.1, 145.2, 143.7, 141.1, 140.6, 140.6, 139.3, 136.7, 136.4, 135.3, 135.2, 134.8, 132.6, 131.7, 131.4, 131.3, 131.3, 131.1, 131.1, 130.8, 129.2, 129.1, 128.0, 127.7, 126.6, 126.3, 126.2, 126.1, 125.8, 125.5, 125.1, 123.8, 123.1, 122.9, 122.7, 119.9, 115.2, 113.3, 112.4, 95.6, 69.8, 66.3, 64.4, 52.8, 49.6, 49.1, 45.6, 44.9, 44.9, 43.8, 43.6, 41.5, 40.3, 36.2, 36.1, 36.0, 35.9, 35.1, 35.0, 34.8, 34.8, 34.8, 34.6, 31.8, 31.7, 31.6, 31.6, 31.5, 31.2, 31.1, 29.2, 27.8, 27.0, 26.4, 25.4, 22.9, 22.9, 22.8, 22.7, 20.8, 20.6, 19.6, 19.3, 19.1, 18.9, 18.9, 14.5, 14.2, 11.6, 1.1 ppm.

MS (ESI, pos. Mode, DCM/ACN)

m/z: calculated 2271.0164 found 2271.0182 ([M+H]⁺),
m/z: calculated 2292.9984 found 2293.0027 ([M+Na]⁺),
m/z: calculated 2308.9723 found 2308.9734 ([M+K]⁺),
m/z: calculated 1147.0028 found 1147.0055
([M+H+Na]²⁺), m/z: ber. 1154.9898 found 1154.9885
([M+H+K]²⁺), m/z: calculated 1157.9938 found 1157.9973
([M+2 Na]²⁺), m/z: calculated 1165.9808 found 1165.9831
([M+H+Na]²⁺).

7.5.4. Synthesis of Rot9



Rot8 (100 mg, 0.044 mmol), 4'-ethynyl-2,2':6',2''-terpyridine (22.6 mg, 0.088 mmol), bis(triphenylphosphine)palladium(II) dichloride (3.08 mg, 0.004 mmol), copper(I) iodide (0.84 mg, 4.4 μ mol) and triphenylphosphine (4.00 mg, 0.015 mmol) were dissolved in dry DMF (16 mL) and dry diisopropylethylamine (4 mL). The solution was degassed with an argon stream for about 5 min and stirred at room temperature for 5 d. 4'-Ethynyl-2,2':6',2''-terpyridine (11.3 mg, 0.044 mmol), bis(triphenylphosphine)palladium(II) dichloride (3.08 mg, 0.004 mmol) and copper(I) iodide (0.84 mg, 4.4 μ mol) were added and the solution stirred for further 2 d. The solvents were evaporated and the residue was dissolved in DCM (10 mL) and filtered over a short column (neutral alox, DCM + 8% MeOH + 4% TEA). The solvents were evaporated and the residue was dissolved in DCM (100 mL), washed with dest. water (2 x 50 mL), dried with magnesium sulfate, filtered and the solvent evaporated. The residue was purified by dialysis (MWCO 1000, DCM/MeOH 2:1, 14 h, 4 h), which afforded the product as an orange solid.

^1H NMR (700 MHz, CDCl_3) δ = 10.39 (s, 2H, H_{NH}), 8.77 – 8.74 (m, 2H, $\text{H}_{\text{terpyridine}}$), 8.64 (d, J = 7.7 Hz, 2H, $\text{H}_{\text{terpyridine}}$), 8.57 (s, 2H, $\text{H}_{\text{terpyridine}}$), 8.47 – 8.43 (m, 2H, $\text{H}_{\text{isophthal}}$), 8.40 (s, 2H, H_{NH}), 8.37 – 8.33 (m, 1H, $\text{H}_{\text{isophthal}}$), 8.32 (d, J = 1.5 Hz, 1H, $\text{H}_{\text{isophthal}}$), 8.11 (t, J = 7.8 Hz, 2H, $\text{H}_{\text{terpyridine}}$), 7.90 (t, J = 7.1 Hz, 2H, $\text{H}_{\text{isophthal}}$), 7.79 (d, J = 6.9 Hz, 2H, $\text{H}_{\text{azobenzene}}$), 7.56 (d, J = 2.4 Hz, 1H, $\text{H}_{\text{xanthene}}$), 7.51 (d, J = 2.4 Hz, 1H, $\text{H}_{\text{xanthene}}$), 7.46 (d, J = 2.2 Hz, 1H, $\text{H}_{\text{xanthene}}$), 7.44 – 7.40 (m, 3H, $\text{H}_{\text{azobenzene}}$), 7.41 – 7.37 (m, 2H, $\text{H}_{\text{terpyridine}}$), 7.37 (d, J = 8.1 Hz, 2H, H_{phenyl}), 7.30 – 7.26 (m, 2H, H_{phenyl}), 7.25 – 7.13 (m, 15H, H_{trityl}), 7.13 (d, J = 2.2 Hz, 1H, $\text{H}_{\text{xanthene}}$), 7.06 (d, J = 9.1 Hz, 2H, H_{phenyl}), 6.99 (s, 4H, $\text{H}_{\text{aryl TLM}}$), 6.96 (s, 4H, H_{aryl})

δ_{TLM} , 6.72 (d, $J = 8.6$ Hz, 2H, H_{phenyl}), 6.58 (d, $J = 8.2$ Hz, 2H, H_{phenyl}), 6.45 (d, $J = 9.1$ Hz, 2H, H_{phenyl}), 5.03 (s, 2H, H_{CHe}), 5.10 – 4.76 (br, 2H, $H_{\text{diketopiperazine}}$), 4.32 – 3.98 (br, 2H, $H_{\text{diketopiperazine}}$), 4.17 (s, 2H, H_{CH_2}), 3.80 (s, 2H, H_{CH_2}), 3.29 (s, 2H, H_{CH_2}), 2.37 (s, 6H, $H_{\text{CH}_3 \text{ xanthene}}$), 2.36 – 2.22 (m, 6H, $H_{\text{CH}_3 \text{ diamide}}$), 2.21 – 2.15 (m, 2H, $H_{\text{ch}_2 \text{ diamide}}$), 2.13 (s, 12H, $H_{\text{CH}_3 \text{ TLM}}$), 2.01 (s, 12H, $H_{\text{CH}_3 \text{ TLM}}$), 1.96 – 1.91 (m, 2H, $H_{\text{CH}_2 \text{ diamide}}$), 1.69 (m, 10H, $H_{\text{cyclohexyl}}$), 1.59 (m, 6H, $H_{\text{cyclohexyl}}$), 1.52 – 1.43 (m, 4H, $H_{\text{cyclohexyl}}$), 1.36 (s, 9H, $H_{\text{t-Bu}}$), 1.32 (s, 9H, $H_{\text{t-Bu}}$) ppm.

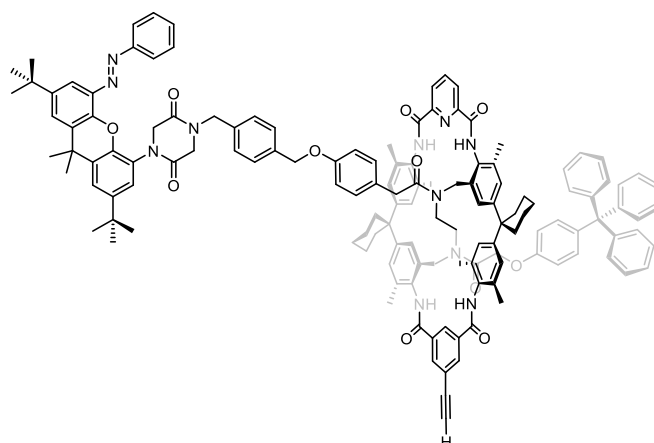
^{13}C NMR (176 MHz, CDCl_3)

$\delta = 172.7, 168.7, 165.1, 164.5, 164.5, 162.0, 157.8, 155.9, 155.8, 155.6, 155.4, 155.3, 155.3, 154.5, 153.8, 153.5, 149.4, 148.9, 148.1, 147.8, 146.9, 146.7, 146.5, 146.1, 146.1, 145.2, 143.7, 143.4, 141.9, 141.1, 140.6, 140.5, 140.3, 140.0, 139.3, 137.0, 137.0, 136.7, 136.5, 136.4, 135.4, 135.2, 134.9, 134.7, 132.7, 132.5, 132.2, 132.1, 131.6, 131.6, 131.5, 131.3, 131.3, 131.1, 130.8, 129.3, 129.2, 129.1, 128.8, 128.7, 128.7, 128.6, 128.3, 128.0, 128.0, 127.9, 127.7, 126.6, 126.5, 126.1, 126.1, 125.8, 125.5, 125.1, 124.7, 124.3, 124.2, 123.8, 123.6, 123.1, 123.0, 122.7, 122.7, 121.3, 119.8, 115.1, 113.3, 112.3, 91.9, 89.5, 69.8, 66.3, 64.4, 52.8, 49.6, 49.1, 45.9, 44.9, 43.8, 43.7, 40.2, 36.1, 35.9, 35.1, 35.0, 34.9, 34.8, 34.8, 34.5, 31.6, 31.5, 31.2, 29.8, 26.4, 22.9, 19.3, 19.0, 18.9, 8.7, 1.1$ ppm.

MS (ESI, pos. Mode, DCM/ACN)

m/z : calculated 2422.1814 found 2422.1807 ($[\text{M}+\text{Na}]^+$),
 m/z : calculated 1211.5943 found 1211.5929 ($[\text{M}+\text{H}+\text{Na}]^{2+}$),
 m/z : calculated 1222.5853 found 1211.5878 ($[\text{M}+2\text{Na}]^{2+}$).

7.5.5. Synthesis of Rot10



In a pressure tube, **Rot8** (100 mg, 0.044 mmol), trimethylsilylacetylene (13.0 mg, 0.132 mmol), bis(triphenylphosphine)palladium(II) dichloride (3.08 mg, 4.4 μ mol) and copper(I) iodide (0.84 mg, 4.4 μ mol) were dissolved in a mixture of dry THF (8 mL), dry DMF (2 mL) and dry diisopropylethylamine (6 mL) and stirred at 40 °C for 24 h. The solution was diluted with DCM (50 mL), washed with dest. water (2 x 50 mL) and brine (50 mL), dried with magnesium sulfate, filtered and the solvent evaporated. The residue was purified by preparative TLC (silica, ethyl acetate/*n*-hexane 6:5), which afforded the TMS-protected intermediate as an orange solid. The intermediate and potassium fluoride (26.0 mg, 0.44 mmol) were dissolved in THF (8 mL) and MeOH (6 mL) and stirred for 24 h at room temperature. The solvents were evaporated and the residue dissolved in DCM (50 mL). The solution was washed with dest. water (2 x 50 mL), dried with magnesium sulfate, filtered and the solvent evaporated. The residue was purified by preparative TLC (silica, ethyl acetate/cyclohexane 5:7), which afforded the product as an orange solid (87.7 mg, 0.04 mmol, 92 %).

¹H NMR (500 MHz, CDCl₃)

δ = 10.40 (s, 2H, H_{NH}), 8.57 (s, 1H, H_{isophthal}), 8.48 (d, J = 7.7 Hz, 2H, H_{isophthal}), 8.40 – 8.37 (m, 2H, H_{NH}), 8.26 (d, J = 1.6 Hz, 2H, H_{isophthal}), 8.13 (t, J = 7.8 Hz, 1H, H_{isophthal}), 7.86 – 7.82 (m, 2H, H_{azobenzene}), 7.59 (d, J = 2.4 Hz, 1H, H_{xanthene}), 7.54 (d, J = 2.4 Hz, 1H, H_{xanthene}), 7.50 (d, J = 2.4 Hz, 1H, H_{xanthene}), 7.48 – 7.44 (m, 3H, H_{azobenzene}), 7.42 (d, J = 8.4 Hz, 2H, H_{phenyl}), 7.29 (d, J = 6.1 Hz, 2H, H_{phenyl}), 7.28 – 7.25 (m, 5H, H_{trityl}), 7.26 – 7.13 (m, 10H, H_{trityl}), 7.19 (d, J = 2.4 Hz, 1H, H_{xanthene}), 7.09 (d, J = 9.0 Hz, 2H, H_{phenyl}), 7.00 (s, 4H, H_{aryl TLM}), 6.97 (s, 4H, H_{aryl TLM}), 6.72 (d, J = 8.7 Hz, 2H, H_{phenyl}), 6.59 (d, J = 8.5 Hz, 2H, H_{phenyl}), 6.46 (d, J = 9.1 Hz, 2H, H_{phenyl}), 5.04 (s, 2H, H_{CH₂}), 5.22 – 4.78 (br, 2H, H_{diketopiperazine}), 4.17 (s, 2H, H_{CH₂}), 4.33 – 3.93

(br, 2H, H_{diketopiperazine}), 3.87 (s, 2H, H_{CH2}), 3.31 (s, 2H, H_{CH2}), 3.17 (s, 1H, H_{acetylene}), 2.41 – 2.25 (m, 12H, H_{CH3}), 2.19 (m, 2H, H_{CH2 diamide}), 2.15 (s, 12H, H_{CH3 TLM}), 2.11 (m, 2H, H_{CH2 diamide}), 2.01 (s, 12H, H_{CH3 TLM}), 1.72 (m, 10H, H_{cyclohexyl}), 1.61 (m, 6H, H_{cyclohexyl}), 1.54 – 1.47 (m, 4H, H_{cyclohexyl}), 1.39 (s, 9H, H_{t-Bu}), 1.36 (s, 9H, H_{t-Bu}) ppm.

¹³C NMR (126 MHz, CDCl₃)

δ = 172.7, 168.7, 165.1, 164.5, 162.0, 157.8, 155.3, 153.6, 148.9, 148.0, 147.8, 146.7, 146.6, 146.1, 145.2, 143.7, 141.0, 140.6, 139.3, 136.7, 135.3, 135.2, 134.9, 134.8, 132.5, 131.6, 131.5, 131.3, 131.3, 131.1, 130.8, 129.3, 129.2, 129.1, 128.0, 127.7, 127.0, 126.6, 126.5, 126.1, 126.1, 125.8, 125.4, 125.1, 124.5, 123.8, 123.0, 122.7, 115.1, 113.2, 112.4, 82.0, 79.5, 69.7, 66.3, 64.4, 53.5, 52.8, 49.6, 49.1, 44.9, 43.8, 43.6, 40.2, 36.1, 35.9, 35.9, 35.0, 34.9, 34.8, 34.7, 31.6, 31.5, 26.3, 22.9, 22.8, 19.3, 18.9 ppm.

MS (ESI, pos. Mode, DCM/ACN)

m/z: calculated 2191.1017 found 2191.0993 ([M+Na]⁺),
m/z: calculated 1104.0415 found 1104.0411 ([M+H+K]²⁺),
m/z: calculated 1107.0455 found 1107.0453 ([M+2Na]²⁺),
m/z: calculated 1115.0324 found 1115.0321 ([M+Na+K]²⁺).

7.5.6. Peak assignments for ESI-FTICR IRMPD MS/MS spectra of Rot1

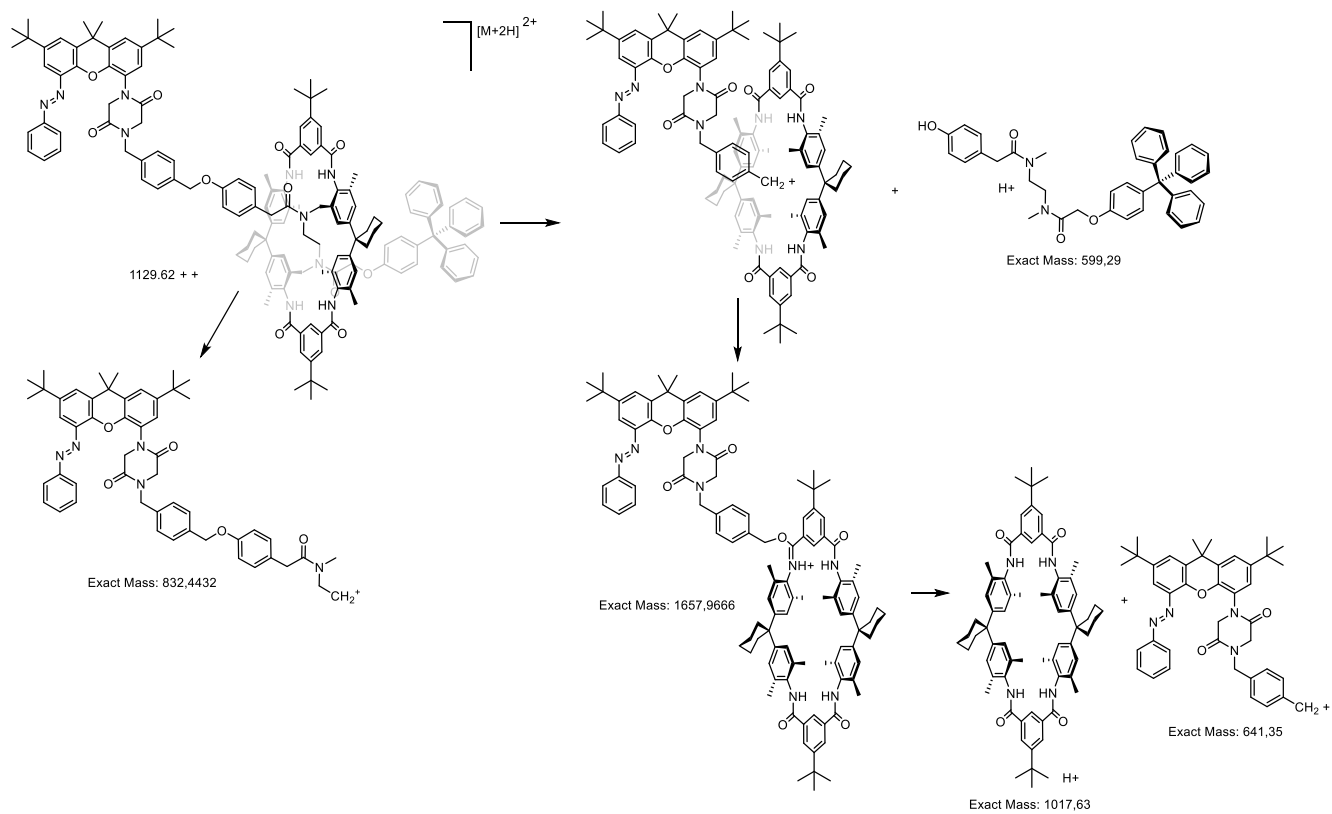


Figure 137: Peak assignment for IRMPD spectra of Rot7.

7.5.7. Variable temperature ^1H NMR spectra of Rot7

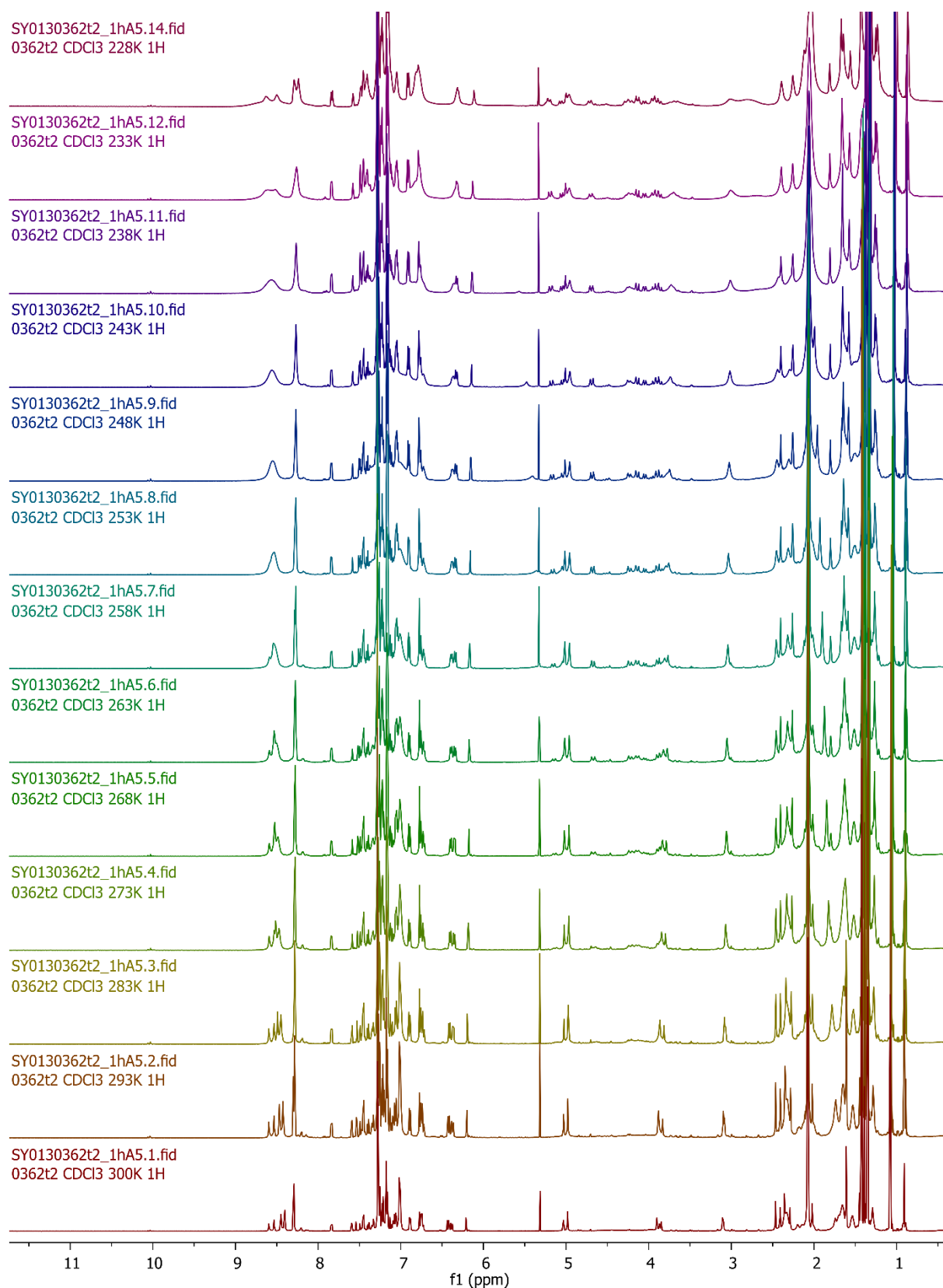


Figure 138: Variable temperature 500 MHz ^1H NMR spectra of Rot7 in CDCl_3 from 300 K to 228 K.

7.5.8. Determination of binding constants

The binding behaviour of diamide **18** to TLM **19** was investigated with NMR experiments. Since there is a fast exchange on the NMR timescale, the binding constants were evaluated by NMR titration analysis.^[162] A solution of TLM **19** (5.00 mg) in CDCl₃ (0.65 mL) was placed in an NMR tube and treated with different amounts of **18**. A ¹H NMR spectrum was measured after each injection and the guest concentrations were determined by integration of the signals. The binding constant was determined based on a 1:1 binding model to be 1,400 ± 140 M⁻¹.

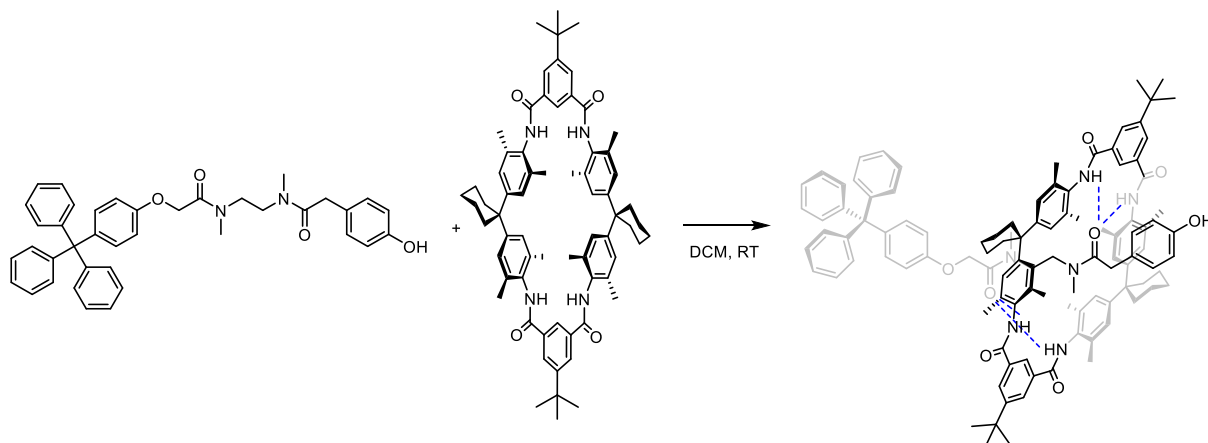


Figure 139: Pseudorotaxane formation.

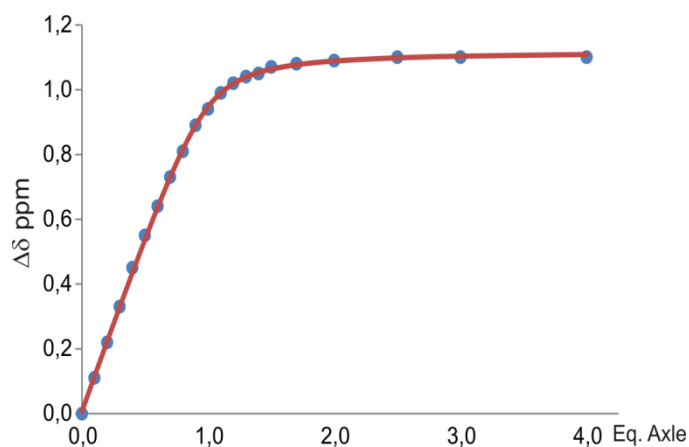


Figure 140: NMR titration.

7.5.9. Surface preparations

The surface preparation procedures were developed in previous studies of the Schalley group. In here, only a simple work instruction without further explanations is given.^[15b, 15d, 139, 178-179, 181]

Surface cleaning

Glass slides and silicon wafers were cut to 2 cm² size and cleaned by immersing them for 30 min in piranha solution (H₂O₂ 30% : conc. H₂SO₄ 1:3). The surfaces were then rinsed with dest. water for 1 min.

Deposition of Rot9

Cleaned surfaces were dipped in EtOH to remove remaining water, then dipped two times in DCM and then immersed in a 5 mM solution of **PDS** in DCM for 24 h. The surfaces were then dipped two times in DCM followed by immersion in DCM for 10 min to remove any unspecific bound molecules. The surfaces were then dried with an argon stream to record background UV spectra.

The surfaces were immersed in a 1 mM solution of Pd(CH₃CN)₄(BF₄)₂ in acetonitrile for 30 min, then dipped two times in acetonitrile followed by immersion in acetonitrile for 10 min, and then two times in DCM followed by immersion in a 1 mM solution of **Rot9** in DCM for 24 h. Afterwards, the surfaces were dipped two times in DCM, immersed in DCM for 10 min, and dried with an argon stream. The solvents used for washing the substrates by dipping or immersing were changed after each surface contact.

Deposition of Rot10

Cleaned surfaces were dipped in EtOH to remove remaining water, subsequently washed two times with toluene and immersed in a 5 mM solution of **AUS** in toluene at 80 °C for 24 h. Followed by rinsing in toluene, twice in DCM and subsequent immersion for 10 min in DCM. The surfaces were then dried with an argon stream to record background UV spectra.

The surfaces were afterwards immersed in a 1 mM solution of **Rot10** containing 5 mol% catalyst **9** for 24 h, then dipped two times in DCM followed by immersion in DCM for 10 min and dried under an argon stream.

7.5.10. Additional XPS and NEXAFS spectra

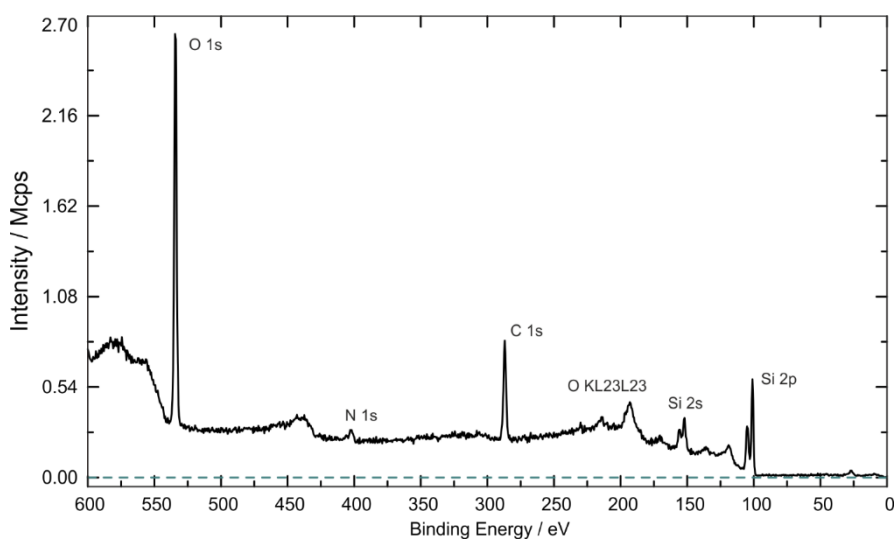


Figure 141: Survey XP-spectrum ($h\nu = 849$ eV) of the **AUS** monolayer.

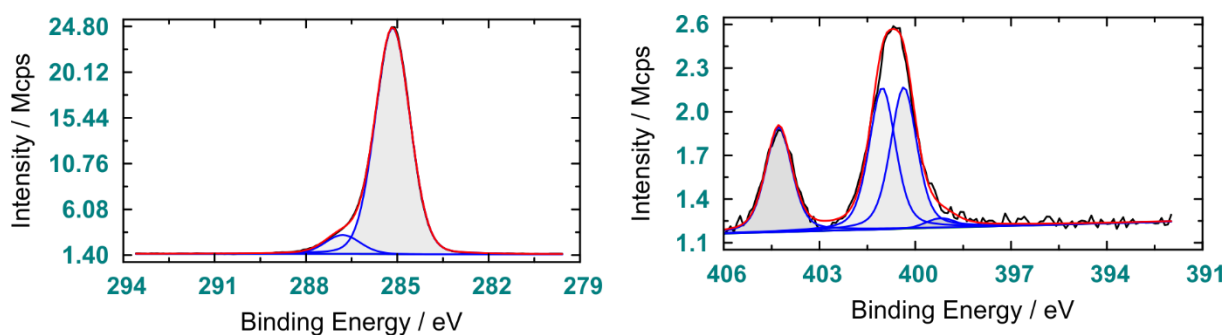


Figure 142: C 1s ($h\nu = 385$ eV) and N 1s ($h\nu = 500$ eV) Xp-spectra of the **AUS** monolayer. Chemical shifts are in line with literature.^[224]

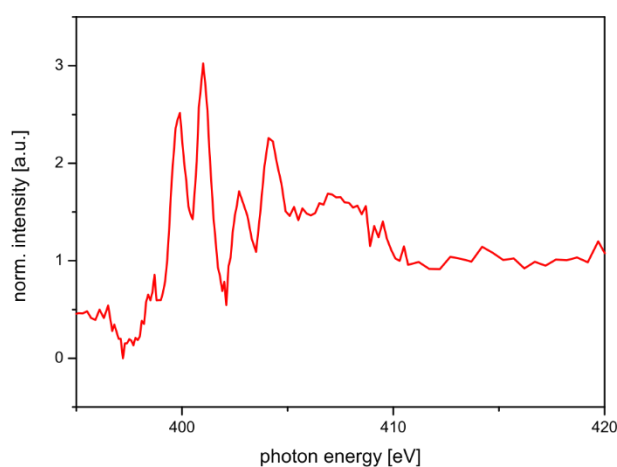


Figure 143: N K-edge NEXAFS spectrum of the **AUS** monolayer.

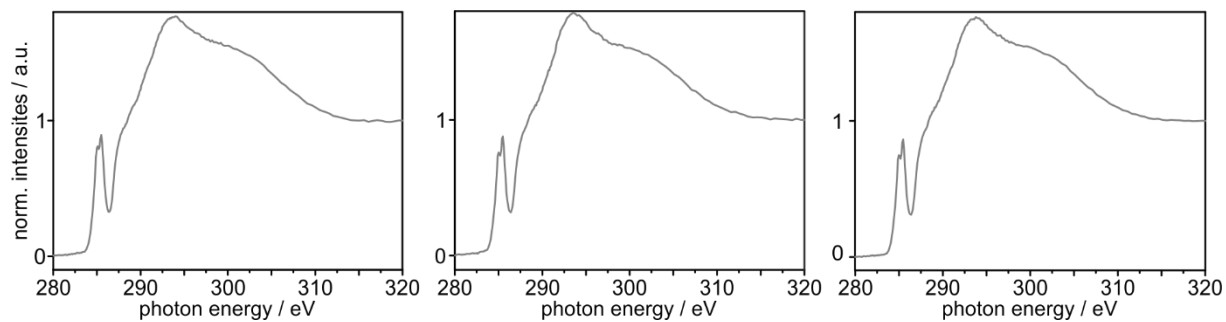


Figure 144: (angle-resolved) C-K NEXAFS spectra of a **Rot9**-monolayer deposited to Pd-**PDS**; pristine (left), after irradiation with 365 nm for 1 h (middle), and after 1 h irradiation with 365 nm plus 1.5 h with 470 nm (right).

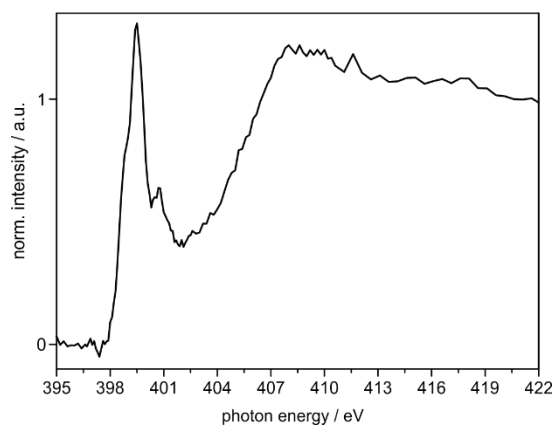


Figure 145: N K-edge NEXAFS spectrum of a **Rot9** monolayer deposited to **PDS-Pd (PDS-Pd-Rot9)**.

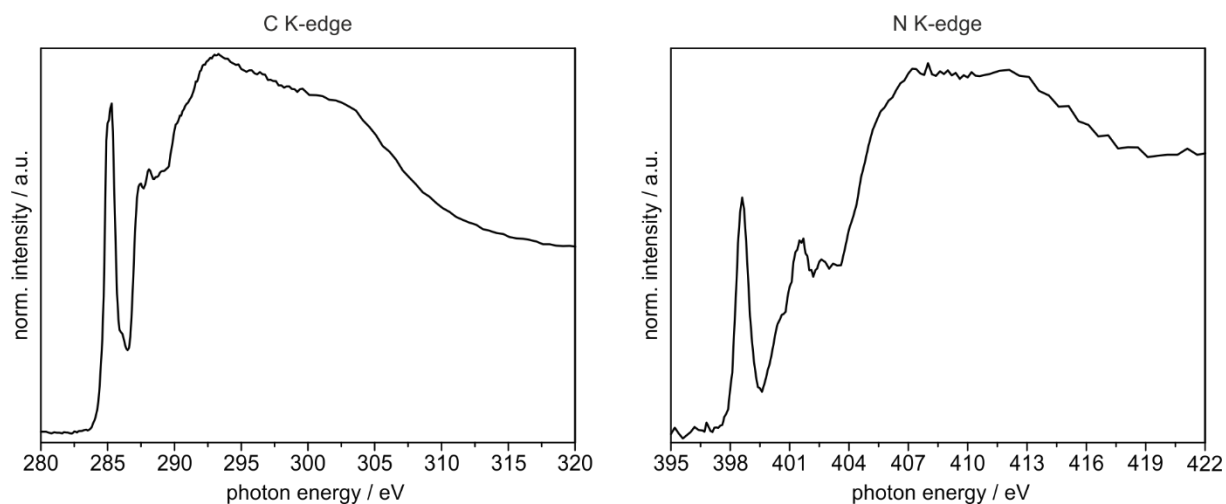


Figure 146: C K-edge (left) and N K-edge (right) of dropcoated **Rot9**.

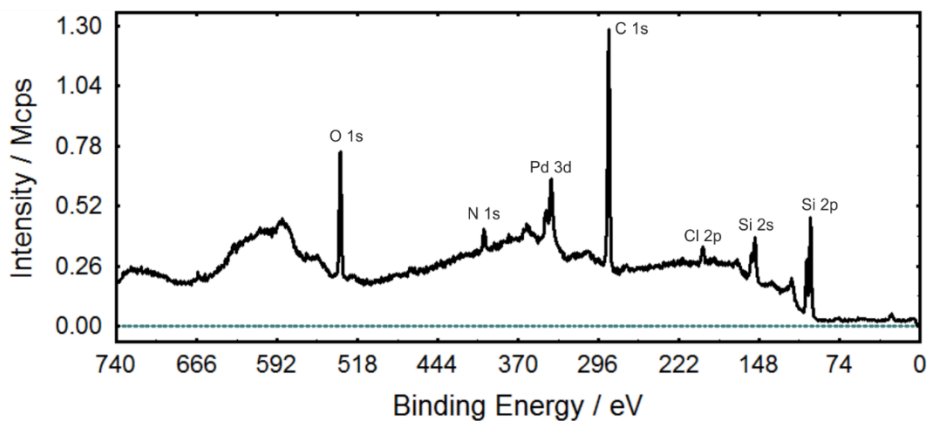


Figure 147: Survey SR-XP spectrum of **PDS-Pd-Rot9**.

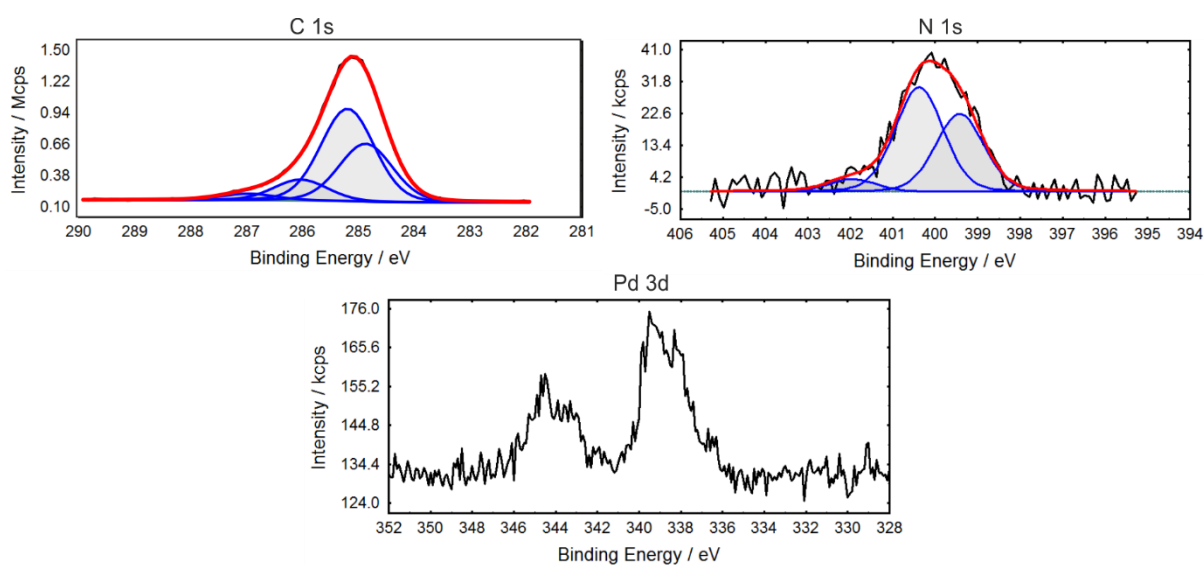


Figure 148: C 1s, N 1s, and Pd 3d SR-XP spectra of **PDS-Pd-Rot9**.

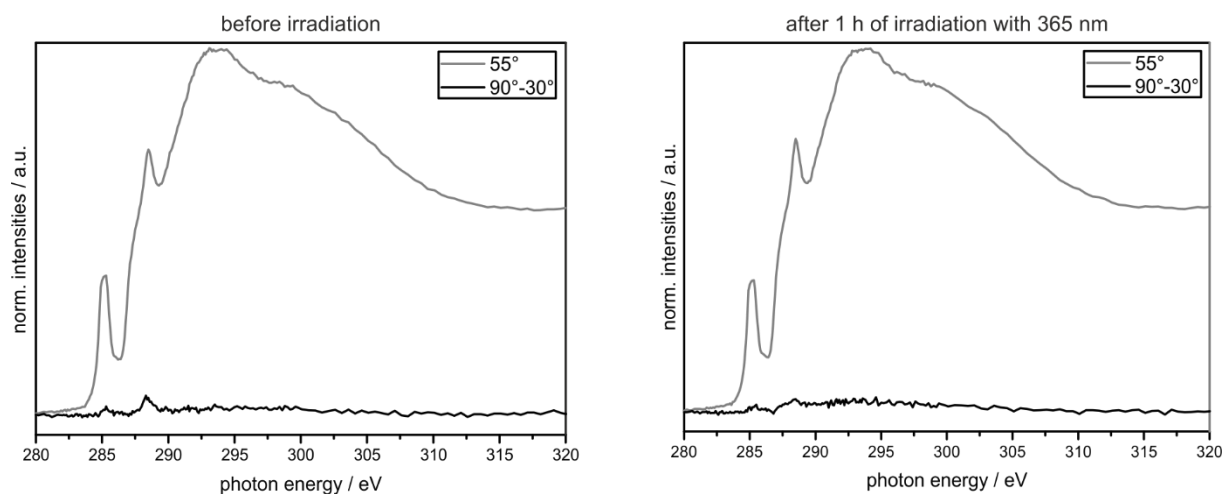


Figure 149: (angle-resolved) C K-edge NEXAFS spectra of **Rot10** clicked to **AUS (AUS-Rot4)**.

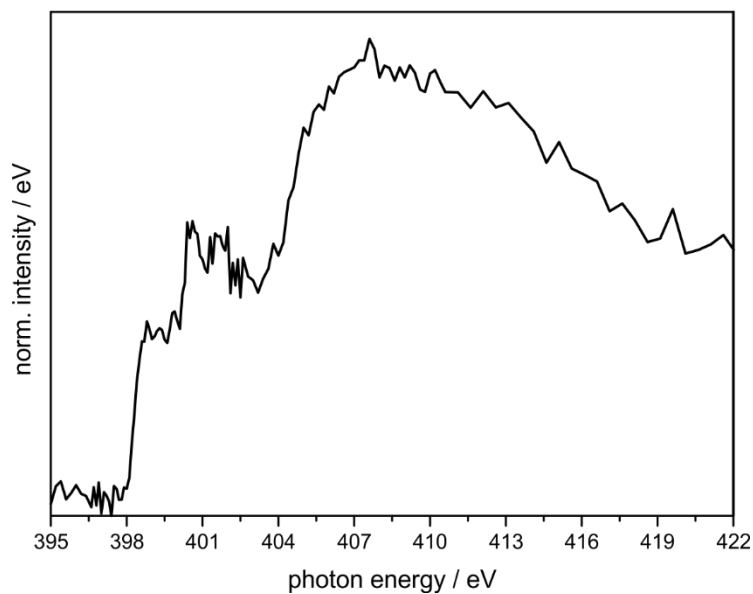


Figure 150: N K-edge NEXAFS of **AUS-Rot4**.

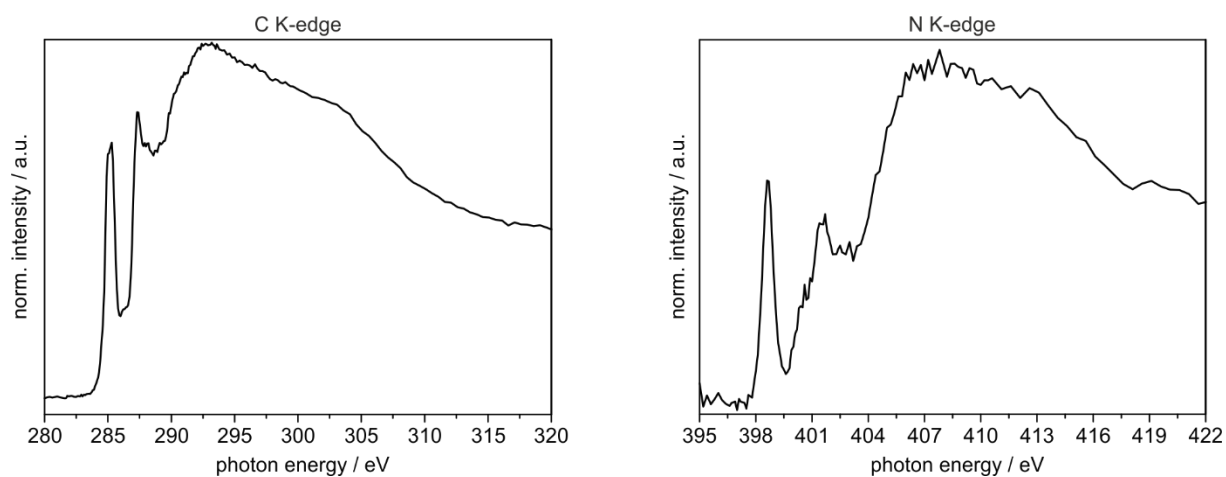


Figure 151: C K-edge (left) and N K-edge (right) NEXAFS spectra of drop-coated **Rot4**.

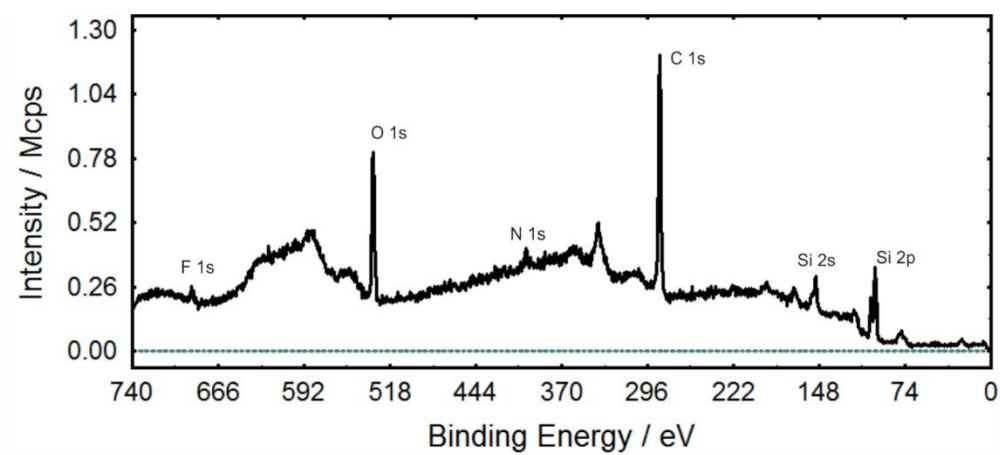


Figure 152: Survey SR-XP spectrum of **AUS-Rot4**.

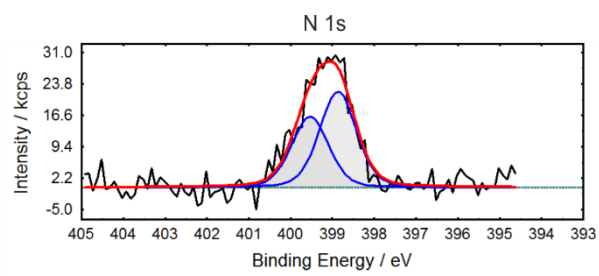
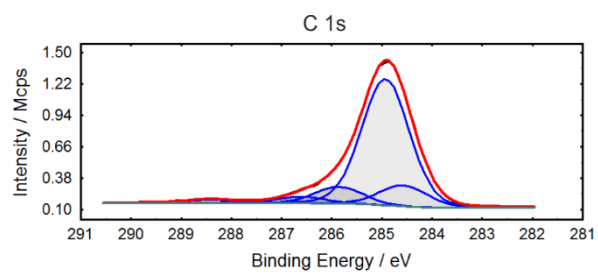


Figure 153: C 1s and N 1s SR-XP spectra of **AUS-Rot4**.

7.6. Experimental procedures for chapter 5.1

7.6.1. Synthesis of NDI diamine **42**

1,4,5,8-naphthalenetetracarboxylic dianhydride (1.00 g, 3.73 mmol) and 1,4-diaminobenzene (1.00 g, 9.33 mmol) were suspended in 40 mL of dry DMF, in a 100 mL round bottom flask and sonicated for 30 min. Triethylamine (2.6 mL, 18.7 mmol) was added and the reaction mixture was heated to reflux for 10 min at 140 ± 5 °C under microwave irradiation. The resulting mixture was filtered and the residue was washed with copious amounts of water, acetone and then chloroform. NDI **42** was isolated as a dark brown powder (1.55 g, 93%) and was used without further purification.

^1H NMR (400 MHz: $[\text{D}_6]$ -DMSO) δ = 8.70 (4H, s, H⁴), 7.03 (4H, d, J = 8.5 Hz, H³) 6.69 (4H, d, J = 8.5 Hz, H²) 5.32 (4H, s, H¹) ppm.

^{13}C NMR (125 MHz: $[\text{D}_6]$ -DMSO) δ = 164.2, 149.8, 131.4, 130.1, 127.9, 127.5, 124.2, 114.6 ppm.

HR-MS (EI⁺) m/z calcd. for $\text{C}_{26}\text{H}_{16}\text{N}_4\text{O}_4[\text{M}^+]$ 448.1172, found: 448.1171.

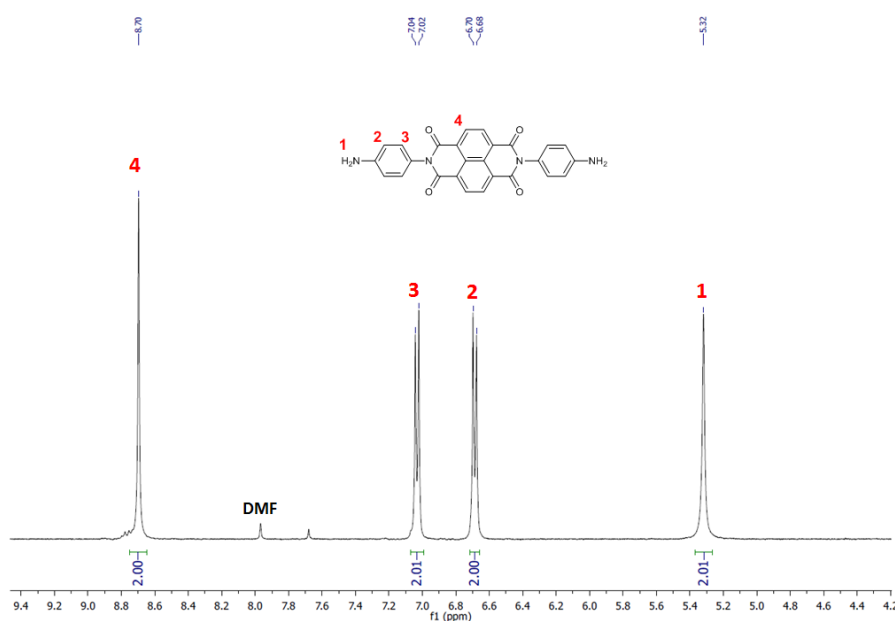


Figure 154: ^1H NMR (400 MHz: $[\text{D}_6]$ -DMSO) of NDI ligand **42**.

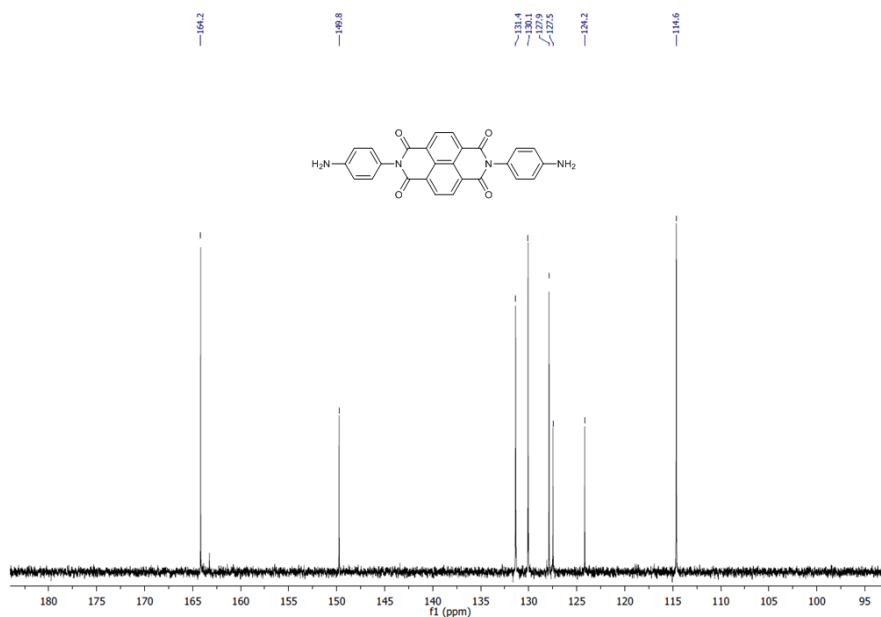


Figure 155: ^{13}C NMR (500 MHz: $[\text{D}_6]\text{-DMSO}$) of NDI ligand **42**.

7.6.2. Synthesis of cage **N₆**

NDI **42** (224 mg, 0.5 mmol), zinc(II) triflimide (208 mg, 0.33 mmol) and 2-formylpyridine (95 μL , 1.0 mmol) were combined in MeCN (20 mL). The flask was heated at 50 $^\circ\text{C}$ under N_2 for 24 h. The crude product was purified by filtration through Celite and precipitation with diethyl ether. The resultant dark yellow crystalline solid was isolated and washed with excess diethyl ether (349 mg, 67%).

^1H NMR (500 MHz: $\text{CD}_3\text{CN}/\text{CHCl}_3$ 1:1) δ = 8.75-8.61 (3H, m, H^5 & H^8), 8.50-8.48 (1H, m, H^3), 8.34-8.28 (1H, m, H^4), 8.25-8.07 (1H, m, H^1), 7.97-7.94 (1H, m, H^2), 7.43-7.32 (2H, m, H^7), 6.33-6.00 (2H, m, H^6) ppm.

^{13}C NMR (125 MHz: $\text{CD}_3\text{CN}/\text{CHCl}_3$ 1:1) δ = 166.6, 166.0, 165.8, 164.4, 164.3, 151.0, 150.8, 149.0, 148.9, 148.7, 147.4, 144.3, 136.5, 136.2, 136.0, 132.4, 132.2, 131.9, 128.6, 128.4, 128.4, 128.3, 128.3, 124.9, 123.1, 122.4, 119.8, 117.2.

HR-MS (ESI-FTICR, CHCl_3/ACN 1:1): m/z = 502.6777 $[\text{N}_6]^{8+}$, 614.5039 $[\text{N}_6(\text{NTf}_2^-)]^{7+}$, 763.6273 $[\text{N}_6(\text{NTf}_2^-)_2]^{6+}$, 972.8152 $[\text{N}_6(\text{NTf}_2^-)_3]^{5+}$.

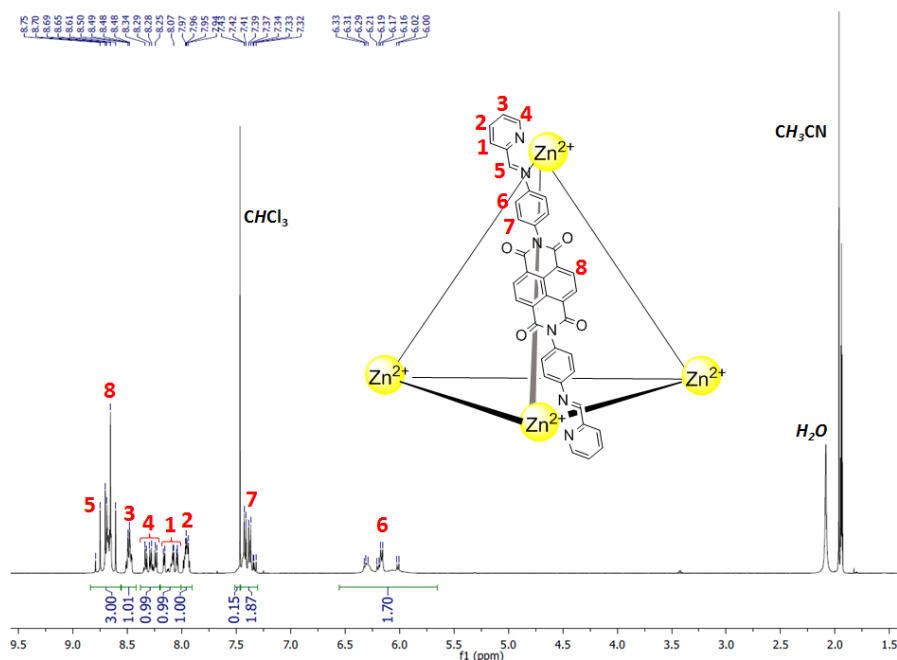


Figure 156: ¹H NMR (500 MHz: CD₃CN/CDCl₃ 1:1) of **N**₆ with assignments. **N**₆ exists predominantly the low symmetry *S*₄ diastereomer along with a smaller proportion of the *T* and *C*₃ diastereomers; several signals per ligand environment were therefore observed. Mixtures of diastereomers have been observed and reported in previous studies of M₄L₆ tetrahedral assemblies.^[203a, 203c]

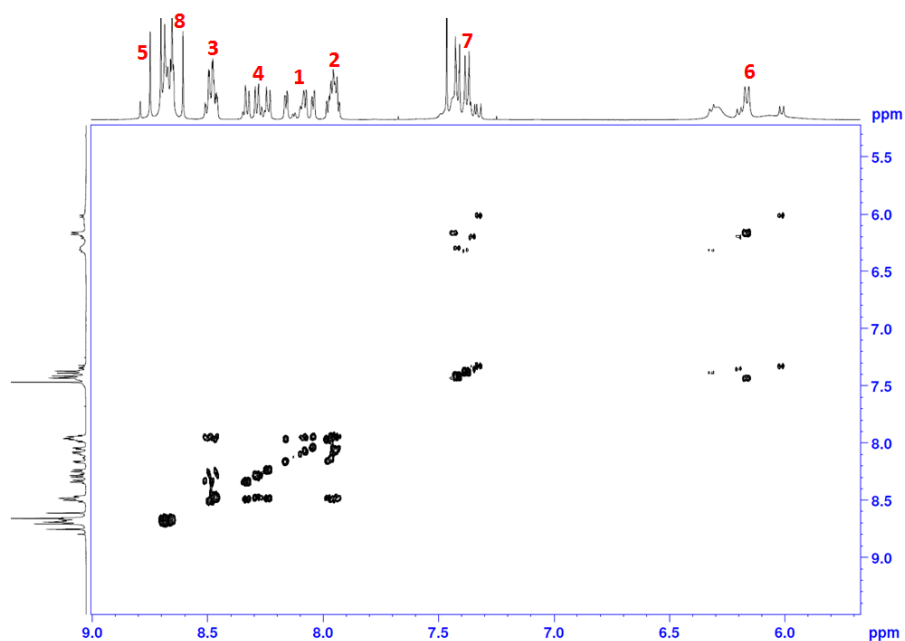


Figure 157: COSY NMR (500 MHz: CD₃CN/CDCl₃ 1:1, 298 K) of **N**₆.

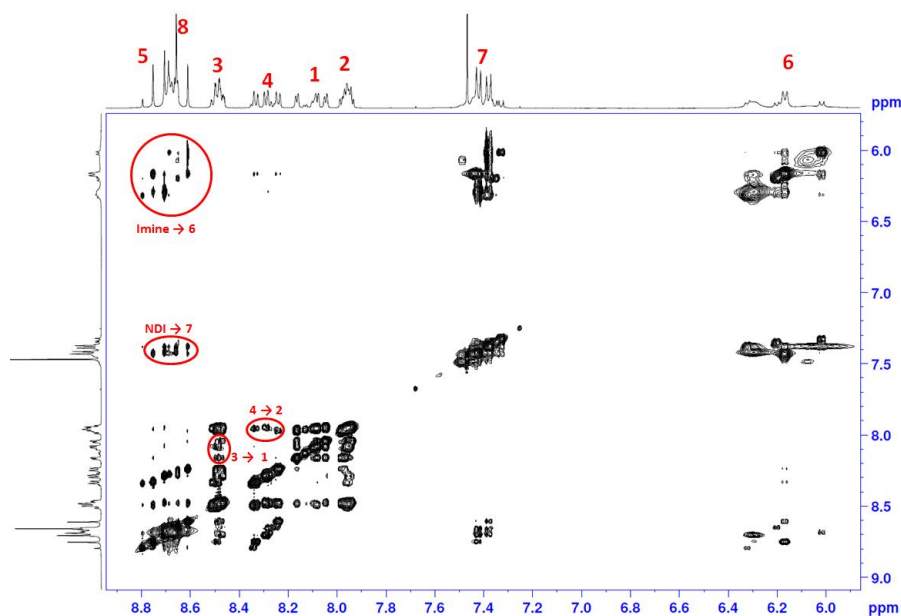


Figure 158: NOESY NMR (500 MHz: CD₃CN/CDCl₃ 1:1) of N₆.

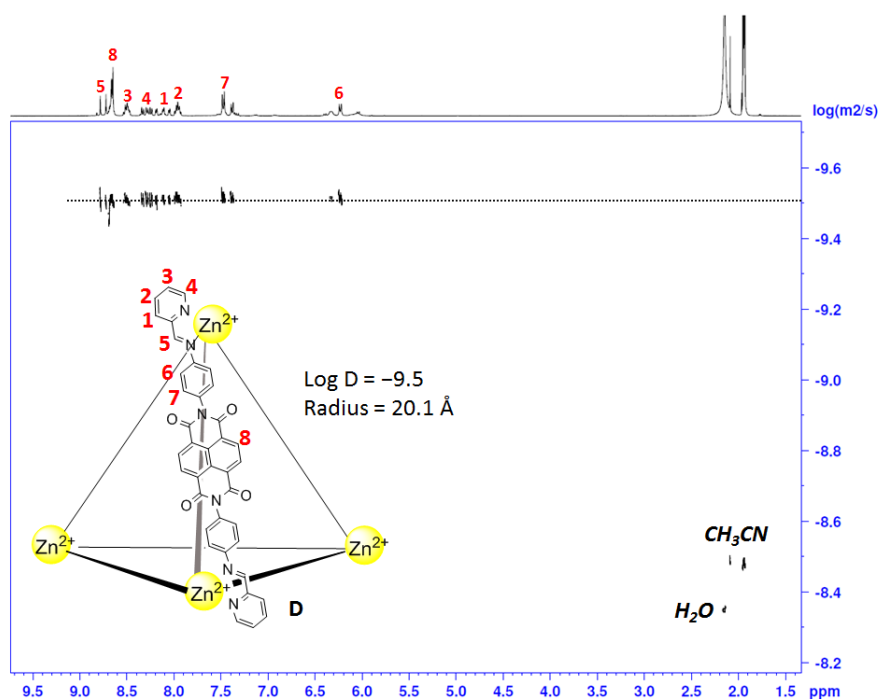


Figure 159: DOSY NMR spectrum (400 MHz: CD₃CN) of Zn₄L₆ N₆ with assignments.

7.6.3. NMR analysis of the interaction between N₆ and C

Solid N₆ (6.26 mg, 1 μM) was added to a J-Young NMR tube and dissolved with 250 μL of 1:1 CD₃CN/CDCl₃. A solution of C (6.36 mg in 250 μL of 1:1 CD₃CN/CDCl₃, 10 μM) was added into the solution of N₆, and the cap was sealed. This tube was briefly shaken to obtain a

homogenous solution then left to equilibrate over 48h. ^1H NMR of the sample showed the occurrence of multiple new resonances similar to those observed in our previous system^[204] and indicative of the formation of catenated adducts between **N₆** and **C**.

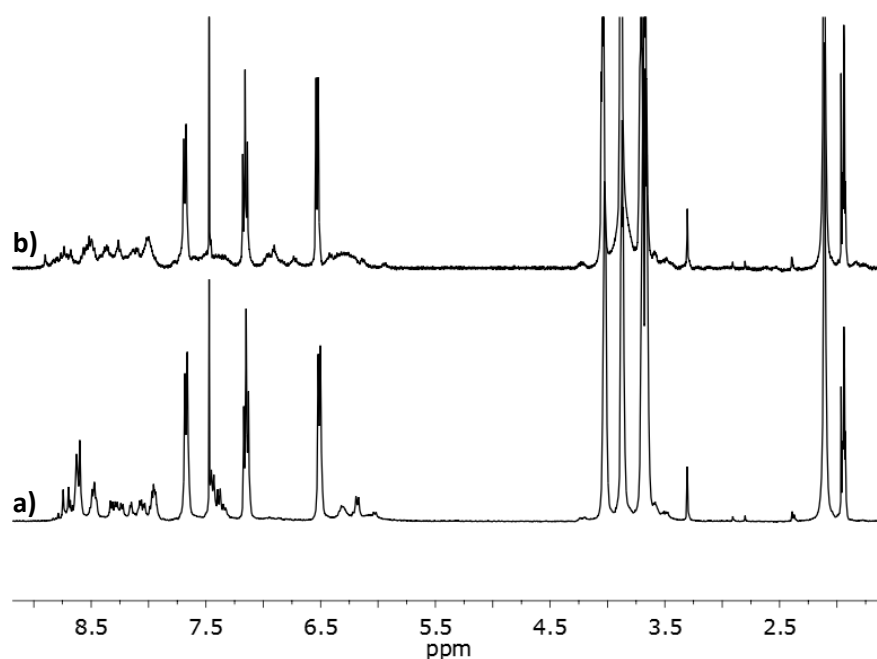
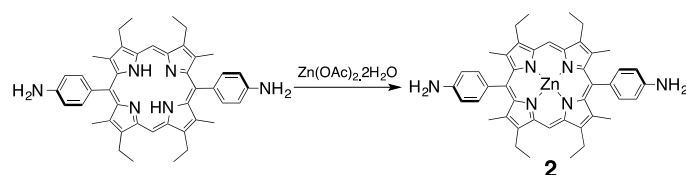


Figure 160: ^1H NMR spectra (400 MHz: $\text{CD}_3\text{CN}/\text{CD}_3\text{Cl}$ 1:1) of **N₆** and **C** (10 equivalents) at a) time = 0 min and b) after 400 min (top).

7.6.4. Synthesis of porphyrin diamine **43**



4,4'-(2,8,12,18-tetraethyl-3,7,13,17-tetramethylporphyrin-5,15-diyl)dianiline precursor was prepared by a previously reported method.^[207]

4,4'-(2,8,12,18-tetraethyl-3,7,13,17-tetramethylporphyrin-5,15-diyl)dianiline (100 mg, 0.15 mmol) was dissolved in CHCl_3 (20 mL). A solution of zinc acetate dihydrate (132 mg, 0.60 mmol) in methanol (5 mL) was added and the solution was stirred at rt for 5 h. The solution was washed with H_2O (2 x 50 mL), the organic solution was retained and dried with MgSO_4 . The solution was concentrated *in vacuo* then precipitated from hexane to give a pink solid that was isolated by filtration and dried (91 mg, 0.13 mmol, 87 %).

^1H NMR (400 MHz, CDCl_3) δ = 10.16 (2H, s), 7.78 (4H, d, J = 8.36 Hz) 7.01 (4H, d, J = 8.36 Hz) 4.01 (8H, q, J = 7.95 Hz), 3.91 (4H, s), 2.58 (12H, s), 1.77 (12H, t, J = 7.95 Hz) ppm.

^{13}C NMR (125 MHz, CDCl_3) δ = 148.6, 146.2, 146.1, 144.6, 138.2, 134.5, 134.0, 119.6, 114.5, 97.0, 20.1, 17.8, 15.5 ppm.

MS (ESI-TOF) m/z = 723.3 [2] $^+$.

Elemental analysis calcd (%) for $\text{C}_{44}\text{H}_{46}\text{N}_6\text{Zn}\cdot 0.4\text{CHCl}_3$ = C 69.08, H 6.06, N 10.89, found: C 69.00, H 5.96, N 10.52.

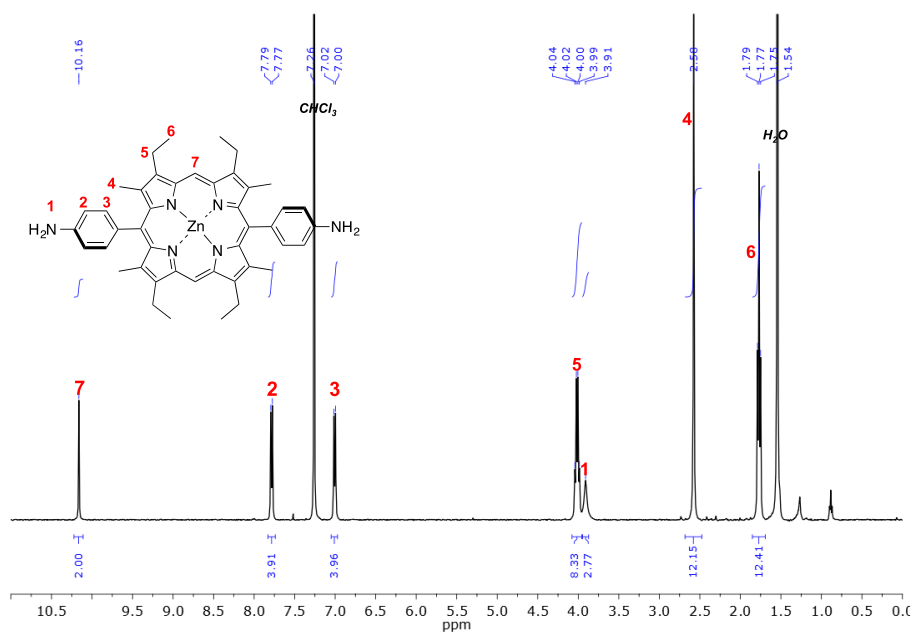


Figure 161: ^1H NMR (400 MHz, CDCl_3) spectrum of **43** with assignments.

7.6.5. Synthesis of porphyrin Zn_4L_6 cage **P6**

Porphyrin **43** (40.0 mg, 55 μmol), zinc(II) triflimide (23.0 mg, 37 μmol) and 2-formylpyridine (10.5 μL , 110 μmol) were combined in $\text{MeCN}/\text{CHCl}_3$ (7:3, 20 mL) and sonicated. The resultant red solution was heated at 343 K under N_2 for 16 h. The solution was concentrated *in vacuo* then added dropwise into diethyl ether. The resultant precipitate was isolated by filtration through Celite, washed with additional Et_2O , and then redissolved in MeCN . The solution was reduced to dryness to give a dark red powder (65.0 mg, 89%).

^1H NMR (500 MHz, CD_3CN) δ = 10.06 – 9.62 (m, 1H), 9.28 (m, 1H), 8.73 – 8.25 (m, 3H), 8.20 – 7.87 (m, 3H), 7.63 – 7.27 (m, 3H),

4.11 – 3.36 (m, 4H), 2.52 – 2.06 (m, 6H), 1.77 – 0.83 (m, 6H) ppm.

^{13}C NMR (125 MHz, CD_3CN) δ = 166.2, 165.5, 165.0, 151.0, 150.7, 150.4, 148.5, 148.1, 148.0, 147.9, 147.8, 147.7, 146.8, 146.7, 146.6, 146.5, 146.4, 146.2, 146.0, 145.9, 145.8, 145.8, 144.0, 138.0, 137.8, 135.5, 132.1, 131.9, 131.8, 131.5, 124.8, 122.5, 122.3, 122.2, 122.1, 98.0, 97.9, 97.7, 20.4, 20.3, 20.2, 20.0, 18.1, 17.9, 17.9, 17.6, 16.4, 16.3, 16.2, 16.2 ppm.

HR-MS (ESI-FTICR, CHCl_3/ACN 1:1) m/z = 709.6964 [P_6] $^{8+}$, 851.1489 [$\text{P}_6(\text{NTf}_2)$] $^{7+}$, 1040.1088 [$\text{P}_6(\text{NTf}_2)_2$] $^{6+}$.

Elemental analysis calcd (%) for $\text{C}_{352}\text{H}_{312}\text{F}_{48}\text{N}_{56}\text{O}_{32}\text{S}_{16}\text{Zn}_{10} \cdot 3\text{H}_2\text{O} \cdot 4\text{CHCl}_3$ = C 50.61, H 3.84, N 9.28, found: C 50.88, H 3.68, N 9.00.

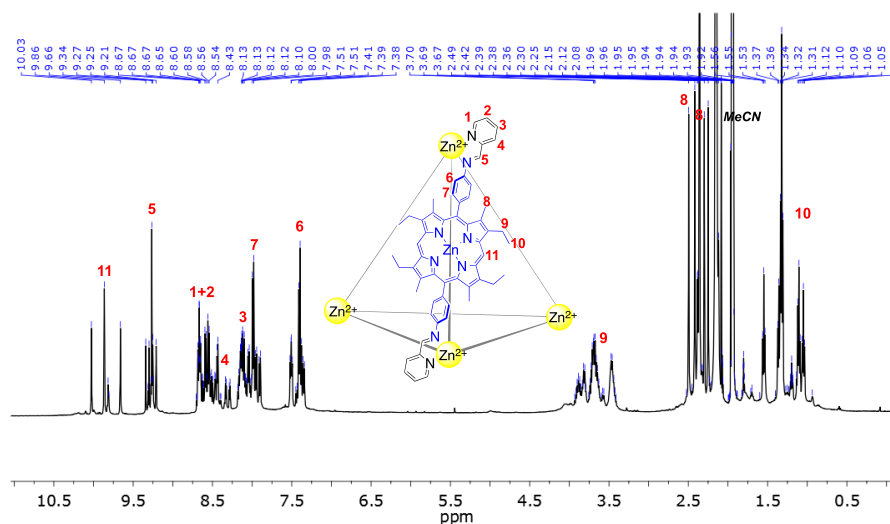


Figure 162: ^1H NMR spectrum (500 MHz, CD_3CN) of P_6 .

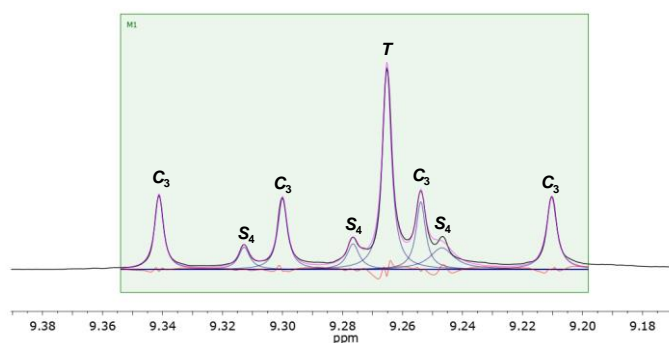


Figure 163: Imine-H resonances in the ^1H NMR (500 MHz, CD_3CN) spectrum of P_6 . Labels indicate which of 3 diastereomeric forms of P_6 each resonance corresponds to.^[203a, 203c]

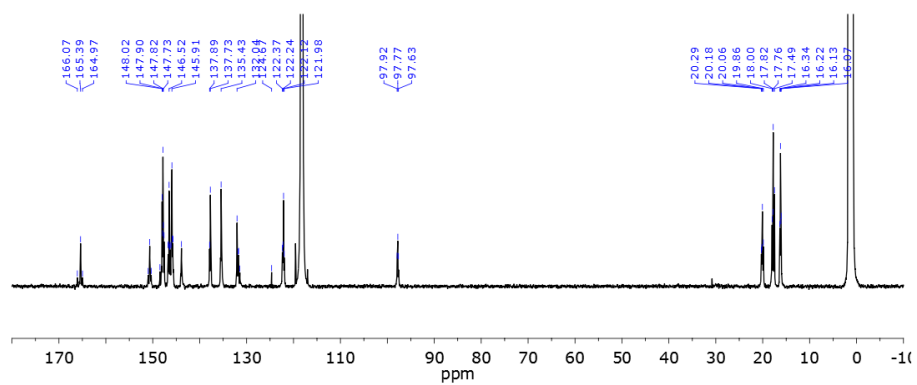


Figure 164: ^{13}C NMR (125 MHz, CD_3CN) spectrum of **P₆**.

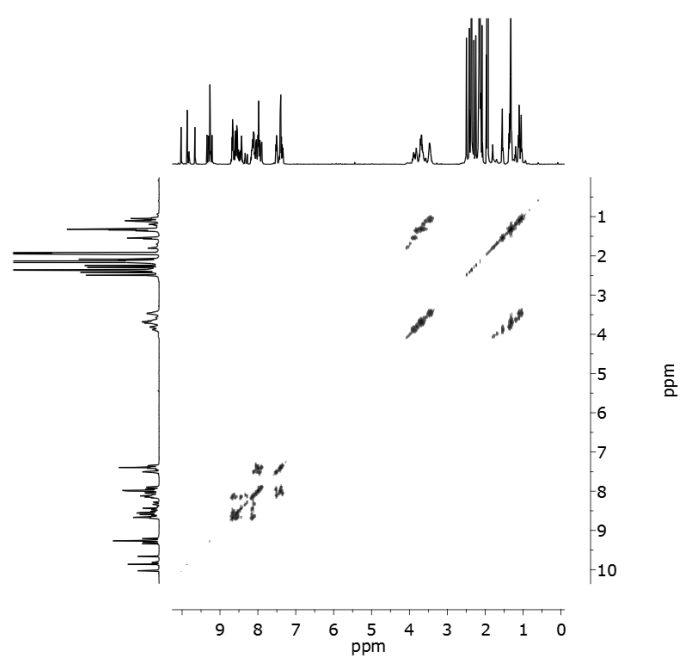


Figure 165: ^1H - ^1H COSY NMR (500 MHz, CD_3CN) spectrum of **P₆**.

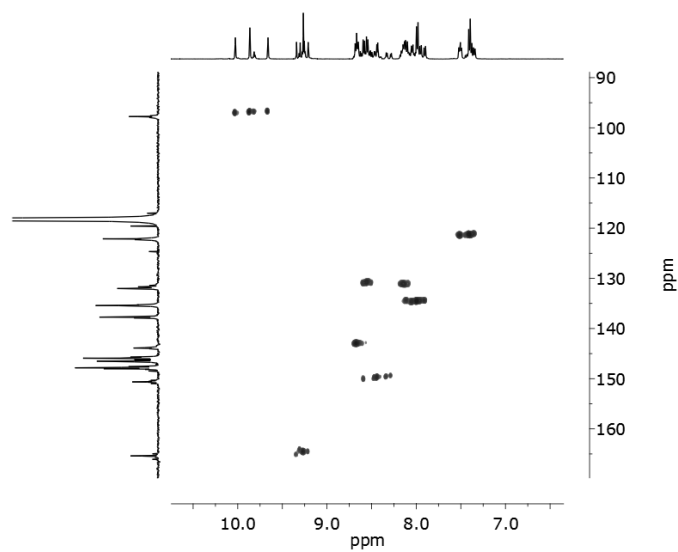


Figure 166: Aromatic region of the HSQC spectrum (CD_3CN) of **P₆**.

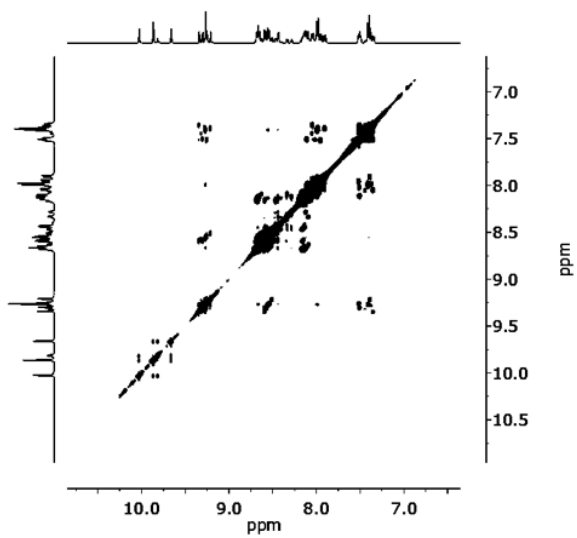
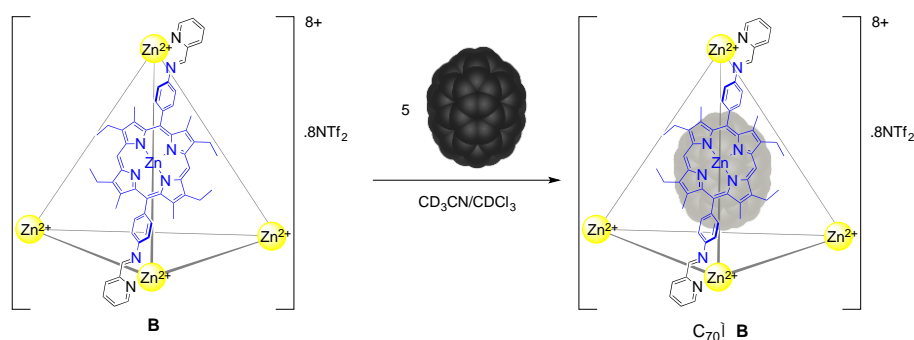


Figure 167: Aromatic region of the NOESY NMR spectrum (CD_3CN) of **P₆**.

7.6.6. Preparation of host-guest complex $C_{70}C\text{P}_6$



43 (4.0 mg, 5.5 μmol), $\text{Zn}(\text{NTf}_2)_2$ (2.3 mg, 3.7 μmol) and 2-formylpyridine (1.1 μL , 11 μmol) were combined in $\text{CD}_3\text{CN}/\text{CDCl}_3$ (7:3, 0.7 mL) and sonicated. The resultant red solution was heated at 323 K for 16 h. C_{70} (4.0 mg, 4.7 μmol) was added to the solution followed by sonication and heating at 323 K for a further 24h. On completion, the solution was added dropwise into Et_2O . The resultant precipitate was isolated by filtration through Celite, washed with additional Et_2O , then redissolved in MeCN. The solution was reduced to dryness to give a dark red powder (6.9 mg, 0.8 μmol , 87 %).

^1H NMR (500 MHz, CD_3CN) δ = 9.94 – 9.62 (m, 1H), 9.39 – 9.09 (m, 1H), 8.76 – 8.61 (m, 1H), 8.61 – 8.50 (m, 1H), 8.47 – 8.28 (m, 1H), 8.16 – 8.07 (m, 1H), 7.99 (br, 2H), 7.63 – 7.25 (m, 2H), 4.24 – 3.31 (m, 4H), 2.59 – 2.21 (m, 6H), 1.60 – 0.81 (m, 6H) ppm.

^{13}C NMR (125 MHz, CD_3CN) δ = 165.96, 165.46, 150.72, 148.32, 148.05, 147.95, 147.83, 146.98, 146.79, 146.73, 146.65, 146.35, 146.21, 146.07, 145.92, 143.90, 143.83, 143.49, 143.12, 141.07, 140.68, 137.26, 135.51, 132.16, 131.83, 126.56, 126.00, 124.77, 122.42, 122.22, 98.24, 20.11, 17.94, 17.88, 17.69, 16.24, 15.62 ppm.

HR-MS (ESI-FTICR, CHCl_3/ACN 1:1) m/z = 814.8504 $[\text{C}_{70}\text{C}\text{P}_6]^{8+}$, 971.3282 $[\text{C}_{70}\text{C}\text{P}_6(\text{NTf}_2)]^{7+}$;

Elemental analysis calcd (%) for $\text{C}_{422}\text{H}_{312}\text{F}_{48}\text{N}_{56}\text{O}_{32}\text{S}_{16}\text{Zn}_{10} \cdot 12\text{CHCl}_3$ = C 54.29, H 3.40, N 8.17, found: C 54.41, H 3.51, N 7.84.

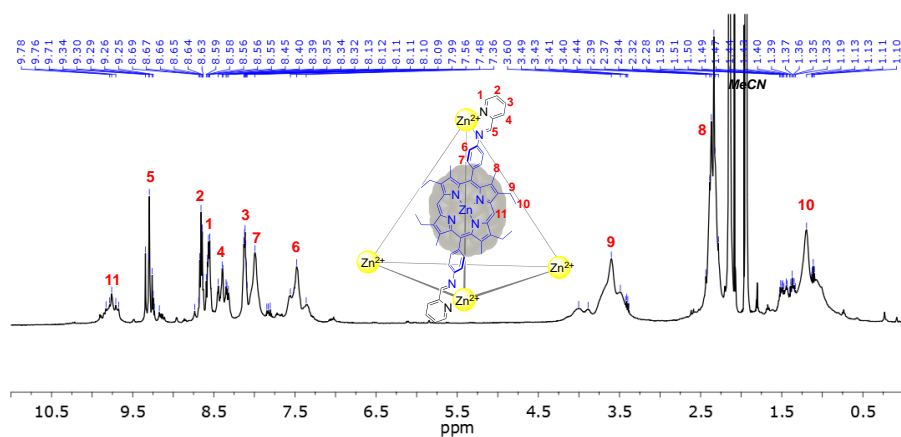


Figure 168: ^1H NMR (500 MHz, CD_3CN) spectrum of $\text{C}_{70}\text{C-P}_6$

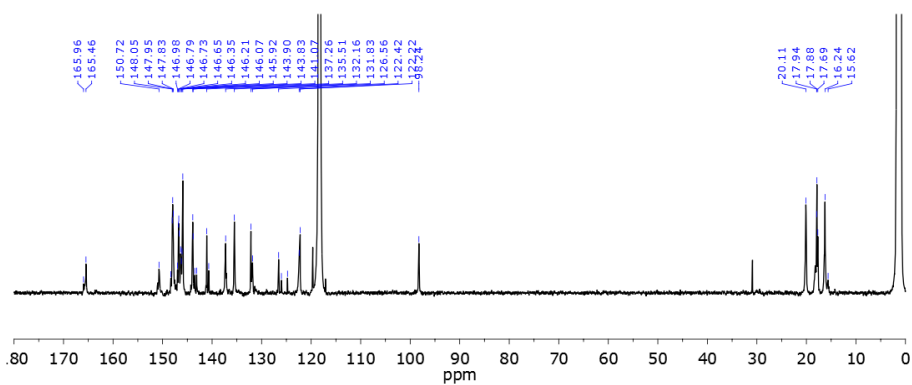


Figure 169: ^{13}C NMR (125 MHz, CD_3CN) spectrum of $\text{C}_{70}\text{C-P}_6$, showing new resonances between 140-145 ppm corresponding to C_{70} .

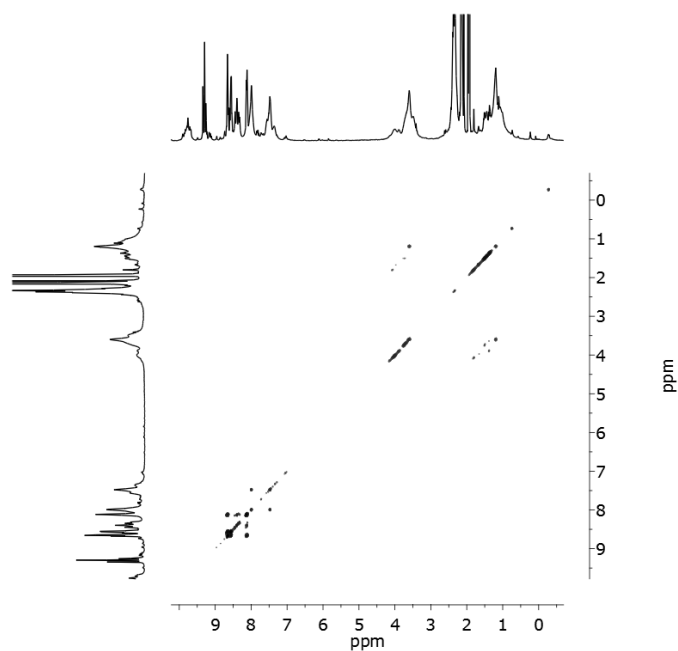


Figure 170: ^1H - ^1H COSY (500 MHz, CD_3CN) spectrum of $\text{C}_{70}\text{C-P}_6$.

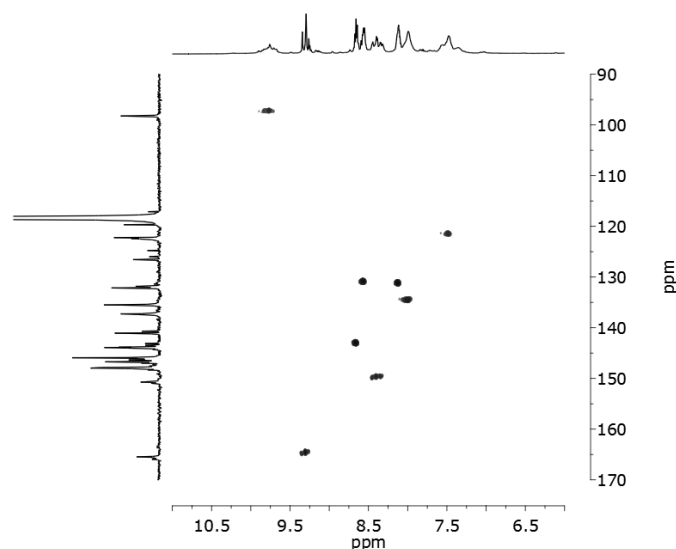


Figure 171: Aromatic region of the HSQC spectrum (CD_3CN) of $\text{C}_{70}\text{C-P}_6$.

7.6.7. Interactions between P_6 and C

It was anticipated that the porphyrin components of P_6 would be too bulky to allow catenation to occur with C . To investigate this, an experiment was conducted where P_6 and C were mixed in a 1:1 ratio in a 1:1 solution of CDCl_3 and CD_3CN . The solution was analysed by ^1H NMR immediately after mixing (Figure S19) and no further change in the spectrum was observed after heating to 323 K for 2 h. The resultant NMR spectrum showed the presence of broad resonances between 6-7 ppm that correspond to the aromatic protons of C . The upfield shift of these resonances is indicative of an interaction between the naphthalene units in C and P_6 , however, their rapid appearance and broadness are consistent with a fast-exchange process whereby π -interactions occur without a catenation event taking place. As observed in the case of N_6 and in our previously reported system,^[204] the formation of catenanes with C yields sharp NMR resonances consistent with a specific interaction between C and the tetrahedral assemblies.

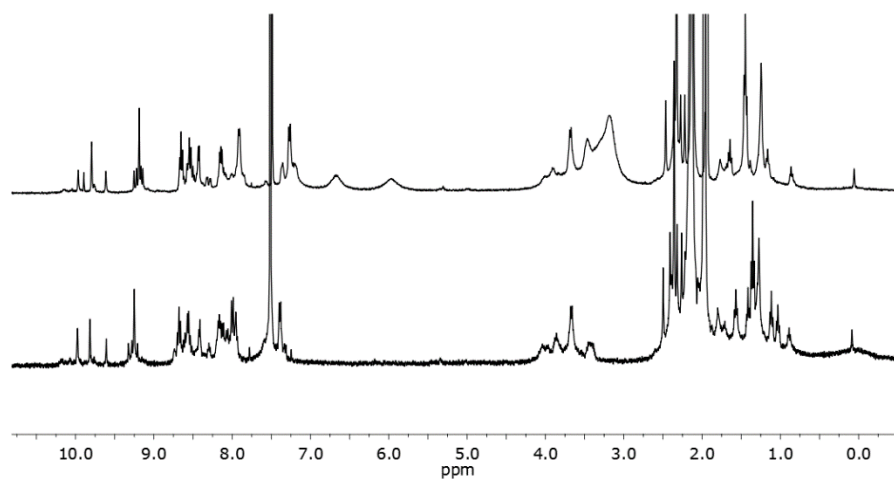


Figure 172: ^1H NMR (400 MHz, 1:1 $\text{CD}_3\text{CN}/\text{CDCl}_3$) spectrum of P_6 (bottom) and P_6 and C (1 equiv, top).

7.6.8. Infrared multiphoton dissociation (IRMPD) MS/MS of catenated cages

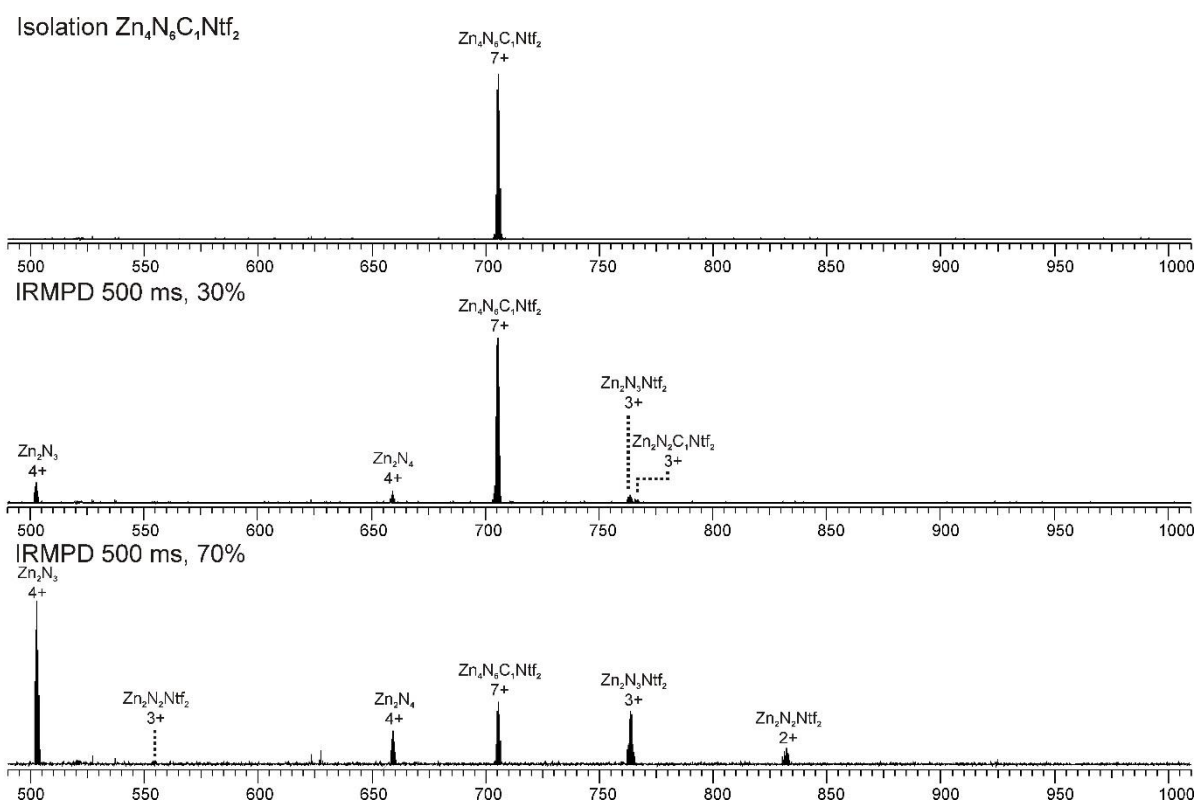


Figure 173: ESI-FTICR MS isolation and fragmentation of $[\text{Zn}_4\text{N}_6\text{C}_1(\text{NTf}_2)]^{7+}$ ($m/z = 704$).

Isolation $Zn_4N_6C_2Ntf_2$

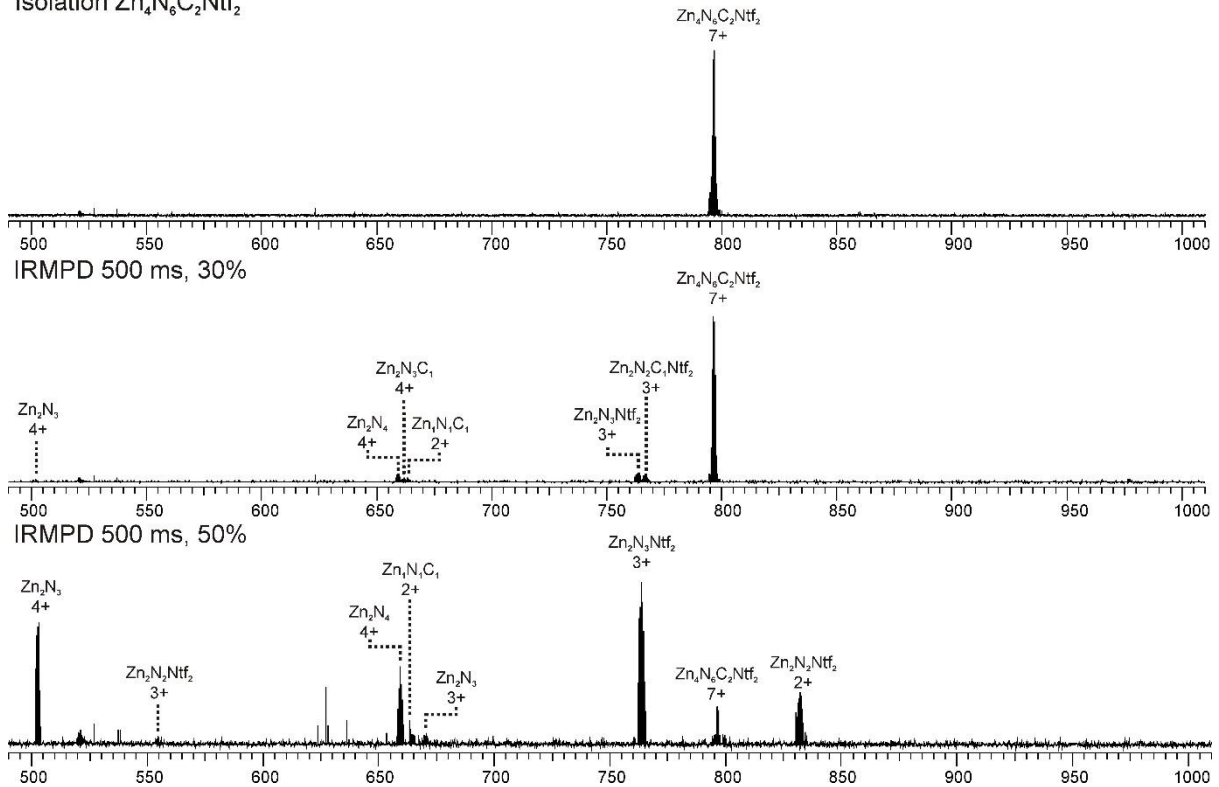


Figure 174: ESI-FTICR MS isolation and fragmentation of $[Zn_4N_6C_2(NTf_2)]^{7+}$ ($m/z = 795$).

Isolation $Zn_4N_6C_3Ntf_2$

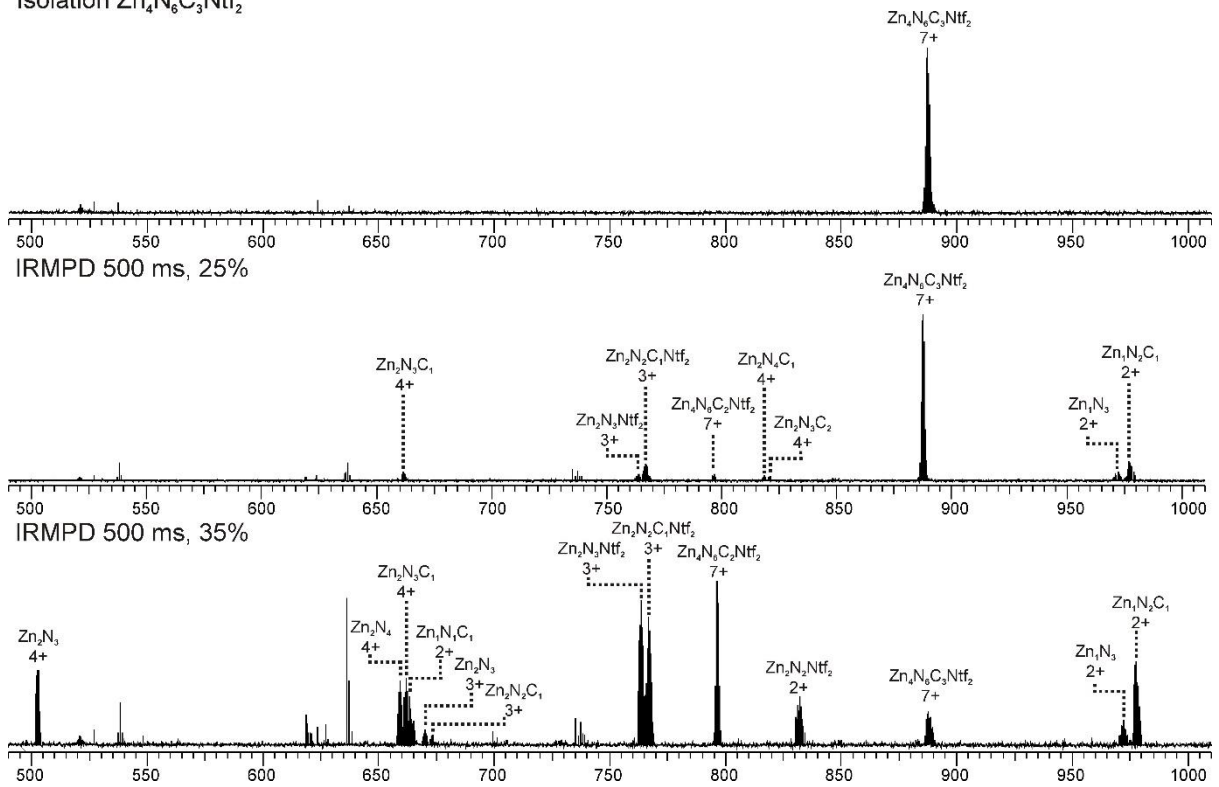


Figure 175: ESI-FTICR MS isolation and fragmentation of $[Zn_4N_6C_3(NTf_2)]^{7+}$ ($m/z = 887$).

Isolation $Zn_4N_6C_4Ntf_2$

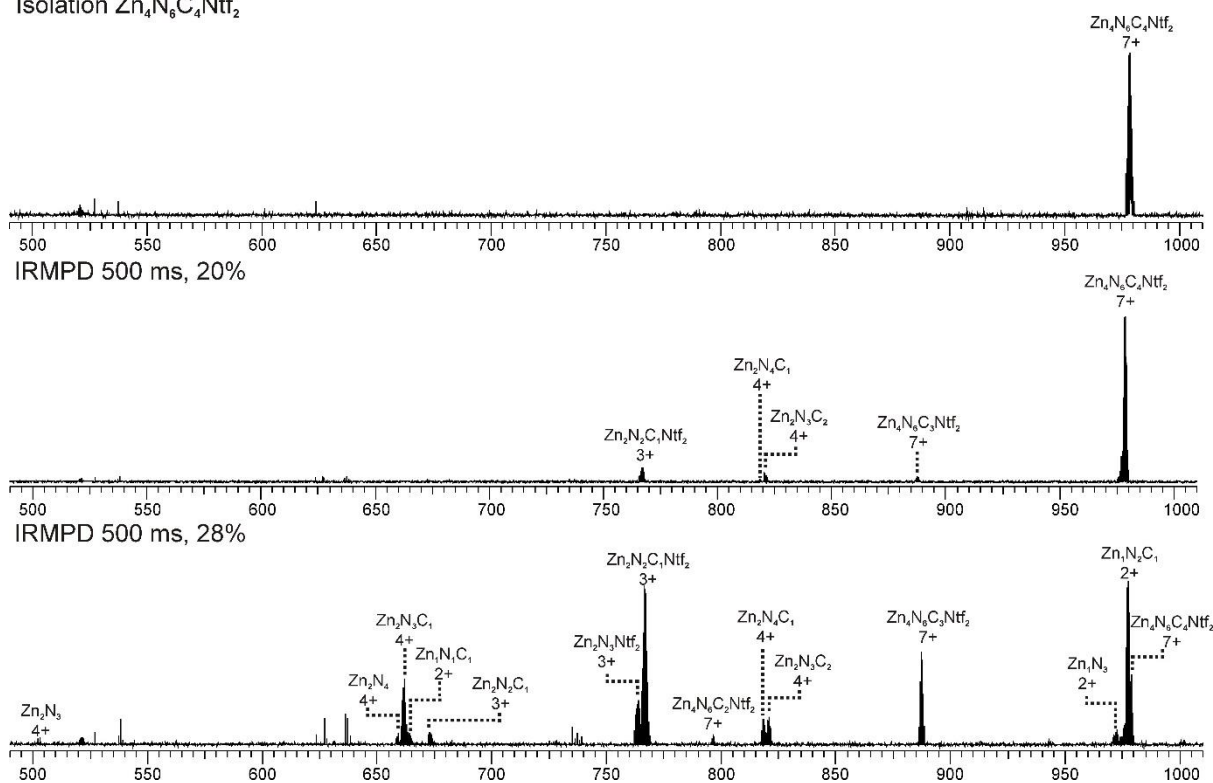


Figure 176: ESI-FTICR MS isolation and fragmentation of $[Zn_4N_6C_4(NTf_2)]^{7+}$ ($m/z = 979$).

7.6.9. Analysis of a mixed ligand cage DCL

General procedure for DCL Preparation

For ESI-MS analysis DCLs were created using 1:1 mixtures of the purified cages N_6 and P_6 (1:1 MeCN/ $CHCl_3$, 1mM). These solutions were combined in glass vials and allowed to equilibrate at room temperature for at least 24 h. For ESI-MS measurements the solutions were extracted, diluted (25 μ M) and mixed by hand for 1 min before injection.

For templation studies, C_{70} was added as a solid (4 equivalents relative to total cage content) to an equilibrated DCL solution. C was synthesised using the methods previously described^[204] and was also introduced to equilibrated DCL as a solid (0.5 or 4 equivalents). Templated libraries were allowed to re-equilibrate at room temperature for a further 24 h prior to ESI-MS analysis.

Procedure for DCL Analysis.

MS data were processed using the instrument's Omega MS software.^[225] In each experiment, the intensities of the + 8 and + 7 charge states of each species were summed to give an overall observable intensity per species. These values were

combined for all species with the same **N:P** ratio (*i.e.* including host-guest adducts). Once summed, all intensities were normalised with respect to the maximum signal intensity obtained. These values were then plotted to give the relative distribution of the $N_xP_{(6-x)}$ species.

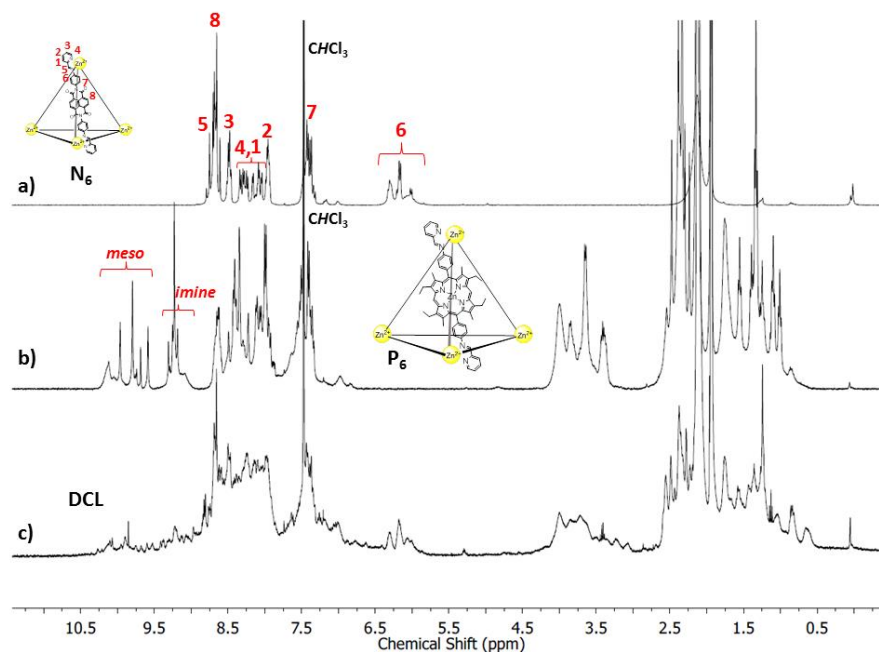


Figure 177: ^1H NMR (400 MHz, 1:1 $\text{CD}_3\text{CN}/\text{CDCl}_3$) spectra of a) N_6 , b) P_6 and c) the DCL obtained from a 1:1 mixture of N_6 and P_6 24h after mixing.

7.6.10. Preparation of a DCL from cage building blocks

As a control experiment to confirm the equilibrium state, a DCL was prepared by an independent synthesis from a mixture of all building blocks and not as usual from the purified cages.

Therefore, porphyrin ligand (7.24 mg, 0.01 mM), NDI ligand (4.48 mg, 0.01 mM) and metal salt (0.0133 mM, 9.39 mg for $\text{Fe}[\text{NTf}_2]_2 \cdot 5\text{H}_2\text{O}$ or 8.32 mg for $\text{Zn}[\text{NTf}_2]_2$) were added to a flask. 2ml of MeCN and 2ml of CHCl_3 were added and the reaction mixture was sonicated in a warm ultrasonic bath for 30 mins. 2-pyridinecarboxylate (0.02 mM, 2.14 mg) was then added to the suspension and the reaction was allowed to equilibrate for 7d at 50°C .

7.6.11. X-ray crystallography

Data were collected with an Oxford Gemini Ultra employing confocal mirror monochromated $\text{Cu-K}\alpha$ radiation generated from a sealed tube (1.5418 \AA) with ω and

ψ scans at 120(2) K or at Beamline I19 of Diamond Light Source^[226] employing silicon double crystal monochromated synchrotron radiation (0.6889 Å) with ω scans at 100(2) K.^[227] Data integration and reduction were undertaken with CrysAlisPro^[228] or with SAINT and XPREP^[229] (following treatment with ECLIPSE^[230]). Subsequent computations were carried out using the WinGX-32 or ShelXle^[231] graphical user interface.^[232] Gaussian absorption corrections were applied using CryAlisPro^[228] and multi-scan empirical absorption corrections were applied to the data using SADABS.^[229] Structures were solved by direct methods using SHELXT^[233] or SUPERFLIP^[234] then refined and extended with SHELXL.^[233b] In general, non-hydrogen atoms with occupancies greater than 0.5 were refined anisotropically. Carbon-bound hydrogen atoms were included in idealised positions and refined using a riding model. Nitrogen and oxygen-bound hydrogen atoms were first located in the difference Fourier map before refinement. Disorder was modelled using standard crystallographic methods including constraints, restraints and rigid bodies where necessary. Crystallographic data along with specific details pertaining to the refinement follow. Crystallographic data have been deposited with the CCDC (CCDC 1061975 - 1061977).

7.6.11.1. 43(MeOH)·0.5MeOH.

Formula $C_{45.5}H_{52.5}N_6O_{1.5}Zn$, M 772.80, Monoclinic, space group $P2_1$ (#4), a 8.3889(4), b 21.3112(10), c 11.1950(6) Å, β 93.127(3), V 1998.43(17) Å³, D_c 1.284 g cm⁻³, Z 2, crystal size 0.08 by 0.01 by 0.002 mm, colour red, habit needle, temperature 100(2) Kelvin, λ (synchrotron) 0.6889 Å, μ (synchrotron) 0.610 mm⁻¹, T (SADABS)_{min,max} 0.6027, 0.7454, $2\theta_{max}$ 53.14, hkl range -10 10, -25 27, -14 14, N 26343, N_{ind} 8316 (R_{merge} 0.0636), N_{obs} 6057 ($I > 2\sigma(I)$), N_{var} 525, residuals* $R1(F)$ 0.0584, $wR2(F^2)$ 0.1776, $GoF(all)$ 1.045, $\Delta\rho_{min,max}$ -0.376, 1.262 e⁻ Å⁻³.

Specific refinement details:

The zinc atom and coordinated methanol were modelled as disordered over two positions on opposite sides of the porphyrin ring with occupancies of 0.70 and 0.30. As a consequence of this disorder the structure displays strong pseudosymmetry. However structure solution in $P2_1/c$ (with the occupancies of the disordered parts fixed at 0.50 by symmetry) resulted in significantly worse residuals and the structure was thus refined as a racemic twin in $P2_1$ with the Flack parameter refining to 0.44(3).

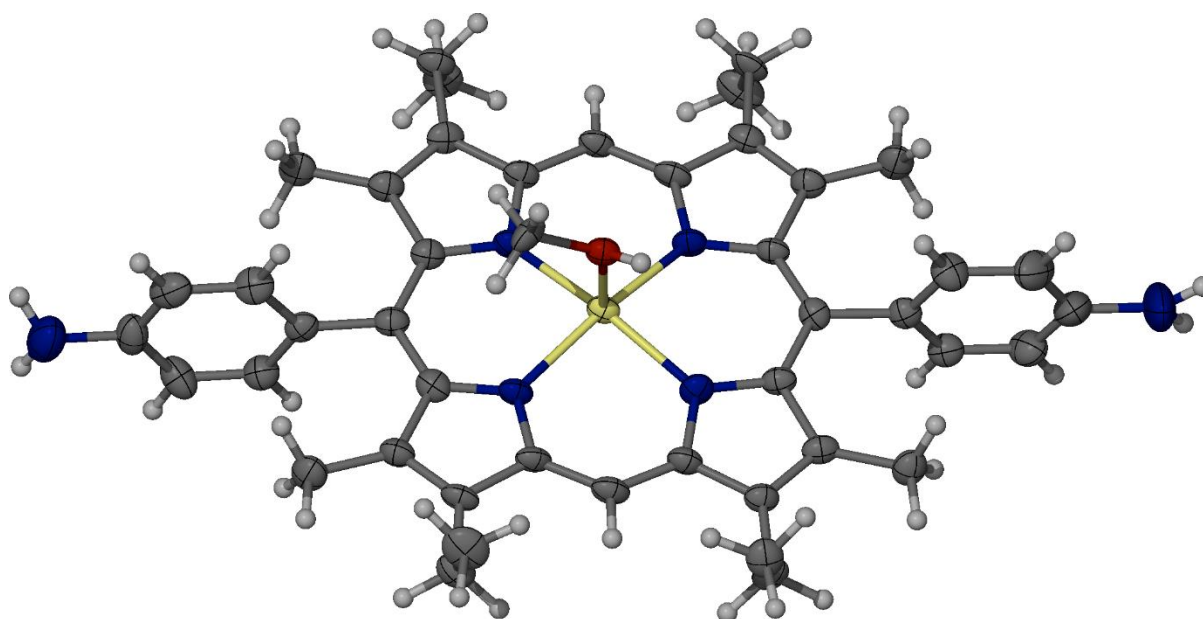


Figure 178: Crystal structure of **43**, with a single molecule of MeOH axially bound to the Zn center of the porphyrin (ORTEP 50%, disorder omitted for clarity). Zn = yellow, C = grey, H = white, N = blue, O = red.

Table 6: Hydrogen bonds in the structure of **43**(MeOH)·0.5MeOH [Å and °].

D-H...A	d(D-H)	d(H...A)	d(D...A)	<(DHA)
O(1)-H(1A)...N(5)#1	0.82	2.10	2.794(9)	142.5
N(5)-H(5A)...O(1A)#2	0.91	2.15	3.044(12)	167.8
N(6)-H(6B)...O(1A)#3	0.91	1.81	2.494(15)	130.4

Symmetry transformations used to generate equivalent atoms:

#1 -x,y+1/2,-z+1 #2 -x,y-1/2,-z #3 -x,y+1/2,-z

7.6.11.2. [N₆]-5NTf₂·3PF₆.

Formula C₂₃₀H₁₃₂F₂₄N₃₇O₂₈P₃S₂Zn₄, *M* 4736.23, monoclinic, space group P 21/c (#14), *a* 29.307(5), *b* 45.110(9), *c* 26.896(6) Å, *b* 91.52(3), *V* 35545(12) Å³, *D_c* 0.885 g cm⁻³, *Z* 4, crystal size 0.443 by 0.327 by 0.177 mm, colour yellow, habit block, temperature 120(2) Kelvin, λ(CuKa) 1.54184 Å, μ(CuKa) 1.310 mm⁻¹, *T*(CRYALISPRO)_{min,max} 0.692, 1.287, 2θ_{max} 77.62, *hkl* range -23 14, -36 36, -21 21, *N* 37642, *N*_{ind} 19847 (*R*_{merge} 0.0526), *N*_{obs} 15247 (*I* > 2σ(*I*)), *N*_{var} 2953, residuals* *R*1(*F*) 0.1969, *wR*2(*F*²) 0.5324, *GoF*(all) 2.255, Δρ_{min,max} -0.664, 0.923 e⁻ Å⁻³.

Specific refinement details:

The crystals of [N₆]-5NTf₂·3PF₆ were extremely unstable, immediately decaying once removed from the mother liquor and required rapid handling to facilitate data collection. This structure resembles that of a small protein in that only weak diffraction up to 1.2 Å

resolution was achieved, resulting in poor quality data (e.g high R_{int} and wR_2). However the data are more than sufficient to establish the connectivity of the structure. Macromolecular refinement techniques were carefully adapted to build a molecular model, increase the robustness of the refinement and establish the connectivity of all modelled structural components with acceptable precision. To achieve this, similar organic building blocks in the structure (NDI ligands, PF_6^- and triflimide counter ions) were grouped into residues. Stereochemical restraint dictionaries^[235] for each of these building blocks were generated with the GRADE program^[236] using the GRADE Web Server^[237] and applied in the structure refinement. The GRADE dictionary for SHELXL contains target values and standard deviations for 1,2-distances (DFIX) and 1,3-distances (DANG), as well as restraints for planar groups (FLAT). Local structural similarity^[238] was exploited to make the geometries of NDI ligands similar using non-crystallographic symmetry restraints (NCSY) for 1,4 distances. The refinement of ADPs for all non-hydrogen atoms was enabled by employing similarity (SIMU) and enhanced rigid bond restraints (RIGU)^[239] in SHELXL.^[233b] Disordered solvent/counterion areas occupy 11% of the unit cell. In contrast to indications from refinement statistics, the final model is in good agreement with experimentally observed electron density (Figure S28). Five anions per cage were significantly disordered; no satisfactory model for the electron-density associated with them could be found despite numerous attempts at modeling. Therefore the SQUEEZE^[240] function of PLATON^[241] was employed to remove the contribution of the electron density associated with these anions and further disordered solvent molecules.

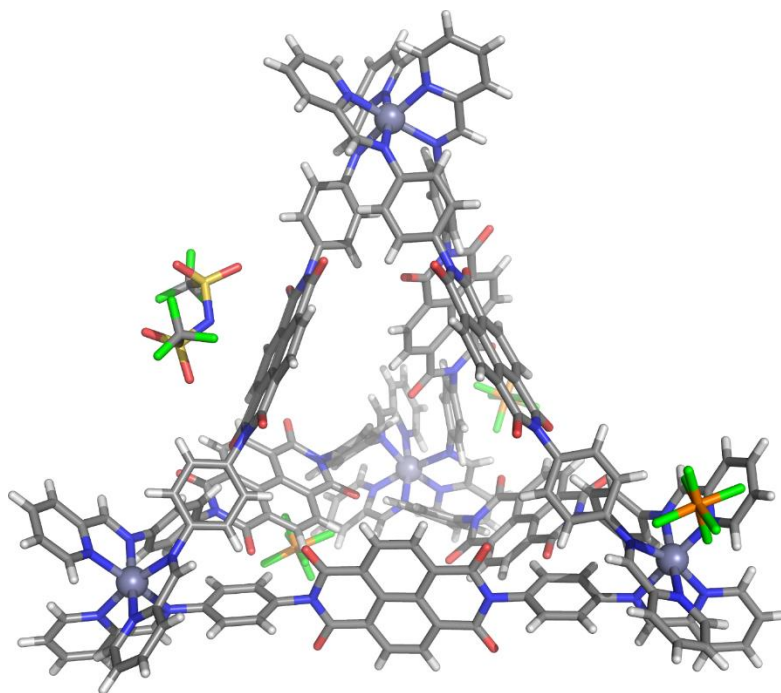


Figure 179: Atomic representation of the asymmetric unit of NDI cage **N₆** including all modelled hexafluorophosphate and triflimide counter ions.

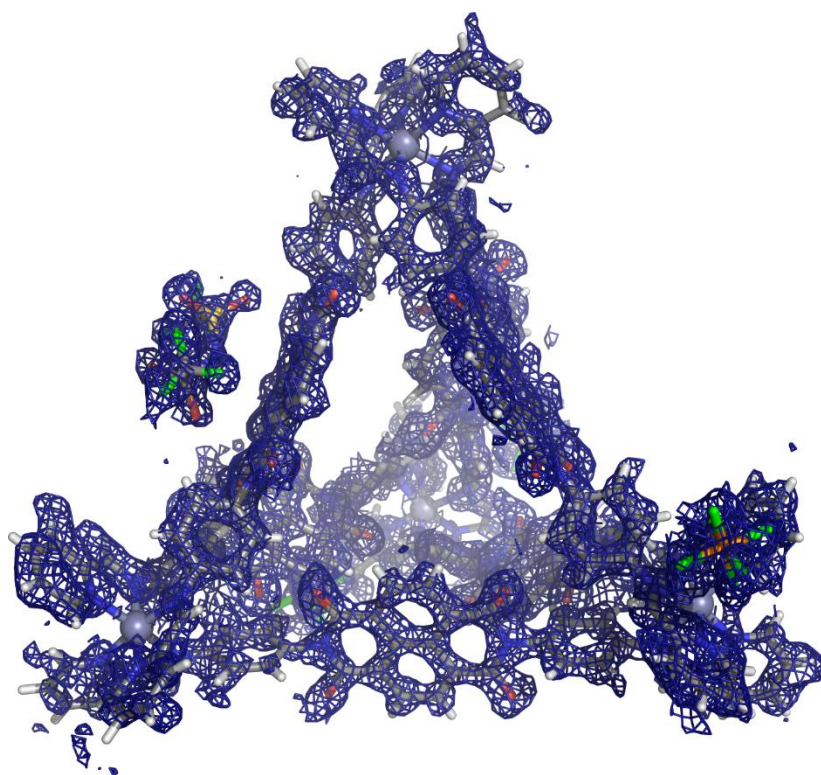


Figure 180: Atomic representation of the asymmetric unit of NDI cage **N₆** including all modelled hexafluorophosphate and triflimide counter ions. In addition to the previous figure the observed electron density (F_o) is shown as a blue mesh at 1.0 σ level, indicating a good fit of the final model into the observed electron density.

7.6.11.3. $[\text{P}_6(\text{H}_2\text{O})_3(\text{MeCN})_3]\cdot 8\text{OTf}$.

Formula $\text{C}_{350}\text{H}_{327}\text{F}_{24}\text{N}_{51}\text{O}_{27}\text{S}_8\text{Zn}_{10}$, M 7045.79, Trigonal, space group P-3c1 (#165), a 35.2240(14), b 35.2240(14), c 43.354(2) Å, $\gamma 120^\circ$, V 46584(4) Å³, D_c 1.005 g cm⁻³, Z 4, crystal size 0.010 by 0.010 by 0.002 mm, colour dark red, habit block, temperature 100(2) Kelvin, $\lambda(\text{synchrotron})$ 0.6889 Å, $\mu(\text{synchrotron})$ 0.522 mm⁻¹, T(SADABS)_{min,max} 0.4689, 0.7440, $2\theta_{\text{max}}$ 33.36, hkl range -29 29, -29 29, -36 34, N 244576, N_{ind} 9422 (R_{merge} 0.1946), Nobs 6832 ($I > 2\sigma(I)$), N_{var} 1257, residuals* $R1(F)$ 0.1034, $wR2(F^2)$ 0.2977, GoF(all) 1.129, $\Delta\rho_{\text{min,max}}$ -0.284, 0.520 e⁻ Å⁻³.

Specific refinement details:

The crystals of $[\text{P}_6(\text{H}_2\text{O})_3(\text{MeCN})_3]\cdot 8\text{OTf}$ were extremely unstable, immediately decaying once removed from the mother liquor and required rapid handling to facilitate data collection. The crystals were also weakly diffracting with very few reflections recorded at higher than 1.2 Å resolution despite the use of synchrotron radiation; however the data are more than sufficient to establish the connectivity of the structure. The tetrahedron lies astride a centre of symmetry such that one third of it is crystallographically unique. Three of the ethyl groups were modelled as disordered over two positions. There is a significant amount of thermal motion in the extremities of the molecule and extensive thermal parameter (SIMU and DELU were applied to all non-hydrogen atoms except for Zn) and bond length restraints (DFIX) were required to facilitate realistic modeling of the organic parts of the structures. Four anions per cage were significantly disordered; no satisfactory model for the electron-density associated with them could be found despite numerous attempts at modeling. Therefore the SQUEEZE^[240] function of PLATON^[241] was employed to remove the contribution of the electron density associated with these anions and further disordered solvent molecules.

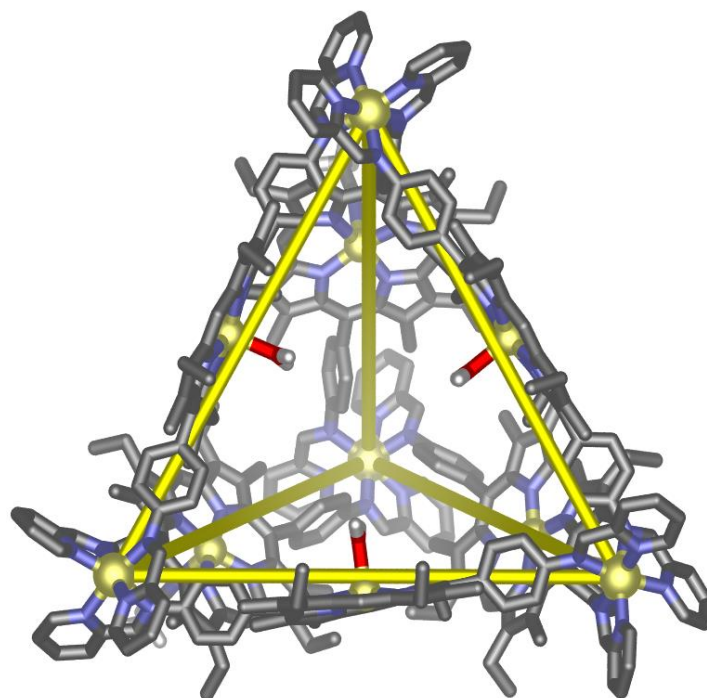


Figure 181: Representation of the crystal structure of **P₆**, showing the three axial-bound water molecules directed inside the assembly. Yellow lines between the Zn^{II} atoms are included to highlight the tetrahedral framework. Hydrogen atoms (excluding those of H₂O), other solvent molecules, and anions are omitted for clarity. Zn = yellow, C = grey, H = white, N = blue, O = red.

8. Acknowledgements

First of all, I would like to thank Prof. Dr. Christoph Schalley for giving me the opportunity to accomplish my Ph.D. thesis under his supervision: I enjoyed the numerous fruitful discussions with you, the support and suggestions for my work, but also the freedom you left me in shaping my research projects.

Second, I wish to express my gratitude to Prof. Dr. Rainer Haag for being my second supervisor.

Many thanks to all present and former group members of the AG Schalley for the friendly working environment, the cooperative atmosphere and the lots of fruitful discussions. In particular, I would like to thank the former and current members of the surface team in the AG Schalley: Dr. Johannes Poppenberg, Dr. Sebastian Richter, Dr. Christoph Traulsen und Dr. Thomas Heinrich. Especially, I am grateful to Thomas for the close collaboration, the help with surface experiments and the measurement of numerous XPS and NEXAFS spectra.

I would like to thank Jan Ole Kaufmann and Verena Will for their excellent lab work during their bachelor's theses and internships. I thank Sebastian Müller for his valuable synthetic support as lab technician. Furthermore, I am grateful to Dr. Felix Limberg for lots of valuable discussions about our research projects.

I would like to thank Prof. Kari Rissanen for the warm welcome in his working group in Jyväskylä and the successful collaboration, Dr. Rakesh Puttreddy for measuring and solving crystal structures and the German Academic Exchange Service (DAAD) for funding my stay in Finland. For the successful collaboration on surface analysis, I am grateful to Dr. Wolfgang Unger and Andreas Lippitz from the Federal Institute for Materials Research and Testing. Furthermore, I would like to thank Prof. Jonathan Nitschke and his group, especially Sam Black and Daniel Wood, for the fruitful cooperation project.

I am very thankful to the MS department, in particular Dr. Andreas Springer and Fabian Klautzsch, for the support during my own MS measurements and for the many service measurements they conducted for me. I also acknowledge Dr. Andreas Schäfer and his colleagues in the NMR department for the measurement of numerous NMR spectra.

I thank the Beilstein-Institut for a Ph.D. fellowship and the Deutsche Forschungsgemeinschaft (SFB 765) for financial support.

Last but not least, I want to express my heartfelt gratitude to Dr. Lena Kaufmann, Renate Fiedler-Schwarz and Karl Georg Schwarz for their loving attention and support!

9. Appendix

9.1. Publications

- [1] Catenation and encapsulation induce distinct reconstitutions within a dynamic library of mixed-ligand Zn_4L_6 cages
S. P. Black, D. M. Wood, F. B. Schwarz, T. K. Ronson, J. J. Holstein, A. R. Stefankiewicz, C. A. Schalley, J. K. M. Sanders, J. R. Nitschke, *Chem. Sci.* **2016**, 7, 2614-2620.
- [2] Photocontrolled On-Surface Pseudorotaxane Formation with Well-Ordered Macrocyclic Multilayers
F. B. Schwarz, T. Heinrich, J. O. Kaufmann, A. Lippitz, R. Puttreddy, K. Rissanen, W. E. S. Unger, C. A. Schalley, *Chem. Eur. J.* **2016**, 22, 14383-14389.
- [3] A photoswitchable rotaxane operating in monolayers on solid support
F. B. Schwarz, T. Heinrich, A. Lippitz, W. E. S. Unger, C. A. Schalley, *Chem. Commun.* **2016**, Accepted Manuscript.

9.2. Oral and poster presentations

- [1] Surface Chemistry – Multilayers of Switchable Rotaxanes
F. B. Schwarz, T. Heinrich
Oral presentation, G4 Meeting, 23.08.2013, Freie Universität Berlin, Germany.

- [2] Photoswitchable Rotaxanes for Deposition in ordered Multilayers on Gold Surfaces
F. B. Schwarz, C. A. Schalley
Poster presentation, SupraChem 2015, 22.02.2015 – 24.02.2015, Freie Universität Berlin, Germany.

- [3] Photoswitchable Rotaxanes as Building Blocks for Stimuli Responsive Multilayer Architectures on Surfaces
F. B. Schwarz, C. A. Schalley
Poster presentation, Gordon Research Conference on Artificial Molecular Switches & Motors, 07.06.2015. – 12.06.2015, Stonehill College, Easton, MA, United States.

- [4] Mass spectrometric studies of Nitschke's tetrahedral [n] catenanes: From following their structural evolution by IMS to biasing dynamic catenane libraries
F. B Schwarz
Oral presentation, G4 Meeting, 14.08.2015, Rheinische Friedrich-Wilhelms-Universität Bonn, Germany.

- [5] Photoswitchable Rotaxanes as Building Blocks for Stimuli Responsive Multilayer Architectures on Surfaces
F. B. Schwarz
Oral presentation, supramolecular chemistry seminar, 24.09.2015, University of Jyväskylä, Finland.

9.3. Curriculum Vitae

Der Lebenslauf ist in der Online-Version aus Gründen des Datenschutzes nicht enthalten.

Der Lebenslauf ist in der Online-Version aus Gründen des Datenschutzes nicht enthalten.

10. References

- [1] "Anatomy & Physiology", OpenStax College, <http://cnx.org/contents/FPtK1zmmh@8.26:s3XqfSLV@7/Sensory-Perception> (25.11.2016, 18:10).
- [2] M. W. Urban, *Stimuli-Responsive Materials: From Molecules to Nature Mimicking Materials Design*, Royal Society of Chemistry, **2016**.
- [3] P. Iqbal, J. A. Preece, P. M. Mendes, in *Supramolecular Chemistry: From Molecules to Nanomaterials*, John Wiley & Sons, Chichester **2012**.
- [4] V. Balzani, A. Credi, F. M. Raymo, J. F. Stoddart, *Angew. Chem. Int. Ed.* **2000**, *39*, 3348-3391.
- [5] E. R. Kay, D. A. Leigh, F. Zerbetto, *Angew. Chem. Int. Ed.* **2007**, *46*, 72-191.
- [6] "The Nobel Prize in Chemistry 2016", Nobel Media AB, http://www.nobelprize.org/nobel_prizes/chemistry/laureates/2016/, (26.11.2016, 09:10).
- [7] C. O. Dietrich-Buchecker, J. P. Sauvage, J. M. Kern, *J. Am. Chem. Soc.* **1984**, *106*, 3043-3045.
- [8] A. Livoreil, C. O. Dietrich-Buchecker, J.-P. Sauvage, *J. Am. Chem. Soc.* **1994**, *116*, 9399-9400.
- [9] R. A. Bissell, E. Cordova, A. E. Kaifer, J. F. Stoddart, *Nature* **1994**, *369*, 133-137.
- [10] J. D. Badjić, V. Balzani, A. Credi, S. Silvi, J. F. Stoddart, *Science* **2004**, *303*, 1845-1849.
- [11] R. A. van Delden, M. K. J. ter Wiel, M. M. Pollard, J. Vicario, N. Koumura, B. L. Feringa, *Nature* **2005**, *437*, 1337-1340.
- [12] V. Balzani, A. Credi, M. Venturi, *ChemPhysChem* **2008**, *9*, 202-220.
- [13] a) J. Berna, D. A. Leigh, M. Lubomska, S. M. Mendoza, E. M. Perez, P. Rudolf, G. Teobaldi, F. Zerbetto, *Nat. Mater.* **2005**, *4*, 704-710; b) Y. Liu, A. H. Flood, P. A. Bonvallet, S. A. Vignon, B. H. Northrop, H.-R. Tseng, J. O. Jeppesen, T. J. Huang, B. Brough, M. Baller, S. Magonov, S. D. Solares, W. A. Goddard, C.-M. Ho, J. F. Stoddart, *J. Am. Chem. Soc.* **2005**, *127*, 9745-9759.
- [14] a) S. Richter, Dissertation, Freie Universität Berlin, Berlin, **2013**; b) J. Poppenberg, Dissertation, Freie Universität Berlin, Berlin, **2013**; c) C. H. H. Traulsen, Dissertation, Freie Universität Berlin, Berlin, **2014**.
- [15] a) J. Poppenberg, S. Richter, E. Darlatt, C. H. H. Traulsen, H. Min, W. E. S. Unger, C. A. Schalley, *Surf. Sci.* **2012**, *606*, 367-377; b) S. Richter, C. H. H. Traulsen, T. Heinrich, J. Poppenberg, C. Leppich, M. Holzweber, W. E. S. Unger, C. A. Schalley, *J. Phys. Chem. C* **2013**, *117*, 18980-18985; c) C. H. H. Traulsen, V. Kunz, T. Heinrich, S. Richter, M. Holzweber, A. Schulz, L. K. S. von Krbek, U. T. J. Scheuschner, J. Poppenberg, W. E. S. Unger, C. A. Schalley, *Langmuir* **2013**, *29*, 14284-14292; d) T. Heinrich, C. H. H. Traulsen, M. Holzweber, S. Richter, V. Kunz, S. K. Kastner, S. O. Krabbenborg, J. Huskens, W. E. S. Unger, C. A. Schalley, *J. Am. Chem. Soc.* **2015**, *137*, 4382-4390.
- [16] J.-M. Lehn, *Angew. Chem.* **1990**, *102*, 1347-1362.
- [17] J. W. Steed, P. A. Gale, *Supramolecular Chemistry: From Molecules to Nanomaterials*, Wiley-VCH, **2012**.
- [18] W. M. Latimer, W. H. Rodebush, *J. Am. Chem. Soc.* **1920**, *42*, 1419-1433.
- [19] C. J. Pedersen, *J. Am. Chem. Soc.* **1967**, *89*, 7017-7036.
- [20] a) J.-M. Lehn, *Angew. Chem. Int. Ed.* **1988**, *27*, 89-112; b) D. J. Cram, *Angew. Chem. Int. Ed.* **1988**, *27*, 1009-1020; c) C. J. Pedersen, *Angew. Chem. Int. Ed.* **1988**, *27*, 1021-1027.
- [21] G. M. Whitesides, B. Grzybowski, *Science* **2002**, *295*, 2418-2421.
- [22] J. W. Steed, J. L. Atwood, *Supramolecular Chemistry*, Wiley, Chichester, **2009**.
- [23] a) H.-J. Schneider, A. K. Yatsimirsky, *Chem. Soc. Rev.* **2008**, *37*, 263-277; b) F. Vögtle, E. Weber, *Host Guest Complex Chemistry Macrocycles: Synthesis, Structures, Applications*, Springer-Verlag, Berlin Heidelberg New York Tokyo, **1985**;

- c) D. J. Cram, J. M. Cram, *Science* **1974**, *183*, 803-809; d) J. F. Stoddart, *Annu. Rep. Prog. Chem., Sect. B: Org. Chem.* **1988**, *85*, 353-386; e) C. A. Schalley, *Int. J. Mass Spectrom.* **2000**, *194*, 11-39.
- [24] a) C. A. Hunter, *J. Am. Chem. Soc.* **1992**, *114*, 5303-5311; b) F. Vögtle, S. Meier, R. Hoss, *Angew. Chem. Int. Ed.* **1992**, *31*, 1619-1622.
- [25] a) E. V. Dzyuba, L. Kaufmann, N. L. Löw, A. K. Meyer, H. D. F. Winkler, K. Rissanen, C. A. Schalley, *Org. Lett.* **2011**, *13*, 4838-4841; b) G. M. Hübner, J. Gläser, C. Seel, F. Vögtle, *Angew. Chem. Int. Ed.* **1999**, *38*, 383-386; c) R. Jäger, F. Vögtle, *Angew. Chem. Int. Ed.* **1997**, *36*, 930-944.
- [26] B. Baytekin, S. S. Zhu, B. Brusilowskij, J. Illigen, J. Ranta, J. Huuskonen, L. Russo, K. Rissanen, L. Kaufmann, C. A. Schalley, *Chem. Eur. J.* **2008**, *14*, 10012-10028.
- [27] D. B. Amabilino, J. F. Stoddart, *Chem. Rev.* **1995**, *95*, 2725-2828.
- [28] J. P. Sauvage, C. O. Dietrich-Buchecker, *Molecular Catenanes, Rotaxanes and Knots*, Wiley, Weinheim, **1999**.
- [29] K. S. Chichak, S. J. Cantrill, A. R. Pease, S.-H. Chiu, G. W. V. Cave, J. L. Atwood, J. F. Stoddart, *Science* **2004**, *304*, 1308-1312.
- [30] a) J. F. Nierengarten, C. O. Dietrich-Buchecker, J. P. Sauvage, *J. Am. Chem. Soc.* **1994**, *116*, 375-376; b) C. O. Dietrich-Buchecker, J. F. Nierengarten, J. P. Sauvage, N. Armaroli, V. Balzani, L. De Cola, *J. Am. Chem. Soc.* **1993**, *115*, 11237-11244; c) H. Adams, E. Ashworth, G. A. Breault, J. Guo, C. A. Hunter, P. C. Mayers, *Nature* **2001**, *411*, 763-763.
- [31] a) E. Wasserman, *J. Am. Chem. Soc.* **1960**, *82*, 4433-4434; b) H. L. Frisch, E. Wasserman, *J. Am. Chem. Soc.* **1961**, *83*, 3789-3795.
- [32] C. O. Dietrich-Buchecker, J. P. Sauvage, J. P. Kintzinger, *Tetrahedron Lett.* **1983**, *24*, 5095-5098.
- [33] a) G. Barin, R. S. Forgan, J. F. Stoddart, *Proc. R. Soc. A* **2012**, *468*, 2849-2880; b) L. Fang, M. A. Olson, D. Benitez, E. Tkatchouk, W. A. Goddard, J. F. Stoddart, *Chem. Soc. Rev.* **2010**, *39*, 17-29.
- [34] P. L. Anelli, N. Spencer, J. F. Stoddart, *J. Am. Chem. Soc.* **1991**, *113*, 5131-5133.
- [35] P. R. Ashton, P. J. Campbell, P. T. Glink, D. Philp, N. Spencer, J. F. Stoddart, E. J. T. Chrystal, S. Menzer, D. J. Williams, P. A. Tasker, *Angew. Chem. Int. Ed.* **1995**, *34*, 1865-1869.
- [36] C. A. Schalley, T. Weilandt, J. Brüggemann, F. Vögtle, in *Templates in Chemistry I* (Eds.: C. A. Schalley, F. Vögtle, K. H. Dötz), Springer Berlin Heidelberg, Berlin, Heidelberg, **2004**.
- [37] K. E. Griffiths, J. F. Stoddart, *Pure Appl. Chem.* **2008**, *80*, 485-506.
- [38] a) E. R. Kay, D. A. Leigh, *Angew. Chem. Int. Ed.* **2015**, *54*, 10080-10088; b) M. Peplow, *Nature* **2015**, *525*, 18-21; c) S. Erbas-Cakmak, D. A. Leigh, C. T. McTernan, A. L. Nussbaumer, *Chem. Rev.* **2015**, *115*, 10081-10206.
- [39] C. G. Collins, E. M. Peck, P. J. Kramer, B. D. Smith, *Chem. Sci.* **2013**, *4*, 2557-2563.
- [40] N. Armaroli, V. Balzani, J.-P. Collin, P. Gaviña, J.-P. Sauvage, B. Ventura, *J. Am. Chem. Soc.* **1999**, *121*, 4397-4408.
- [41] H.-R. Tseng, S. A. Vignon, J. F. Stoddart, *Angew. Chem. Int. Ed.* **2003**, *42*, 1491-1495.
- [42] a) M.-M. Russew, S. Hecht, *Adv. Mater.* **2010**, *22*, 3348-3360; b) S. Yagai, A. Kitamura, *Chem. Soc. Rev.* **2008**, *37*, 1520-1529; c) X. Yan, F. Wang, B. Zheng, F. Huang, *Chem. Soc. Rev.* **2012**, *41*, 6042-6065; d) T. Muraoka, K. Kinbara, *J. Photochem. Photobiol. C* **2012**, *13*, 136-147.
- [43] G. v. Büнау, T. Wolff, *Photochemie*, Wiley-VCH, Weinheim, **1987**.
- [44] S. K. Upadhyay, *Chemical Kinetics and Reaction Dynamics*, Springer, New York, **2006**.
- [45] D. Wöhrle, M. W. Tausch, W.-D. Stohrer, *Photochemie*, Wiley-VCH, Weinheim, **1998**.
- [46] R. B. Woodward, R. Hoffmann, *Angew. Chem. Int. Ed.* **1969**, *8*, 781-853.
- [47] H. M. D. Bandara, S. C. Burdette, *Chem. Soc. Rev.* **2012**, *41*, 1809-1825.
- [48] M. Irie, *Chem. Rev.* **2000**, *100*, 1685-1716.
- [49] Y. Yokoyama, *Chem. Rev.* **2000**, *100*, 1717-1740.

- [50] G. Berkovic, V. Krongauz, V. Weiss, *Chem. Rev.* **2000**, *100*, 1741-1754.
- [51] E. Mitscherlich, *Ann. Pharm.* **1834**, *12*, 311-311.
- [52] G. S. Hartley, *Nature* **1937**, *140*, 281-281.
- [53] K. Hunger, *Industrial Dyes: Chemistry, Properties, Applications*, Wiley-VCH, Weinheim, **2003**.
- [54] K. G. Yager, C. J. Barrett, *J. Photochem. Photobiol. A* **2006**, *182*, 250-261.
- [55] A. A. Beharry, G. A. Woolley, *Chem. Soc. Rev.* **2011**, *40*, 4422-4437.
- [56] H. Fliegl, A. Köhn, C. Hättig, R. Ahlrichs, *J. Am. Chem. Soc.* **2003**, *125*, 9821-9827.
- [57] H. Koshima, N. Ojima, H. Uchimoto, *J. Am. Chem. Soc.* **2009**, *131*, 6890-6891.
- [58] J. Griffiths, *Chem. Soc. Rev.* **1972**, *1*, 481-493.
- [59] S. Monti, G. Orlandi, P. Palmieri, *Chem. Phys.* **1982**, *71*, 87-99.
- [60] F. W. Schulze, H. J. Petrick, H. K. Cammenga, H. Klinge, *Z. Phys. Chem.* **1977**, *107*, 1-19.
- [61] H. Rau, *Angew. Chem. Int. Ed.* **1973**, *12*, 224-235.
- [62] E. V. Brown, G. R. Granneman, *J. Am. Chem. Soc.* **1975**, *97*, 621-627.
- [63] a) C.-W. Chang, Y.-C. Lu, T.-T. Wang, E. W.-G. Diao, *J. Am. Chem. Soc.* **2004**, *126*, 10109-10118; b) T. Asano, T. Yano, T. Okada, *J. Am. Chem. Soc.* **1982**, *104*, 4900-4904.
- [64] D. P. Hoffman, S. R. Ellis, R. A. Mathies, *J. Phys. Chem. A* **2013**, *117*, 11472-11478.
- [65] a) M. Baroncini, S. Silvi, M. Venturi, A. Credi, *Angew. Chem. Int. Ed.* **2012**, *51*, 4223-4226; b) T. Avellini, H. Li, A. Coskun, G. Barin, A. Trabolsi, A. N. Basuray, S. K. Dey, A. Credi, S. Silvi, J. F. Stoddart, M. Venturi, *Angew. Chem. Int. Ed.* **2012**, *51*, 1611-1615; c) E. Merino, M. Ribagorda, *Beilstein J. Org. Chem.* **2012**, *8*, 1071-1090; d) M. Baroncini, G. Ragazzon, S. Silvi, M. Venturi, A. Credi, *Pure Appl. Chem.* **2015**, *87*, 537.
- [66] H. Murakami, A. Kawabuchi, K. Kotoo, M. Kunitake, N. Nakashima, *J. Am. Chem. Soc.* **1997**, *119*, 7605-7606.
- [67] a) K.-S. Jeong, K.-J. Chang, Y.-J. An, *Chem. Commun.* **2003**, 1450-1451; b) K.-J. Chang, Y.-J. An, H. Uh, K.-S. Jeong, *J. Org. Chem.* **2004**, *69*, 6556-6563.
- [68] a) E. Fischer, Y. Hirshberg, *J. Chem. Soc.* **1952**, *11*, 4522-4524; b) R. Heiligman-Rim, Y. Hirshberg, E. Fischer, *J. Phys. Chem.* **1962**, *66*, 2470-2477.
- [69] R. Klajn, *Chem. Soc. Rev.* **2014**, *43*, 148-184.
- [70] H. Gorner, *Phys. Chem. Chem. Phys.* **2001**, *3*, 416-423.
- [71] J. Whelan, D. Abdallah, J. Wojtyk, E. Buncel, *J. Mater. Chem.* **2010**, *20*, 5727-5735.
- [72] F. M. Raymo, S. Giordani, *J. Am. Chem. Soc.* **2001**, *123*, 4651-4652.
- [73] V. I. Minkin, *Chem. Rev.* **2004**, *104*, 2751-2776.
- [74] R. Rosario, D. Gust, M. Hayes, F. Jahnke, J. Springer, A. A. Garcia, *Langmuir* **2002**, *18*, 8062-8069.
- [75] K. Wagner, R. Byrne, M. Zanoni, S. Gambhir, L. Dennany, R. Breukers, M. Higgins, P. Wagner, D. Diamond, G. G. Wallace, D. L. Officer, *J. Am. Chem. Soc.* **2011**, *133*, 5453-5462.
- [76] C. Lenoble, R. S. Becker, *J. Phys. Chem.* **1986**, *90*, 62-65.
- [77] G. O'Bryan, B. M. Wong, J. R. McElhanon, *ACS Appl. Mater. Interfaces* **2010**, *2*, 1594-1600.
- [78] S. A. Krysanov, M. V. Alfimov, *Chem. Phys. Lett.* **1982**, *91*, 77-80.
- [79] S. Swansburg, E. Buncel, R. P. Lemieux, *J. Am. Chem. Soc.* **2000**, *122*, 6594-6600.
- [80] N. W. Tyer, R. S. Becker, *J. Am. Chem. Soc.* **1970**, *92*, 1289-1294.
- [81] K. H. Fries, J. D. Driskell, S. Samanta, J. Locklin, *Anal. Chem.* **2010**, *82*, 3306-3314.
- [82] G. Smets, F. de Blauwe, *Pure Appl. Chem.* **1974**, *39*, 225-238.
- [83] T. Sakata, Y. Yan, G. Marriott, *Proc. Natl. Acad. Sci. U. S. A.* **2005**, *102*, 4759-4764.
- [84] I. Willner, R. Blonder, A. Dagan, *J. Am. Chem. Soc.* **1994**, *116*, 9365-9366.
- [85] D. Samanta, R. Klajn, *Adv. Opt. Mater.* **2016**, *4*, 1373-1377.
- [86] W. Zhou, D. Chen, J. Li, J. Xu, J. Lv, H. Liu, Y. Li, *Org. Lett.* **2007**, *9*, 3929-3932.
- [87] D. Hernandez-Melo, J. Tiburcio, *Chem. Commun.* **2015**, *51*, 17564-17567.
- [88] S. Silvi, A. Arduini, A. Pochini, A. Secchi, M. Tomasulo, F. M. Raymo, M. Baroncini, A. Credi, *J. Am. Chem. Soc.* **2007**, *129*, 13378-13379.

- [89] D. P. Woodruff, T. A. Delchar, *Modern Techniques of Surface Science*, Cambridge University Press, Cambridge, **1994**.
- [90] A. Ulman, *An Introduction to Ultrathin Organic Films*, Academic Press, San Diego, **1991**.
- [91] a) I. Langmuir, *Trans. Faraday Soc.* **1920**, *15*, 62-74; b) K. B. Blodgett, *J. Am. Chem. Soc.* **1935**, *57*, 1007-1022.
- [92] W. C. Bigelow, D. L. Pickett, W. A. Zisman, *J. Colloid Sci.* **1946**, *1*, 513-538.
- [93] L. Netzer, J. Sagiv, *J. Am. Chem. Soc.* **1983**, *105*, 674-676.
- [94] D. L. Allara, R. G. Nuzzo, *Langmuir* **1985**, *1*, 45-52.
- [95] R. G. Nuzzo, D. L. Allara, *J. Am. Chem. Soc.* **1983**, *105*, 4481-4483.
- [96] J. C. Love, L. A. Estroff, J. K. Kriebel, R. G. Nuzzo, G. M. Whitesides, *Chem. Rev.* **2005**, *105*, 1103-1170.
- [97] C. Vericat, M. E. Vela, G. Benitez, P. Carro, R. C. Salvarezza, *Chem. Soc. Rev.* **2010**, *39*, 1805-1834.
- [98] a) L. H. Dubois, R. G. Nuzzo, *Annu. Rev. Phys. Chem.* **1992**, *43*, 437-463; b) A. Hatzor, T. Moav, H. Cohen, S. Matlis, J. Libman, A. Vaskevich, A. Shanzer, I. Rubinstein, *J. Am. Chem. Soc.* **1998**, *120*, 13469-13477; c) C. Silien, M. Buck, G. Goretzki, D. Lahaye, N. R. Champness, T. Weidner, M. Zharnikov, *Langmuir* **2009**, *25*, 959-967; d) P. E. Laibinis, G. M. Whitesides, D. L. Allara, Y. T. Tao, A. N. Parikh, R. G. Nuzzo, *J. Am. Chem. Soc.* **1991**, *113*, 7152-7167; e) A. Carvalho, M. Geissler, H. Schmid, B. Michel, E. Delamarche, *Langmuir* **2002**, *18*, 2406-2412.
- [99] a) E. Ruckenstein, Z. F. Li, *Adv. Colloid Interface Sci.* **2005**, *113*, 43-63; b) D. D. Gandhi, M. Lane, Y. Zhou, A. P. Singh, S. Nayak, U. Tisch, M. Eizenberg, G. Ramanath, *Nature* **2007**, *447*, 299-302; c) A. R. Morrill, D. T. Duong, S. J. Lee, M. Moskovits, *Chem. Phys. Lett.* **2009**, *473*, 116-119; d) B. M. Silverman, K. A. Wieghaus, J. Schwartz, *Langmuir* **2005**, *21*, 225-228.
- [100] D. L. Allara, R. G. Nuzzo, *Langmuir* **1985**, *1*, 52-66.
- [101] J. M. Buriak, *Chem. Rev.* **2002**, *102*, 1271-1308.
- [102] a) H. A. Biebuyck, C. D. Bain, G. M. Whitesides, *Langmuir* **1994**, *10*, 1825-1831; b) A. Ulman, *Chem. Rev.* **1996**, *96*, 1533-1554.
- [103] L. Strong, G. M. Whitesides, *Langmuir* **1988**, *4*, 546-558.
- [104] M. Malicki, Z. Guan, S. D. Ha, G. Heimel, S. Barlow, M. Rumi, A. Kahn, S. R. Marder, *Langmuir* **2009**, *25*, 7967-7975.
- [105] A. Ulman, *Adv. Mater.* **1990**, *2*, 573-582.
- [106] M. E. McGovern, K. M. R. Kallury, M. Thompson, *Langmuir* **1994**, *10*, 3607-3614.
- [107] T. P. Sullivan, W. T. S. Huck, *Eur. J. Org. Chem.* **2003**, *2003*, 17-29.
- [108] G. M. Credo, A. K. Boal, K. Das, T. H. Galow, V. M. Rotello, D. L. Feldheim, C. B. Gorman, *J. Am. Chem. Soc.* **2002**, *124*, 9036-9037.
- [109] K. Ariga, J. P. Hill, Q. Ji, *Phys. Chem. Chem. Phys.* **2007**, *9*, 2319-2340.
- [110] R. K. Iler, *J. Colloid Interface Sci.* **1966**, *21*, 569-594.
- [111] a) G. Decher, J. D. Hong, *Ber. Bunsen-Ges. Phys. Chem.* **1991**, *95*, 1430-1434; b) G. Decher, J. D. Hong, J. Schmitt, *Thin Solid Films* **1992**, *210*, 831-835; c) G. Decher, J.-D. Hong, *Macromol. Symp.* **1991**, *46*, 321-327.
- [112] U. S. Schubert, H. Hofmeier, G. R. Newkome, *Modern Terpyridine Chemistry*, Wiley-VCH, Weinheim **2006**.
- [113] a) J. J. Richardson, M. Björnalm, F. Caruso, *Science* **2015**, *348*, 6233; b) C. R. South, M. Weck, *Langmuir* **2008**, *24*, 7506-7511; c) V. Piñón, M. Weck, *Langmuir* **2012**, *28*, 3279-3284; d) M. Wanunu, R. Popovitz-Biro, H. Cohen, A. Vaskevich, I. Rubinstein, *J. Am. Chem. Soc.* **2005**, *127*, 9207-9215; e) Y. Chaikin, H. Leader, R. Popovitz-Biro, A. Vaskevich, I. Rubinstein, *Langmuir* **2011**, *27*, 1298-1307; f) P. C. Mondal, J. Yekkoni Lakshmanan, H. Hamoudi, M. Zharnikov, T. Gupta, *J. Phys. Chem. C* **2011**, *115*, 16398-16404; g) T. Gupta, P. C. Mondal, A. Kumar, Y. L. Jeyachandran, M. Zharnikov, *Adv. Funct. Mater.* **2013**, *23*, 4227-4235; h) G. de Ruiter, M. Lahav, M. E. van der Boom, *Acc. Chem. Res.* **2014**, *47*, 3407-3416; i) M. Altman, A. D. Shukla, T. Zubkov, G. Evmenenko, P. Dutta, M. E. van der Boom, *J. Am. Chem. Soc.* **2006**, *128*, 7374-7382; j) N. Tuccitto, I. Delfanti, V. Torrisi, F.

- Scandola, C. Chiorboli, V. Stepanenko, F. Wurthner, A. Licciardello, *Phys. Chem. Chem. Phys.* **2009**, *11*, 4033-4038; k) N. Tuccitto, V. Ferri, M. Cavazzini, S. Quici, G. Zhavnerko, A. Licciardello, M. A. Rampi, *Nat. Mater.* **2009**, *8*, 41-46.
- [114] V. V. Rostovtsev, L. G. Green, V. V. Fokin, K. B. Sharpless, *Angew. Chem. Int. Ed.* **2002**, *41*, 2596-2599.
- [115] D. Samanta, A. Sarkar, *Chem. Soc. Rev.* **2011**, *40*, 2567-2592.
- [116] N. K. Devaraj, G. P. Miller, W. Ebina, B. Kakaradov, J. P. Collman, E. T. Kool, C. E. D. Chidsey, *J. Am. Chem. Soc.* **2005**, *127*, 8600-8601.
- [117] G. K. Such, J. F. Quinn, A. Quinn, E. Tjijto, F. Caruso, *J. Am. Chem. Soc.* **2006**, *128*, 9318-9319.
- [118] a) W. R. Browne, B. L. Feringa, *Annu. Rev. Phys. Chem.* **2009**, *60*, 407-428; b) J. L. Zhang, J. Q. Zhong, J. D. Lin, W. P. Hu, K. Wu, G. Q. Xu, A. T. S. Wee, W. Chen, *Chem. Soc. Rev.* **2015**, *44*, 2998-3022; c) A. M. Ross, H. Nandivada, J. Lahann, in *Handbook of Stimuli-Responsive Materials*, Wiley-VCH, Weinheim, **2011**, pp. 139-163.
- [119] R. Klajn, J. F. Stoddart, B. A. Grzybowski, *Chem. Soc. Rev.* **2010**, *39*, 2203-2237.
- [120] a) N. Katsonis, M. Lubomska, M. M. Pollard, B. L. Feringa, P. Rudolf, *Prog. Surf. Sci.* **2007**, *82*, 407-434; b) R. Klajn, *Pure Appl. Chem.* **2010**, *82*, 2247-2279.
- [121] a) M. J. Comstock, N. Levy, A. Kirakosian, J. Cho, F. Lauterwasser, J. H. Harvey, D. A. Strubbe, J. M. J. Fréchet, D. Trauner, S. G. Louie, M. F. Crommie, *Phys. Rev. Lett.* **2007**, *99*, 038301; b) X. L. Zhou, X. Y. Zhu, J. M. White, *Surf. Sci. Rep.* **1991**, *13*, 73-220.
- [122] K. Morgenstern, *Prog. Surf. Sci.* **2011**, *86*, 115-161.
- [123] a) L. Raehm, J.-M. Kern, J.-P. Sauvage, C. Hamann, S. Palacin, J.-P. Bourgoïn, *Chem. Eur. J.* **2002**, *8*, 2153-2162; b) A. N. Shipway, E. Katz, I. Willner, in *Molecular Machines and Motors*, Springer, Berlin, Heidelberg, **2001**, pp. 237-281; c) E. Katz, O. Lioubashevsky, I. Willner, *J. Am. Chem. Soc.* **2004**, *126*, 15520-15532.
- [124] I. Willner, V. Pardo-Yissar, E. Katz, K. T. Ranjit, *J. Electroanal. Chem.* **2001**, *497*, 172-177.
- [125] a) B. C. Bunker, D. L. Huber, J. G. Kushmerick, T. Dunbar, M. Kelly, C. Matzke, J. Cao, J. O. Jeppesen, J. Perkins, A. H. Flood, J. F. Stoddart, *Langmuir* **2007**, *23*, 31-34; b) D. Patra, H. Zhang, S. Sengupta, A. Sen, *ACS Nano* **2013**, *7*, 7674-7679.
- [126] I. A. Banerjee, L. Yu, H. Matsui, *J. Am. Chem. Soc.* **2003**, *125*, 9542-9543.
- [127] H. J. Whitlow, K. Kristiansen, O. Hunderi, in *Surface Characterization*, Wiley-VCH, Weinheim **2007**, pp. 1-52.
- [128] J. C. Vickerman, I. Gilmore, *Surface Analysis: The Principal Techniques*, Wiley, Chichester, **2009**.
- [129] M. Hesse, H. Meier, B. Zeeh, *Spektroskopische Methoden in der organischen Chemie, Vol. 7*, Thieme, Stuttgart, New York **2005**.
- [130] O. Ivashenko, J. T. van Herpt, B. L. Feringa, P. Rudolf, W. R. Browne, *Langmuir* **2013**, *29*, 4290-4297.
- [131] K. L. Mittal, *Contact Angle, Wettability and Adhesion, Vol. 6*, CRC Press, **2009**.
- [132] T. Young, *Philos. Trans. R. Soc. London* **1805**, *95*, 65-87.
- [133] P. Wan, Y. Jiang, Y. Wang, Z. Wang, X. Zhang, *Chem. Commun.* **2008**, *44*, 5710-5712.
- [134] A. Einstein, *Ann. Phys.* **1905**, *322*, 132-148.
- [135] J. Stöhr, *NEXAFS Spectroscopy*, Springer, Heidelberg, **1996**.
- [136] a) W. Kossel, *Z. Phys.* **1920**, *1*, 119-134; b) R. d. L. Kronig, *Z. Phys.* **1931**, *70*, 317-323.
- [137] Helmholtz-Institut Berlin, https://www.helmholtz-berlin.de/quellen/bessy/elektronenspeicherring/wie-funktioniert-bessy_en.html, (26.10.2016, 17:22).
- [138] E. Darlatt, Dissertation, Freie Universität Berlin (Berlin), **2013**.
- [139] S. Richter, J. Poppenberg, C. H. H. Traulsen, E. Darlatt, A. Sokolowski, D. Sattler, W. E. S. Unger, C. A. Schalley, *J. Am. Chem. Soc.* **2012**, *134*, 16289-16297.

- [140] H. Hamoudi, P. Kao, A. Nefedov, D. L. Allara, M. Zharnikov, *Beilstein J. Nanotechnol.* **2012**, *3*, 12-24.
- [141] a) F. B. L. Cougnon, J. K. M. Sanders, *Acc. Chem. Res.* **2012**, *45*, 2211-2221; b) P. T. Corbett, J. Leclaire, L. Vial, K. R. West, J.-L. Wietor, J. K. M. Sanders, S. Otto, *Chem. Rev.* **2006**, *106*, 3652-3711; c) J.-M. Lehn, *Chem. Soc. Rev.* **2007**, *36*, 151-160.
- [142] a) A. R. Stefankiewicz, E. Tamanini, G. D. Pantoş, J. K. M. Sanders, *Angew. Chem. Int. Ed.* **2011**, *50*, 5725-5728; b) G. D. Pantoş, P. Pengo, J. K. M. Sanders, *Angew. Chem. Int. Ed.* **2007**, *46*, 194-197.
- [143] Y. R. Hristova, M. M. J. Smulders, J. K. Clegg, B. Breiner, J. R. Nitschke, *Chem. Sci.* **2011**, *2*, 638-641.
- [144] J. R. Nitschke, in *Tomorrow's Chemistry Today*, Wiley-VCH, Weinheim, **2009**, pp. 1-29.
- [145] S. P. Black, D. M. Wood, F. B. Schwarz, T. K. Ronson, J. J. Holstein, A. R. Stefankiewicz, C. A. Schalley, J. K. M. Sanders, J. R. Nitschke, *Chem. Sci.* **2016**, *7*, 2614-2620.
- [146] A. G. Marshall, C. L. Hendrickson, G. S. Jackson, *Mass Spectrom. Rev.* **1998**, *17*, 1-35.
- [147] a) J. B. Fenn, M. Mann, C. K. Meng, S. F. Wong, C. M. Whitehouse, *Mass Spectrom. Rev.* **1990**, *9*, 37; b) J. Fenn, M. Mann, C. Meng, S. Wong, C. Whitehouse, *Science* **1989**, *246*, 64-71.
- [148] E. V. Dzyuba, J. Poppenberg, S. Richter, R. W. Troff, C. A. Schalley, in *Supramolecular Chemistry: From Molecules to Nanomaterials*, John Wiley & Sons, Chichester **2012**.
- [149] a) J. V. Iribarne, B. A. Thomson, *J. Chem. Phys.* **1976**, *64*, 2287-2294; b) B. A. Thomson, J. V. Iribarne, *J. Chem. Phys.* **1979**, *71*, 4451-4463.
- [150] J. B. Fenn, J. Rosell, C. K. Meng, *J. Am. Soc. Mass Spectrom.* **1997**, *8*, 1147-1157.
- [151] a) M. Dole, L. L. Mack, R. L. Hines, R. C. Mobley, L. D. Ferguson, M. B. Alice, *J. Chem. Phys.* **1968**, *49*, 2240-2249; b) P. Kebarle, G. Peschke, *Anal. Chim. Acta* **2000**, *406*, 11-35.
- [152] OMEGA Version 9.2.30, Varian Inc.
- [153] a) L. Schweikhard, G. M. Alber, A. G. Marshall, *J. Am. Soc. Mass Spectrom.* **1993**, *4*, 177-181; b) A. G. Marshall, L. Schweikhard, *Int. J. Mass Spectrom. Ion Processes* **1992**, *118*, 37-70.
- [154] A. G. Marshall, C. L. Hendrickson, G. S. Jackson, *Mass Spectrom. Rev.* **1998**, *17*, 1.
- [155] C. A. Schalley, A. Springer, *Mass Spectrometry and Gas-Phase Chemistry of Non-Covalent Complexes*, Wiley, Hoboken **2009**.
- [156] N. C. Polfer, *Chem. Soc. Rev.* **2011**, *40*, 2211-2221.
- [157] J. Laskin, J. H. Futrell, *Mass Spectrom. Rev.* **2005**, *24*, 135-167.
- [158] a) J. Buback, M. Kullmann, F. Langhojer, P. Nuernberger, R. Schmidt, F. Würthner, T. Brixner, *J. Am. Chem. Soc.* **2010**, *132*, 16510-16519; b) J. Buback, P. Nuernberger, M. Kullmann, F. Langhojer, R. Schmidt, F. Würthner, T. Brixner, *J. Phys. Chem. A* **2011**, *115*, 3924-3935; c) B. Seefeldt, R. Kasper, M. Beining, J. Mattay, J. Arden-Jacob, N. Kemnitzer, K. H. Drexhage, M. Heilemann, M. Sauer, *Photochem. Photobiol. Sci.* **2010**, *9*, 213-220.
- [159] Cache WorkSystem Pro Version 6.1.12.3, Fujitsu Ltd, Krakow, Poland, **2000-2004**.
- [160] L. Kaufmann, E. V. Dzyuba, F. Malberg, N. L. Low, M. Groschke, B. Brusilowskij, J. Huuskonen, K. Rissanen, B. Kirchner, C. A. Schalley, *Org. Biomol. Chem.* **2012**, *10*, 5954-5964.
- [161] F. M. Raymo, S. Giordani, A. J. P. White, D. J. Williams, *J. Org. Chem.* **2003**, *68*, 4158-4169.
- [162] a) K. Hirose, *J. Inclusion Phenom. Macrocyclic Chem.* **2001**, *39*, 193-209; b) K. Hirose, in *Analytical Methods in Supramolecular Chemistry*, Wiley-VCH Weinheim, **2012**, pp. 27-66.
- [163] A. G. Johnston, D. A. Leigh, L. Nezhat, J. P. Smart, M. D. Deegan, *Angew. Chem. Int. Ed.* **1995**, *34*, 1212-1216.

- [164] R. Eelkema, M. M. Pollard, J. Vicario, N. Katsonis, B. S. Ramon, C. W. M. Bastiaansen, D. J. Broer, B. L. Feringa, *Nature* **2006**, *440*, 163-163.
- [165] N. Herzer, S. Hoepfener, U. S. Schubert, *Chem. Commun.* **2010**, *46*, 5634-5652.
- [166] S. Wang, Y. Song, L. Jiang, *J. Photochem. Photobiol. C* **2007**, *8*, 18-29.
- [167] a) J. M. Mativetsky, G. Pace, M. Elbing, M. A. Rampi, M. Mayor, P. Samorì, *J. Am. Chem. Soc.* **2008**, *130*, 9192-9193; b) K. Smaali, S. Lenfant, S. Karpe, M. Oçafrain, P. Blanchard, D. Deresmes, S. Godey, A. Rochefort, J. Roncali, D. Vuillaume, *ACS Nano* **2010**, *4*, 2411-2421; c) M. del Valle, R. Gutierrez, C. Tejedor, G. Cuniberti, *Nat. Nanotechnol.* **2007**, *2*, 176-179; d) N. Katsonis, T. Kudernac, M. Walko, S. J. van der Molen, B. J. van Wees, B. L. Feringa, *Adv. Mater.* **2006**, *18*, 1397-1400.
- [168] a) F. L. Callari, S. Petralia, S. Conoci, S. Sortino, *New J. Chem.* **2008**, *32*, 1899-1903; b) Z. Wang, A.-M. Nygård, M. J. Cook, D. A. Russell, *Langmuir* **2004**, *20*, 5850-5857.
- [169] T. Hugel, N. B. Holland, A. Cattani, L. Moroder, M. Seitz, H. E. Gaub, *Science* **2002**, *296*, 1103-1106.
- [170] a) A. C. Fahrenbach, S. C. Warren, J. T. Inconvati, A.-J. Avestro, J. C. Barnes, J. F. Stoddart, B. A. Grzybowski, *Adv. Mater.* **2013**, *25*, 331-348; b) R. H. El Halabieh, O. Mermut, C. J. Barrett, *Pure Appl. Chem.* **2004**, *76*, 1445; c) H. S. Lim, J. T. Han, D. Kwak, M. Jin, K. Cho, *J. Am. Chem. Soc.* **2006**, *128*, 14458-14459.
- [171] D. Tarn, D. P. Ferris, J. C. Barnes, M. W. Ambrogio, J. F. Stoddart, J. I. Zink, *Nanoscale* **2014**, *6*, 3335-3343.
- [172] H. Adams, F. J. Carver, C. A. Hunter, N. J. Osborne, *Chem. Commun.* **1996**, 2529-2530.
- [173] S. A. Nagamani, Y. Norikane, N. Tamaoki, *J. Org. Chem.* **2005**, *70*, 9304-9313.
- [174] a) K. C. Majumdar, K. Ray, S. Ganai, *Synlett* **2010**, *2010*, 2122-2124; b) R. M. Williams, J. Cao, H. Tsujishima, R. J. Cox, *J. Am. Chem. Soc.* **2003**, *125*, 12172-12178.
- [175] R. J. Lindquist, K. M. Lefler, K. E. Brown, S. M. Dyar, E. A. Margulies, R. M. Young, M. R. Wasielewski, *J. Am. Chem. Soc.* **2014**, *136*, 14912-14923.
- [176] J. Harada, K. Ogawa, S. Tomoda, *Acta Crystallogr. Sect. B* **1997**, *53*, 662-672.
- [177] K. Hirose, *J. Inclusion Phenom. Macrocyclic Chem.* **2001**, *39*, 193-209.
- [178] C. H. H. Traulsen, V. Kunz, T. Heinrich, S. Richter, M. Holzweber, A. Schulz, L. K. S. von Krbek, U. T. J. Scheuschner, J. Poppenberg, W. E. S. Unger, C. A. Schalley, *Langmuir* **2013**, *29*, 14284-14292.
- [179] J. Poppenberg, S. Richter, C. H. H. Traulsen, E. Darlatt, B. Baytekin, T. Heinrich, P. M. Deutinger, K. Huth, W. E. S. Unger, C. A. Schalley, *Chem. Sci.* **2013**, *4*, 3131-3139.
- [180] L. Sharma, T. Matsuoka, T. Kimura, H. Matsuda, *Polym. Adv. Technol.* **2002**, *13*, 481-486.
- [181] T. Heinrich, C. H. H. Traulsen, E. Darlatt, S. Richter, J. Poppenberg, N. L. Traulsen, I. Linder, A. Lippitz, P. M. Dietrich, B. Dib, W. E. S. Unger, C. A. Schalley, *RSC Advances* **2014**, *4*, 17694-17702.
- [182] a) M. Baroncini, S. d'Agostino, G. Bergamini, P. Ceroni, A. Comotti, P. Sozzani, I. Bassanetti, F. Grepioni, T. M. Hernandez, S. Silvi, M. Venturi, A. Credi, *Nat. Chem.* **2015**, *7*, 634-640; b) O. S. Bushuyev, A. Tomberg, T. Friščić, C. J. Barrett, *J. Am. Chem. Soc.* **2013**, *135*, 12556-12559.
- [183] J. G. Victor, J. M. Torkelson, *Macromolecules* **1987**, *20*, 2241-2250.
- [184] S. Erbas-Cakmak, D. A. Leigh, C. T. McTernan, A. L. Nussbaumer, *Chem. Rev.* **2015**, *115*, 10081-10206.
- [185] a) A. Coskun, M. Banaszak, R. D. Astumian, J. F. Stoddart, B. A. Grzybowski, *Chem. Soc. Rev.* **2012**, *41*, 19-30; b) M. M. Boyle, R. A. Smaldone, A. C. Whalley, M. W. Ambrogio, Y. Y. Botros, J. F. Stoddart, *Chem. Sci.* **2011**, *2*, 204-210; c) J. J. Davis, G. A. Orłowski, H. Rahman, P. D. Beer, *Chem. Commun.* **2010**, *46*, 54-63.
- [186] E. Coronado, P. Gavina, S. Tatay, *Chem. Soc. Rev.* **2009**, *38*, 1674-1689.
- [187] F. B. Schwarz, T. Heinrich, J. O. Kaufmann, A. Lippitz, R. Puttreddy, K. Rissanen, W. E. S. Unger, C. A. Schalley, *Chem. Eur. J.* **2016**, *22*, 14383-14389.
- [188] V. Grosshenny, F. M. Romero, R. Ziessel, *J. Org. Chem.* **1997**, *62*, 1491-1500.

- [189] a) M. Mauro, A. Aliprandi, D. Septiadi, N. S. Kehr, L. De Cola, *Chem. Soc. Rev.* **2014**, *43*, 4144; b) M. J. Wiester, P. A. Ulmann, C. A. Mirkin, *Angew. Chem. Int. Ed.* **2011**, *50*, 114-137.
- [190] a) J. T. Foy, D. Ray, I. Aprahamian, *Chem. Sci.* **2015**, *6*, 209-213; b) D. Ray, J. T. Foy, R. P. Hughes, I. Aprahamian, *Nat. Chem.* **2012**, *4*, 757-762; c) H. Li, A. C. Fahrenbach, A. Coskun, Z. Zhu, G. Barin, Y. L. Zhao, Y. Y. Botros, J. P. Sauvage, J. F. Stoddart, *Angew. Chem. Int. Ed.* **2011**, *50*, 6782-6788; d) J. Jo, A. Olasz, C. H. Chen, D. Lee, *J. Am. Chem. Soc.* **2013**, *135*, 3620-3632; e) J. M. Dragna, G. Pescitelli, L. Tran, V. M. Lynch, E. V. Anslyn, L. Di Bari, *J. Am. Chem. Soc.* **2012**, *134*, 4398-4407.
- [191] a) J. B. Beck, S. J. Rowan, *J. Am. Chem. Soc.* **2003**, *125*, 13922-13923; b) K. M. Wong, V. W. Yam, *Acc. Chem. Res.* **2011**, *44*, 424-434; c) Y. Tidhar, H. Weissman, S. G. Wolf, A. Gulino, B. Rybtchinski, *Chem. Eur. J.* **2011**, *17*, 6068-6075; d) T. Mitra, K. E. Jelfs, M. Schmidtman, A. Ahmed, S. Y. Chong, D. J. Adams, A. I. Cooper, *Nat. Chem.* **2013**, *5*, 276-281; e) L. Motiei, M. Lahav, D. Freeman, M. E. van der Boom, *J. Am. Chem. Soc.* **2009**, *131*, 3468-3469.
- [192] a) J.-M. Lehn, A. V. Eliseev, *Science* **2001**, *291*, 2331-2332; b) P. T. Corbett, J. Leclaire, L. Vial, K. R. West, J.-L. Wietor, J. K. M. Sanders, S. Otto, *Chem. Rev.* **2006**, *106*, 3652-3711; c) F. B. L. Cougnon, J. K. M. Sanders, *Acc. Chem. Res.* **2012**, *45*, 2211-2221; d) J. Li, P. Nowak, S. Otto, *J. Am. Chem. Soc.* **2013**, *135*, 9222-9239.
- [193] a) M. E. Belowich, J. F. Stoddart, *Chem. Soc. Rev.* **2012**, *41*, 2003-2024; b) N. Giuseppone, J.-M. Lehn, *Chem. Eur. J.* **2006**, *12*, 1715-1722.
- [194] M. Mondal, A. K. H. Hirsch, *Chem. Soc. Rev.* **2014**, *44*, 2455-2488.
- [195] a) P. Mukhopadhyay, P. Y. Zavalij, L. Isaacs, *J. Am. Chem. Soc.* **2006**, *128*, 14093-14102; b) A. Wu, L. Isaacs, *J. Am. Chem. Soc.* **2003**, *125*, 4831-4835.
- [196] K. Osowska, O. S. Miljanic, *Angew. Chem. Int. Ed.* **2011**, *50*, 8345-8349.
- [197] a) A. R. Stefankiewicz, J. K. M. Sanders, *Chem. Commun.* **2013**, *49*, 5820-5822; b) N. Ponnuswamy, F. B. L. Cougnon, G. D. Pantoş, J. K. M. Sanders, *J. Am. Chem. Soc.* **2014**, *136*, 8243-8251; c) I. A. Riddell, M. M. J. Smulders, J. K. Clegg, Y. R. Hristova, B. Breiner, J. D. Thoburn, J. R. Nitschke, *Nat. Chem.* **2012**, *4*, 751-756.
- [198] a) S. Lo, J. Lu, L. Krause, D. Stalke, B. Dittrich, G. H. Clever, *J. Am. Chem. Soc.* **2014**, *137*, 1060-1063; b) M. Han, D. M. Engelhard, G. H. Clever, *Chem. Soc. Rev.* **2014**, *43*, 1848-1860; c) T. R. Cook, P. J. Stang, *Chem. Rev.* **2015**, *115*, 7001-7045; d) N. Kishi, M. Akita, M. Yoshizawa, *Angew. Chem. Int. Ed.* **2014**, *53*, 3604-3607; e) S. Hiraoka, K. Harano, M. Shiro, M. Shionoya, *Angew. Chem. Int. Ed.* **2005**, *44*, 2727-2731.
- [199] a) K. Ghosh, H. B. Yang, B. H. Northrop, M. M. Lyndon, Y. R. Zheng, D. C. Muddiman, P. J. Stang, *J. Am. Chem. Soc.* **2008**, *130*, 5320-5334; b) G. Gil-Ramirez, D. A. Leigh, A. J. Stephens, *Angew. Chem. Int. Ed.* **2015**, *54*, 6110-6150.
- [200] a) A. M. Johnson, R. J. Hooley, *Inorg. Chem.* **2011**, *50*, 4671-4673; b) C. Gütz, R. Hovorka, G. Schnakenburg, A. Lützen, *Chem. Eur. J.* **2013**, *19*, 10890-10894; c) A. Jiménez, R. A. Bilbeisi, T. K. Ronson, S. Zarra, C. Woodhead, J. R. Nitschke, *Angew. Chem. Int. Ed.* **2014**, *53*, 4556-4560.
- [201] A. G. Marshall, C. L. Hendrickson, G. S. Jackson, *Mass Spectrom. Rev.* **1998**, *17*, 1-35.
- [202] a) T. K. Ronson, S. Zarra, S. P. Black, J. R. Nitschke, *Chem. Commun.* **2013**, *49*, 2476-2490; b) X.-P. Zhou, Y. Wu, D. Li, *J. Am. Chem. Soc.* **2013**, *135*, 16062-16065; c) Y. Wu, X.-P. Zhou, J.-R. Yang, D. Li, *Chem. Commun.* **2013**, *49*, 3413-3415; d) J. Dömer, J. C. Sloatweg, F. Hupka, K. Lammertsma, F. E. Hahn, *Angew. Chem. Int. Ed.* **2010**, *49*, 6430-6433.
- [203] a) W. Meng, J. K. Clegg, J. D. Thoburn, J. R. Nitschke, *J. Am. Chem. Soc.* **2011**, *133*, 13652-13660; b) R. W. Saalfrank, B. Demleitner, H. Glaser, H. Maid, D. Bathelt, F. Hampel, W. Bauer, M. Teichert, *Chem. Eur. J.* **2002**, *8*, 2679-2683; c) T. Beissel, R. E. Powers, T. N. Parac, K. N. Raymond, *J. Am. Chem. Soc.* **1999**, *121*, 4200-4206.
- [204] S. P. Black, A. R. Stefankiewicz, M. M. J. Smulders, D. Sattler, C. A. Schalley, J. R. Nitschke, J. K. M. Sanders, *Angew. Chem. Int. Ed.* **2013**, *52*, 5749-5752.

- [205] C. A. Hunter, H. L. Anderson, *Angew. Chem. Int. Ed.* **2009**, *48*, 7488-7499.
- [206] a) A. R. Stefankiewicz, E. Tamanini, G. D. Pantoş, J. K. M. Sanders, *Angew. Chem. Int. Ed.* **2011**, *50*, 5725-5728; b) D. Canevet, E. M. Pérez, N. Martín, *Angew. Chem. Int. Ed.* **2011**, *50*, 9248-9259; c) P. D. W. Boyd, C. a. Reed, *Acc. Chem. Res.* **2005**, *38*, 235-242.
- [207] D. M. Wood, W. Meng, T. K. Ronson, A. R. Stefankiewicz, J. K. M. Sanders, J. R. Nitschke, *Angew. Chem. Int. Ed.* **2015**, *54*, 3988-3992.
- [208] E. Leize, A. Jaffrezic, A. V. Dorsselaer, *J. Mass. Spec.* **1996**, *31*, 537-544.
- [209] P. N. Baxter, R. G. Khoury, J.-M. Lehn, G. Baum, D. Fenske, *Chem. Eur. J.* **2000**, *6*, 4140-4148.
- [210] M. M. Safont-Sempere, G. Fernandez, F. Würthner, *Chem. Rev.* **2011**, *111*, 5784-5814.
- [211] a) K. Acharyya, P. S. Mukherjee, *Chem. Eur. J.* **2014**, *20*, 1646-1657; b) D. Samanta, P. S. Mukherjee, *Chem. Eur. J.* **2014**, *20*, 12483-12492; c) K. Acharyya, S. Mukherjee, P. S. Mukherjee, *J. Am. Chem. Soc.* **2013**, *135*, 554-557; d) B. H. Northrop, Y. R. Zheng, K. W. Chi, P. J. Stang, *Acc. Chem. Res.* **2009**, *42*, 1554-1563.
- [212] N. Sun, J. Sun, E. N. Kitova, J. S. Klassen, *J. Am. Soc. Mass. Spectrom.* **2009**, *20*, 1242-1250.
- [213] S. Bhattacharya, A. Sharma, S. K. Nayak, S. Chattopadhyay, A. K. Mukherjee, *J. Phys. Chem. B* **2003**, *107*, 4213-4217.
- [214] ISO15472:2010, **2010**.
- [215] J. Stöhr, *NEXAFS spectroscopy*, Vol. 25, Springer, Berlin **1992**.
- [216] P. E. Batson, *Phys. Rev. Lett.* **1982**, *49*, 936-940.
- [217] Y. Leydet, F. J. Romero-Salguero, C. Jiménez-Sanchidrián, D. M. Bassani, N. D. McClenaghan, *Inorg. Chim. Acta* **2007**, *360*, 987-994.
- [218] S. L. Potisek, D. A. Davis, N. R. Sottos, S. R. White, J. S. Moore, *J. Am. Chem. Soc.* **2007**, *129*, 13808-13809.
- [219] A. Bheemaraju, J. W. Beattie, Y. Danylyuk, J. Rochford, S. Groysman, *Eur. J. Inorg. Chem.* **2014**, *2014*, 5865-5873.
- [220] *CrysAlisPro 2014*, Agilent Technologies, Version 1.171.136.135.
- [221] G. Sheldrick, *Acta Crystallogr. Sect. A* **2008**, *64*, 112-122.
- [222] O. V. Dolomanov, L. J. Bourhis, R. J. Gildea, J. A. K. Howard, H. Puschmann, *J. Appl. Crystallogr.* **2009**, *42*, 339-341.
- [223] M. Holzweber, T. Heinrich, V. Kunz, S. Richter, C. H. H. Traulsen, C. A. Schalley, W. E. S. Unger, *Anal. Chem.* **2014**, *86*, 5740-5748.
- [224] G. T. Carroll, G. b. London, T. F. n. Landaluce, P. Rudolf, B. L. Feringa, *ACS Nano* **2011**, *5*, 622-630.
- [225] Varian Inc., Santa Clara, USA, **2006**.
- [226] H. Nowell, S. A. Barnett, K. E. Christensen, S. J. Teat, D. R. Allan, *J. Synchrotron Rad.* **2012**, *19*, 435.
- [227] CrystalClear, 2.0 ed., Rigaku Americas and Rigaku Corporation., 9009 TX, USA **1997-2009**.
- [228] CrysAlisPro, 1.171.35.11 ed., Agilent Technologies Yarton, Oxfordshire, UK, **2009-2011**.
- [229] Bruker-Nonius, *APEX, SAINT and XPREP*, Bruker AXS Inc., Madison, Wisconsin, USA, **2013**.
- [230] S. Parsons, *ECLIPSE*, University of Edinburgh, Edinburgh, UK, **2004**.
- [231] C. B. Hubschle, G. M. Sheldrick, B. Dittrich, *J. Appl. Crystallogr.* **2011**, *44*, 1281-1284.
- [232] L. J. Farrugia, *J. Appl. Crystallogr.* **1999**, *32*, 837-838.
- [233] a) G. Sheldrick, *Acta Cryst.* **2008**, *A64*, 112-122; b) G. M. Sheldrick, *Acta. Cryst.* **2015**, *C71*, 3-8.
- [234] L. Palatinus, G. Chapuis, *J. Appl. Crystallogr.* **2007**, *40*, 786-790.
- [235] P. R. Evans, *Acta. Cryst.* **2007**, *D63*, 58-61.
- [236] G. Bricogne, E. Blanc, M. Brandle, C. Flensburg, P. Keller, W. Paciorek, P. Roversi, A. Sharff, O. S. Smart, C. Vonrhein, T. O. Womack, 2.11.2 ed., Global Phasing Ltd., Cambridge, United Kingdom, **2011**.

- [237] O. S. Smart, T. O. Womack, Global Phasing Ltd. , **2014**.
- [238] O. S. Smart, T. O. Womack, C. Flensburg, P. Keller, W. Paciorek, A. Sharff, C. Vonrhein, G. Bricogne, *Acta. Cryst.* **2012**, *D68*, 368-380.
- [239] A. Thorn, B. Dittrich, G. M. Sheldrick, *Acta. Cryst.* **2012**, *A68*, 448-451.
- [240] a) P. van der Sluis, A. L. Spek, *Acta Cryst.* **1990**, *A46*, 194-201; b) A. L. Spek, *Acta. Cryst.* **2015**, *C71*, 9-18.
- [241] A. L. Spek, Dissertation, Utrecht University, Utrecht, The Netherlands, **2008**.